Evolutionary behaviour of AGN: Investigations on BL Lac objects and Seyfert II galaxies

Dissertation
zur Erlangung des Doktorgrades
des Fachbereichs Physik
der Universität Hamburg

vorgelegt von
Volker Beckmann
aus Hamburg

Hamburg
2000

Gutachter der Dissertation:
Prof. Dr. D. Reimers
Prof. Dr. L. Maraschi

Gutachter der Disputation:
Prof. Dr. D. Reimers
Prof. Dr. J. H. M. M. Schmitt

Datum der Disputation:
12. Januar 2001

Dekan des Fachbereichs Physik und Vorsitzender des Promotionsausschusses:
Prof. Dr. F.-W. Büßer

Contents

Abstract

The evolution and nature of AGN is still one of the enigmatic questions in astrophysics. While large and complete Quasar samples are available, special classes of AGN, like BL Lac objects and Seyfert II galaxies, are still rare objects. In this work I present two new AGN samples. The first one is the HRX-BL Lac survey, resulting in a sample of X-ray selected BL Lac objects. This sample results from 223 BL Lac candidates based on a correlation of X-ray sources with radio sources. The identification of this sample is 98% complete. 77 objects have been identified as BL Lac objects and form the HRX-BL Lac complete sample, the largest homogeneous sample of BL Lac objects existing today. For this sample, redshifts are now known for 62 objects (81 %). In total I present 101 BL Lac objects in the enlarged HRX-BL Lac survey, for which redshift information is available for 84 objects. During the HRX-BL Lac survey I found several objects of special interest. 1ES 1517+656 turned out to be the brightest known BL Lac object in the universe. 1ES 0927+500 could be the first BL Lac object with a line detected in the X-ray region. RX J1211+2242 is probably the the counterpart of the up to now unidentified gamma-ray source 3EG J1212+2304. Additionally I present seven candidates for ultra high frequency peaked BL Lac objects. RX J1054+3855 and RX J1153+3517 are rare high redshift X-ray bright QSO or accreting binary systems with huge magnetic fields. For the BL Lac objects I suggest an unified scenario in which giant elliptical galaxies, formed by merging events of spiral galaxies at $z \gtrsim 2$, start as powerful, radio dominated BL Lacs. As the jet gets less powerful, the BL Lacs start to get more X-ray dominated, showing less total luminosities (for $z < 1$). This effect is seen in the different evolutionary behavior detected in high and low frequency cut off BL Lac objects (HBL and LBL, respectively). The model of negative evolution is supported by assumptions about the energetic effects which contribute to the BL Lac phenomenon. I also suggest an extension of the BL Lac definition to objects with a calcium break up to 40 %, but do not support for the HBL the idea of allowing emission lines in the spectra of BL Lac galaxies.

A way to find high redshift BL Lac objects might be the identification of faint X-ray sources (e.g. from the ROSAT All-Sky Survey) with neither optical nor radio counterpart in prominent databases (e.g. POSS plates for the optical, and NVSS/FIRST radio catalogues).

The Seyfert II survey on the southern hemisphere derived a sample of 29 galaxies with 22 in a complete sample. The selection procedure developed in this work is able to select Seyfert II candidates with a success rate of $\sim 40\%$. The Seyfert II galaxies outnumber the Seyfert I by a factor of $3 \ldots 4$ when comparing the total flux of the objects, but are less numerous than the type I objects when studying the core luminosity function. This luminosity function of the Seyfert II cores is the first one presented up to now. Hence it is possible to estimate the number of luminous Type II AGN, and the conclusion is drawn that absorbed AGN with $M_V \lesssim -28\,\mathrm{mag}$ might not exist within the universe. In 25% of the Seyfert II galaxies I find evidence for merging events. In collaboration with Roberto Della Ceca I also showed that it is possible to find Type II AGN by selecting "hard" X-ray sources. I present a prototype of a Type II AGN found within this project.

This work might be the basis to explore the universe for rare objects like BL Lacs and Seyfert II galaxies at higher redshifts. This could give an answer to the question: Whether there are BL Lac objects at redshifts $z \gg 1$ and Type II Quasars or not.

In summary the AGN phenomenon appears to be linked closely to merging and interacting events. For the BL Lac phenomenon the merging area seems to form the progenitor, while the Seyfert II phenomenon could be triggered by merging events. The role of star burst activity in terms of activity of the central engine remains illusive.

Zusammenfassung

Die Entwicklung und Natur der AGN ist nach wie vor eine ungelöste Frage der Astrophysik. Während große und vollständige Sammlungen von Quasaren verfügbar sind, sind vollständige Sammlungen von speziellen AGN-Klassen selten. In dieser Arbeit präsentiere ich zwei neue AGN Sammlungen. Die HRX-BL Lac Suche basiert auf 223 BL Lac Kandidaten aus einer Korrelation von Radio- und Röntgenquellen. Die Identifikation dieser Kandidaten ist zu 98% abgeschlossen. 77 Objekte konnten als BL Lacertae Galaxien identifiziert werden und bilden die vollständige HRX-BL Lac Sammlung, die größte homogene Sammlung dieser Art. Für 62 Objekte (81 %) dieser Sammlung ist die Rotverschiebung bekannt. Insgesamt wurden in der erweiterten HRX-BL Lac Suche 101 BL Lac gefunden, wovon bei 84 die Rotverschiebung bekannt ist. Im Rahmen der BL Lac Suche wurden außerdem mehrere pekuliare Objekte entdeckt und untersucht. 1ES 1517+656 ist der hellste bisher bekannte BL Lac im Universum ist. 1ES 0927+500 könnte der erste BL Lac sein, bei dem sich eine Emissionslinie im Röntgenbereich nachweisen lässt. RX J1211+2242 ist wahrscheinlich das Gegenstück zu der bisher unidentifizierten Gammaquelle 3EG J1212+2304. Weiterhin wurden sieben Kandidaten für BL Lac Objekte mit extrem hohen Peak Frequenzen gefunden. Die Objekte RX J1054+3855 und RX J1153+3517 sind entweder sehr seltene röntgenhelle Quasare, oder aber akkretierende Doppelsterne mit starken Magnetfeldern.

Für die BL Lac Objekte schlage ich ein vereinheitlichendes Modell vor, in dem große elliptische Galaxien, die durch Verschmelzung von Spiralgalaxien bei $z \gtrsim 2$ gebildet wurden, als leuchtkräftige, radiodominierte BL Lac Objekte beginnen. Wenn der Materiestrom aus dem AGN energieärmer wird, so wird der BL Lac stärker röntgendominiert und leuchtärmer (bei $z < 1$). Dieser Effekt äußert sich in unterschiedlichem Entwicklungsverhalten von BL Lac Objekten mit hohen und niedrigen Peak Frequenzen (HBL und LBL). Gestützt wird dieses Modell durch theoretische Arbeiten zur Energieentwicklung von der relevanten Prozesse. Weiterhin schlage ich eine Ausweitung der BL Lac Definition hin zu Objekten mit Kalzium-Kanten bis zu 40% vor, finde für HBL allerdings keinen Hinweis auf deutliche Emissionslinien.

Die Seyfert II Suche auf der südlichen Hemisphäre ergab eine Sammlung von 29 Galaxien von denen 22 eine vollständige Sammlung bilden. Die hierfür entwickelte Suchmethode ermöglicht die Selektion von Seyfert II Kandidaten mit einer Erfolgsrate von $\sim 40\%$. Werden die Gesamthelligkeiten der Objekte untersucht, so finden sich drei- bis viermal mehr Seyfert II als Seyfert I. Der Vergleich der Kernhelligkeiten ergibt jedoch, dass die Seyfert I Galaxien doppelt so häufig sind wie die Seyfert II Objekte. Die erstellte Kernleuchtkraft ist die erste ihrer Art. So kann erstmals die Anzahl von Typ 2 AGN abgeschätzt werden und die Leuchtkraftfunktion lässt den Schluss zu, dass eventuell keine absorbierten AGN mit einer absoluten Helligkeit von $M_V \lesssim -28\,\mathrm{mag}$ im Universum existieren. Bei 25 % der Seyfert II Galaxien finden sich Hinweise auf Verschmelzungsprozesse.

In Zusammenarbeit mit Roberto Della Ceca zeige ich, dass es möglich ist Typ 2 AGN aufgrund ihrer "harten" Röntgenstrahlung zu finden. Ich präsentiere hier einen so gefunden Typ 2 AGN.

Diese Arbeit kann als Basis dienen, um im Universum nach seltenen Objekten wie BL Lac und Seyfert II Galaxien bei hohen Rotverschiebungen zu suchen. Dies könnte die Frage klären, ob BL Lac Objekte bereits bei Rotverschiebungen $z \gg 1$ und Typ II Quasare exisitieren. So schlage ich mehrere Vorgehensnweisen vor, um hochrotverschobene BL Lac Objekte und Seyfert II Galaxien zu finden.

Insgesamt erscheint das AGN Phänomen stark an Verschmelzungs- und Wechselwirkungsprozesse der Muttergalaxien gebunden zu sein. Während bei BL Lac Galaxien die Verschmelzungsphase vor der Existenz des BL Lac stattgefunden hat, ist die Seyfert II Aktivität durch Verschmelzungsprozesse gesteuert. Die Rolle der Sternentstehungsrate in Bezug auf die Aktivität der zentralen AGN Quelle bleibt allerdings weiterhin rätselhaft.

Chapter 1

Introduction

In this chapter I want to address the main questions of this work.

The investigation of the evolution of the universe is one of the main topics in astrophysics. The most luminous objects, for which evolutionary behaviour can be studied, are the galaxies with an active galactic nucleus (AGN)[1]. The class of AGN comprises Seyfert galaxies, LINER, NELG, quasi-stellar objects (QSO), and BL Lac objects. The classification of a galaxy as an AGN is given if at least one of the following attributes is fulfilled:

- bright, point-like, and compact core
- non-thermal continuum emission
- brighter luminosities compared to normal galaxies in all wavelength regions
- broad emission lines
- polarized radiation, especially in BL Lac objects
- variability of the continuum and of the emission lines
- morphological structures like lobes (especially in the radio regime) and jets

The classification into the different groups, like Seyfert I or QSO, is based on phenomenological appearance. The following classification scheme is describes the typical properties, but nevertheless there are transition objects and the classes are not well separated from each other. This fact sometimes causes confusion, when an AGN is classified differently by different authors.

- *Seyfert galaxies.* Most of the Seyfert galaxies are hosted in spiral galaxies (Sarajedini 1999) and show a bright, point-like core. The spectrum is dominated by emission lines, which could be broadened by the velocity dispersion of the emitting gas. Broad emission lines, caused by gas velocities up to $10^4\,\mathrm{km\,sec^{-1}}$ are thought to be emitted from the so-called broad line region (BLR). These features are the allowed low ionized lines (HI, HeI, HeII, FeII, MgII). The forbidden lines seem to originate from a different location within the AGN, the narrow line region (NLR), where velocities have to be as low as $100\ldots1500\,\mathrm{km\,sec^{-1}}$. The most prominent forbidden lines result from oxygen and nitrogen ([OII], [OIII], [NII], [NeIII], [NeIV]).

  While Seyfert I galaxies show narrow forbidden and broad allowed emission lines, the Seyfert II galaxies emit only narrow lines. In the type II class, the allowed lines have similar equivalent widths to the forbidden lines. This is thought to arise from dusty torus which hides the BLR in the case, if Seyfert II galaxies. While Seyfert I galaxies exhibit often strong X-ray, ultraviolet and infrared emission, the Seyfert II galaxies are less luminous in the X-rays. Transition objects between both types are classified as Seyfert 1.5 ... Seyfert 1.9 which refers to the different intensity ratio between

[1] Up to now it is not clear whether Gamma-ray bursts are the most luminous objects in the universe. But these sources fade down rapidly, and AGN are the brightest objects on longer time scales

the broad and the narrow component. Thus the higher the type of the Seyfert, the more the BLR is hidden by the dusty torus (Krull 1997). The Seyfert II phenomenon will be discussed in detail in Chapter 8.

- *LINER and NELG.* The Low Ionization Nuclear Emission Line Regions (LINER) show faint core luminosities and strong emission lines originating from low ionized gas. Expected line widths are $200 \ldots 400\,\mathrm{km\,sec^{-1}}$ and there properties are very similar to the Seyfert II galaxies, but LINER do have weaker forbidden lines. The LINER seem to mark the low energy end of the AGN phenomenon. Narrow Emission Line Galaxies (NELG) show strong X-ray emission like Seyfert I galaxies, but while the H_α line is broad the H_β line is narrow at the same time. Therefore they seem to be reddened Seyfert I galaxies, where the absorption is effective only at wavelengths $\lambda \gg \lambda(\mathrm{H}_\alpha)$. Due to their similar properties in comparison to the Seyfert II galaxies, LINER and NELG will be included in the framework of Chapter 8.

- *Quasars.* The classification of a quasar as a point-like, unresolvable Seyfert galaxy at cosmological distances is based on the historical phenomenological identification. Nowadays it seems that quasars are just luminous Seyfert galaxies (typically Seyfert I type). They are also hosted in galaxies though, due to the bright core and the larger distance, it is much more difficult to examine the environment of the quasars. The distinction from Seyfert I galaxies is done by a luminosity limit. Thus Seyfert galaxies with absolute magnitudes $M_B < 23^{mag}$ are called quasars (Schmidt & Green 1983). Only a small fraction of quasars shows radio emission: Most of the quasars, unlike the BL Lac objects, are radio quiet. Radio loud quasars are distinguished into the class of the radio bright Flat Spectrum Radio Quasars (FSRQ), and the Steep Radio Spectrum Quasars (SRSQ). The latter ones are dominated by radio lobes of the host galaxy, the former have a compact radio structure.

- *Radio galaxies* If the central region of a quasar is hidden but the object ejects bright radio jets and shows bright radio luminosities, the existence of an AGN core is assumed. These radio galaxies are divided into two subgroups, the low-luminosity FR-I galaxies, and the high luminosity FR-II objects, in which the structure is dominated by the radio lobes (Fanaroff & Riley 1974).While the radio lobes are large structures related to the host galaxy, the radio jets seem to originate directly from the central engine. The jets show polarized emission and non-thermal continua, and thus are thought to result from synchrotron emission in the core.

- *Blazars.* The blazars are a special subclass of quasars. This class is dominated by high variability and is subdivided into the BL Lac objects, which are discussed extensively in Chapter 2, the Optical Violent Variables (OVV), and the Highly Polarized Quasars (HPQ). While BL Lacs do not show prominent features in the optical spectrum, OVV and HPQ have broad emission lines. Additionally HPQ show polarization in their continua.

An important question is whether the different AGN types all belong to the same phenomena or not. To examine the distribution of a class of objects in space and to compare their luminosity function with other types of AGN is a powerful tool to determine if they belong to the same parent population or not. The local luminosity function of Seyfert II galaxies will be determined within this work in Chapter 8.

In the case of Seyfert galaxies and Quasars it is widely accepted that they belong to the same class of objects (e.g. Antonucci 1993). On the other hand it was not possible up to now to identify the type II quasars, and thus to find the bright equivalent to the Seyfert II galaxies (e.g. Halpern et al. 1998, Salvati & Maiolino 2000). This question will be discussed in Chapter 9.

For the Blazars the question of unification is even more difficult to decide, while the Blazar phenomenon itself occurs in different types with different evolutionary behaviour. This work wants not only to discuss the properties of BL Lac objects (Chapter 5), but also gives some ideas how to solve the problems with the different types of BL Lac objects (Chapter 7). Based on this, I will make some suggestions how to extend the BL Lac research to more extreme objects, such as radio quiet and high redshift BL Lacs .

Chapter 8 and 7 include the discussion about the unified scheme of BL Lacs and the luminosity function of Seyfert II galaxies. The brief outlook concerning the whole work is written in Chapter 10.

Finally you can find a list of the abbreviations used within this thesis on page 157.

Chapter 2

BL Lac Objects

This chapter will give a description of the history how the BL Lac phenomenon was discovered and studied. After that I will briefly describe the properties of BL Lac objects, the variability, radio and optical properties and the environment in which BL Lacs are found. In section 2.3 the different classes of BL Lac objects will be introduced and the following section gives an overview about the different existing models and unification schemes.

2.1 History of BL Lac astrophysics

The AGN class of BL Lac objects is named after the prototype BL Lacertae (J2000.0: $22^h 02^m 43.3^s + 42^d 16^m 40^s$). This variable object was found by Hoffmeister (1929) at the Sonneberg observatory in Thüringen who classified it as a short period star of $13 - 15$ magnitude and listed it as "363.1929 Lac". The name "BL Lacertae" was given by van Schewick (1941) from the *Universitäts Sternwarte Berlin-Babelsberg* who searched on photographic plates which had been taken at the Sonneberg observatory between December 1927 and September 1933. He found that BL Lacertae is an irregular variable star[1] whose photographic magnitude varies between 13.5 mag and 15.1 mag.

Schmitt (1968) reported that the variable star BL Lacertae coincided with the radio source VRO 42.22.01. This source showed linear polarization at 4.5 and 2.8 cm (MacLeod & Andrew 1968) and rapid variations in the radio spectral flux (Biraud & Véron 1968, Andrew et al. 1969, Gower 1969). A high polarization of 9.8 % was also visible in the steep ($\Gamma = -2.78$) optical spectrum (Visvanathan 1969). The spectrum of BL Lacertae seemed to follow a single power law but, different to other quasars, showed no emission lines (Du Puy et al. 1969, Oke et al. 1969). Racine (1970) reported 0.1 mag variation over a few hours in the optical and flicker of amplitude $\Delta V \simeq 0.03$ mag with durations as short as $\Delta t = 2$ minutes.

The next BL Lac objects to be identified, OJ 287 and PKS 0735+17, were also selected on the basis of unusual radio spectra (Blake 1970). Of course, at that time it was not clear whether BL Lac objects are extragalactic sources or not.

Subsequent optical, infrared, and radio observations by several investigators led Strittmatter et al. (1972) to suggest that objects similar to BL Lacertae comprise a class of quasi-stellar objects.

But due to the lack of emission and absorption lines it was not possible to determine the distance of these variable objects. Pigg and Cohen (1971) tried to put constraints on the redshift by analyzing the radio data of BL Lacertae, but could only give a lower limit of the distance ($d > 200$ pc). Finally Oke and Gunn (1974) were able to determine the redshift of BL Lacertae by identifying absorption features in spectra taken with the 5m Hale telescope between 1969 and 1973. They found the MgI line, the G-band and the calcium-break and derived a redshift of $z \simeq 0.07$ (more accurate measurements show $z = 0.0686$). They also determined the type of the host galaxy from the spectral energy distribution (SED) to be an elliptical galaxy and suggested that the central source is similar to those in 3C 48, 3C 279, and 3C 345. These objects have later been identified as a Sy1.5, a BL Lac object, and a Blazar respectively.

[1] van Schewick wrote: *BL Lac. Unregelmäßig. Halbregelmäßiger Lichtwechsel zeitweise angedeutet, doch erlaubt das geringe Beobachtungsmaterial keinen einwandfreien Schluß auf RV Tauri-Charakter. [...] Der Stern ist nicht rot.*

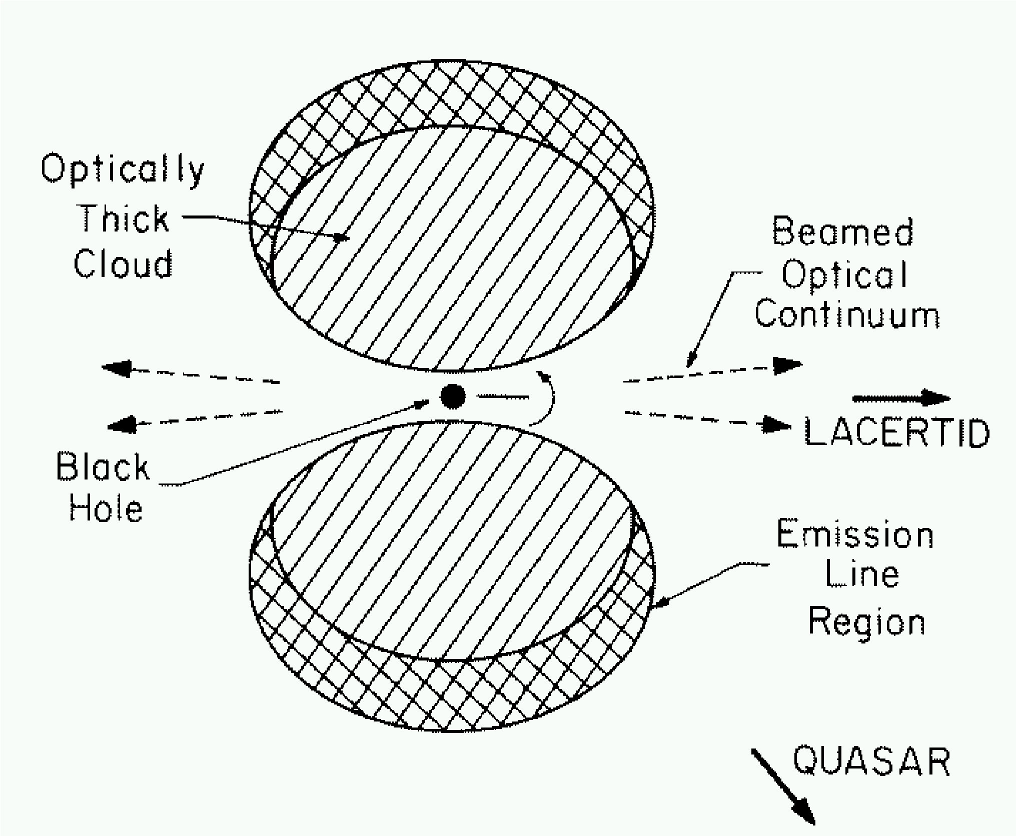

Figure 2.1: Schematic representation of a geometrical interpretation of the BL Lac phenomenon by Blandford & Rees (1978). If the optical continuum is beamed along the symmetry axis, then the emission lines may be suppressed when the source is viewed from this direction. In this figure Lacertid stands for BL Lacs .

The identification of the host galaxy was supported by Kinman (1975), who reported that the surface brightness profile of BL Lacertae is consistent with that of an elliptical galaxy.

It was now clear that BL Lac objects are extragalactic sources with very unusual properties - they showed rapid variability at radio, infrared and visual wavelengths, non-thermal continuum, strong and rapidly varying polarization, and absence of emission lines in the optical spectra. Stein et al. (1976) gave a first overview about the BL Lac topic and listed 30 up to then known objects of this class. For only eight of them a redshift had been determined, sometimes tentative only.

Since the period of discovering the BL Lac phenomenon, three major conferences mark the way of exploring and understanding the nature of this class of AGN.

On the "Pittsburgh Conference on BL Lac Objects" (1978) it was already common sense that BL Lac objects are extragalactic and related to the quasar phenomenon. Stein suggested that BL Lac objects are our most direct observable link to the ultimate energy source of the quasi-stellar objects. He also put up the working hypothesis that the non-thermal BL Lac characteristics are the prototype of the required non-thermal continuum of QSOs in general, with the strength of the non-thermal component being the variable parameter (Stein 1978). Only Markarian 421 was known to be an X-ray bright BL Lac object (Ricketts et al. 1976, Margon et al. 1978). Thus BL Lac objects could only be identified by searching for radio sources with extreme properties, as long as there was no X-ray mission to search effectively for BL Lac candidates. The most important insight from this conference was probably the work presented by Blandford & Rees (1978). They suggested that BL Lac objects are AGN where the continuum emission is enhanced through beaming toward us. This may occur because the emitting region moves relativistically outwards in the form of a jet which is fixed in space (see Fig. 2.1). Then the probability ($\Omega/4\pi$) of a suitable orientation would be as small as Γ^{-2}, where Γ is the bulk Lorentz factor for a relativistic jet. They predicted a high spatial density of the counterparts whose beams are not oriented toward us and suggested that M87 would be a BL Lac if its jet were pointing directly toward us. Still this work of Blandford & Rees (1978) is the most cited one in the field of BL Lac astronomy.

Campaigns at different wavelengths increased the knowledge about the physical state of the BL Lacs. Maccagni et al. (1983) found out that the spectral properties indicate that synchrotron radiation is the dominant mechanism at all wavelengths observed so far (radio to X-ray).

Both, X-ray selected BL Lacs (XBL) and radio selected BL Lacs (RBL), seemed to have the same X-ray luminosities but the RBL showed higher radio luminosities. This lead Maraschi et al. (1986) to the idea that they only differ in the orientation with respect to the line of sight. In the case of the RBL we would see directly into the jet whereas in XBL the jet would be misaligned by several degrees. Therefore in an XBL we would see the isotropic X-ray emission of the BL Lac core, while the radiation at lower frequencies is relativistically beamed.

On the next BL Lac conference in Como 1988, the questions how many classes of BL Lac objects exist and if they could be put together to one group was still unresolved. Another problem were the "missing" Compton photons, which are expected to be produced through inverse Compton scattering by high energetic electrons. Still, large complete samples of BL Lac objects were missing to study statistical properties of this group. Woltjer (1988) suggested that there might be no BL Lac objects with $z > 1$ because the radio galaxies and that distance are much stronger and would have correspondingly stronger emission lines so that they are not identified as BL Lac objects. Browne (1988) preferred two different unified schemes, one for BL Lac objects and one for OVV/HPQ quasars because X-ray selected BL Lacs (XBL) and radio selected BL Lacs (RBL) seemed to have different evolution and therefore should belong to different populations. As host galaxies the FRI radio galaxies were discussed.

With the CGRO EGRET Telescope (see page 39) it was possible for the first time to detect BL Lac objects in the gamma-ray region (Lin et al. 1992) and the gamma-ray telescope at the Whipple Observatory detected the BL Lac Markarian 421 as the first extragalactic TeV source (Punch et al. 1992).

In the mid-nineties Padovani and Giommi (1995) presented a catalogue of all known 233 BL Lac objects compiled through an extensive bibliographic search. They also presented here the idea that the differences between the XBL and RBL is only based on the different peak frequency of the synchrotron branch (see section 2.3).

Based on historical data dating back to 1890's Sillanpää et al. (1988) predicted that the next outburst in OJ 287 should happen during fall 1994. In order to verify this a large monitoring campaign in different wavelengths was organized (Takalo 1996). The outburst occurred at the predicted time and the first long-term 12 year periodicity in a BL Lac object was discovered (Sillanpää et al. 1996). Still OJ 287 is the best observed BL Lac object and is monitored steadily (also by myself; see Pursimo et al. 2000a).

The last BL Lac conference has taken place in Turku 1998[2]. Urry (1999) remarked that the discovery of strong gamma-ray emission from blazars had changed the understanding of their energy output. Multi-wavelength campaigns had helped to derive the correlations between the different bands (Wagner 1999). The knowledge of BL Lac host galaxies had increased a lot thanks to the HST and ground based observing campaigns. And also several new surveys to get sufficiently large BL Lac samples were presented on this conference: the *ROSAT All-Sky Survey Green Bank sample* (RGB, Laurent-Muehleisen et al. 1999), the *Radio Emitting X-ray survey* (REX, Maccacaro et al. 1998, Caccianiga et al. 1999), and the *Hamburg/RASS X-ray Bright BL Lac Sample* (HRX-BL Lac, Beckmann 1999).

Nowadays more than 10,000 quasars are known, while thanks to the new surveys the number of BL Lac objects has increased to 500 (Pursimo 2000b).

2.2 Properties of BL Lac objects

As mentioned in the historic description of the BL Lac research, this class of AGN is defined by several properties. Up to now there is still debate on the question, what exactly defines a BL Lac object. I will summarize the properties of BL Lacs here and also mention the open questions of the definition problem.

[2]The Turku conference proceedings, published as *Astronomical Society of the Pacific Conference Series* Volume 159, edited by Takalo and Silanpää, give a good overview of the recent knowledge in the BL Lac research

2.2.1 Variability

Blazars show dramatic variations on all time scales. This was the first property to find and identify BL Lac objects. Variations are reported on time scales from years down to less than a day, the so-called Intraday Variability (IDV; for a review see Wagner & Witzel 1995). In the radio band very high amplitudes ($\Delta f_r / f_r \sim 1$) on hourly time scales are observed (Kedziora-Chudczer et al. 1997). The optical band is well studied and variations down to minute time scale are found with amplitudes up to 20% (Wagner & Witzel 1995). The long term periodicity of OJ 287 was already mentioned in the last section. Fast X-ray variations have been reported by several investigations. Typically BL Lac objects in the X-rays spend most of the time in a quiescent state, which is superposed by large outbursts (McHardy 1998). The fraction of time, in which the BL Lac is variable, the so-called "duty cycle" depends strongly on the overall spectral type of the source. X-ray selected BL Lac objects show a duty cycle of $\lesssim 0.4$ while radio selected ones have duty cycles of ~ 0.8 and also show stronger variability (Heidt & Wagner 1998). While RBL show variabilities up to $\sim 30\%$ within one day, this value is $< 5\%$ for the XBL. This dependency has also been reported by several other authors (Villata et al. 2000, Mujica et al. 1999, and Januzzi et al. 1994). Well sampled light curves in the gamma-ray region are rare. But when monitored, BL Lac objects show rapid variations (Mattox et al. 1997).

Up to now only four BL Lacs are detected in the TeV region: Markarian 421 (Punch et al. 1992), Markarian 501 (Quinn et al. 1996), 1ES 2344+514 (Catanese et al. 1998), and PKS 2155-304 (Chadwick et al. 1999). Observations at the high end of the spectral energy distribution revealed that they exhibit extreme variability. Markarian 501 shows significant variations on timescales from years to as short as two hours (Quinn 1999). While this object appears to have a baseline level which changes on monthly to yearly timescales, Markarian 421 seems to have a stable baseline emission with rapid flares on top (Buckley et al. 1996). Maraschi et al. (1999) observed Markarian 421 in the X-ray and TeV region simultaneously, revealing a correlation between the X-ray and TeV flares.

Variability can be caused by several physical mechanisms. Marscher (1993) and Qian et al. (1993) assumed that the special geometry is a main reason for variation. An explanation for the flux changes on very short time scales could be given by the formation of shock fronts within the jet (Ball & Kirk 1992; Kirk, Rieger & Mastichiadis 1999; Krülls & Kirk 1999).

Some of the variations seen at different frequencies seem to be correlated to each other, while others, even in the same objects, only appear in one wavelength region (Wagner 1999).

2.2.2 Polarization

Strong ($P > 3\%$) and variable polarization is seen in blazars in the radio and in the optical region. Extensive study of polarization has been done by i.e. Kühr & Schmidt (1990) who examined 43 BL Lac objects from the S5 and 1Jy samples, while a study of X-ray selected BL Lacs was done by Januzzi et al. (1994) on 37 EMSS objects. For radio selected ones they find polarization up to $\sim 40\%$ with varying strength and orientation, while the EMSS BL Lac have a maximum of $P_{max} \simeq 15\%$ and do not exhibit strong variability. Also the duty cycles[3] differ between RBL ($\sim 60\%$) and XBL ($\sim 44\%$). Pursimo et al. (2000c) did polarimetry on the 127 objects of the RASS Green Bank (RGB) BL Lac sample (Brinkmann et al. 1997, Laurent-Muehleisen et al. 1999). They find evidence for a correlation between the peak frequency of the synchrotron branch and the degree of polarization in a sense that more X-ray dominated objects show less polarization in the optical region, confirming earlier results. At the same time they do not find a correlation of polarization with luminosity.

2.2.3 Featureless optical spectra

The criteria to identify a BL Lac object have been mostly determined by practical observing considerations rather than real physical distinctions between different types of objects. To distinguish the BL Lac galaxies from non-active elliptical galaxies, a criterion was applied to the strength of the calcium break at 4000 Å. A non-active elliptical galaxy has a break strength of $\sim 40\%$. Therefore Stocke et al. (1991) used a criterion of a break $\leq 25\%$ for BL Lac objects of the EMSS sample. In fact, there are no objects within their candidates with a break value of $25\% \leq \mathrm{Ca_{break}} \leq 40\%$. But later on Marchã et al. (1996) found

[3] duty cycle: fraction of time of an object spent with a degree of polarization $> 3\%$

several transition objects, which could be identified as BL Lacs due to their radio properties. It might be that the existence of a break $\geq 25\%$ in BL Lac objects is more frequent in radio selected samples. Also in the sample presented here, there are only a very few BL Lacs with $\mathrm{Ca_{break}} > 25\%$.

The $\mathrm{Ca_{break}}$ will be discussed in detail in section 5.3.

2.2.4 Host galaxies and environment of BL Lacs

Studying the host galaxies of BL Lac objects is often difficult, because the strong non-thermal core outshines the galaxy in many cases, especially at higher redshifts. To determine the type of the host galaxy, one has to deconvolve the the object into an unresolved core, presented by a point spread function (PSF) and a galaxy. The galaxy then can be examined by fitting the surface brightness to the following intensity model (Caon et al. 1993):

$$I(r) = I_e \cdot 10^{\left(-b_\beta\left(\left(\frac{r}{r_e}\right)^\beta - 1\right)\right)} \tag{2.1}$$

where r_e is the effective radius, b_β is a β-dependent constant and β the shape parameter. A shape value of $\beta \sim 1$ represents an exponential profile (disk galaxy), and $\beta \sim 0.25$ a de Vaucouleurs profile (elliptical galaxy). In average, the host galaxies of BL Lac objects are elliptical galaxies (Wurtz et al. 1996, Heidt 1999, Falomo & Kotilainen 1999, Urry et al. 2000, Pursimo et al. 2000d). The galaxies are luminous ($M_R = -23.5 \pm 1\,\mathrm{mag}$) and large ($r_e = 10 \pm 7\,\mathrm{kpc}$) (Heidt 1999). They seem to be fainter in the radio regime than typical radio galaxies of the Fanaroff-Riley type I (FR I) and appear to be rather FR II galaxies. Nevertheless the favoured parent population for BL Lacs in general are the FR-I galaxies (see e.g. Padovani & Urry 1990, Capetti et al. 2000). Only very few BL Lacs are reported to be associated with a spiral galaxy. OQ530 and PKS 1413+135 show disk-dominated systems. Lensing was thought to be important to the BL Lac phenomenon, but nowadays only the BL Lac B2 0218+357 is clearly a lensed system (Grundahl & Hjorth 1995), and only three more are promising candidates.

In the local environment, many BL Lacs show nearby ($< 50\,\mathrm{kpc}$) companions (e.g. Stickel et al. 1993; this work: RX J0959+2123[4]) and some show evidence for interaction.

Up to now it seems that BL Lac objects avoid rich clusters (i.e. Wurtz et al. 1993, 1997; Owen, Ledlow & Keel 1996; Smith et al. 1994): Most of them are located in poor clusters (Abell ≤ 0).

2.3 Classes of BL Lac objects

Principally there are two successful ways to find BL Lac objects: to search for radio sources which show polarization and/or variability, or to take X-ray sources with a high X-ray flux compared to the optical value. Thus at first there were two classes of BL Lac objects: the radio selected ones (RBL) and the X-ray selected objects (XBL). Although they have many properties in common, like high variability and the non-thermal optical continuum without emission lines, both groups show different radio to X-ray spectra. As the radio and X-ray surveys got more and more sensitive, the gap between both groups was closed with several objects, the so-called intermediate BL Lacs (IBL). Padovani & Giommi (1995a) noticed that the spectral energy distribution of radio and X-ray selected BL Lacs showed peaks (in a $\log\nu - \log\nu F_\nu$ or in a $\log\nu - \log\nu L_\nu$ representation) at different frequencies, and suggested that this difference is a physical way to distinguish between the classes of BL Lacs . They introduced the notation of *high-energy cutoff BL Lacs* (HBL) and *low-energy cutoff BL Lacs* (LBL) to distinguish between both groups. Most, but not all, XBL are HBL, while the group of LBL is preferentially selected in the radio region. The advantage of the new notation is the fact that it is a more physical way to determine the class the BL Lac object belongs to, while the energy band where a BL Lac is detected first is more accidental.

While at first the two classes seemed to be well separated, by the time of discovering more BL Lacs with deeper radio and X-ray survey, also objects with properties in between the LBL and HBL classification have been found. These objects are sometimes (and also in this work) called Intermediate BL Lacs (IBL). Throughout this thesis I will use the term HBL for objects with an overall spectral index $\alpha_{OX} < 0.9$ ($\log\nu_{peak} \lesssim 16.4$) and the term IBL for objects with $0.9 \leq \alpha_{OX} < 1.4$ ($16.4 \lesssim \log\nu_{peak} \lesssim 14.6$). The overall spectral index α_{OX} will be explained in the next section. For the relation between α_{OX} and peak

[4]this object has a nearby companion galaxy at the same redshift $z = 0.367$

frequency of the synchrotron branch see Equation 5.5. The definition used here follows the denotation in Bade et al. (1998).

To summarize, the LBL show more extreme properties than the HBL. They seem to be brighter at radio and optical wavelengths, they show higher variability and stronger polarization.

2.4 Overall spectral indices

The distinction in HBL and LBL leads to another way to distinguish both classes. An object, which has a peak in the SED within the X-ray region, will probably have a high flux ratio of f_X/f_r and LBL will show higher values of $f_{optical}/f_X$ than HBL. This fact can be described by using over all spectral indices. Assuming a single power law of the form

$$f_\nu \propto \nu^{-\alpha_E}\text{[5]} \tag{2.2}$$

with α_E being the energy index, Ledden and O'Dell (1985) defined the overall spectral index between two bands:

$$\alpha_{1/2} = -\frac{\log(f_1/f_2)}{\log(\nu_1/\nu_2)} \tag{2.3}$$

Here f_1 and f_2 are the fluxes at two frequencies ν_1 and ν_2. To compare this value for different objects it should be determined for the same frequencies in the source rest frame. Therefore a K-correction has to be applied (Schmidt & Green 1986). This correction takes into account two effects, the different energy region, which is observed when transforming to a redshift z, and the narrowing of a given band with redshift. This means that a bandwidth $\Delta\lambda$ is narrowed by a factor of $(1+z)^{-1}$. For a given spectral slope α the transformation from the observed flux $f_{observed}$ to the emitted flux f_{source} at a redshift z is thus given by

$$f_{source} = f_{observed} \cdot (1+z)^{\alpha-1} \tag{2.4}$$

This means that the observed flux is lower than the emitted flux if $\alpha > 1$, because the frequency region with the lower flux is shifted into the observed wavelength region by the redshift z. If no redshift information is available one can also use the observed fluxes to derive overall spectral indices. As in the radio band the spectra of BL Lac objects are flat ($\alpha \sim 0.2$ for HBL and $\alpha \sim -0.2$ for LBL; Padovani & Giommi 1996), a K-correction means that the observed flux is larger than the emitted one. In the optical and near infrared the spectra have a spectral slope of $\alpha \sim 0.6$ and K-correction does not change much. For the X-ray fluxes this is negligible, because the X-ray spectra of BL Lac objects are quite steep ($\alpha \gtrsim 1$; see page 46). It is worth noticing that the K-correction always is applied using the assumption of a continuous spectral slope. If any curvature occurs, breaks or strong lines in the spectra, the correction is not applicable. Due to extrapolation this problem is most important for high redshift objects and for broad emission line AGN (see Wisotzki 2000a).

Overall spectral indices can also be used to search for BL Lac candidates (e.g. Nass et al. 1996, Giommi et al. 1999). The consequences will be discussed later.

Figure 2.2 shows the different types of BL Lac objects within the α_{RO} - α_{OX} plane. IBL are located in this diagram in the transition region between "HBL" and "Radio loud AGNs". The area covered by the HRX-BL Lac sample does not have an overlap with the 1 Jy sample, but matches quite well the properties of the EINSTEIN Slew Survey BL Lac objects.

2.5 Models and unification for BL Lac objects

From the first dedicated conference in Pittsburgh (1978) about the BL Lac phenomenon until today there is an ongoing discussion about the physical model of blazars. The model of Blandford and Rees (1978) is still the most accepted basis for understanding the blazar properties. The central point of their idea is a relativistic jet, moving towards the observer in case of a BL Lac object. The emitting region of the jet must be small to allow fast flux variations. Such a jet could be formed by an AGN accretion disk. The differential rotation of the disk could form a magnetic field perpendicular to the disk. The heated disk could produce a particle wind which would be guided and bound in the direction of the magnetic

[5]The energy index α_E is related to the photon index $\Gamma = \alpha_E + 1$

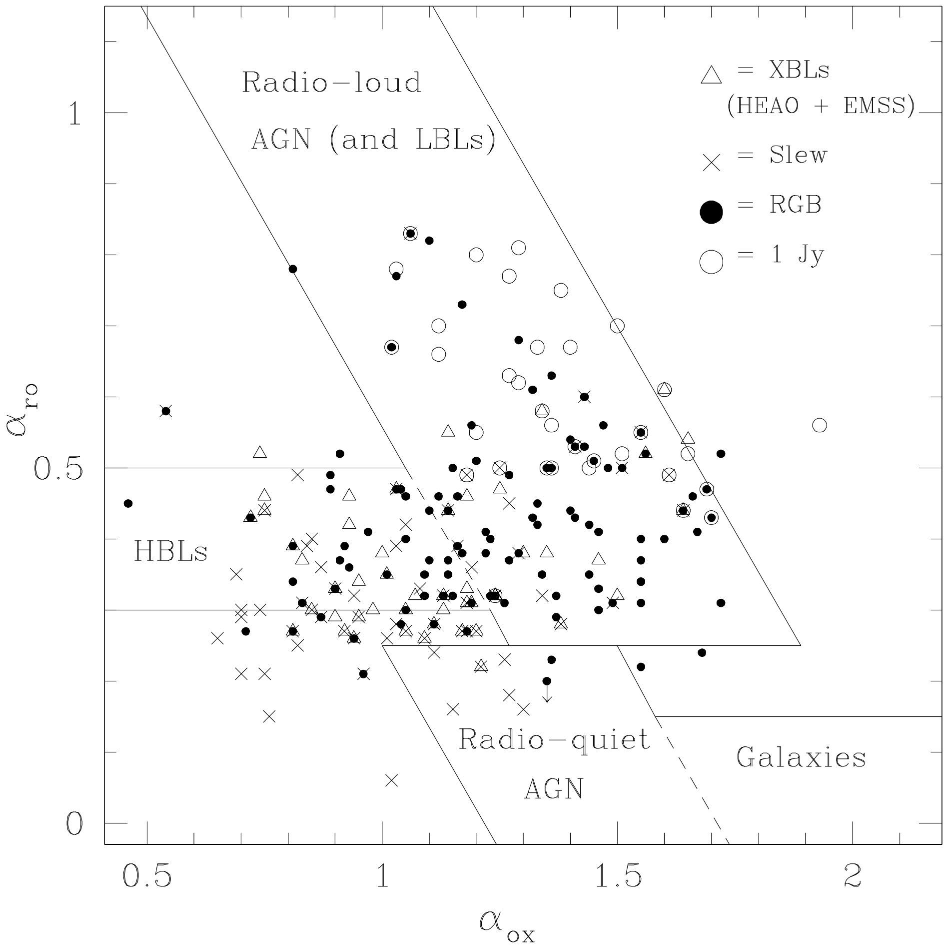

Figure 2.2: α_{RO} vs. α_{OX} for some BL Lac samples. Nearly all objects of the HRX-BL Lac sample lie in the "HBL" quoted area. Graphic taken from Laurent-Muehleisen et al. (1999).

field lines[6]. The resulting jet cannot start its high energetic "life" very near to the black hole. There the density of radiation and particles would be high enough for pair production. This would cause cascades and it would not be possible to see high-energy emission, because the radiative zone would be optically thick. Therefore, the emission must originate at some distance from the central engine.

The model of the relativistic jet pointing towards the observer does not explain the differences between the different classes of BL Lac objects. Additional assumptions have to be made. Also the connection to the OVVs and to QSOs in general is not well understood yet.

On the basis of the relativistic jet model of Blandford & Rees different explanations exist. The following assumptions can also be connected to form combined models.

- *relativistic beaming*: The effect of relativistic beaming was studied by Urry & Shaefer (1984). For a relativistic jet the observed luminosity, L_{obs}, is related to the emitted luminosity, L_{emi}, via

$$L_{obs} = \delta^p L_{emi} \tag{2.5}$$

with the Doppler factor δ of the jet being

$$\delta = \frac{1}{\gamma(1 - \frac{v}{c_0}\cos\theta)} \tag{2.6}$$

[6]formation of jets in astrophysics in general and especially in AGN is a complex area and still not very well understood. For a review on this topic see Ferrari (1998) and Bulgarella, Livio, & O'Dea (1993)

where v is the bulk velocity of the jet, c_0 is the speed of light, θ the angle of the jet with respect to the line of sight. γ is the Lorentz factor:

$$\gamma = \frac{1}{\sqrt{1-\frac{v^2}{c_0^2}}} \tag{2.7}$$

This effect gives rise to a very strong, angle-dependent, amplification of the emitted radiation by a factor $\propto \delta^p$, where p depends on the spectral slope α in the observed energy region[7]: $p = 3 + \alpha$. Thus in the radio region $p \sim 3$ and we get an observed synchrotron luminosity L_{sync} of the source:

$$L_{sync} = U_{sync} \cdot 4 \cdot \pi \cdot R^2 \cdot c_0 \cdot \delta^p \tag{2.8}$$

with the energy density of the synchrotron source U_{sync}, and its size radius R. Nowadays Lorentz factors of $\gamma \sim 5$ are assumed (Lähteenmäki & Valtaoja 1999).

Since it was mainly accepted since the 1980's that the parent population of BL Lac objects are AGN it was possible to determine the degree of beaming we see in BL Lacs. Comparing the number counts of the BL Lac objects with those of the un-beamed AGN and applying the luminosity function (LF) of AGN, one can predict the BL Lac LF. The beamed objects will have higher observed powers and will be less numerous. Urry, Padovani, & Stickel (1991) fitted the radio LF of BL Lacs (based on the FR I radio galaxies) and derived $5 \lesssim \gamma \lesssim 30$, where γ is the Lorentz factor depending on the bulk velocity of the jet. Based on the FR I LF they argued that the opening angle of the BL Lac jet should be $\theta \sim 10°$. This would mean that a fraction of $< 2\%$ of the FR I galaxies would be BL Lac objects because the probability to detect a source with an opening angle θ_{open} is $P(\theta \leq \theta_{open}) = 1 - \cos\theta$.

- *Viewing angle*: Stocke, Liebert, & Schmidt (1985) compared the properties of XBL and RBL and found out that the XBL show less extreme behavior than the radio selected objects. The variability and luminosity is especially lower[8]. They made the suggestion that, within the relativistic beaming hypothesis, XBL were viewed at a larger angle to the line of sight. This model was independently found and supported by Maraschi et al. (1986). They made the point that XBL and RBL showed roughly the same X-ray luminosity and therefore are essentially the same. Working on a sample of 75 blazars they suggested that the beaming cone of the XBL was much wider than the radio-optical ones. Maraschi & Rovetti (1994) developed a unified relativistic beaming model, obtaining bulk Lorentz factors of $10 < \gamma_{radio} < 20$ and an opening angle for the radio emission of $6° < \theta_{open} < 9°$, and $6 < \gamma_{X-ray} < 9$ with $12° < \theta_{open} < 17°$ for the radio emission. Urry & Padovani (1995) suggested opening angles of $\theta_X \sim 30°$ for the XBL and $\theta_r \sim 10°$ for the radio selected ones. Therefore, in RBL we would see a jet which is more beamed making RBL having a higher luminosity, while the isotropic X-ray emission would be the same in both types of BL Lac objects. This would make the X-ray selected BL Lac objects much more numerous than the RBL, because the ratio of number densities of the two classes will be $N_{XBL}/N_{RBL} = (1 - \cos\theta_X)/(1 - \cos\theta_r) \simeq 10$). This relation is true for an X-ray selected sample (Urry, Padovani, & Stickel 1991), but is not holding for a sample with a radio flux limit. Only 10% of the 1Jy selected BL Lac sample (Stickel et al. 1991, Rector & Stocke 2000) are XBL.

  Sambruna, Maraschi, & Urry (1996) applied the jet model to the multi-frequency spectra of the 1Jy and EMSS BL Lacs (see section 3.2). They found out that not only viewing angle, but also systematic change of intrinsic physical parameters are required to explain the large differences in peak frequencies between HBL and LBL. They proposed that HBL have higher magnetic fields and electron energies but smaller sizes than LBL.

  Also the existence of high energetic gamma-rays from HBL seem to argue against the isotropic X-ray emission prediction. In this case one would expect the gamma-ray photons to be absorbed by pair production. But in the beamed case the photon density within the jet is much lower and therefore gamma-ray photons can manage to escape the jet (Maraschi, Ghisellini & Celotti 1992).

[7] This is valid for monochromatic luminosities. For bolometric luminosities $p = 4 + \alpha$ because the observed bandwidth is then also changed by a factor δ

[8] This is generally true, although there are exceptions like PKS 2155-304. This HBL showed a variations of factor ~ 4 within a few hours in the X-rays, as reported by Zhang et al. 1999)

- *SSC model*: One problem in understanding the blazar SED is to find out what kind of radiation we see from the jet. The accelerated electrons (or protons) within the jet should interact with the magnetic field enclosing the jet by emitting synchrotron radiation. These photons can than be accelerated again by inverse Compton (IC) scattering on relativistic electrons. In this process the photon would be up-scattered to higher energies, while the electron is decelerated. This interaction using the synchrotron photons produced by the jet is called Synchrotron Self Compton Scattering (SSC; Maraschi, Ghisellini & Celotti 1992, Ghisellini et al. 1993, Bloom & Marscher 1996). The SSC model results in a blazar emission of synchrotron photons, and a second emission at higher energies of photons produced by IC scattering. This two branches of the SED are not independent. The ratio of the peak frequencies $\nu_{Compton}/\nu_{Synchrotr.} \propto \gamma_{peak}$, where γ_{peak} is the energy of the electrons radiating at the synchrotron peak.

- *EC model*: The External Compton Scattering (EC) model is similar to the SSC model, but it uses for the IC seed photons which are produced by the accretion disk and/or the host galaxy (Sikora, Begelman & Rees 1994; Dermer & Schlickeiser 1993; Blandford & Levinson 1995; Ghisellini & Madau 1996). Also this model results in two peaks in the SED, the synchrotron branch and the EC branch at higher energies. But in this scenario the ratio of peak frequencies depends on the mean frequency ν_{seed} of the seed photons and on the magnetic field strength: $\nu_{Compton}/\nu_{Synchrotr.} \propto \nu_{seed}/B$. Also a mixture of SSC and EC is possible: Sources with stronger emission lines (like OVV, FSRQ) could be dominated by the EC mechanism, at least at GeV energies. In Blazars without emission lines (BL Lacs) the SSC mechanism might dominate the entire gamma-ray region.

- *other models*: Mannheim (1993) suggested that the jet of the blazars could also be formed by protons and that the second peak in the SED could be caused by another more energetic synchrotron component.

Chapter 3

X-ray missions

This chapter gives a brief overview of the X-ray missions, from which data have been used in this work. The special point of interest herein is the contribution of the X-ray satellites to the exploration of the nature of BL Lac objects. A graphical overview of the energy ranges of the different missions started since 1990 is given in figure 3.1.

3.1 The early X-ray missions

X-ray astronomy is a fairly young part of astrophysics, because extraterrestrial X-ray radiation ($\lambda \approx 0.06$ Å bis 10 Å) is effectively absorbed by the atmosphere. Therefore stratospheric balloons, rockets or satellites are necessary to study the the universe in the X-rays. The first survey was done by the UHURU satellite, which was launched in December 1970. It found 339 sources in the 2-6 keV energy range. These sources were combined in the *Fourth UHURU Catalog of X-ray sources* (Forman et al. 1978) and included at that time only one BL Lac object (Mrk 421). Mrk 501 was also detected, but not on a high confidence level (Cooke et al. 1978).

3.2 EINSTEIN

The first satellite with an imaging telescope in the X-ray region was the EINSTEIN (HEAO2) satellite, which was launched in November 1978. Many pointed observations were carried out with this instrument, using the *EINSTEIN* Imaging Proportional Counter (IPC, Giacconi et al. 1979), which had an energy resolution of $\Delta E/E \approx 1$ and detected X-ray sources in the 0.3–3.5 keV energy range. With these exposures it was not only possible to get information about the target, but also about serendipitous sources within the field of view. These 835 sources were combined to form the "EINSTEIN Observatory Extended Medium Sensitivity Survey" (EMSS, Gioia et al. 1990, Stocke et al. 1991, Maccacaro et al. 1994). Thus it was possible to achieve a sample of weak X-ray sources with a flux limit of $f_X(0.3 - 3.5\,\mathrm{keV}) = 7 \cdot 10^{-14} \mathrm{erg\,cm^{-2}\,sec^{-1}}$. The survey area of the EMSS is $778\,\mathrm{deg}^2$. Based on the EMSS, a sample of 22 X-ray selected BL Lac objects was formed with fluxes $f_X > 5 \cdot 10^{-13} \mathrm{erg\,cm^{-2}\,sec^{-1}}$ (Morris et al. 1991). Later this sample was enlarged by combining all BL Lac objects ever found in the EMSS, achieving a sample of 41 BL Lacs (Rector et al. 2000). Doubtless the advantage of this sample is the huge number of follow up observations which has been carried out on EMSS sources. Therefore these BL Lacs are well studied and there is little doubt about the identification of EMSS BL Lacs. Only the radio selected 1Jy sample (Stickel et al. 1991, Rector & Stocke 2000) has been studied that intense.

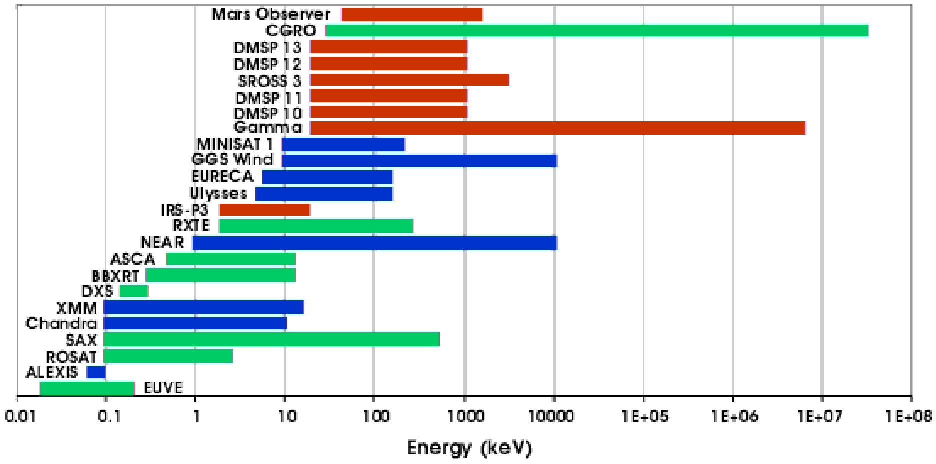

Figure 3.1: Missions in the X-ray and gamma range, which have been launched since 1990 (Graphic: HEASARC).

3.3 ROSAT and the RASS

The X-ray selected sample of BL Lacs presented in this work is based on data taken with the ROSAT satellite.

The focal plane of the X-ray telescope hosted the "Position Sensitive Proportional Counter" (PSPC, Trümper 1983) which detected photons in the 0.07–2.4 keV energy band. Compared to EINSTEIN, ROSAT examined a significantly "softer" energy region. Thus it was possible to detect X-ray sources with steeper and softer X-ray spectra. The PSPC detected the incoming photons in 240 energy channels. Because of the low energy resolution (Brinkmann 1991),

$$\frac{\Delta E}{E} = \frac{0.415}{\sqrt{E}} \text{ (mit E in keV)} \tag{3.1}$$

it is not possible to determine directly the photon energy from the channel, in which the photon has been detected. It is only possible to have four independent "colors" within the PSPC energy band. The color definition used in the optical astronomy is not useful for X-rays. Instead of colors, two hardness ratios are defined by the following formula:

$$HR = \frac{H-S}{H+S} \tag{3.2}$$

Herein H is the hard and S is the soft X-ray energy band. Hardness ratio 1 ($HR1$) is defined with S being the number of photons within the channels 11–41 while H uses the hard channels 52–201. $HR2$ is defined with $S = [52-90]$ and $H = [91-200]$. Thus the hardness ratio is a measure for the hardness of the detected X-ray radiation. It ranges by definition from -1 for extreme soft up to +1 for very hard X-ray sources.

ROSAT was launched on June 1, in 1990 and saw first light on June 16, 1990 (Trümper et al. 1991a). The following six weeks were used for calibration and verification. End of July ROSAT started to do the first complete X-ray survey of the entire sky with an imaging X-ray telescope. The "ROSAT All Sky Survey" (RASS; Voges 1992) was performed while the satellite scanned the sky in great circles whose planes were oriented roughly perpendicular to the solar direction. This resulted in an exposure time varying between about 400 sec and 40,000 sec at the ecliptic equator and poles respectively. During the passages through the auroral zones and the South Atlantic Anomaly the PSPC had been switched off, leading to a decrease of exposure over parts of the sky. For exposure times larger than 50 seconds the sky coverage is 99.7 %; a 97% completeness is reached for ≥ 100 seconds exposure time (Voges et al. 1999).A secure detection of point sources is possible, when the count rate exceeds $0.05\,\text{sec}^{-1}$ (Beckmann 1996).

The first analysis of the RASS data was performed for 2 degree wide strips containing the data taken during two days. The disadvantage of this procedure is that it is not sufficiently taking into account the overlap between the strips. The problems resulting from this are discussed in Voges et al. 1999. The data used for this work are based on the second processing of the all sky survey, the RASS-II. The main differences between these processings are as follows: the photons were not collected in strips but were merged in 1,376 sky fields of size $6.4° \times 6.4°$ to avoid the problems with the overlapping strips at the ecliptic poles; neighboring fields overlapped by at least 0.23 degrees, to ensure detection of sources near the field boundaries, which was a problem during the RASS-I processing; the determination of the background was improved resulting in better determined count-rates (Voges et al. 1999).

Finally, a catalogue of all sources within the RASS-II was combined using a count-rate limit of $0.05\,\mathrm{sec}^{-1}$, the *ROSAT All-Sky Survey Bright Source Catalogue* (RASS-BSC, Voges et al. 1999) containing 18,811 X-ray sources. The difference between the RASS-I and RASS-II is more important for the faint X-ray sources. There are only a few sources in the RASS-BSC, which were not already detected as RASS-I sources (Bade et al. 1998b). The RASS-BSC contains information about the X-ray position in the sky, the count-rate, two hardness ratios, extension radius, exposure time, and a detection likelihood value.

3.4 The *Beppo*SAX Satellite

The X-ray satellite *Beppo*SAX (*Satellite per Astronomia X*, "Beppo" in honor of Giuseppe Occhialini) is a program of the Italian Space Agency (ASI) with participation of the Netherlands Agency for Aerospace Programs (NIVR). The satellite was developed by a consortium of Italian and Dutch institutes and the Max Planck Institute for Extraterrestrial Physics (MPE) has supported the tests and calibrations of the X-ray optics and the focal plane detectors. *Beppo*SAX was launched in April 1996.

The scientific payload comprises four detectors with a small field of view, the Narrow Field Instruments (NFI) and two Wide Field Cameras (WFI) which are orientated perpendicular to the NFI. For this work only the data from the NFI are relevant. In the low energy range ($0.1 - 10\,\mathrm{keV}$) the Low Energy Concentrator Spectrometer (LECS) is sensitive (Parmar et al. 1997). It has a field of view of 37 arcmin diameter and a energy resolution which is by a factor of ~ 2.4 better than that of the ROSAT-PSPC. Nevertheless the effective area is smaller by a factor of ~ 6 and ~ 2 (at 0.28 and 1.5 keV respectively). Three Medium Energy Concentrator Spectrometer (MECS) with a field of view of 56 arcmin are working on the $1 - 10\,\mathrm{keV}$ energy range with an energy resolution of $\frac{\Delta E}{E} = 0.08$ at $6\,\mathrm{keV}$. The spatial resolution at this energy is 0.7 arcmin (Boella et al. 1997). Usually, the data from all three MECS are summed together. On May 6, 1997 a technical failure caused the switch off of unit 1; since then, only unit 2 and 3 are available. The effective X-ray mirror surface is only $150\,\mathrm{cm}^2$ at $6.4\,\mathrm{keV}$. Therefore *Beppo*SAX uses much larger exposure times than the other currently active X-ray missions. A most striking advantage of *Beppo*SAX is the wide energy range which is covered: At high energies ($15 - 300\,\mathrm{keV}$) *Beppo*SAX is sensitive using the Phoswich Detector System (PDS, Frontera et al. 1997). This instrument has no spatial resolution. Therefore it is not possible to directly identify the source of hard photons within the field of view of 1.3° diameter. The PDS consists of a square array of four independent scintillation detectors. Two of the detectors are observing the target, while two are measuring the background at 3.5 degree distance to the aim point. Every 96 seconds this configuration is switched. The energy resolution of the PDS is $\frac{\Delta E}{E} = 0.15$ ($60\,\mathrm{keV}$). It allows a 3σ detection of a source with a $\alpha = 1$ spectral slope and flux of 10 mCrab within 10 ksec (Guainazzi & Matteuzzi, 1997).

3.5 ASCA

The Japanese *Advanced Satellite for Cosmology and Astrophysics* (ASCA) was launched in February 1993 and describes a nearly circular orbit at $520 - 620$km height. ASCA was the first X-ray astronomy mission to combine imaging capability with a broad pass band, good spectral resolution, and a large effective area. The mission also was the first satellite to use CCDs for X-ray astronomy. The four X-ray telescopes on board have a total effective area of $1300\mathrm{cm}^2$ (at $1\,\mathrm{keV}$). Similar to ROSAT, ASCA uses a Gas Imaging Spectrometer (GIS) which is sensitive in the $0.7 - 10\,\mathrm{keV}$ energy range. The energy resolution ($\frac{\Delta E}{E} = 0.08$

at 5.9 keV) is comparable to that of the *Beppo*SAX MECS instrument. The field of view has a diameter of 50arcmin and a angular resolution of 2.9 arcmin is reached. The Solid-state Imaging Spectrometers (SIS) has an energy range of $0.4 - 10$ keV with a resolution of $\frac{\Delta E}{E} = 0.02$ at 5.9 keV and a field of view of $22 \times 22\,\mathrm{arcmin}^2$.

Next year in March 2001 the end of the mission will be reached, when the orbit of the satellite is too low for a stable pointing of the telescope.

Chapter 4

The Hamburg RASS X-ray bright BL Lac sample

This chapter will describe the basis of the HRX-BL Lac sample, the Hamburg RASS Catalogue, the definition of the HRX-BL Lac sample, and the candidate selection procedure (page 30). Also the different sources for the data in the radio, infrared, optical, and gamma-ray region will be presented. The sources for X-ray data have been already presented in the previous chapter. Three samples will be defined: the HRX-BL Lac *core sample* with 39 BL Lacs, which is based on complete optical identification of 350 X-ray sources, the HRX-BL Lac *complete sample* with 77 BL Lacs, which is based on 223 objects resulting from an X-ray/radio correlation and which is 98% complete identified, and the HRX-BL Lac *total sample*, which is highly incomplete but includes 101 BL Lacs.

4.1 Hamburg RASS Catalogue and Hamburg RASS X-ray bright sample

X-ray data from the RASS-BSC are not sufficient to classify the source. Optical follow up spectroscopy is necessary to identify the X-ray source. But slit spectroscopy for an amount of several 10,000 sources, as detected in the ROSAT All-Sky Survey, is not possible. A clear picture of the objects which are the sources of the RASS can be achieved, when identifying a well-defined and complete subsample of the catalogue. Two projects with this aim have been carried out at the Hamburger Sternwarte.

One project is the (still ongoing) identification of RASS sources based on photographic plates which have been taken for the Hamburg Quasar Survey (HQS; Hagen et al. 1995, Engels et al. 1997, Hagen et al. 1999). The HQS provides objective prism plates for 567 fields of the northern high Galactic latitude sky with $|b| > 20°$ and direct plates for most of them. The plates were taken with the Hamburg Schmidt telescope on Calar Alto (Birkle 1984) between 1980 and 1998. One plate covers a sky region of $5°.5 \times 5°.5$. The 1.7° prism provides a non-linear dispersion with 1390 Å/mm at H_γ. Kodak IIIa-J emulsion is used, giving a wavelength coverage between the atmospheric UV-limit at ~ 3400 Å and the cut-off of the emulsion at 5400 Å (KODAK 1973). After ~ 1 hour exposure the limiting magnitude for the spectral plates is $B \sim 18.5$ mag but can differ because of different quality of the plates and the weather conditions when they have been exposed. Objects brighter than 12 . . . 14 mag are saturated. The direct plates have a lower flux limit of $B \sim 20$ mag. For further analysis, the objective prism plates are scanned with a PDS 1010G microdensitometer. After on-line background reduction and object recognition the density spectra are stored on magneto-optical disc and on CD-ROM.

These data are the basis for the identification of the RASS sources. The X-ray positions are correlated with direct plates to obtain candidate positions. At these positions the objective prism plates are then scanned to retrieve density spectra. The magnitude limit of the objective prism plates is $\simeq 18$ mag. Whenever an object is optically fainter than the magnitude limit of the direct plate (~ 19.5 mag), the source was classified as an "empty field" ($\sim 3\%$ of the RASS-BSC sources). Other problems within the identification process result in cases where more than one optical counterpart lies within the RASS error circle. Therefore the fraction of unidentified sources is still quite high ($\sim 16\%$).

The classified objects are combined in the Hamburg RASS Catalogue (HRC). A detailed description and a first list of 3847 sources covering an area of $8480\,\mathrm{deg}^2$ can be found in Bade et al (1998b).

Based on the objective prism plates a fraction of ~ 32 % could not be identified. Therefore a second identification project on a smaller area has been carried out at the Hamburger Sternwarte.

In this project all RASS sources with "hard" $(0.5-2.0\,\mathrm{keV})$ PSPC count-rates $hcps \geq 0.075\,\mathrm{sec}^{-1}$ have been identified on an area of $1687\,\mathrm{deg}^2$ ($45° < \delta < 70°$ and $8^h < \alpha < 17^h$), and on a second (patchy) area with a count rate limit of $hcps \geq 0.15\,\mathrm{sec}^{-1}$. The detailed description of this area is listed in Bade et al. (1998).

350 X-ray sources within the total area of $2800\,\mathrm{deg}^2$ are listed in the RASS-BSC. This sample is completely optically identified using long-slit spectroscopy. It has to be noted that for this sample only an X-ray limit had been applied: No optical or radio limit was used. These 350 objects form the Hamburg/ROSAT X-ray bright sample (HRX, Cordis et al. 1996). After classifying the known objects within this sample and identification based on the objective prism plates, slit spectroscopy was done on the AGN candidates to verify their identification and to determine redshifts. Follow up spectroscopy was done using the 2.2m and the 3.5m telescope on Calar Alto[1]. The classification of the 350 objects is shown in Figure 4.1. Within the sample 39 sources are identified as BL Lac objects. These BL Lacs are comprised to the *core sample* of the *Hamburg ROSAT X-ray bright BL Lac sample* (HRX-BL).

To avoid confusion the basic sample criteria of the samples discussed here are summarized in Table 4.2.

4.2 HRX-BL Lac sample - candidate selection

Based on the first HRX-BL Lac sample, investigations on the evolution of BL Lac objects have been carried out (Bade et al. 1998). But the sample of 39 BL Lacs, for 90% of them the redshift was known, was too small to clearly determine evolutionary behavior of different subsamples of the HRX-BL Lac.

To increase the sample the experience from previous campaigns was used; all BL Lacs of the HRX-BL Lac sample are also radio sources. To the authors knowledge, up to now there is no BL Lac object known in the entire sky without a radio counter-part on a ~ 2.5 mJy level, which is above the flux level of the *Faint Images of the Radio Sky at twenty-centimeters* (FIRST, Becker et al. 1995, White et al. 1997) and similar to the detection limit of the NRAO VLA Sky Survey (NVSS, Condon et al. 1998) radio catalogue. These catalogues have been therefore cross-correlated with the X-ray positions derived from the RASS-BSC to obtain BL Lac candidates. Details to the radio catalogues can be found in Section 4.4.

In the beginning of this work, neither the NVSS nor the FIRST Survey was covering the entire HRX-BL Lac Survey region; therefore we used a combination of both surveys to cover the whole region ($7^h < \alpha < 16^h$ and $\delta > 20°$). Nowadays, the NVSS is available in total, so that the candidate selection is now based on the NVSS.

In the further analysis, when available the radio positions from the FIRST Survey have been used due to their higher accuracy. The correlation between the BSC and the NVSS was done on the first defined HRX-BL Lac Survey region[2] ($7^h < \alpha^3 < 16^h$ and $\delta > 20°$: $5089\,\mathrm{deg}^2$) and resulted in a number of 681 objects which are both, radio and X-ray sources. Selecting only those objects with a hard count rate $hcps \geq 0.05\,\mathrm{sec}^{-1}$ in the BSC reduced the number to 585 BL Lac candidates (the count-rate limit for the BSC is $cps(0.1-2.4\,\mathrm{keV}) \geq 0.05\,\mathrm{sec}^{-1}$ for the whole ROSAT-PSPC band). The count-rate limit for the complete HRX-BL Lac sample was later chosen as $hcps \geq 0.09\,\mathrm{sec}^{-1}$; above this limit we found 235 objects from the radio/X-ray correlation. The selection process for the HRX-BL Lac *total* and *complete* sample is shown in Table 4.2. This sample will be used to investigate the evolutionary effects.

The complete list of the objects resulting from the radio/X-ray correlation is comprised in Table 11.1 (page 134).

[1] German-Spanish Astronomical Center, Calar Alto, operated by the Max-Planck-Institut für Astronomie, Heidelberg, jointly with the Spanish National Commission for Astronomy

[2] I decreased this area later to decrease the number of unidentified sources; see page 30

[3] coordinates for J2000.0

Table 4.1: Selection process for the HRX-BL Lac total and complete sample

selection	number of objects	comment
NVSS-BSC correlation[a]	681	area: 5089 $\deg^2$
only objects with $hcps \geq 0.05$	585	HRX-BL Lac *total sample*: 101 BL Lacs
only objects with $hcps \geq 0.09$	235	95 % identified
decreased area to 4770 $\deg^2$	223	98 % identified (77 BL Lacs) (HRX-BL Lac *complete sample*)

[a] flux-limits: $f_R(1.4\,\mathrm{GHz}) = 2.5\,\mathrm{mJy}$, $f_X(0.1 - 2.4\,\mathrm{keV}) > 0.05\,\mathrm{sec}^{-1}$

Table 4.2: Properties of the Hamburg BL Lac samples in comparison to the RGB and EMSS sample

sample	Reference	number of objects	X-ray limit	radio limit	optical limit
HRX core sample	Bade et al. 1998	39	$0.075/0.15\,\mathrm{sec}^{-1}$ [a]	-	-
HRX-BL Lac total	this work	101	$0.05\,\mathrm{sec}^{-1}$ [a]	2.5 mJy[b]	-
HRX-BL Lac complete	this work	77	$0.09\,\mathrm{sec}^{-1}$ [a]	2.5 mJy[b]	-
RGB	Laurent-Muehleisen	127	$0.05\,\mathrm{sec}^{-1}$ [c]	15 ... 24 mJy[d]	18.5 mag[e]
RGB complete	et al. 1999	33	$0.05\,\mathrm{sec}^{-1}$ [c]	15 ... 24 mJy[d]	18.0 mag[e]
EMSS	Rector & Stocke 2000	41	2×10^{-13} [f]	-	-

[a] ROSAT All Sky Survey count rate limit for the hard $(0.5 - 2\,\mathrm{keV})$ PSPC energy band.
[b] NVSS radio flux limit at 1.4 GHz
[c] RASS count rate limit for the whole $(0.1 - 2.4\,\mathrm{keV})$ PSPC energy band.
[d] GB catalog flux limit at 5 GHz
[e] O magnitude determined from POSS-I photographic plates
[f] EINSTEIN IPC $(0.3 - 3.5\,\mathrm{keV})$ flux limit in $[\mathrm{erg\,cm^{-2}\,sec^{-1}}]$

These objects then have been checked in the NASA/IPAC Extragalactic Database (NED)[4] for known optical counterparts. Some Galactic objects have been identified by using SIMBAD[5]. A classification of the object in the NED as a "Galaxy" without redshift information was not counted as an identification, as long as nearby BL Lac objects in elliptical galaxies could be misidentified on direct images. Galaxies with redshift information have been checked before counted as identified. Also some confusing identification like "AGN" or "QSO" without an additional remark have been re-checked in the literature. The cross-check with the NED has been done many times during this project, especially before every observation run, conference presentation, and paper work. An actual status of the NED shows the following distribution: 48 of the 235 objects are galaxies or galaxy clusters, 146 are AGN with 62 being Seyfert galaxies and 55 BL Lacs. 7 of the candidates are stars, and 2 are super nova remnants. 35 objects have no identification in the NED. Of course, some of the information included now in the NED is based on the work presented here. 122 objects have been re-observed within the course of the BL Lac project, revealing ~ 30 previously unknown BL Lac objects and determing ~ 70 previously unknown redshifts (within the HRX-BL Lac *total sample*).

The total list of all 235 objects is given in Table 11.1 (Appendix, page 134). The α and δ listed is the radio source position (J2000.0) which has a higher accuracy than X-ray position measurement. "Name" refers to any other than the ROSAT name, when available. This list includes not only the information derived from NED and SIMBAD, but also the work which is presented here. The identification of 1RXS J081929.5+704221 was provided by Axel Schwope who examined bright BSC sources ($cps > 0.2\,\mathrm{sec}^{-1}$) which have been published in Schwope et al. (2000). Also some of the information we got from Sally Laurent-Muehleisen before she published them in Laurent-Muehleisen et al. (1999). To decrease the number of objects without identification in the sample, I decreased the HRX-BL Lac survey for the complete sample by setting the following area limits:

border (α)	border (δ)	area
$7^h \leq \alpha < 8^h$	$30° < \delta < 85°$	$426\,\mathrm{deg}^2$
$8^h \leq \alpha < 12^h$	$20° < \delta < 85°$	$2248\,\mathrm{deg}^2$
$12^h \leq \alpha < 14^h$	$20° < \delta < 65°$	$970\,\mathrm{deg}^2$
$14^h \leq \alpha \leq 16^h$	$20° < \delta < 85°$	$1124\,\mathrm{deg}^2$

Thus the area of the HRX-BL Lac sample is $4770\,\mathrm{deg}^2$, which is more than 11% of the entire sky, with 223 candidates from the NVSS/BSC correlation with the X-ray ($hcps \geq 0.09\,\mathrm{sec}^{-1}$) flux limit. This defined sample will be referred to as the *complete sample*. The optical identification leads to the following distribution of object classes within the radio/X-ray correlation: 35% are BL Lac objects, 34 % are other AGN (QSO, Seyfert I/II, Blazar), 13 % galaxies (including star-burst galaxies and LINERs), 12 % galaxy clusters, and 5 % stars (including 2 Super Nova remnants). Only a fraction of 2 % of the 223 candidates is yet not identified. The results of the identification are summarized in Table 4.3 and shown in Figure 4.2.

It is worth noticing that the fraction of BL Lac objects within the radio/X-ray correlation is much higher compared to identification of X-ray sources: 35 % of the radio/X-ray sources are BL Lacs, while only a fraction of $\sim 10\%$ are BL Lacs if we take all X-ray sources (e.g. in the HRX).

Of course the newly defined *complete sample* is not independent compared to the HRX-BL Lac *core sample* of 39 BL Lacs. 34 objects from the *core sample* are also included in the *complete sample*.

In the beginning of the project I planned to set a X-ray count rate limit of $hcps \geq 0.05\,\mathrm{sec}^{-1}$. Therefore I also did follow-up spectroscopy on several objects, which are now not included in the HRX-BL Lac sample. These objects could also be used for statistical work whenever it is not important to have a flux limited sample. This sample will be called the *HRX-BL Lac total sample*, or briefly *total sample*, as it includes the *complete sample* and all objects of the *core sample* with $\alpha < 16^h$.

To avoid confusion, I would like to recall the terms of the different samples I will refer to within this thesis:

- *core sample*. This is the basic sample of 39 BL Lac objects, collected from the HRX on an area of

[4]The NED is operated by the Jet Propulsion Laboratory, California Institute of Technology, under contract with the National Aeronautics and Space Administration.

[5]The SIMBAD Astronomical Database is operated by the Centre de Données astronomiques de Strasbourg

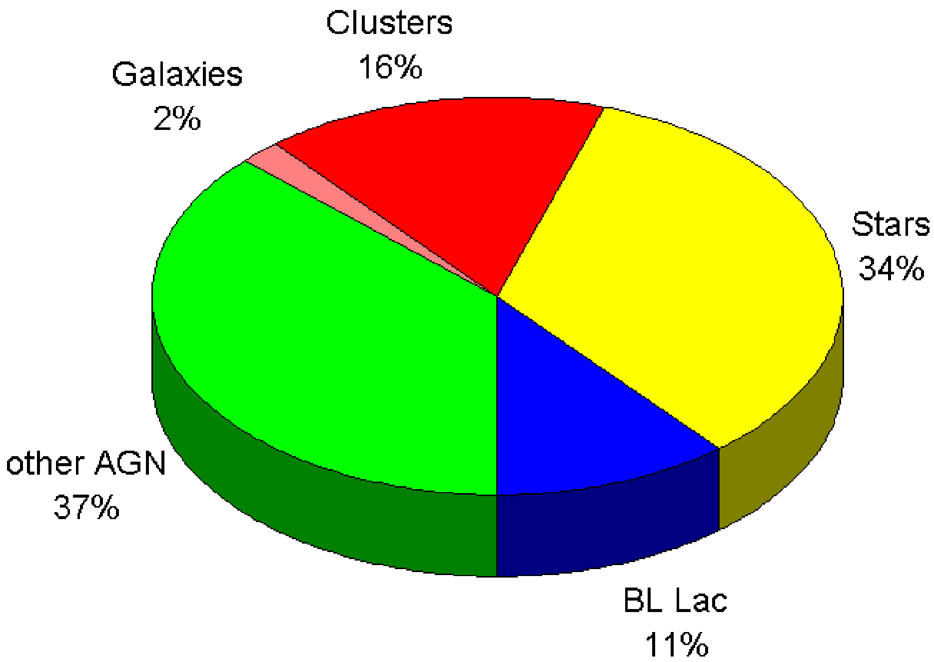

Figure 4.1: The distribution of objects within the complete identification of 350 X-ray sources in the ROSAT All-Sky Survey. The 39 BL Lac objects form the HRX-BL Lac *core sample*.

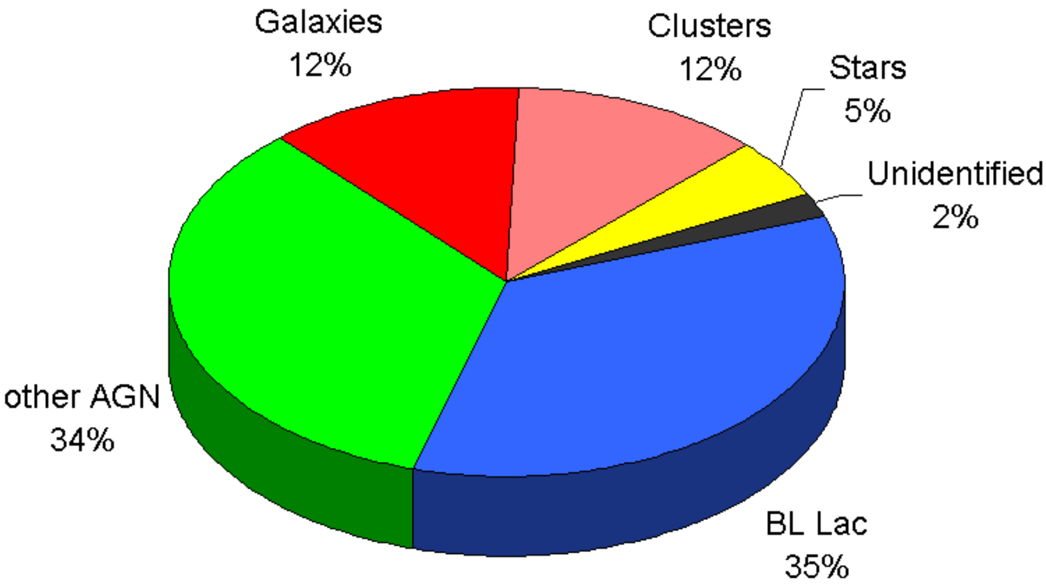

Figure 4.2: The distribution of objects derived from the radio/X-ray correlation. The 77 BL Lacs found within this sample form the HRX-BL Lac *complete sample*. Applying a combined X-ray and radio limit is much more effective than looking for X-ray sources only.

Table 4.3: The identification of the sources from the radio/X-ray correlation on the area of the HRX-BL Lac complete sample

object type	total number	fraction
BL Lac	77	34.5 %
Seyfert 1	59	26.5 %
Seyfert 2	6	2.7 %
Quasar	8	3.6 %
Blazar	2	0.9 %
LINER	4	1.8 %
Galaxy Cluster	26	11.7 %
Galaxies	26	11.7 %
Stars	9	4.0 %
SNR	2	0.9 %
Unidentified	4	1.8 %
Total	223	

2837 deg^2. The X-ray count rate limit is $hcps \geq 0.075\,\mathrm{sec}^{-1}$ for 1687 deg^2, and $hcps \geq 0.15\,\mathrm{sec}^{-1}$ for 1150 deg^2. No optical or radio limit was applied. This sample is presented and discussed in detail in Bade et al. (1998).

- *complete sample.* This sample comprises 77 BL Lac objects with $hcps \geq 0.09\,\mathrm{sec}^{-1}$ and NVSS radio flux $f_R(1.4\,\mathrm{GHz}) > 2.5\,\mathrm{mJy}$. No optical limit was applied. Candidate selection resulted in 223 objects of which 98% are optically identified. The borders of the 4770 deg^2 wide area are defined in Table 4.2. This sample includes 34 objects from the core sample (the other 5 objects have $hcps < 0.09\,\mathrm{sec}^{-1}$).
- *total sample.* This sample includes all 101 BL Lac objects found within the course of this work and the known BL Lacs within the area $7^h < \alpha < 16^h$ and $\delta > 20°$ (5089 deg^2) and a detection within the ROSAT All-Sky Survey.

The basic properties are also presented in Table 4.2.

4.3 X-ray flux limit of the HRX-BL Lac survey

Of course a count rate limit is not a flux limit. The flux of an X-ray source is related to the count rate by $f_x = CF \cdot countrate$ with CF being the conversion factor which is a function of the photon-index (Γ) and the absorption. The absorption is mainly determined by the Galactic neutral hydrogen column density (N_H). The function for CF was determined by Tananbaum et al. (1979):

$$CF(\Gamma, N_H) = \frac{\int_{E_1}^{E^2} E^{1-\Gamma} \cdot \exp\left(-N_H \cdot \sigma(E)\right) dE}{\int_{E_1}^{E^2} E^{-\Gamma} \cdot A(E)\, dE} \tag{4.1}$$

Here $\sigma(E)$ is the photoelectric cross section, computed by Morrison and McCammon (1983), based on the distribution of elements in the interstellar matter (Anders and Ebihara 1982) and on the atomic cross sections (Henke et al. 1982). $A(E)$ stands for the effective area of the ROSAT X-ray telescope at the photon energy E (Trümper, 1991b).

To determine the flux limit on the area of the HRX-BL Lac survey, the hydrogen column densities from the Leiden/Dwingeloo Survey (LDS, Hartmann and Burton 1997). This survey has a resolution of 0.25° and covers the sky north of $\delta = 30°$. Hence I determined flux limits within the 4770 deg^2 of the HRX-BL Lac complete sample in a raster of $0.25° \times 0.25°$. In each point the flux limit was determined

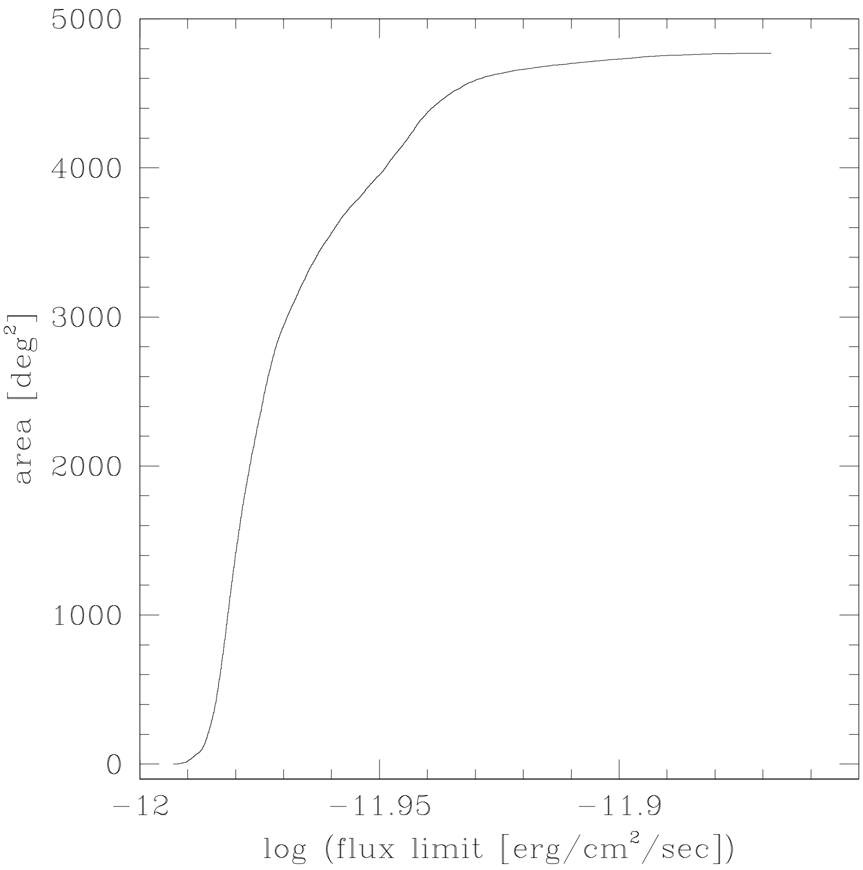

Figure 4.3: The sky coverage of the HRX-BL Lac complete sample.

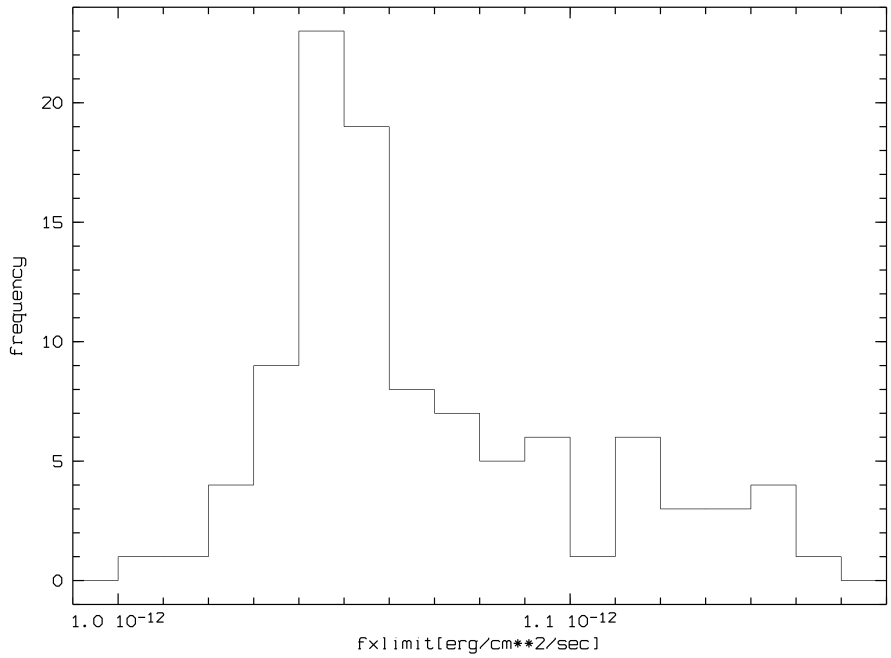

Figure 4.4: The X-ray flux limits for the whole HRX-BL Lac sample.

applying the formula 4.1 with a spectral slope of $\Gamma = -2.0$ and count rate limit $hcps = 0.09\,\mathrm{sec}^{-1}$ in the ROSAT-PSPC $0.5 - 2.0\,\mathrm{keV}$ energy band. The different exposure times within the RASS are neglected, because the high count rate limit guarantees a secure detection of the X-ray sources. The resulting flux limits are shown in Figure 4.3. The flux limit $1.34 \cdot 10^{-12}\mathrm{erg\,cm^{-2}\,sec^{-1}}$ encloses the whole survey area, and no position within the survey has a flux limit lower than $1.0 \cdot 10^{-12}\mathrm{erg\,cm^{-2}\,sec^{-1}}$. The mean flux limit is $(1.08 \pm 0.05) \cdot 10^{-12}\mathrm{erg\,cm^{-2}\,sec^{-1}}$.

Of course the assumption of one spectral index for all sources is not valid. The true flux limit is different for every source due to different spectral slope. Another approach to determine the flux limit is to determine the individual detection limit for every BL Lac found within the HRX-BL Lac survey. The distribution of the flux limits for all 102 BL Lac objects which are included in the enlarged HRX-BL Lac sample ($7^h < \alpha < 16^h$ and $hcps \geq 0.05$) is shown in Figure 4.4. The flux limits are based on the count rate limit of $hcps = 0.09\,\mathrm{sec}^{-1}$, on the spectral index derived from the X-ray data, and on the Galactic hydrogen column densities derived from the LDS. The distribution of flux limits is quite narrow ($1.01 \times 10^{-12}\mathrm{erg\,cm^{-2}\,sec^{-1}} < f_{x,limit} < 1.23 \times 10^{-12}\mathrm{erg\,cm^{-2}\,sec^{-1}}$) with a mean value of $< f_{x,limit} >= (1.07 \pm 0.04) \times 10^{-12}\mathrm{erg\,cm^{-2}\,sec^{-1}}$. The flux limits of both ways, the first based on the total survey area and assuming a mean spectral slope of $\Gamma = -2.0$, and the second, using the individual flux limits of the BL Lacs found within the survey, are consistent. Therefore it is justified to call the HRX-BL Lac sample a flux limited one with a limiting flux of $f_X(0.5 - 2.0\,\mathrm{keV}) = 1.1 \times 10^{-12}\mathrm{erg\,cm^{-2}\,sec^{-1}}$.

4.4 The NVSS and the FIRST radio catalogue

The FIRST is a project designed to produce the radio equivalent of the Palomar Observatory Sky Survey over $10,000\,\mathrm{deg}^2$ of the North Galactic Cap. Using the NRAO VLA in its B-configuration, the FIRST provides radio maps that have a pixel size of 1.8 arc-sec, a typical RMS of 0.15 mJy, and a resolution of 5 arc-sec. The astrometric reference frame of the maps is accurate to 0.05", and individual sources have 90% confidence error circles of radius < 0.5" at the 3 mJy level and 1" at the survey threshold of 1 mJy. The northern sky coverage of the FIRST Survey is displayed in Figure 4.5. The Catalogue

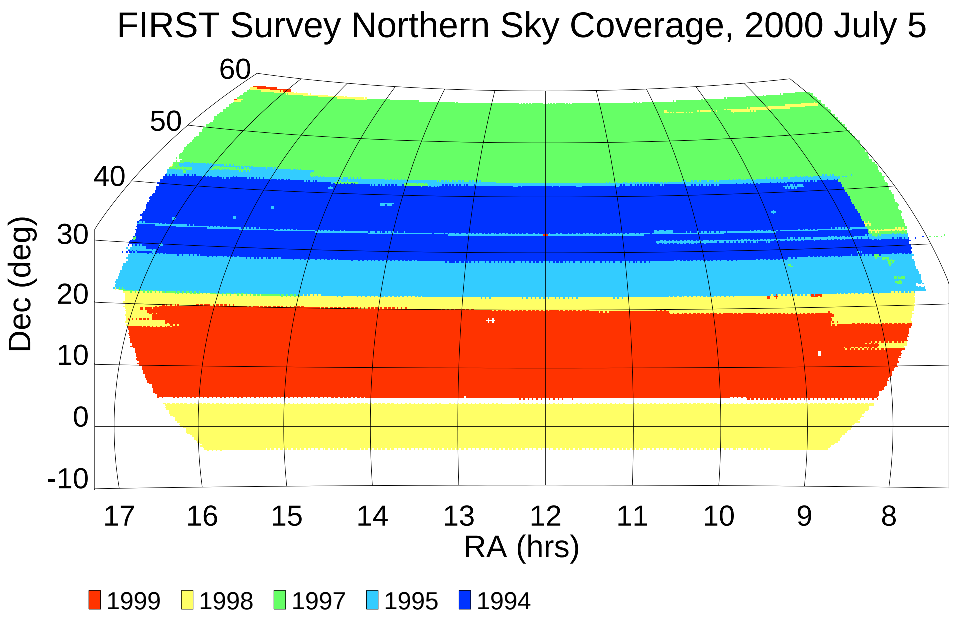

Figure 4.5: The FIRST Survey covers the area of the HRX-BL Lac sample in the region $22.2° < \delta < 57.6°$ since 1997.

version (1998 February 4) which was used for the candidate selection contains 382,892 sources from the north Galactic cap. In the north it covers about 4150 square degrees of sky, including most of the area $7^h20^m < \alpha(\mathrm{J2000.0}) < 17^\mathrm{h}20^\mathrm{m}$, $22.2° < \delta < 57.6°$.

The observations for the 1.4 GHz NVSS began in 1993 and cover the sky north of $\delta = -40°$. This project uses the compact D and DnC configurations of the Very Large Array to make 1.4 GHz continuum total-intensity and linear polarization images. The NVSS is based on 217,446 snapshot observations of partially overlapping primary beam areas, each of which is mapped separately. The RMS uncertainties in right ascension and declination vary from $0''.3$ for strong ($f_R \gg 30$ mJy) point sources to $5''$ for the faintest (~ 2.5 mJy) detectable sources. The NVSS catalogue contains 1,814,748 radio sources.

Thus the error of these radio positions is $\leq 5''$. The distribution of the position error of the X-ray sources in the ROSAT Bright Source Catalogue is shown in Figure 4.6. 99.96 % of the sources in the BSC have a positioning error $\leq 25''$. Therefore we have chosen a radius of $r = 30''$ for the radio/X-ray correlation.

4.5 Optical follow up observation - spectroscopy

> "I prepared several times in different places where I worked telescope proposals. And as soon as you say you want to do spectroscopy on BL Lac objects you go down in flames."
> C. Impey (1988)

BL Lac objects are defined to have spectra with no or very weak emission lines (as described on page 15). Therefore it is difficult to determine the redshift of these elusive objects. One has to find the absorption lines of the host galaxy which is often out-shined by the non-thermal continuum of the point-like synchrotron source. Also many of the X-ray selected BL Lacs presented here, are optical weak (see Table 11.3) and have magnitudes as faint as $B > 20$ mag. Telescopes of the 4m class are needed to get spectra of sufficient signal-to-noise for those BL Lac candidates and to determine their redshift.

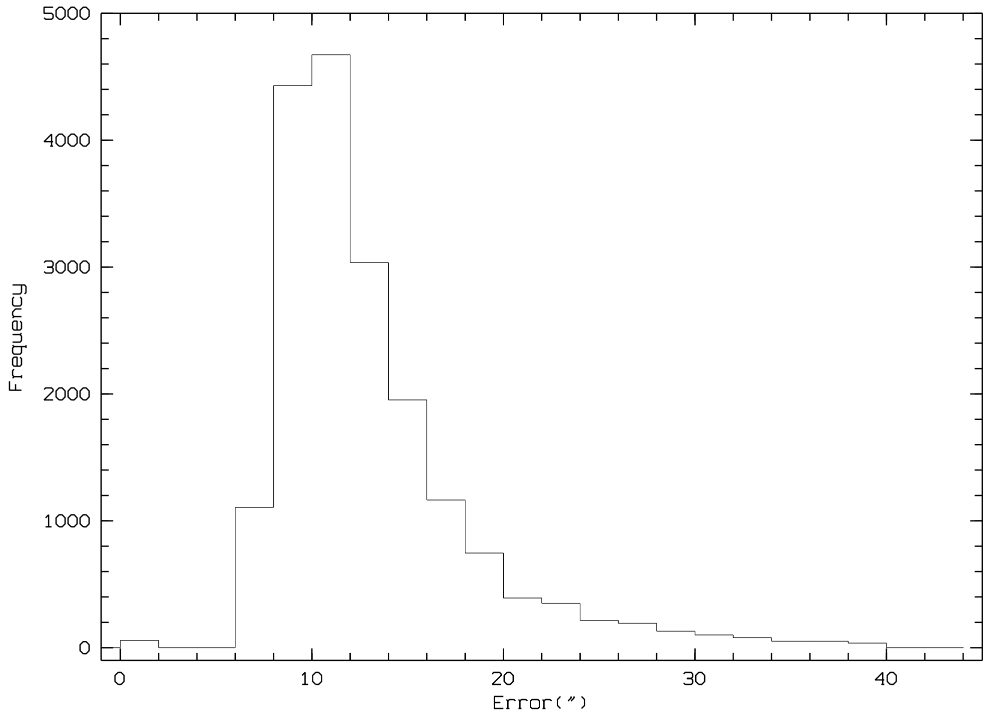

Figure 4.6: Histogram of the 1σ errors of the ROSAT-PSPC positions in the Bright Source Catalogue.

Table 4.4: Observation runs to do follow-up on HRX-BL Lac candidates.

Telescope	Instrument	Date	#nights	observed obj.
3.5m CA	MOSCA	March 1997	4	30
WHT / La Palma	ISIS	April 1997	2	19
3.5m CA	MOSCA	February 1998	6	121
3.5m CA	MOSCA	February 1999	$\sim 1^a$	9

[a] morning and evening hours of five nights.

The spectroscopy done on the BL Lac candidates of the HRX-BL Lac sample has been done within four observation runs. The first two observation runs were done in 1997 by Norbert Bade, at the Calar Alto 3.5m telescope using the MOSCA focal reducer, and by Dieter Engels at the William Herschel Telescope (WHT) on La Palma with the ISIS double spectrograph. The most important run was done in February 1998 by Norbert Bade and myself at the 3.5m telescope on Calar Alto, and the last one again at the Calar Alto 3.5m in February 1999 by myself within a combined observation program together with Olaf Wucknitz. An overview of these four observation runs is given in Table 4.4. The last column in this table refers to the number of *different* objects observed in the observation run. Some objects are also included in more than one observation run, e.g. 1517+656 was included in all programs. Most of the results from the 1997 observation runs have been already presented in Bade et al. (1998). Working with MOSCA we used the G500 grism to identify BL Lac objects and, if necessary, the G1000 and R1000 grisms to determine redshifts (see Table 4.5). The spectra from the last two observation runs have been reduced using software which has been developed by Hans Hagen at the Hamburger Sternwarte. The spectra have been bias subtracted and flat-field corrected, using morning and evening skyflats as well as flats taken with a continuum lamp. Flats have always been taken with the same configuration (slit width and grism) as the scientific exposures. Then I corrected the spectra for the response of the detector using spectrophotometric standard stars taken within the same night as the object. But because none of the

Table 4.5: Grisms used for spectroscopy with MOSCA at Calar Alto 3.5m telescope.

Grism	coverage	resolution
G500	4250 – 8400 Å	12 Å
R1000	5900 – 8000 Å	6 Å
G1000	4400 – 6600 Å	6 Å

spectroscopic observation runs have been taken under photometric conditions, flux values based on the spectra are only clues to the real source intensity.

The characterizing feature of BL Lac spectra in the optical is a non-thermal continuum which is well described with a single power law. A second component is contributed by the host galaxy. If the BL Lac itself shows no emission lines at all, it is only possible to determine the redshift of the object by identifying absorption features of the host galaxy. The host galaxies are in majority giant elliptical galaxies (e.g. Urry et al. 2000), as already described on page 17. These galaxies show strong absorption features which are caused by the stellar content. Expected absorption features in the optical are an iron feature at 3832 Å, the Ca H and K (3934 Å and 3968 Å, respectively), the G Band at 4300 Å, magnesium at 5174 Å and the natrium D doublet at 5891 Å. A feature which is also prominent in most galaxy spectra is the so-called "calcium break" at 4000 Å. When identifying candidates for the HRX-BL Lac sample, the calcium break was used to distinguish between normal elliptical galaxies and BL Lac objects. The calcium break is defined as follows (Dressler & Shectman 1987):

$$Ca - break[\%] = 100 \cdot \frac{f_{upper} - f_{lower}}{f_{upper}} \tag{4.2}$$

with f_{upper} and f_{lower} being the mean fluxes measured in the $3750\,\text{Å} < \lambda < 3950\,\text{Å}$ and $4050\,\text{Å} < \lambda < 4250\,\text{Å}$ objects rest frame band respectively. In galaxies with a late stellar population, as expected in elliptical galaxies, this contrast is about $\geq 40\%$ with the higher flux to the red side of the break. Due to low signal to noise within some spectra, the error of this value can be of the order of the measured break. Nevertheless only a few objects within the HRX-BL Lac survey exhibit a calcium break in the range $25\% < Ca - break < 40\%$ (8 objects within the HRX-BL Lac *total sample*, and only 3 of the complete sample). As will discussed later, these objects have also been included in the HRX-BL Lac *total sample*. Objects with a calcium break $> 40\%$ have been identified as galaxies.

The interstellar medium can cause weak narrow emission lines in the spectrum, like the hydrogen Balmer lines. In normal elliptical galaxies they are expected to be weak but can be seen in the most powerful ellipticals, cD galaxies, with LINER properties. For higher redshifts, these features move out of the optical wavelength region. Absorption lines from the interstellar gas become detectable. The strongest lines are then the MgII doublet (2796.4 Åand 2803.5 Å, c.f. page 81), MgI 2853 Å, three FeII lines (2382.8 Å, 2586.6 Å, and 2600.2 Å), and FeI 2484 Å. Expected equivalent widths are of the order of several Å (Verner et al. 1994). A weak MnII line at 2576.9 Å might also be observable. These lines can also be produced by intervening material and redshifts derived on this basis are lower limits rather then firm values as derived from the lines produced by the stellar population. This is for example seen in 0215+015 (Blades et al. 1985) with several absorbing systems in the line of sight.

Reliable redshifts can only be derived when more than one line is detectable. Some objects, like PG 1437+398, do not show any absorption lines or other features, even in high signal to noise spectra taken within several hours with telescopes of the 4m class. Also these objects are not necessarily optical weak. PG 1437+398 for example has an optical magnitude of $B \sim 16$ mag and is therefore one of the brightest objects in the HRX-BL Lac sample.

4.6 Optical follow up observation - photometry

The photometry of 49 X-ray selected BL Lac objects has been published in Beckmann (2000).

Besides the measurement of redshift and spectral shape values of the optical fluxes are important to understand the nature of the BL Lac objects. Several results in the field of BL Lac physics are based on the spectral energy distribution, e.g. the overall spectral indices α_{OX} and α_{RO}. But accurate measurements of the optical flux, especially for faint BL Lac objects, are rare. The first glimps might give the impression that this is obsolete due to the variability of BL Lac objects. Additionally magnitudes with an accuracy of ~ 0.5 mag could be obtained by using the APM Sky Catalogue, the USNO data base, or the calibrated objective prism plates of the HQS.

But the determination of brightnesses is only possible for objects with $B < 18$ mag. For fainter sources the uncertainty in the calibration increases dramatically. Values taken from literature are not satisfying for a statistical study of a larger sample of objects.

The argument that photometry of BL Lac objects only makes sense if observations are carried out simultaneously (like combined campaigns with X-ray and optical telescopes for example) is only valid for the highly variable objects. On the other hand the variability of BL Lac objects strongly depends on the X-ray dominance α_{OX}; for a definition of the X-ray dominance α_{OX} see page 18. This has been shown by e.g. Heidt & Wagner (1998), Villata et al. (2000), Mujica et al. (1999), and Januzzi et al. (1994).

For photometry the acquisition exposures of the different follow up campaigns could have been used. But because these observation runs were carried out to verify BL Lac candidates and to determine redshifts, not much work had been applied to achieve a good photometry with sufficient standard fields. Also no observation run was done under photometric conditions. Nevertheless some exposures, which were made directly before or after observing a photometric standard, can be used for photometry.

To obtain a more homogeneous database for determining magnitudes, an observation run was carried out in spring 2000. A total number of seven nights (28.4.–4.5.2000) was available at the Calar Alto 1.23m telescope. The detector was a CCD with a SITe#18b 2k $\times$ 2k chip, which covered a sky area of $\sim 10' \times 10'$. Whenever no photometric measurements were possible, relative photometry on selected BL Lacs of the sample was done.

Photometric B magnitudes have been derived by comparison with standard stars. For that purpose magnitudes of stars determined with the HST from the "Guide Star Photometric Catalog" (GSPC, Lasker et al. 1988) have been used. Directly before and/or after each exposure of a BL Lac the nearest GSPC star was observed to get an absolute calibration. In total it was possible to measure magnitudes for 51 HRX-BL Lac, especially the optically faintest BL Lac of the sample. The direct images have been subtracted by a bias, determined on the overscan area of the CCD (the CCD was cooled with liquid nitrogen and no dark current subtraction is needed). After that the images were corrected with combined flat fields which had been taken in the dusk and dawn sky. The analysis of the direct images was done with the IRAF package (Tody 1993). Instrumental magnitudes were obtained in simulated aperture. The photometric radius was kept large enough (typically 6 arcsec or larger, if the objects appeared to be extended) to include all the light of the objects. Errors of magnitudes were estimated using standard IRAF procedures and including the uncertainties of the used reference stars from GSPC.

Results of the photometry are listed in Table 11.3 (Appendix, page 138). The uncertainties are of the order of ≤ 0.2 mag (the detailed measurements can be found in Beckmann 2000).

4.7 Infrared data for HRX-BL Lac

To derive a good coverage of the entire spectral energy distribution (SED) also data from two infrared surveys have been used.

The IRAS Faint Source Catalogue contains only data for two HRX-BL Lac (see Table 4.6). Only one of the two sources has a known redshift (RX J1419+5423; $z = 0.151$). Therefore only this object offers the opportunity to determine the luminosity in the infrared energy range. Also this object is not part of the complete HRX-BL Lac sample, because its count-rate in the RASS-BSC is $hcps = 0.055\,\mathrm{sec}^{-1}$. The spectral slope in the total IRAS band is $\alpha_{IRAS} = -1.0$ with a steeper slope to the lower energy range for both objects. This is in agreement to the observations done by Impey & Neugebauer (1988) who found out that the continuum emission of BL Lac steepens gradually towards shorter wavelengths from

Table 4.6: HRX-BL Lac in the IRAS Faint Source Catalogue. Fluxes in mJy.

Name	z	$F_{12\mu m}$	$F_{25\mu m}$	$F_{60\mu m}$	$F_{100\mu m}$	$\log \nu L_\nu^a$
RX J0721+7120	?	112	126	237	783	45.2
RX J1419+5423	0.151	66	86	212	546	44.9

[a] this value is constant for both objects within the IRAS energy region. For RX J0721+7120 a redshift of $z = 0.2$ is assumed.

Table 4.7: HRX-BL Lac in the 3rd EGRET Catalogue

Name	EGRET	z	$F_{400\mathrm{MeV}}$[pJy]	$\log \nu L_\nu^a$
RX J0721+7120	3EG J0721+7120	?	29.8 ± 1.7	45.59
Mkn 421	3EG J1104+3809	0.030	24.5 ± 1.6	43.96
ON 231	3EG J1222+2841	0.102	20.2 ± 1.6	44.89
RX J1211+2242 ?	3EG J1212+2304	0.455	23.6 ± 6.4	46.07

[a] applying $\alpha = 1$ (Lin et al. 1992) at 10^{23} Hz ($\simeq 400\,\mathrm{MeV}$). For RX J0721+7120 $z = 0.2$ is assumed.

the radio to the UV regime. These data are used to compute the $\log \nu L_\nu$ values listed in table 4.6 and are used for the further analysis of the spectral energy distribution.

In the near infrared the "Two-Micron All-Sky Survey" (2MASS, Skrutskie et al. 1995, Stiening et al. 1995) provides data for 52 objects of the HRX-BL Lac total sample (43 sources (57 %) of the complete sample). The 2MASS is a survey of the sky using two ground based telescopes, one on the Mt. Hopkins in Arizona and the other at the CTIO in Chile. Both telescopes are identical and are equipped with a three channel camera, each channel consisting of a 256×256 HgCdTe detector. Thus at the same time observations at three energy bands are possible; J ($1.25\mu m$), H ($1.65\mu m$) and K_s ($2.17\mu m$). Up to now the surveys covers 98.3% of the entire sky. Not all observations have already been analyzed. At the time of writing, the *2MASS Second Incremental Release Point Source Catalog* (2MASS-PSC) is available which contains 160 million point sources. For extended sources an extra catalogue is constructed, the *2MASS Second Incremental Release Extended Source Catalog* (2MASS-XSC).

4.8 Gamma-ray data for HRX-BL Lac

A great fraction of the emitted radiation of BL Lac objects is set free in the high energy region beyond the X-ray region. Therefore gamma-ray data are of high interest to the BL Lac community. The *Energetic Gamma-Ray Experiment Telescope* (EGRET, Kanbach et al. 1988) on board the Compton Gamma Ray Observatory (CGRO) covered the energy range between 20 MeV to over 30 GeV. EGRET worked for nearly ten years before CGRO was safely de-orbited and re-entered the Earth's atmosphere in June 2000 to avoid an uncontrolled re-entry in the atmosphere. The effective surface of the telescope was $0.15\,\mathrm{m}^2$ in the 0.2–10 GeV region. The angular resolution was strongly energy dependent, with a 67 % confinement angle of 5.5° at 100 MeV, falling to 0.5° at 5 GeV on axis; bright gamma-ray sources could be localized with approximately 10 arcmin accuracy. The energy resolution of EGRET was 20 – 25 % over most of its range of sensitivity. The data for the comparison with the HRX-BL Lac sample were taken from the Third EGRET Catalogue (Hartman et al., 1999). This catalogue contains 271 gamma-ray sources ($E > 100\,\mathrm{MeV}$) and includes data from 1991 detected April 22 to 1995 October 3.

Three of the HRX-BL Lac objects are included in the EGRET catalogue; the most relevant data are listed in Table 4.7. The flux values at $\sim 10^{23}$ Hz are derived by multiplying the photon count-rates as listed in the Third EGRET Catalogue with the conversion factors from Thompson et al. (1996). The variation of the flux values is remarkable. I used only detections and no upper limits to derive the fluxes. For computing fluxes I applied a weighted mean, based on the flux errors given in the EGRET catalogue. Therefore the true minimal flux value could be even lower. One object of the HRX-BL Lac sample might be a counterpart of the EGRET source 3EG J1212+2304. It is included in Table 4.7 and will be discussed in the chapter about special single objects on page 89. The spectral energy distribution for these gamma bright objects is also shown in this chapter on page 90.

Chapter 5

Properties of HRX-BL Lac

In this chapter I will discuss the properties of the HRX-BL Lac sample in the different wavelength ranges and also their spectral energy distribution. Whenever completeness is necessary to derive results, the 77 objects of the HRX-BL Lac *complete sample* are used. In cases, where the redshift information is needed, only the 62 objects from the *complete sample* with known redshift are used.

Throughout this thesis luminosities are computed by

$$L = 4\pi \cdot d_l^2 \cdot f_{source} \tag{5.1}$$

where f_{source} is the flux density in the source rest frame and d_l is the luminosity distance. Assuming a Friedmann universe ($\Lambda = 0$) the luminosity distance can be computed by the following formula (e. g. Mattig 1958):

$$d_l = \frac{c_0}{H_0 \cdot q_0^2} \cdot [z \cdot q_0 + (q_0 - 1) \cdot (\sqrt{(1 + 2q_0 z)} - 1)] \tag{5.2}$$

The proper distance, which is used to compute volumes in space, is related to the luminosity distance by $d_l = d_p \cdot (1 + z)$.

Throughout this thesis I apply a Hubble parameter $H_0 = 50\,\mathrm{km\,sec^{-1}\,Mpc^{-1}}$ and a deceleration parameter $q_0 = 0.5$, assuming a Friedmann universe with $\Lambda = 0$.

5.1 HRX-BL Lacs in the radio band

By definition all HRX-BL Lac objects are radio sources. The 1.4 GHz fluxes cover the range between 2.8 mJy of the faint end for the most distant object RX J1302+5056 ($z = 0.688$), and 768.5 mJy for Markarian 421 ($z = 0.03$). The faintest BL Lac is MS 1019.0+5139 ($L_r = 4.2 \cdot 10^{23}\,\mathrm{W/Hz}$), the brightest one is RX J0928+7447 ($L_r = 1.3 \cdot 10^{26}\,\mathrm{W/Hz}$, $z = 0.638$). Figure 5.1 shows the distribution of radio luminosities for the HRX-BL Lac sample.

As expected for an X-ray selected sample, the radio luminosities are relatively low, thus still covering a wide range. Applying the definition for radio-loudness ($R_L = \log{(f_{Radio}/f_B)}$) there is only one radio quiet object ($R_L < 1$), the BL Lac RX J1257+2412 ($z = 0.141$, $f_{r,source} = 13.2\,\mathrm{mJy}$, $B = 15.4\,\mathrm{mag}$). Thus, in principle, BL Lac objects seem to be radio loud objects, even when selected due to their X-ray properties. The question whether if radio silent BL Lacs with $R_L \ll 1$ may exist will be discussed in section 5.5.1.

5.2 HRX-BL Lacs in the infrared

Only for one object (RX J0721+7120) in the HRX-BL Lac sample are IRAS infrared data available (see table 4.6). This object shows a spectral slope of $\alpha_{IR} \sim 1$ over the entire IRAS energy range.

For 52 HRX-BL Lacs data are available in the near infrared region ($\lambda = 1 - 3\,\mu\mathrm{m}$) from the 2MASS survey as already described in section 4.7. The mean value for the spectral slope in this regime is $\alpha_{2\,\mu\mathrm{m}} = 0.6 \pm 0.2$. Only one object (RX J1123+7230) shows an "inverse" spectrum with $\alpha_{2\,\mu\mathrm{m}} = -1.1$.

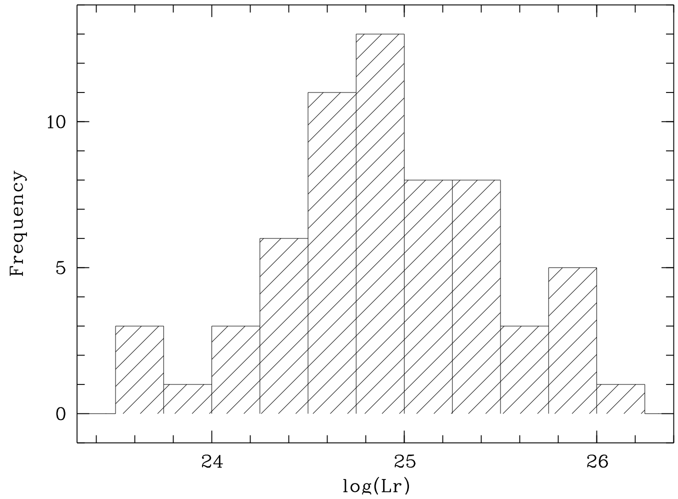

Figure 5.1: Distribution of radio luminosities (in W/Hz) for the HRX-BL Lac objects with known redshifts.

There is no evidence that this BL Lac is different from the rest of the sample, although all other objects have $\alpha_{2\mu\mathrm{m}} > 0$. The redshift of RX J1123+7230 is not determined up to now, but the point-like direct image and a possible detection of the calcium break suggests a redshift $z \sim 0.5$. All other properties are not remarkable compared to other objects of the HRX-BL Lac sample. I assume therefore that the infrared data of this objects are contaminated by the emission from a nearby star seen in the direct image ($\Delta_{pos} \simeq 15$") and omit them from the following analysis. The distribution of luminosities derived from H-magnitudes is shown in Figure 5.2. The mean luminosities are $\overline{L_J} = 23.51 \pm 0.52\,\mathrm{W/Hz}$, $\overline{L_H} = 23.61 \pm 0.51\,\mathrm{W/Hz}$, and $\overline{L_K} = 23.65 \pm 0.52\,\mathrm{W/Hz}$ (at $1.25\,\mu$m, $1.65\,\mu$m, and $2.17\,\mu$m respectively). The strongest infrared source in the HRX-BL Lac sample is RX J0721+7120 which has been included also in the IRAS Faint Source Catalogue (see Table 4.6).

5.3 HRX-BL Lacs in the optical

Because no optical limit was applied when identifying the candidates from the radio/optical correlation, many HRX-BL Lac exhibit low apparent magnitudes, sometimes even fainter than the detection limit of the POSS direct plates (see Figure 5.3). The distribution of optical luminosities for the BL Lacs with known redshift is shown in Figure 5.4. When identifying candidates for the HRX-BL Lac sample, the calcium break was used to distinguish between normal elliptical galaxies and BL Lac objects. Due to low signal to noise within some spectra, the error of this value can be of the order of the measured break. The distribution of calcium break values is shown in Figure 5.5. Nevertheless only a few objects exhibit a calcium break in the range $25\% < Ca - break < 40\%$ (8 objects within the whole HRX-BL Lac sample, and only 3 of the complete sample). Because all their other properties smoothly overlap with those of the BL Lacs obeying the classical definition ($Ca - break \leq 25\%$) I accepted them as bona-fide BL Lacs and included them into the discussion of this thesis (as suggested by Marchã et al. 1996, and confirmed by Laurent-Muehleisen et al. 1998). Only two of them show a radio polarization of less than 1%, and all borderline objects within the HRX-BL Lac complete sample exhibit strong polarization > 6% in the NVSS.

Twelve objects from the NVSS/BSC correlation are listed in the NED as galaxies with redshift information. Of course it cannot be ruled out that some of these 12 galaxies are borderline BL Lacs with break values $25\% < Ca - break < 40\%$. The measurement of the break is only possible when the redshift is known and so low that the break is within the spectral range covered by the observation. Therefore break values are only available for 30 of the HRX-BL Lac . In seven cases the break value is negative, due to a strong underlying power law spectrum and/or to low signal to noise of the spectra. Only for one

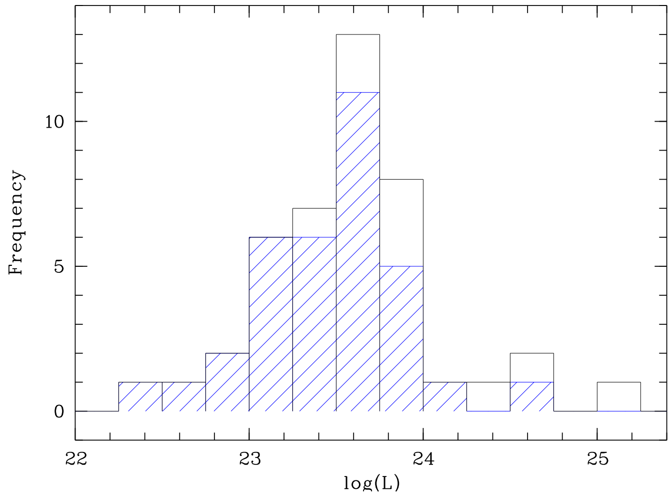

Figure 5.2: Distribution of near-infrared luminosities (at 16500 Å in W/Hz) for the HRX-BL Lac objects. The shaded part refers to the objects with known redshift. For the others the redshift is set to $z = 0.3$

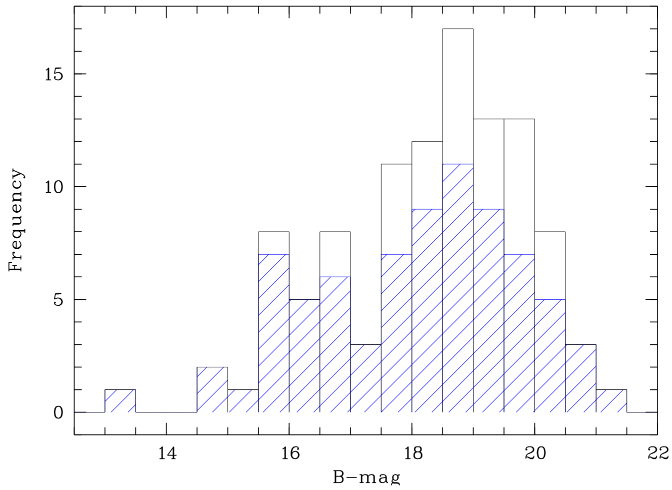

Figure 5.3: Distribution of B magnitudes for HRX-BL Lac. The shaded part refers to the complete sample.

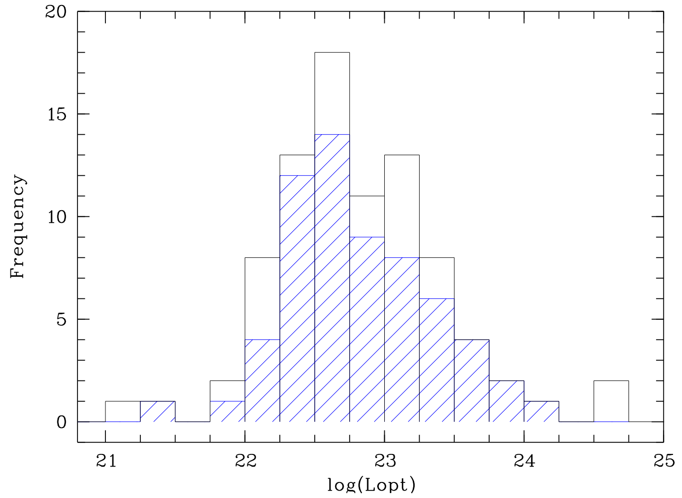

Figure 5.4: Distribution of monochromatic optical luminosities in [W/Hz] at $\lambda = 4400$ Å for the HRX-BL Lacs with known redshift (applying $\alpha_{B-band} = 0.6$). The hashed area refers to the complete sample.

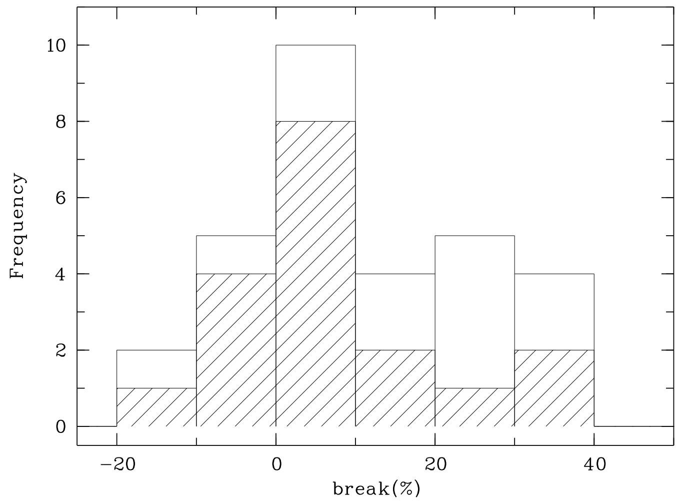

Figure 5.5: Distribution of calcium break values for the 30 BL Lac of the HRX-BL Lac total sample, where it was possible to determine the break (the shaded region marks the *complete sample*). Negative values can arise from a strong underlying non-thermal continuum.

object (RX J1117+2014) is the negative calcium break not consistent with a value of 0%.

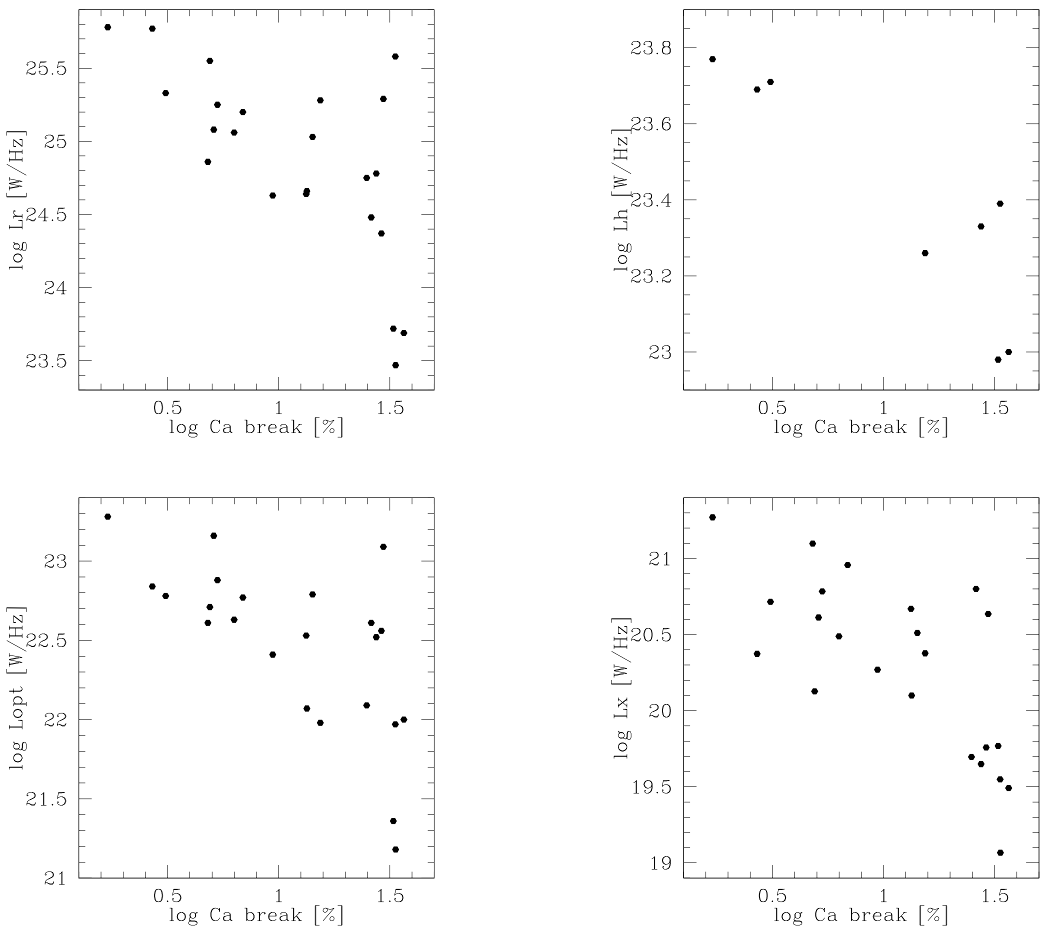

Figure 5.6: Strength of the calcium break versus monochromatic luminosity in the radio, near infrared (H-band), optical, and X-ray. Logarithmic scaling is applied.

The correlation of the break strength with the luminosity in radio, near infrared, optical, and X-rays is shown in Figure 5.6. Negative break values are omitted and logarithmic scaling is used in both axes. In all wavelength regions the correlation between emitted luminosity and break strength is significant. This is in agreement to Landt & Padovani (1999) who found an increase in radio core luminosity as the calcium break gets more and more diluted.

It is remarkable that there was no object found within the NVSS/BSC correlation which shows weak emission lines with equivalent widths of several 10 Å. The only exception might be RX J1424+2514, an object with Balmer lines of line strength $EW \simeq 70$ Å. This object was not classified as a BL Lac. All objects with stronger lines were clearly identified as Seyfert I/II galaxies (see Table 11.4). Therefore the confusion of identification seems to be no problem for X-ray selected BL Lacs with a strong X-ray fluxes ($f_X \gtrsim 10^{-12} \mathrm{erg\,cm^{-2}\,sec^{-1}}$). This does not mean that emission lines are not occurring in BL Lac objects in general. The existence of emission lines within the optical spectra of BL Lac objects has been reported by several authors (e.g. Marchã et al. 1996). But based on the work presented here it seems that emission lines occur only in the less X-ray dominated objects with lower peak frequency, the LBL objects.

5.4 ROSAT BSC data for the HRX-BL Lac objects

The sample of HRX-BL Lac objects is defined by the correlation of radio and X-ray sources. The X-ray data are taken from the RASS-BSC (see section 3.3). As described, the RASS data for most objects only contain very few photons. It is not possible to derive real spectra from this database. But the spectral slope can be determined using the hardness ratios provided by the BSC (see formula 3.2). In principle two methods to do this are possible: the first one is to use the absorption due to Galactic hydrogen and a given spectral slope to simulate a spectrum. With those two parameters it is then possible to determine the conversion factors (formula 4.1) for the different bands which determine the hardness ratios (formula 3.2). Thus a grid of $(HR1, HR2)(\Gamma_X, N_{H,Galactic})$ is produced, where $(HR1, HR2)$ is a pair of hardness ratios, Γ_X is the photon index[1] which describes the X-ray spectrum. The second possibility is to fix the spectral slope only and search for the best parameter combination of ($HR1$, $HR2$, N_H). These methods are described in detail by Schartel et al. (1992, 1994). It is obvious that the resulting errors of the method based on free-fitted absorption (we will call these values $\alpha_{X,free}$ and $N_{H,free}$) are larger than in the procedure where the absorption is fixed to the Galactic value (α_X and $N_{H,gal}$).

Using the latter method, we derive a mean spectral slope of $\alpha_X = 1.09 \pm 0.31$ from the ROSAT-PSPC data. The energy indices cover a range $-1.78 \leq \alpha_X < +0.86$. The values derived with a free fitted N_H are remarkably steeper: $\alpha_{X,free} = 1.41 \pm 0.60$ (covered range $-2.64 < \alpha_{X,free} \leq +0.05$). These values of $\alpha_{X,free}$ are in good agreement with previous studies of the spectral slope of BL Lac objects. Maraschi et al. (1995) reported $\alpha_X = 1.56 \pm 0.43$ for three pointed ROSAT observations on X-ray bright BL Lacs, and Perlman et al. (1996) found $\alpha_X = 1.20 \pm 0.46$ for the EMSS BL Lac sample (Morris et al. 1991). Brinkmann et al. 1997 investigated ROSAT-PSPC spectra for 91 BL Lacs, also finding the spectral slope being steeper for free fitted absorption ($\alpha_X = 1.23 \pm 0.06$ and $\alpha_{X,free} = 1.35 \pm 0.11$). Another work on ROSAT-PSPC data by Comastri et al. (1995a) derived $\alpha_X = 1.30 \pm 0.25$, but different to Brinkmann et al. 1997 they did find the same spectral slope when fitting $\alpha_{X,free}$ and N_H at the same time ($\alpha_{X,free} = 1.26 \pm 0.20$). Bade et al. (1994) found a mean spectral slope of $\alpha_X = 1.49 \pm 0.17$ for 10 new detected HBL, and Fink (1992) derived $\alpha_X = 1.39 \pm 0.07$ for ten already known BL Lacs. More recently Siebert et al. (1998) found a value of $\alpha_X = 1.35 \pm 0.55$ for intermediate BL Lac objects.

The spectral slope of X-ray selected BL Lac objects is thus slightly flatter than the values found for X-ray selected emission-line AGN (e.g. $\alpha_X = 1.50 \pm 0.48$, Walter & Fink 1993; $\alpha_X = 1.42 \pm 0.44$, Ciliegi & Maccacaro 1996; $\alpha_X = 1.53 \pm 0.42$, Beckmann 1996). With the spectral slopes derived from the hardness ratios and the count rates I determined the conversion factors and the fluxes of the HRX-BL Lac by applying $f_x = CF \cdot countrate$ (see page 32). The distribution of fluxes is shown in Figure 5.7. The sharp cut-off at $10^{-12}\mathrm{erg\,cm^{-2}\,sec^{-1}}$ is due to the count-rate limit of $hcps \geq 0.09\,\mathrm{sec}^{-1}$. It is obvious that the distribution of observed fluxes for HBL and IBL[2] in the HRX-BL Lac is equivalent. The mean flux for the HBL and IBL is $(4.8 \pm 4.8) \cdot 10^{-12}\mathrm{erg\,cm^{-2}\,sec^{-1}}$ and $(7.1 \pm 18.6) \cdot 10^{-12}\mathrm{erg\,cm^{-2}\,sec^{-1}}$ respectively. But if we omit the bright source Mrk 421, we get for the IBL a mean flux of $(4.2 \pm 4.9) \cdot 10^{-12}\mathrm{erg\,cm^{-2}\,sec^{-1}}$, which is very similar to the value for the HBL.

For comparison of emission at different wavelengths, monochromatic fluxes are much more useful than integrated fluxes. The formula of the monochromatic flux f_E depends on the energy E_0 at which the monochromatic flux should be determined, on the energy band, defined by the energies E_1 and E_2, on the spectral energy index α_E, and on the integrated flux f_x:

$$f_E = \frac{f_x \cdot (1 - \alpha_E)}{E_2^{(1-\alpha_E)} - E_1^{(1-\alpha_E)}} \cdot E_0^{-\alpha_E} \cdot (1+z)^{\alpha_E - 1} \tag{5.3}$$

Here the last factor $(1+z)^{\alpha_E - 1}$ is the K-correction term (see page 18). The flux is now in units $[\mathrm{erg\,cm^{-2}\,sec^{-1}\,keV^{-1}}]$. Transformation of this flux value f_E into μJy is done by applying

$$f_E[\mu\mathrm{Jy}] = f_E[\mathrm{erg\,cm^{-2}\,sec^{-1}\,keV^{-1}}] \times \frac{h \cdot 10^{26}}{e} \tag{5.4}$$

where $h = 6.6262 \cdot 10^{-34}$Jsec is the Planck constant, and $e = 1.6022 \cdot 10^{-19}$C the electron charge.

[1]The energy index α_E is related to the photon index $\Gamma = \alpha_E + 1$

[2]Here HBL are defined with $\alpha_{OX} < 0.9$ ($\log \nu_{peak} \lesssim 16.4$) and IBL have $0.9 \leq \alpha_{OX} < 1.4$ ($16.4 \lesssim \log \nu_{peak} \lesssim 14.6$).

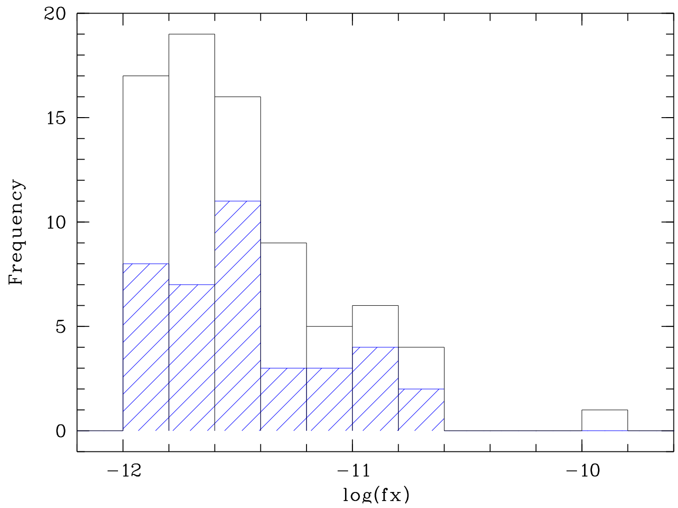

Figure 5.7: Distribution of the ROSAT-PSPC fluxes $f_x(0.5-2.0\,\mathrm{keV})$ in $[\mathrm{erg\,cm^{-2}\,sec^{-1}}]$ for the HRX-BL Lac sample as derived from the Bright Source Catalogue. The shaded area marks the more X-ray dominated objects (HBL) with $\alpha_{OX} < 0.9$. The strong X-ray source with $f_X(0.5-2.0\,\mathrm{keV}) = 1.2\cdot 10^{-10}\mathrm{erg\,cm^{-2}\,sec^{-1}}$ is Markarian 421.

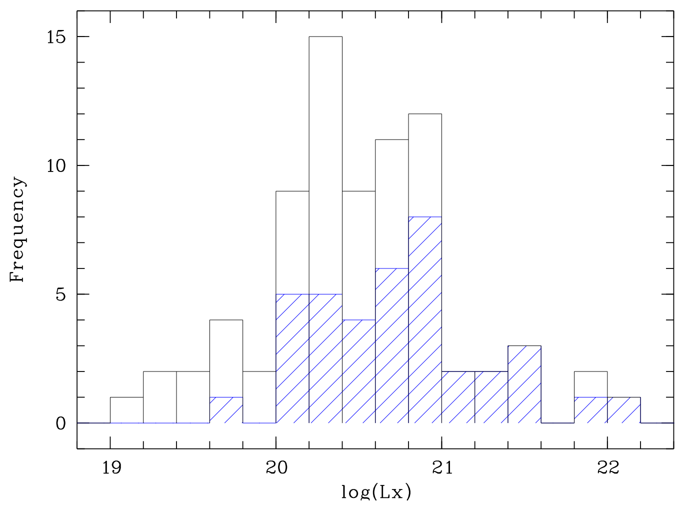

Figure 5.8: Distribution of monochromatic X-ray luminosities ($L_X(1\,\mathrm{keV})[\mathrm{W/Hz}]$) derived from the ROSAT-BSC at 1 keV. The shaded area marks the more X-ray dominated objects with $\alpha_{OX} < 0.9$.

Table 5.1: Overall spectral indices

spectral index	using source fluxes[a]	using observed fluxes
α_{OX}	0.94 ± 0.23	0.95 ± 0.23
α_{RX}	0.55 ± 0.08	0.56 ± 0.08
α_{RO}	0.37 ± 0.09	0.38 ± 0.09

[a] for objects without redshift information $z = 0.3$ is applied

Applying now formula 5.1 and 5.2 I derived monochromatic luminosities from the RASS-BSC data. As reference energy I use 1 keV. Figure 5.8 shows the distribution of luminosities. The more X-ray dominated objects (HBL) cover higher X-ray luminosities than the less X-ray dominated (IBL) ones. This circumstance will be discussed in more detail in section 5.5.1.

5.5 The spectral energy distribution

5.5.1 Overall spectral indices

To study the spectral energy distribution (SED) of the HRX-BL Lac objects, overall spectral indices are useful to derive general correlations within the sample. The overall spectral indices have already been introduced in section 2.4. For reference energies I use 1.4 GHz in the radio ($\lambda \simeq 21\,\mathrm{cm}$), 4400 Å in the optical ($\sim B$), and 1 keV ($\lambda \simeq 12.4$ Å) in the X-ray region.

Because the radio spectra are flat, overall spectral indices depending on radio flux, are changing only when moving from the 1.4 GHz band to the e.g. 5 GHz, because of the different $\Delta\nu$. For a source with a $\alpha_R = 0$ spectrum this would result in an $\alpha_{RX}(5\,\mathrm{GHz}, 1\,\mathrm{keV}) \simeq 1.06 \times \alpha_{RX}(1.4\,\mathrm{GHz}, 1\,\mathrm{keV})$. This has to be considered when comparing overall spectral indices based on different radio bands.

On the other hand, when comparing my results with spectral indices using a larger X-ray reference energy, also larger values, the same values for α_{OX} and α_{RX} are expected. Because $f_\nu \propto \nu^{-\alpha}$, the expected flux at a higher energy is lower, but the frequency increases by the same factor. Also in the optical region, where $\alpha_E \lesssim 1$, dramatic changes are not expected.

These predictions only hold if the spectral shape within each band can be approximated by a single power law and the spectrum is not curved. The HRX-BL Lac sample shows typical values for the overall spectral indices (compare with e.g. Wolter et al. 1998, Laurent-Muehleisen et al. 1999). The values for the HRX-BL Lac complete sample are summarized in Table 5.1. To study the influence of the K-correction, the values in Table 5.1 are computed with and without K-correction. The influence to the overall spectral indices is small and negligible when examining a large sample of objects. Besides this, the larger scatter of the mean α_{OX} value in comparison to the other two indices is remarkable, because it shows that α_{OX} can be a good indicator, while the other values do not seem to be sensitive for the different types of BL Lac objects. The area in the $\alpha_{OX} - \alpha_{RO}$ plane, which is covered by the HRX-BL Lac sample, is shown in Figure 5.9. Objects of the HRX-BL Lac complete sample are marked with points, triangles refer to objects which are additionally included in the HRX-BL Lac *total sample*. The center of the area covered by this sample is similar to that of the EMSS BL Lacs (see Padovani & Gommi 1995a) though a larger range in α_{OX} and α_{RO} is covered.

5.5.2 Can radio silent BL Lac exist?

The $\alpha_{RX} - \log(f_X)$ plane demonstrates the possibility of existing radio-quiet or even radio silent BL Lac objects. Figure 5.10 shows the fluxes of the total HRX-BL Lac sample (also including objects below the $hcps = 0.09\,\mathrm{sec}^{-1}$ limit) versus the overall spectral index α_{RX}. Sources in which the X-ray emission dominates are on the left. The flux limit of $\simeq 1.1 \cdot 10^{-11}$ is marked by the horizontal line. Objects with radio fluxes below the 2 mJy threshold would be positioned below the diagonal line. In the case of the HRX-BL Lac sample the loss of objects due to the 2 mJy limit should be $\leq 3\%$ (this number is estimated by the object density near the interesting area in the $\alpha_{RX} - \log(f_X)$ diagram). Therefore the HRX-BL Lac sample can be treated like a sample which is not radio flux limited due to the high X-ray flux limit.

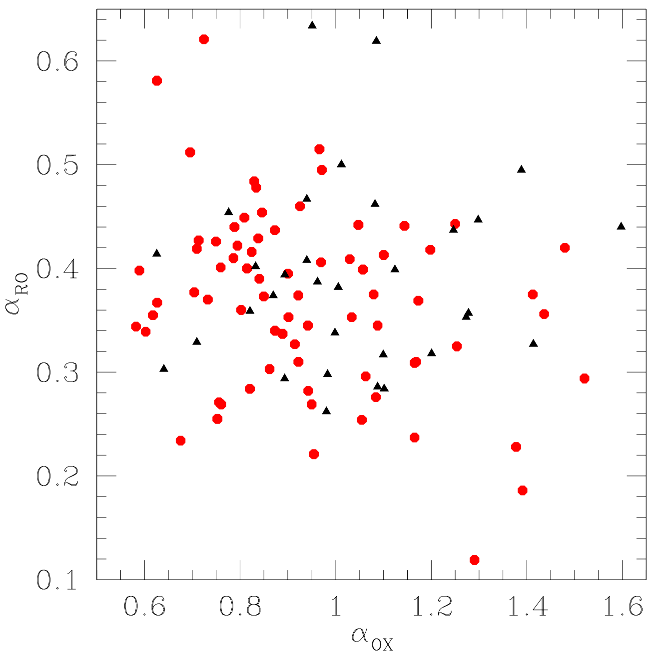

Figure 5.9: The $\alpha_{OX} - \alpha_{RO}$ plane covered by the HRX-BL Lac objects. The points refer to the complete sample, the triangles mark objects which are additionally included in the HRX-BL Lac *total sample* which is not complete. Objects with $\alpha_{RO} < 0.2$ are called radio quiet.

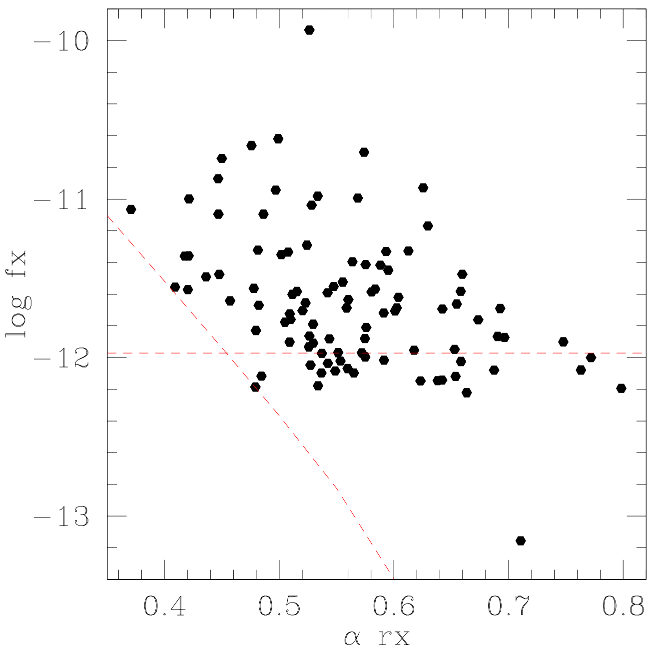

Figure 5.10: X-ray flux (logarithmic scaling) in [erg cm^{-2} sec^{-1}] versus α_{RX}. X-ray loud objects are on the left. The horizontal line marks the flux limit of the HRX-BL Lac complete sample, the diagonal line refers to the 2 mJy limit of the NVSS.

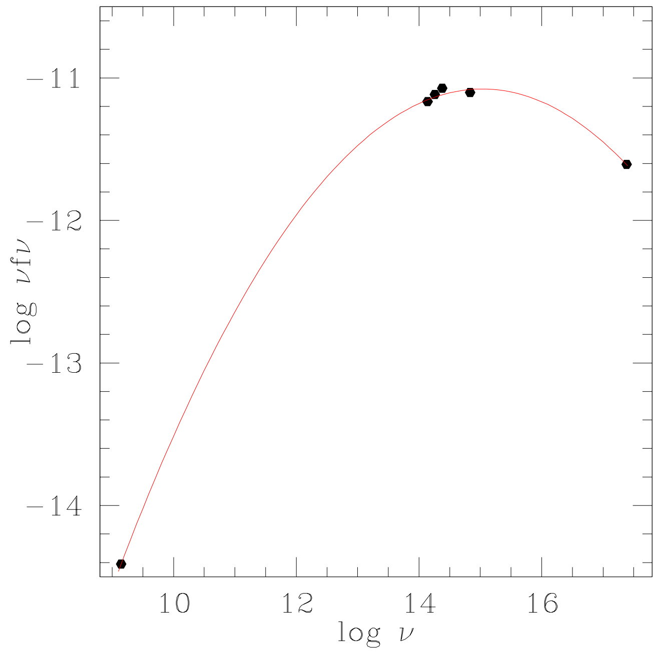

Figure 5.11: Parabolic fit to the data of RX J0915+2933.

But by extrapolating the most extreme values within in the HRX-BL Lac sample ($\alpha_{RX} = 0.38$ and $f_x(1\,\mathrm{keV}) = 0.023\,\mu\mathrm{Jy}$) would result in a radio flux of $f_r = 0.03\,\mathrm{mJy}$. Of course this value is only realistic if simultaneous extrapolation of α_{RX} and f_x to lower values is possible. Objects with simultaneous low α_{RX} and α_{RO} are e.g. not found in the EMSS BL Lac sample (Rector et al. 2000) which has a ~ 10 times lower flux limit than the HRX-BL Lac complete sample. The EMSS sample does not include any X-ray selected BL Lac with a radio flux fainter than $f_R(5\,\mathrm{GHz}) = 0.9\,\mathrm{mJy}$. But in their BL Lac identification procedure they also used the radio data as a BL Lac criterion, thus they might have missed radio quiet BL Lac objects.

This raises the question whether the assumption of Stocke et al. (1991) that there is no evidence for radio-silent BL Lac objects might be wrong. This would have the consequence that up to now BL Lac objects with the most extreme properties could have been missed. They could have too low radio fluxes for radio selected samples (e.g. RGB, Laurent-Muehleisen et al. 1999; DXRBS, Perlman et al. 1998, Padovani et al. 1999) and would not be found by X-ray selected surveys which are working by correlating X-ray sources with radio catalogues (e.g. the REX survey, Caccianiga et al. 1999). I would like to stress the point that loss based on the radio flux limit is not important for high flux-limited samples like the HRX-BL Lac, but might be important for lower flux limits.

5.5.3 Peak frequency

In order to get a more physical description of the spectral energy distribution of the BL Lac objects, I used a simple model to fit the synchrotron branch of the BL Lac. This has the advantage of describing the SED with one parameter (the peak frequency) instead of a set of three parameters (α_{OX}, α_{RO}, and α_{RX}). Applying a parabolic fit to the observed values in the $\log\nu - \log\nu f_\nu$ plane (cf. Landau et al. 1986, Comastri et al. 1995a, Sambruna et al. 1996) the peak position (ν_{peak}) and the total luminosity/flux of the of the synchrotron emission can be derived. I used the parameterization $\log\nu f_\nu = a\cdot(\log\nu)^2 + b\cdot\log\nu + c$.

Using luminosities instead of fluxes would only be a shift and changes therefore not the position of the determined peak frequency. If only three data points are given (one in the radio, optical, and X-ray band), the parabola is definite (see section 11.2.1 on page 139). When more than three data points were available, a χ^2 minimization was used to determine best fit parameters. An example for a parabolic fit is

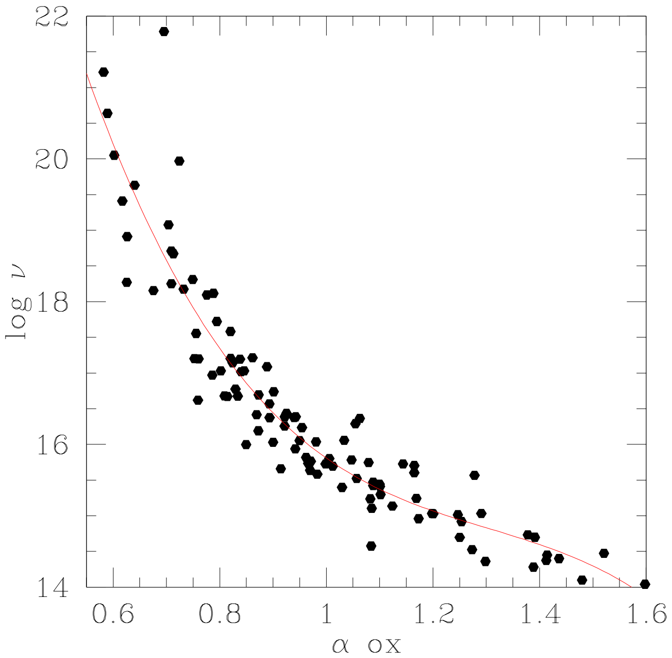

Figure 5.12: Logarithm of the peak frequency vs. α_{OX}. The relation can be approximated by a polynomial of third degree.

shown in Figure 5.11. ν_{peak} is sensitive for the f_x/f_{opt}-relation, and is therefore strongly correlated with α_{OX}. This is shown in Figure 5.12. The relation can be approximated by a polynomial of third degree. Using an F-test the fit shows no better result for a higher degree. Thus the peak frequency could also be determined, if no radio data would be available by applying

$$\log \nu_{peak} = -11.022 \cdot \alpha_{OX}^3 + 43.043 \cdot \alpha_{OX}^2 - 58.275 \cdot \alpha_{OX} + 42.062(\pm 0.54) \tag{5.5}$$

The standard error ($\sigma = 0.54$) is based on the deviation of the data points from the fit in Figure 5.12. A similar correspondence between peak frequency and broad band spectral indices α_{RX} and α_{RO} has been shown by Fossati et al. (1998) for blazars.

Using the fitted SED, integrated luminosities L_{syn} and integrated fluxes f_{syn} were determined. Boundaries were set at 1.4 GHz (radio) and 1 keV (X-ray). An extrapolation to higher frequencies would cause large errors, also because the inverse Compton branch is expected to rise at frequencies near above 1 keV. Thus these values are lower limits for the bolometric values of the synchrotron branch and of the total SED. But comparison of these values for the different objects should derive the same results as with the true values, because in most cases the bulge of the synchrotron emission is located between the infrared and the X-ray region. Additional, the true total luminosity can be approximated by the value given at the peak frequency.

5.6 Evidence for curvature in the X-ray spectra

The possibility of curvature within the spectra has been discussed in Beckmann & Wolter (2000)

As difference in absorption ΔN_H I define the difference between the hydrogen column density $N_{H,free}$ obtained from the fit of the X-ray spectrum and the column density of the Galactic hydrogen in the direction to the BL Lac: $\Delta N_H = N_{H,free} - N_{H,gal}$. The Galactic values were taken from the Leiden/Dwingeloo Survey (LDS, Hartmann and Burton 1997). The errors resulting from the fit of a single-power law with free-fitted absorption (as described on page 46) are quite large, causing also large errors for ΔN_H. The distribution of ΔN_H is shown in Figure 5.13 for the whole HRX-BL Lac sample. There seem to occur both

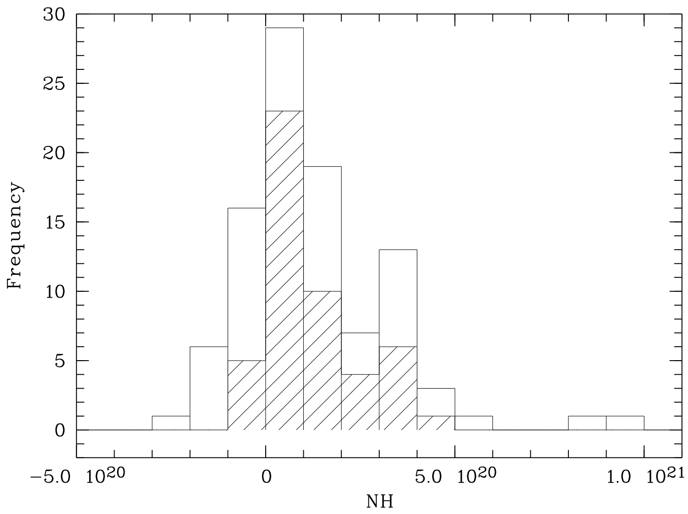

Figure 5.13: Distribution of difference in absorption $\Delta N_H = N_{H,free} - N_{H,gal}$ for all HRX-BL Lac. Shaded are the objects with errors $\sigma_{\Delta N_H} < 3.5 \cdot 10^{20}\,\mathrm{cm}^{-2}$.

Table 5.2: Difference in absorption

selection $[10^{20}\,\mathrm{cm}^{-2}]^a$	$\Delta N_H [10^{20}\,\mathrm{cm}^{-2}]^a$ (all HRX-BL Lac)	$\Delta N_H [10^{20}\,\mathrm{cm}^{-2}]$ (HRX-BL Lac complete sample)
all objects	1.27 ± 1.93 (101)	1.00 ± 1.47 (77)
$\sigma_{N_H} < 3.5$	1.27 ± 1.24 (48)	1.34 ± 1.23 (40)
pointed observations[b]	1.11 ± 0.67 (40)	1.16 ± 0.71 (33)

[a] in brackets the number of objects is given
[b] see Section 5.9

positive and negative differences in absorption. The latter makes physically no sense so that the negative values are probably due to the large uncertainties of the fit. This is supported by their disappearance if the fits with largest errors ($\sigma_{N_H} > 3.5 \cdot 10^{20}\,\mathrm{cm}^{-2}$) are omitted. This is demonstrated in Figure 5.13. The resulting mean values are listed in Table 5.2. Here I also list the difference in absorption measured in pointed observations as will be investigated in section 5.9.

Therefore the result from the HRX-BL Lac sample is that when fitting a single power law with free absorption to the ROSAT-PSPC data, the absorption is significantly higher than the Galactic value. There are three possible explanations for the difference in absorption:

- *intrinsic absorption*: If matter within the BL Lac objects would cause the difference in absorption, the same matter is expected to be heated and radiating thermal emission at lower (e.g. infrared) energy regions. This is not seen: the spectrum of BL Lac objects is non-thermal throughout the entire observed wavelengths. Also, intrinsic absorption should cause a negative correlation between the luminosity and the ΔN_H. A higher absorption should result in lower luminosities, although this effect might not be detectable.

- *absorption in the line of sight*: Absorption in the line of sight with a mean column density of $\sim 10^{20}\,\mathrm{cm}^{-2}$ is not expected in *all* observed cases. At least for the highest values of ΔN_H this should result in absorption lines seen in the optical spectra.

- *absorption mimicked by the fit*: The most plausible reason for the detected ΔN_H could be a curvature in the X-ray spectrum. Then a single-power law without additional absorption would not give a sufficient fit, but an additional N_H would effect the soft X-ray fit much more than the fit at higher

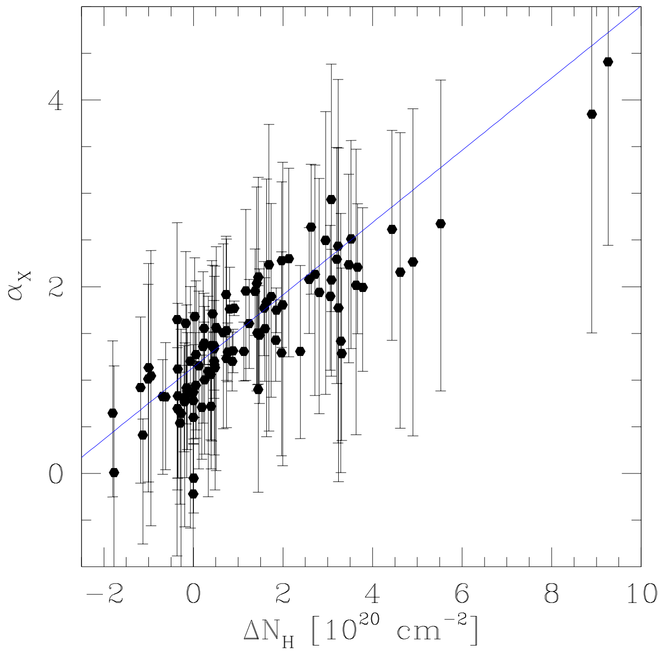

Figure 5.14: X-ray spectral slope α_X versus difference in absorption ΔN_H. The linear regression to retrieve the fit straight line took into account the errors in α_X and $N_{H,free}$ (not shown in this plot, mean error $\sigma_{N_H} \sim 3.9 \cdot 10^{20}\,\mathrm{cm}^{-2}$).

X-ray energies. Thus, if $HR1 > HR2$ the X-ray spectrum would be flatter at lower energies than at the "hard" PSPC end; additional absorption can contribute to this[3].

The correlation of ΔN_H with the overall spectral properties will be discussed in the next section.

5.7 Properties correlated with the peak frequency

If the different types of BL Lac objects depend on the peak frequency ν_{peak} of the synchrotron branch then it is necessary to examine the dependencies of observational parameters on the spectral energy distribution. The synchrotron branch of the SED can be described by the overall spectral index α_{OX}, or by the peak frequency ν_{peak}. The dependencies I will study in this section are the correlation of ν_{peak} with spectral slope, curvature, and luminosity.

Comparing the ΔN_H with the X-ray spectral slope $\alpha_{X,free}$, I find a strong correlation (Figure 5.14). The correlation coefficient is $r_{xy} = 0.881$ which results (via the Student's distribution) in a probability of $\Gamma > 99.9\%$ that the two values are correlated. For a description of the way to derive the probabilities see section 11.2.2 on page 139. On the other hand, the correlation of $\log \nu_{peak}$ versus the spectral energy index α_X shows a correlation coefficient of $r_{xy} = -0.41$ ($r_{xy} = -0.19$ for the spectral slope $\alpha_{X,free}$ with free-fitted N_H) which is less significant though still results in a $\Gamma > 99\%$ ($\Gamma > 90\%$ for $\alpha_{X,free}$) probability that both values are correlated. The connection between spectral slope and the location of the synchrotron peak is displayed in Figure 5.16.

What is seen here is the different curvature of the SED in HBL and IBL. This is illustrated in Figure 5.15. Different to Figure 5.11, this plot is $\log f_\nu$ (not $\log \nu f_\nu$!) versus $\log \nu_{peak}$. Thus it shows directly the spectral shape; the IBL (plotted in red) has a larger α_R in the radio region and a steeper α_{OX} and

[3]A fit to a curved spectrum could be also done by a broken-power law. But due to the low statistics of the RASS-BSC data this was not done, because it would result in at least one more free parameter to be fitted, even when fixing the absorption to the Galactic value

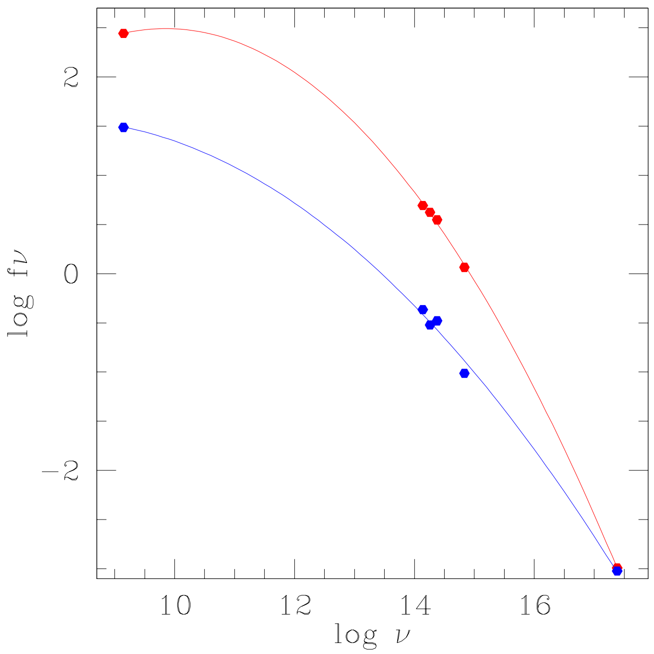

Figure 5.15: Spectral energy distribution of an IBL (top: RX J0915+2933) and an HBL (bottom: RX J0749+7451) in the $\log f_\nu$ versus $\log \nu$ plane to demonstrate the different curvature of the spectral energy distribution.

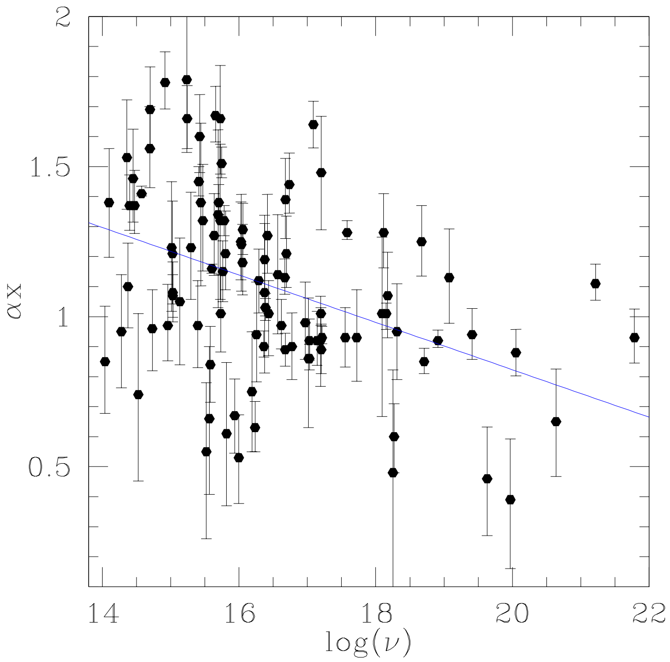

Figure 5.16: X-ray spectral slope versus peak frequency of the synchrotron branch. HBL (on the right) show flatter X-ray spectra than IBL.

α_X respectively, than the HBL (marked in blue). The curvature of both objects is typical for the HBL and IBL within the HRX-BL Lac sample. Here I fitted again a parabola. The curvature is stronger in the SED of the IBL than in the HBL. This results in a higher ΔN_H as explained above.

The differences in curvature can also be detected with the $\alpha_{XOX} = \alpha_{OX} - \alpha_X$ value (Sambruna et al. 1996). This index describes the curvature between the X-ray spectrum and the overall spectral index α_{OX}. A negative value of α_{XOX} stands for a steepening of the spectrum to higher energies (convex spectrum): a positive value results from a concave spectrum. A correlation of α_{XOX} and ΔN_H for the HRX-BL Lac sample can only be found when using the objects with errors in $N_{H,free}$ of $\sigma_{N_H} < 3.5 \cdot 10^{20}\,\mathrm{cm}^{-2}$. Then the correlation coefficient is $r_{XY} = 0.34$ and the probability for an existing correlation is $\Gamma > 95\%$. This is consistent with the results from Sambruna et al. (1996) and Laurent-Muehleisen et al. (1999) who report a correlation of X-ray dominance α_{OX} and α_{RO}.

Another correlation reported by those authors, α_{XOX} vs. α_{RO}, is not detectable in the HRX-BL Lac sample. This might originate from the smaller range in α_{OX} and α_{RO} of objects (no BL Lacs with real low peak frequencies like in the 1Jy sample) inside the HRX-BL Lac sample.

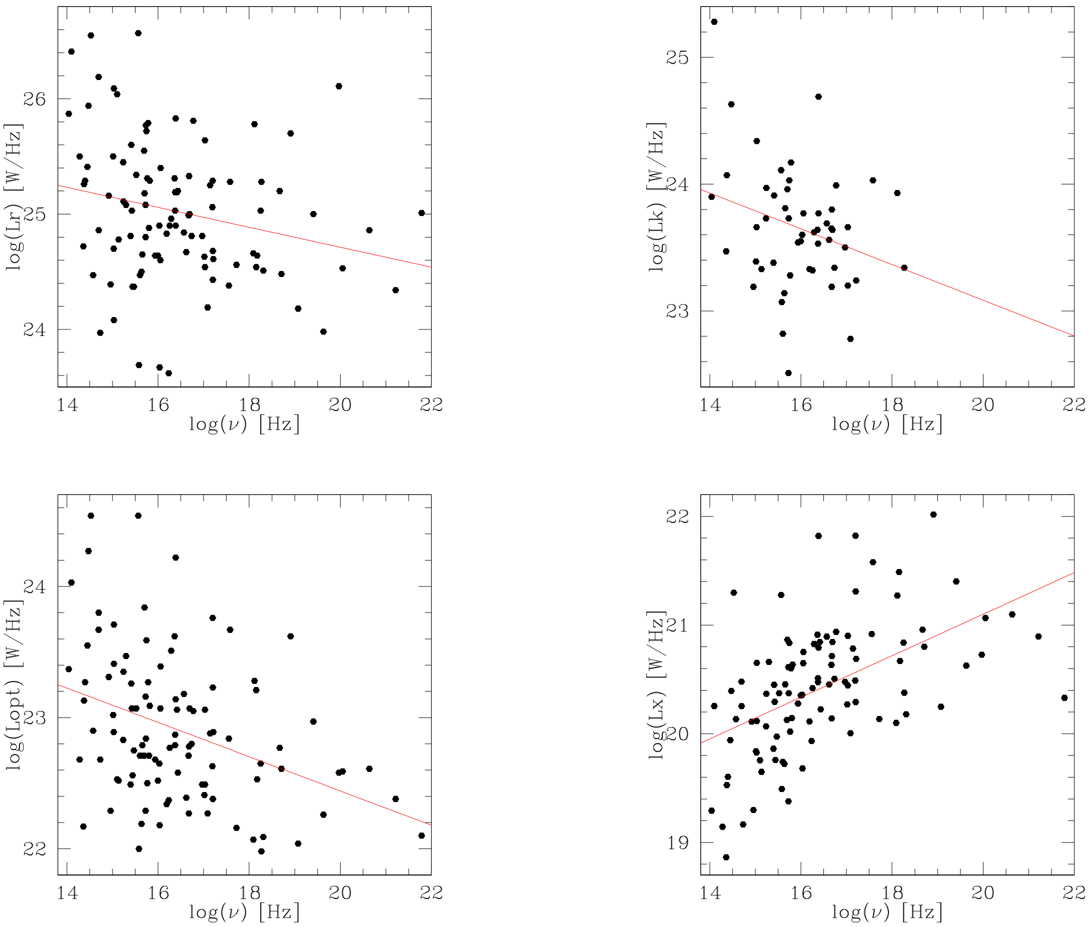

Figure 5.17: Monochromatic luminosities in the radio (1.4 GHz), near infrared (K-band), optical (B-band), and X-ray (1 keV) regime versus peak frequency.

Another important set of physical parameters which are connected with the peak frequency are the luminosities. The correlations with the monochromatic luminosities are presented in Figure 5.17. To compute luminosities, the unknown redshifts were set to $z = 0.3$ which is the mean value for the HRX-BL Lac sample. Luminosities are given in [W/Hz]. The plots also show the linear regression. While in the radio, near infrared, and optical region the luminosity is decreasing with increasing peak frequency,

Table 5.3: Connection of luminosity with peak frequency

region	r_{xy} Pearson coefficient	probability of correlation	linear regression[a]
radio (1.4 GHz)	-0.23	$> 97\%$	$\log L_R = -0.09 \cdot \log \nu_{peak} + 26.4$
near IR (K-band)	-0.28	$> 95\%$[b]	$\log L_K = -0.14 \cdot \log \nu_{peak} + 25.9$
optical (B-band)	-0.37	$> 99.9\%$	$\log L_B = -0.13 \cdot \log \nu_{peak} + 25.1$
X-ray (1 keV)	+0.51	$> 99.9\%$	$\log L_X = +0.19 \cdot \log \nu_{peak} + 17.3$
total (radio – X-ray)	-0.12		$\log L_{tot} = -0.04 \cdot \log \nu_{peak} + 22.0$

[a] Luminosities in [W/Hz]

[b] The lower probability results from the lower number of objects (52) with known K-band magnitudes.

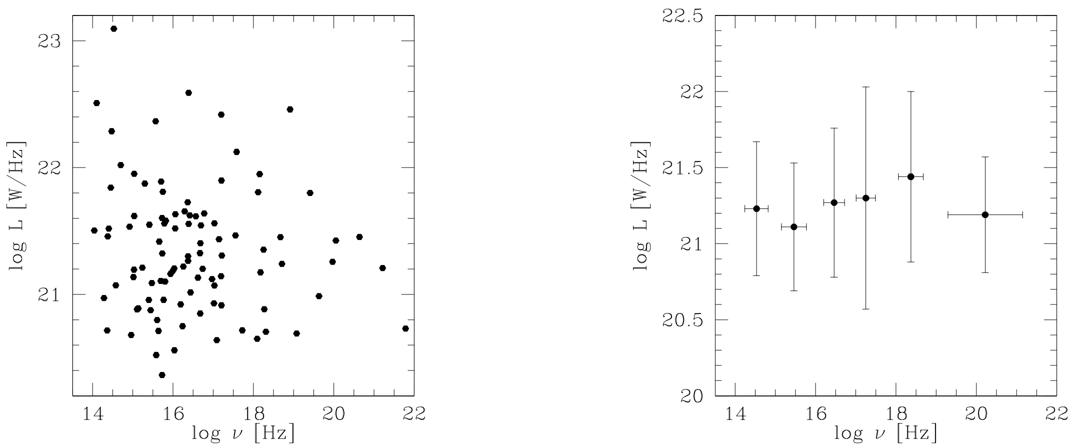

Figure 5.18: Left panel: The integrated luminosity. There seem to be no HBL with high luminosities within the synchrotron branch.
Right panel: Data binned into $\Delta \log \nu_{peak} = 1$. The data seem to be consistent with one mean L_{syn} for HBL and IBL.

the situation at X-ray energies is the other way around. In Table 5.3 there are more details listed to the single regressions, including the probability of correlation.

The total luminosity within the synchrotron branch has been derived as described on page 51 by integrating the spectral energy distribution between the radio and the X-ray band. The relation of peak frequency with the total luminosities does not show a clear correlation. Though a trend to lower luminosities with increasing peak frequency can be seen in Figure 5.18, the significance of the correlation is low due to the wide spread at the low frequency peak end. A problem of this correlation is also that a peak frequency higher than 1 keV is outside the range of the computed integrated flux. Therefore I tried different upper boundaries of the integration, but a correlation between total luminosity and ν_{peak} is not clearly measurable.

Also binning the data due to their peak frequencies does not show a correlation. For the right panel of Figure 5.18 I used a binning of $\Delta \log \nu_{peak} = 1$. The error bars refer to the logarithmic values of ν_{peak} and total luminosity L of the synchrotron branch. Within the errors the values are consistent with a constant mean total luminosities over the whole range of measured peak frequencies.

The non-detection of the correlation between luminosity and ν_{peak} might be based on the fact that for a fraction of $\sim 20\%$ the redshift information is still missing. This leads to a lower statistic, if leaving these objects out of the analysis, or to larger errors, when assuming a medium redshift for those objects. Based on Figure 5.18 it can be at least said that there are no HBL with high luminosities ($L_{syn} \gg 10^{22}$ W/Hz) within the synchrotron branch.

Also I would like to stress the fact that the synchrotron branch is only part of the total emission of the BL Lac objects. A large fraction and perhaps the majority of the emission is expected in the inverse

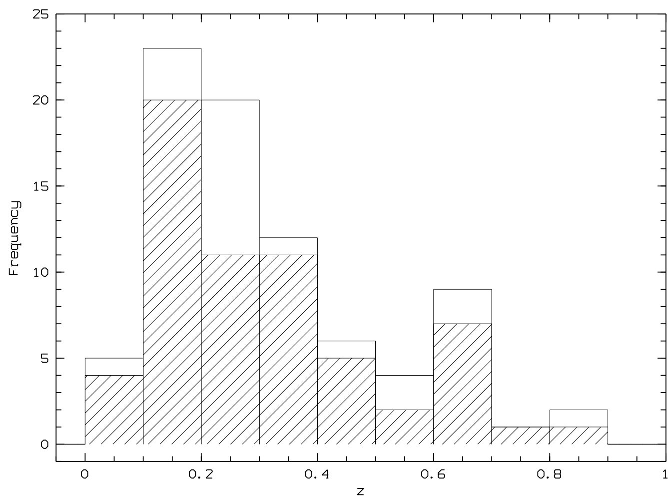

Figure 5.19: Redshifts within the HRX-BL Lac sample. The hashed objects belong to the complete sample.

Compton (IC) branch at energies not covered by this investigation. The IC branch in LBL is expected to be significantly more luminous than the synchrotron branch, while the HBL are thought to have IC emission as powerful as the synchrotron one (Fossati et al. 1998, Ghisellini 1999). Hence the observed equal luminosity of the synchrotron branch for HBL and IBL would not be in contradiction with an expected higher bolometric luminosity of IBL in comparison with HBL. Because the IC component of the IBL is expected to be higher than that for the HBL, a constant luminosity of the synchrotron branch would result in a higher total luminosity of the IBL.

Several of the effects presented here, like the dependency of X-ray luminosity on α_{OX} resp. peak frequency, or different spectral curvature within the IBL and HBL group, can only be seen when using a sufficient quantity of objects, like the HRX-BL Lac sample.

The results of this section can be summarized as follows: the peak frequency of the synchrotron branch is indeed a good parameter to distinguish between the different kinds of BL Lac. A higher peak frequency results in a flatter X-ray spectral slope, in less curved X-ray spectra (and therefore in lower α_{XOX} values), in lower luminosities in the radio, near infrared and optical band, but in higher luminosities in the X-ray regime.

5.8 Distribution in space

5.8.1 Redshift distribution

As redshift information is available for 80% of the objects within the HRX-BL Lac sample, the distribution with redshift can be studied (Fig. 5.19). The mean redshift of the HRX-BL Lac complete sample is $z = 0.312 \pm 0.200$. For the total sample this value is $z = 0.316 \pm 0.200$ if we include objects with a calcium break $25\% < \mathrm{Ca_{break}} < 40\%$, and $z = 0.325 \pm 0.202$ if we exclude these borderline BL Lacs.

The mean mean value of the complete sample is twice as high as derived from the RGB sample ($\bar{z} = 0.16$, Laurent-Muehleisen et al. 1999), similar to the EMSS ($\bar{z} = 0.30$), and smaller than for the 1Jy sample ($\bar{z} = 0.50$). The assumption of Laurent-Muehleisen et al. (1999) that the RGB sample has lower redshifts than the other BL Lac surveys (EMSS, 1Jy, and HRX-BL Lac) results from incompleteness or missing BL Lacs with $25\% < \mathrm{Ca_{break}} < 40\%$ cannot be ruled out as long as the fraction of misidentified BL Lacs within the NED is not known. On the other hand, the inclusion of "borderline" BL Lacs with $25\% < \mathrm{Ca_{break}} < 40\%$ into the HRX-BL Lac sample does not change the mean redshift dramatically. Their mean redshift $\bar{z} = 0.24 \pm 0.17$ is not significantly different from the mean redshift within the HRX-BL Lac complete sample. Differences in the z-distribution are more likely based on different selection

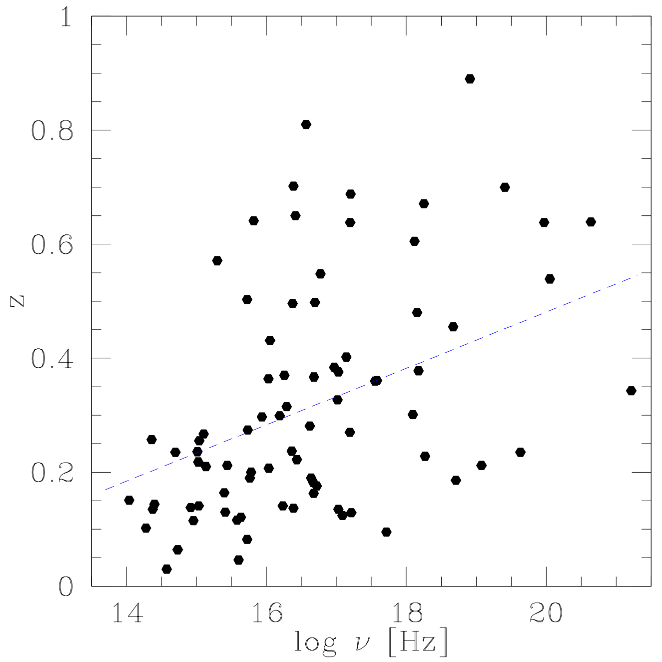

Figure 5.20: The redshift within the sample is increasing with higher peak frequency.

methods and therefore in different classes of BL Lac object, which are found in the surveys. The objects within the HRX-BL Lac sample show a correlation of redshift with peak frequency (Figure 5.20). The significance of the correlation is $\Gamma > 99.9\%$. Therefore it could be possible that an X-ray selected sample (like the EMSS or the HRX-BL Lac) shows higher redshifts than a radio selected one (like the RGB) even though this might be a selection effect.

5.8.2 V_e/V_a for HRX-BL Lac

A simple method to detect evolution in a complete sample of objects, is the application of a V/V_{max} test (Schmidt 1968). This test is based on the ratio of the redshift of the objects in relation to the maximal allowed redshift z_{max} within the survey. If we have a sample of n objects, of which every object encloses a volume V_i and this object would have been detected (due to the survey limit) up to a volume $V_{max,i}$, than the mean

$$\left\langle \frac{V}{V_{max}} \right\rangle = \frac{1}{n} \cdot \sum_{i=1}^{n} \frac{V_i}{V_{max,i}} \tag{5.6}$$

will have a value in between the interval [0..1]. A value of $\langle \frac{V}{V_{max}} \rangle = 0.5$ would refer to an equally distributed sample in space. The area of the survey is not important for this value, because $V_i/V_{max,i} = d_p^3/d_{p,max}^3$ with d_p being the proper distance of the object redshift z and $d_{p,max}$ the value for z_{max}. This test is very sensible to the maximal detected redshift z_{max}. Therefore Avni & Bahcall (1980) improved the test by using V_e/V_a (see Figure 5.21). Here V_e stands for the volume, which is enclosed by the object, and V_a is the accessible volume, in which the object could have been found (e.g. due to a flux limit of a survey). Thus even different surveys with different flux limits in various energy bands can be combined by the V_e/V_a-test.

The error of $\langle V_e/V_a \rangle$ can be determined as follows. For an equally distributed sample the mean value

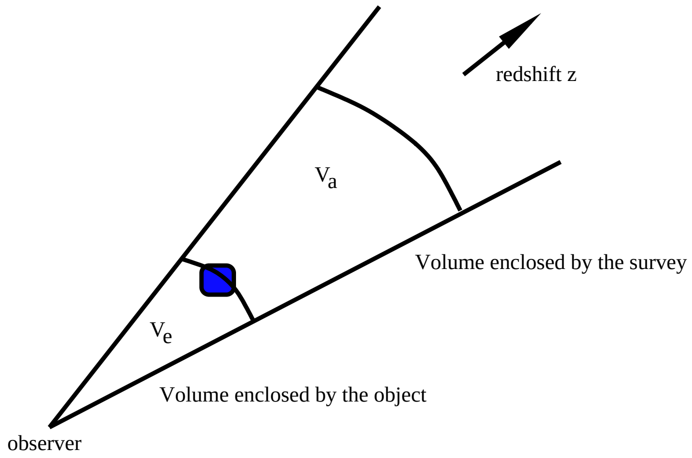

Figure 5.21: The accessible volume is computed for each object individually.

$\langle m \rangle = \langle V_e/V_a \rangle$ is:

$$\langle m \rangle = \frac{\int_0^1 m \, \mathrm{d}m}{\int_0^1 \mathrm{d}m} = 0.5 \tag{5.7}$$

The mean square divergence of the mean value is:

$$\sigma_m^2 = \frac{\int_0^1 (m-0.5)^2 \, \mathrm{d}m}{\int_0^1 \mathrm{d}m} = \left[\frac{1}{3}m^3 - \frac{1}{2}m^2 + \frac{1}{4}m\right]_0^1 = \frac{1}{12} \tag{5.8}$$

Therefore for n objects we get an error of:

$$\sigma_m(n) = \frac{1}{\sqrt{12n}} \tag{5.9}$$

For an arbitrary mean value $\langle m \rangle$ we get an error of:

$$\sigma_m(n) = \sqrt{\frac{1/3 - \langle m \rangle + \langle m \rangle^2}{n}} \tag{5.10}$$

For the HRX-BL Lac sample I computed the accessible volume for each object by applying the survey limits. This volume $V_{a,i}$ is in most cases determined by the X-ray flux limit, while $\sim 10\%$ of the objects show a lower $V_{a,i}$ for the radio data, due to the radio flux limit of 2.5 mJy. Applied to the HRX-BL Lac sample the test derives $\langle V_e/V_a \rangle = 0.42 \pm 0.04$. This result shows that HBL have been less numerous and/or less luminous at cosmological distances, but it has to be noted that the significance is only 2σ. The negative evolution of X-ray selected BL Lac objects has been reported several times before. The value presented here is consistent with the $\langle V_e/V_a \rangle = 0.36 \pm 0.05$ found for the EMSS BL Lacs by Wolter et al. (1994), and also in better agreement with the FR-I galaxies ($\langle V_e/V_a \rangle = 0.40 \pm 0.06$) within the 3CR sample (Laing et al. 1984). On the other hand LBL show weak or positive evolution ($\langle V_e/V_a \rangle = 0.60 \pm 0.05$) as shown for the 1Jy sample by Stickel et al. (1991), and also FR-II radio galaxies, FSRQ, and “normal” quasars seem to be more numerous and/or luminous at cosmological distances than in the neighborhood.

Thanks to the large number of objects with known redshifts within the HRX-BL Lac sample it is possible to examine dependencies of the evolution on other parameters, like the overall spectral indices and the peak frequency. A division into two groups according to α_{OX} was already presented by us (Bade

Table 5.4: V_e/V_a within the HRX-BL Lac complete sample

selection	number of objects	$\langle V_e/V_a\rangle$	$\langle\log\nu_{peak}\rangle$
all	62	0.42 ± 0.04	16.9 ± 1.6
$\log\nu_{peak} > 16.7$	29	0.45 ± 0.06	18.2 ± 1.4
$\log\nu_{peak} < 16.7$	33	0.40 ± 0.05	15.8 ± 0.7
$\alpha_{OX} < 0.9$	35	0.45 ± 0.05	18.1 ± 1.4
$\alpha_{OX} > 0.9$	27	0.40 ± 0.06	15.7 ± 0.8
$\alpha_{RO} < 0.374$	31	0.36 ± 0.06	16.8 ± 1.7
$\alpha_{RO} > 0.374$	31	0.48 ± 0.05	17.1 ± 1.6
$\alpha_{RX} < 0.529$	31	0.39 ± 0.06	17.5 ± 1.5
$\alpha_{RX} > 0.529$	31	0.45 ± 0.05	16.4 ± 1.6
$\log L_{tot} > 45.8\frac{erg}{sec}$	33	0.41 ± 0.06	17.0 ± 1.6
$\log L_{tot} < 45.8\frac{erg}{sec}$	29	0.43 ± 0.06	16.8 ± 1.7

et al. 1998) for 35 BL Lacs and results in a lower $\langle V_e/V_a\rangle$ for the HBL ($\alpha_{OX} < 0.9$) than for the IBL within the sample. The $\langle V_e/V_a\rangle$ for IBL was even consistent with no evolution. For the HRX-BL Lac sample we now get a value $\langle V_e/V_a\rangle(\alpha_{OX} < 0.9^4) = 0.45 \pm 0.05$, and for the IBL we get nearly the same value ($(\langle V_e/V_a\rangle(\alpha_{OX} > 0.9) = 0.40 \pm 0.06)$. Thus there seems to be no different type of evolution within the HBL and the IBL, as reported in Bade et al. 1998. But still there is a number of objects within the HRX-BL Lac sample without known redshift, and nearly all of them are IBL. Their direct images show point-like structure, and most of them exhibit optical spectral consistent with high redshifts ($z > 0.5$). Also the difficulty in determining the redshift seems to origin from a highly core dominated object, where the host galaxy is outshined by the BL Lac core. This leads to the assumption that the luminosity of these objects should be quite high. Therefore the $\langle V_e/V_a\rangle$ for the IBL could be larger than the value detected here, while the value for the HBL is well determined. A clearer detection of different evolution is resulting after subdivision into two halves according to the radio over optical dominance (α_{RO}) or radio over X-ray ratio (α_{RX}). Objects with $\alpha_{RO} > 0.374$ (median of the sample) show no evolution, while the other half of the sample shows strong negative evolution. The same effect is seen for α_{RX}. Hence the radio dominated objects tend to have no evolution, while the radio quite objects exhibit negative evolution.

To get a result which is related stronger to the SED, I tested $\langle V_e/V_a\rangle$ also for different peak frequencies within the sample. The results for the different selections of objects are listed in Table 5.4. There seems to be no correlation of the total luminosity with evolution. In fact their are several hints that the IBL show a more positive evolution than the HBL. To test the different evolution within the HRX-BL Lac sample, I grouped the sample in bins of peak frequency ν_{peak} and computed the $\langle V_e/V_a\rangle$ for each bin. The result is shown in Figure 5.22. A Spearman Rank test gives a Spearman Rank-Order coefficient of -0.76 and a probability for correlation between ν_{peak} over $\langle V_e/V_a\rangle$ of $\Gamma > 90\%$.

The trend for IBL having a more positive evolution than HBL is detectable in several relations: when subdividing the sample according to α_{RX}, α_{RO}, for total luminosity, and also for the peak frequency.

In summary the detected V_e/V_a shows negative evolution, but is consistent with no evolution at all. While the redshifts for several IBL are unknown and expected to be high ($z \gtrsim 0.5$) the V_e/V_a is thought to be higher than the values presented here. The strong dependency on α_{OX} as reported by Bade et al. (1998) cannot be confirmed. It is worth noting that the objects investigated here cover only a small range of the possible "flavours" of the BL Lac phenomenon. The trend of LBL to have positive evolution, as reported for 1Jy sample by Stickel et al. (1991), cannot be confirmed because objects of this kind are not included in the HRX-BL Lac sample.

[4] The median of the HRX-BL Lac is a little bit lower than in Bade et al. (1998), but for comparison reasons we use $\alpha_{OX} = 0.9$ as dividing limit.

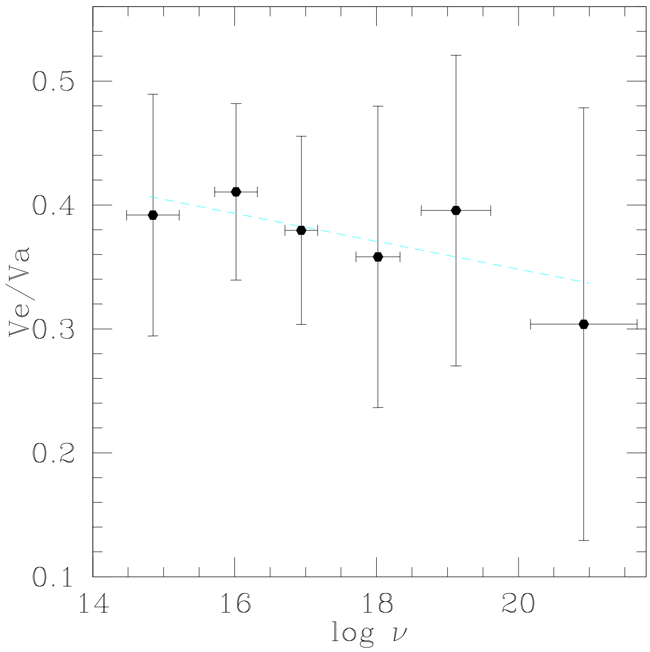

Figure 5.22: $\langle V_e/V_a \rangle$ vs. peak frequency. The IBL show a less negative evolution than the HBL.

5.8.3 Number counts

Assuming a Euclidean space in which all objects are normally distributed with also normally distributed luminosities. Than one expects the number N of objects being correlated with the flux limit f_{limit} in a sense that $N \propto f_{limit}^{-3/2}$. This is just based on the fact that the number of sources increases with the radius r of a sphere in which we search by $N \propto r^3$ and that at the same time the measured flux f of an object is correlated with the distance r by $f \propto r^{-2}$.

The so-called $\log N - \log S$ test is therefore a tool to get a first idea of the distribution in space and flux without any redshift information. Figure 5.23 (left panel) shows the number counts relation for the HRX-BL Lac complete sample of 77 objects. The errors refer to the statistical error only. The object density per square degree above a given flux $f_X(0.5 - 2keV)$ is shown. Therefore one can derive directly the expected surface density of BL Lac objects at a given X-ray flux limit. The linear regression included in this plot was derived by taking into account the errors in both density and flux (not shown in the plot). There is no significant break in the slope of the number counts relation detectable. The relation is well determined by the linear regression as $\log N_{>f_X} = -(13.2 \pm 0.64) - (0.96 \pm 0.05) \cdot \log f_X$. Hence the slope is significant flatter than the Euclidian value of -1.5. The fact that the X-ray bright object on the right (Markarian 421) is placed on the linear regression is just by chance. If I leave out this object the slope does not change significantly, because it is determined mostly by the lower fluxes with the lower errors in space density.

The flat slope of the number counts was already noticed for other samples of X-ray sources. While broad line AGN in the optical show a steep value which is consistent with the positive evolution (see e.g. Hewett & Foltz 1994), these objects also show flatter slope when studied in the X-rays. Gioia et al. (1984) found a $\log N_{>f_X} / \log f_X$ value of -1.45 ± 0.12 when examining EMSS sources. And when using data from the ROSAT satellite, this relation appears to be even steeper. Using the AGN derived by the identification of RASS sources in the HRC (Bade et al. 1998b) I determined a value of $\log N_{>f_X} / \log f_X = -1.39 \pm 0.07$ (Beckmann 1996).

The significant flatter slope can be caused by several effects. The assumption of a Euclidian space is only valid for low redshifts. Because the mean redshift within the HRX-BL Lac sample is $\bar{z} = 0.3$ the influence due to cosmological effects is not expected to be large.

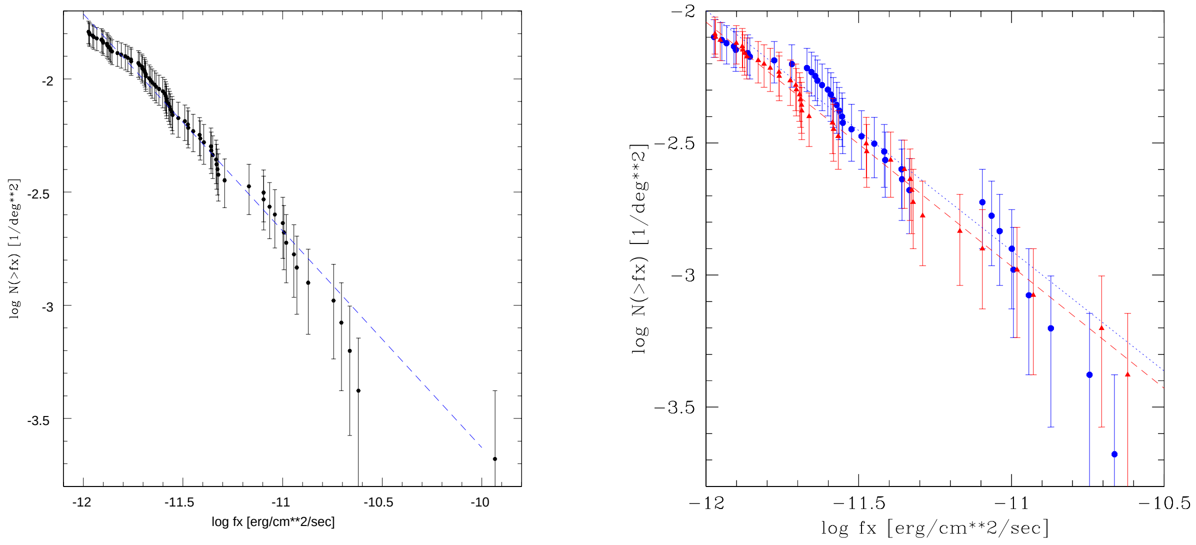

Figure 5.23: Left panel: Number counts for the HRX-BL Lac complete sample. The slope (-0.96 ± 0.05) is determined by a linear regression.
Right panel: Number counts for the HBL ($\log \nu_{peak} > 16.4$; circles) and for the LBL (marked by triangles). The dotted line refers to a linear fit to the HBL data, the dashed line represents the LBL.

Another explanation would be a lack of low flux objects within the sample. But to achieve a value of $\log N_{>f_X} / \log f_X = -1.5$ the density of low-flux objects would have to be more than two times higher than the value determined here. Even if there is a lack of low flux objects, it is not possible that it is that high. On the other hand a misidentification of high flux objects could lead to a flattening of the number counts relation. But also this is not expected, as the brighter objects are in most cases also easier to identify than the apparently faint ones.

The flat slope might be more probably be caused by a lower space density of BL Lac objects at higher redshifts (negative evolution). This would affect the high flux end less than the low flux end, resulting in a slope flatter than the expected -1.5 for normally distributed objects. For the same reason the number counts relation for quasars in the optical band shows a slope < -1.5 because these objects exhibit positive evolution.

The turnover point near $f_X = 8 \times 10^{-12}\mathrm{erg\,cm^{-2}\,sec^{-1}}$ as reported in Bade et al. (1998) for the 39 BL Lacs of the HRX-BL Lac *core sample* is not confirmed by the investigation presented here. The slope might be slightly steeper at fluxes higher than $f_X = 10^{-11}\mathrm{erg\,cm^{-2}\,sec^{-1}}$, but the statistically significance at this level is low due to the small number of objects. On the other hand the objects with fluxes below this value, which were found to have a slope of $\simeq -0.5$ for the *core sample* are clearly not detected within the complete sample. Also, the turnover point around $f_X = 10^{-12}\mathrm{erg\,cm^{-2}\,sec^{-1}}$ as reported from EMSS data (Maccacaro et al. 1988b) cannot be verified here, because the turnover is below the flux limit of the HRX-BL Lac sample.

A difference in the number counts relation for high and low frequency cut-off BL Lac objects within the HRX-BL Lac complete sample is not seen (Fig. 5.23, right panel). The dotted and the dashed line show the linear regression to the number counts of HBL and IBL, respectively. The regression derives nearly the same function: $\log N_{>f_X} = -(12.9 \pm 1.11) - (0.91 \pm 0.09) \cdot \log f_X$ for HBL ($\log \nu_{peak} > 16.4$) and $\log N_{>f_X} = -(13.1 \pm 1.03) - (0.92 \pm 0.09) \cdot \log f_X$ for IBL with $\log \nu_{peak} < 16.4$. Hence the slope is the same in both cases and the straight line is shifted by ~ 0.2 which could be caused by the fact that the IBL are expected to have lower X-ray fluxes due to selection effects, although the shift is only of low significance.

5.8.4 Luminosity function

Redshifts are available for 62 (81%) of the 77 BL Lac objects which form the complete sample. Therefore it is possible to determine a luminosity function (LF) for the HRX-BL Lacs.

To determine the cumulative LF, one has count all objects within a complete sample above a given luminosity, and divide this number by the volume V_a which has been surveyed for these objects as has been described on page 5.8.2. For each object the maximal redshift z_{max}, where this object would have been found due to the survey limit, is computed by using the individual flux limit of the object, and the given redshift. The space density ϕ is then described by:

$$\phi = \sum_{i=1}^{n} \frac{1}{V_{a,i}} \tag{5.11}$$

The corresponding 68% error bars have been determined using the formula

$$\sigma_{\pm} = \left(\sum_{i=1}^{n} V_{a,i}^{-2} \right)^{1/2} \tag{5.12}$$

which weighs each object by its contribution to the sum (see Marshall 1985 for details).

One problem of this method is that the X-ray spectrum is extrapolated up to high redshifts due to the large z_{max} values. There are seven objects within the HRX-BL Lac complete sample with $z_{max} > 1$ and one object with $z_{max} > 2$. The cumulative luminosity function is derived for all 62 objects within the complete sample with known redshift. The survey area of the HRX-BL Lac complete sample is 4770 deg^2. Because the fraction of objects without known redshift is 19% the effective area which is used to compute the luminosity function is decreased by this fraction to 3840 deg^2. This implements the assumption that the redshift distribution of the missing objects is the same as for the up to now determined redshifts ($\bar{z} \simeq 0.3$). It has to be mentioned that the redshifts which are still missing are expected to be higher. This would produce slightly different results.

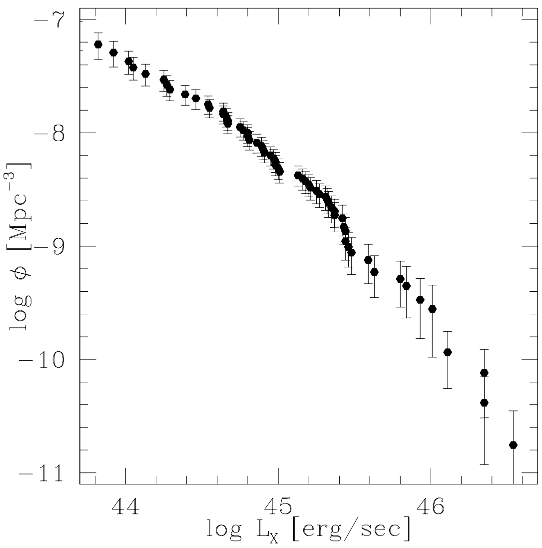

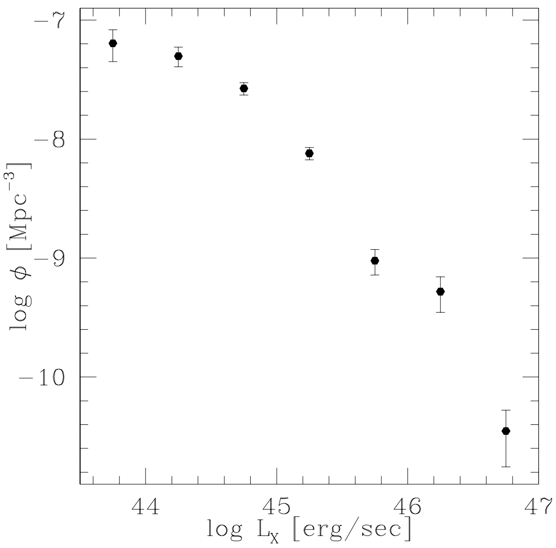

Figure 5.24: Left panel: Cumulative luminosity function of the HRX-BL Lac objects. Objects with unknown redshifts are not included. Right panel: Differential luminosity function of the HRX-BL Lac objects. The x-axis is binned to $\Delta L_X = 0.5$. The density refers to object density per $\Delta L_X = 1.0$.

The cumulative luminosity function of the HRX-BL Lac sample is shown in the left panel of Figure 5.24. The slope is remarkably well matching the LF presented in Bade et al. (1998) for the 31 objects within the HRX-BL Lac core sample.

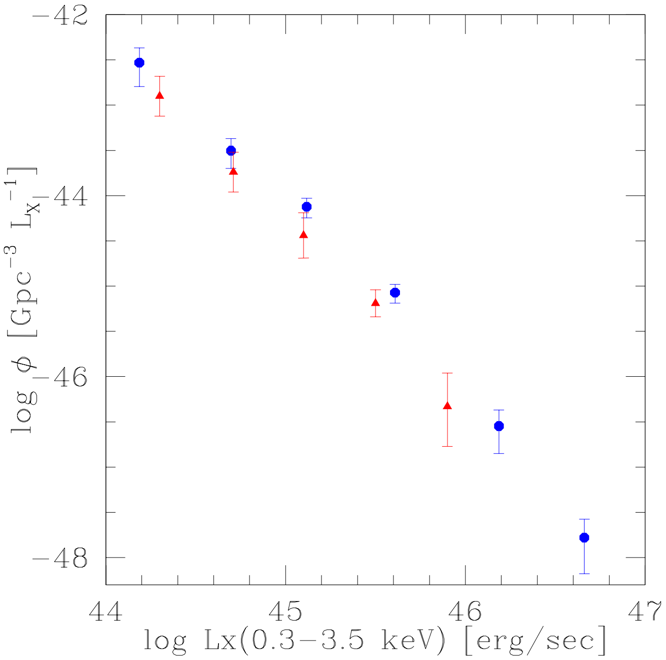

Figure 5.25: The differential X-ray luminosity function of the HRX-BL Lac complete sample (circles) in comparison to EMSS BL Lacs (triangles, Padovani & Giommi 1995a). The X-ray data of the HRX-BL Lac objects have been transformed to the EINSTEIN IPC energy band assuming a spectral slope of $\alpha_X = 1$.

Another way of presenting the distribution of luminosities within a sample is the differential luminosity function. Here the number objects within a luminosity bin is divided by the accessible volume V_a. This presentation suffers from the fact that in most cases the binning of the sample is quite important to the resulting LF. The X-ray LF for the HRX-BL Lac sample is shown in the right panel of Figure 5.24. Here the luminosity is binned to $\Delta L_X = 0.5$, while ϕ refers to the space density of objects per $\Delta L_X = 1.0$ (this was done for easier comparison to other works). The differential LF can be compared with the LF derived from Extended Medium-Sensitivity Survey (EMSS) BL Lacs by Wolter et al. (1994). Therefore I computed the expected luminosities of the HRX-BL Lacs within the EINSTEIN IPC energy band $(0.3 - 3.5\,\mathrm{keV})$ assuming a spectral slope of $\alpha_X = 1.0$ (see Maccacaro et al. 1988a). As presented by Padovani & Giommi (1995a) I use the notation of space density per Gpc^3 and X-ray luminosity. The resulting X-ray LF is shown in Figure 5.25. The data from the EMSS are consistent with those from the HRX-BL Lac complete sample within the 1σ error bars. The marginal effect of higher densities and/or luminosities within the HRX-BL Lac sample can be due to different spectral slope of the objects when moving to the higher energies of the IPC or resulting from different calibration of the IPC and the PSPC detectors. Nevertheless the HRX-BL Lac extends the X-ray LF by one magnitude to brighter X-ray luminosities. As shown by Wolter et al. (1994) this LF is consistent with the Fanaroff-Riley type I (FR I) luminosity function, which is thought to be the parent population of the BL Lac objects (see e.g. Padovani & Urry 1990, Celotti et al. 1993).

Since radio and optical data are available for all HRX-BL Lac objects it is possible to derive also the optical and radio LF for this sample. The result is shown in Figure 5.26. The local optical LF of BL Lac objects can be compared to the local LF of broad line AGN. For comparison I use the work of Della Ceca et al. (1996), who derived the optical LF for 226 broad line AGN with $z \leq 0.3$ selected from the Einstein Observatory Extended Medium Sensitivity Survey (EMSS). To compare these data I constructed a subsample of the complete HRX-BL Lac sample with $z \leq 0.3$.

The luminosity function presented by Della Ceca et al. (1996) is representative for broad line AGN

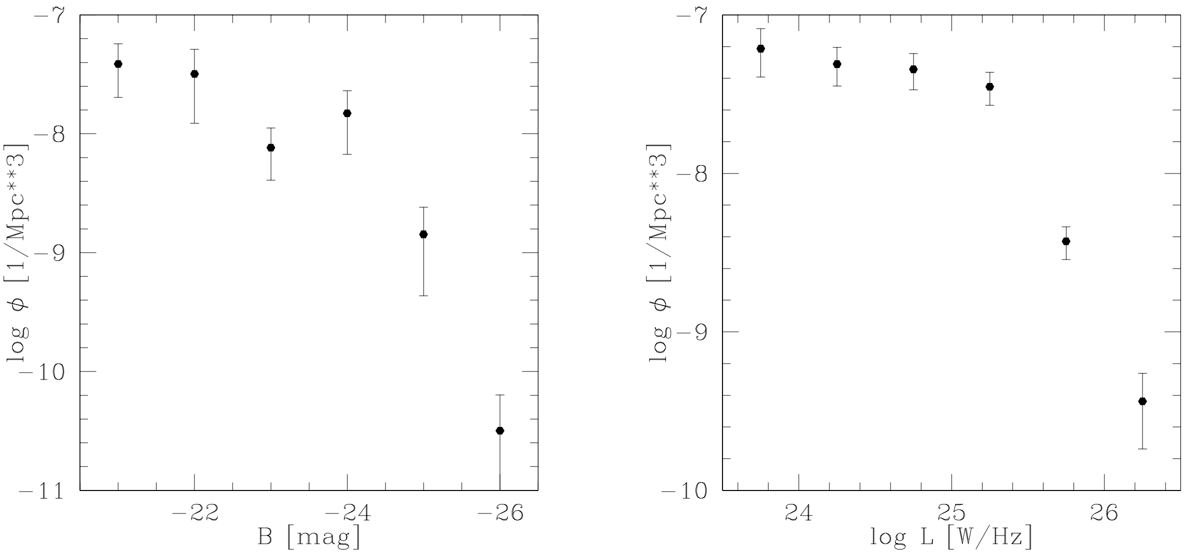

Figure 5.26: The differential luminosity function for the HRX-BL Lac sample in the optical (B-Band) and radio (1.4 GHz). The bin size is 1 mag and $\Delta L_R = 0.5$, respectively.

and does not differ significantly from the e.g. Seyfert 1 LF based on the CfA sample (Huchra & Burg 1992) or on the Markarian survey of galaxies (Meurs & Wilson 1984). It can be clearly seen in Fig. 5.27 that for X-ray selected objects the broad line AGN outnumber the BL Lac objects by a factor of ~ 100 for faint optical luminosities ($M_B \gtrsim -23$ mag). But the LF for the BL Lac objects appears to be flatter. Even though errors are large, it can be clearly derived from this comparison that we expect a larger number of X-ray selected objects to be BL Lacs when comparing objects of $M_B \lesssim -24$ mag. This is even more surprising as it would reveal that in the local universe about every second optical luminous AGN is a BL Lac object. In fact the known number of bright QSO is much larger than for BL Lac objects. This is caused by the circumstance that BL Lac objects are difficult to detect in the optical because of the lack of emission lines.

Also a comparison to the X-ray luminosity function of RASS selected AGN was done. Therefore I used the LF presented by Tesch (2000), which is based on the ROSAC sample. This homogeneous sample of 182 AGN with $z < 0.5$ was derived from RASS sources identified on an area of 363 $\deg^2$ in the constellation of Ursa Major. The luminosities have been corrected for the different X-ray band ($0.1 - 2.4$ keV instead $0.5 - 2.0$ keV) using the same spectral slopes used for the ROSAC sample. As for all values presented here, a cosmology with $H_0 = 50\,\mathrm{km\,sec^{-1}\,Mpc^{-1}}$ and a deceleration parameter $q_0 = 0.5$, assuming a Friedmann universe with $\Lambda = 0$ has been applied[5]

Based on the direct comparison as presented in Figure 5.27 the fraction of BL Lac objects within the X-ray selected AGN class can be estimated. As derived before from the complete identification of bright RASS sources, the fraction of BL Lacs is $\sim 10\%$.

The luminosity functions presented so far do not take into account a possible evolution of the objects. The sample is large enough to divide it into a high redshift and a low redshift bin in order to examine possible differences in their LF. The dividing value was set to the median of the HRX-BL Lac sample $z_{median} = 0.272$. To derive high and low redshift LFs the accessible volume $V_{a,i}$ for the objects with $z < 0.272$ has been restricted to $z = 0.272$ whenever $z_{max,i} > 0.272$. For the high redshift objects the accessible volume was computed from $z = 0.272$ up to $z_{max,i}$. The resulting two cumulative luminosity functions are shown in the right panel of Figure 5.28.

[5]When assuming a different H_0 than the value of $50\,\mathrm{km\,sec^{-1}\,Mpc^{-1}}$ used throughout this thesis, the values for the proper distances decrease by a factor of $50\,\mathrm{km\,sec^{-1}\,Mpc^{-1}}/\mathrm{H_0}$. For the same reason the luminosities decrease by a factor of $(50\,\mathrm{km\,sec^{-1}\,Mpc^{-1}}/\mathrm{H_0})^2$.

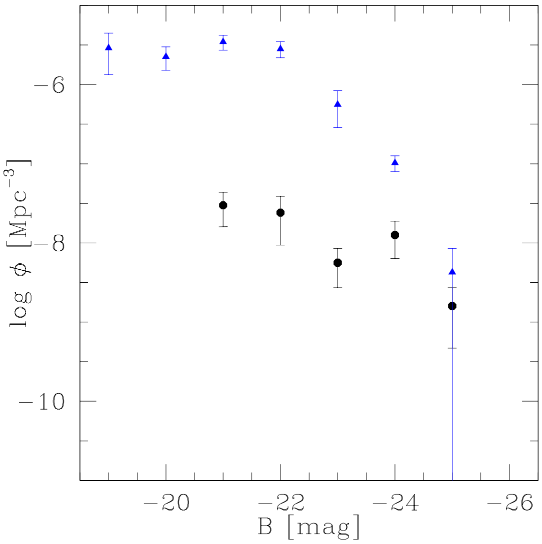

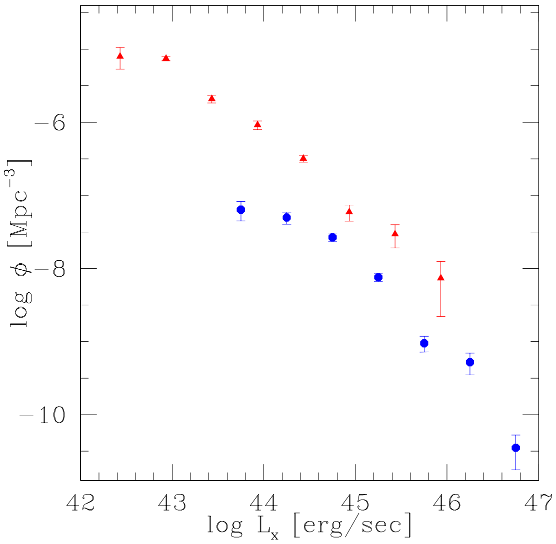

Figure 5.27: Left panel: The local differential optical luminosity function of X-ray selected BL Lacs in comparison with X-ray selected broad line AGN (taken from Della Ceca et al., 1996). With increasing optical luminosity the ratio between broad line AGN and BL Lac objects is decreasing.
Right panel: Comparison of the X-ray luminosity function of RASS selected AGN from the ROSAC sample (triangles; Tesch 2000) with HRX-BL Lacs (circles). The expected density of BL Lacs is ~ 10 times lower than for all AGN.

There seems to be no major difference between the high and low redshift LF. The slope of the low redshift objects is flatter, a linear regression results in -0.9 while for $z > 0.272$ the slope is -1.4. But in the overlapping regime around $L_X(0.5-2.0\,\mathrm{keV}) \sim 10^{45}$ the luminosity functions show the same behavior. The difference might originate from the circumstance that there have been more X-ray faint BL Lacs at cosmological distances than in the nearby universe, but more X-ray bright BL Lacs at small redshifts than for $z > 0.272$. This would result in the already found trend that at high z there have been more IBL (X-ray faint) than in the local universe, and that the number of HBL (X-ray bright) has increased.

The effect that the HBL have higher X-ray luminosities is also seen when comparing the luminosity functions of HBL and IBL (right panel in Fig. 5.28). But it is worth noting that, since we still miss 15 redshifts within the HRX-BL Lac sample, this result can be changed in a way that there are more high luminous IBL than detected up to now.

5.9 ROSAT PSPC pointings of HRX-BL Lac

Many of the HRX-BL Lac objects are not only included in the RASS-BSC, but were also contained in PSPC pointed observations. This gives the opportunity to check the reliability of the results based on the RASS-BSC.

For all positions of the HRX-BL Lac sample the ROSAT data archive was checked. Several objects have been observed within the field of view ($\sim 2°$ diameter) of pointed observations of other targets. Thus pointed observations are available for 40 HRX-BL Lacs. In cases where more than one pointing was available, the exposure with the best statistics was used. This is in most cases the pointing with the longest exposure time.

For the pointed observations I used the standard reduction procedure as described in Comastri, Molendi & Ghisellini (1995a).

For all objects I applied two models; a single-power law with free fitted absorption and one with absorption fixed to the Galactic value. For the pointed observations the power law model with free absorption gives acceptable results. The sample of pointed observations is a biased selection. Several of

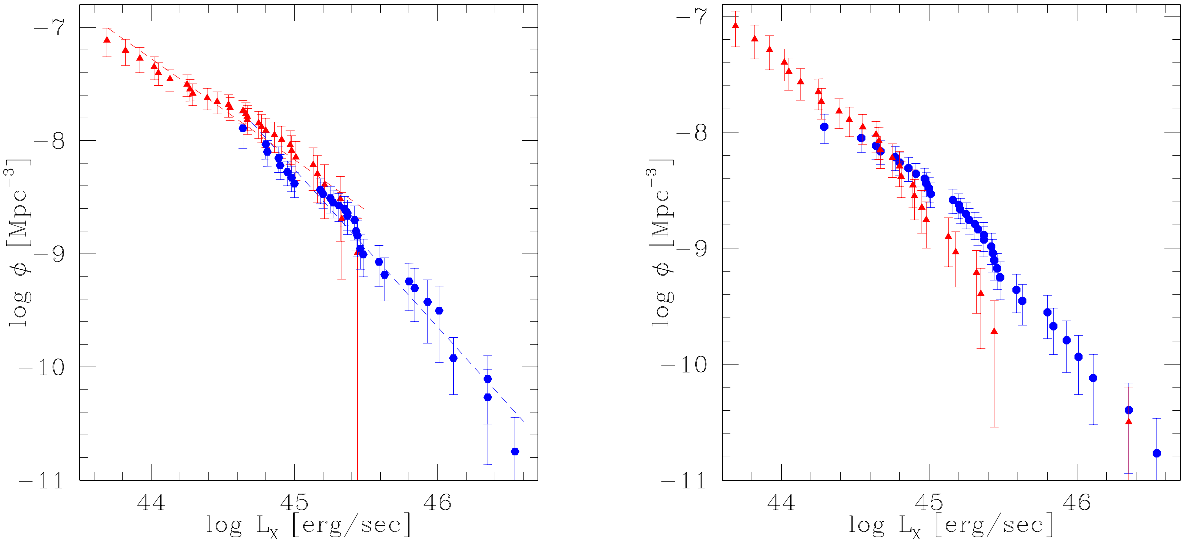

Figure 5.28: Left panel: Cumulative luminosity function of the two subsamples with $z > 0.272$ (circles) and $z < 0.272$ (triangles).
Right panel: Cumulative luminosity function of IBL (triangles) and HBL (circles). The trend that HBL tend to have higher X-ray luminosities than IBL is clearly seen.

the objects have been detected first in the RASS-BSC and were then re-observed with a longer pointing. This circumstance can be seen in Figure 5.29. 24 sources show lower fluxes within the pointed observations and only 16 are brighter than in the All-Sky survey. The mean decrease in flux is 6% compared to the BSC. Also pointed observations normally favour bright sources over faint ones. Thus the pointed sample is in no way complete. But the sample of pointed observations is on the other hand distributed in parameter space like the HRX-BL Lac sample, e.g. concerning the distribution of fluxes, redshift, luminosities etc. This enables us to test the relations found for the complete sample within the RASS-BSC data with these more detailed data from pointed observations.

The trend that the spectral index gets steeper for the fit with free fitted absorption is also seen in the pointed observations. For 40 HRX-BL Lac the values are $\overline{\alpha_X} = 1.20 \pm 0.38$, and $\overline{\alpha_{X,free}} = 1.58 \pm 0.43$. All fits show a higher absorption when fitted than the Galactic value. Also the increase of ΔN_H with spectral slope is significant for the pointed observations (see Figure 5.30). The correlation analysis results in a Pearson coefficient of $r_{xy} = 0.42$ and a probability for the correlation of $\Gamma > 99\%$. This confirms the result from section 5.7 for the BSC data. Another dependency which was checked using the pointed observations is $\log \nu_{peak}$ versus α_X (Figure 5.31). It seems that the effect of steeper X-ray spectra for lower peak frequency is stronger than in the investigation based on the BSC (Figure 5.16 on page 54). The analysis gives a probability of $\Gamma > 99.9\%$ for the correlation. Finally, X-ray luminosities were computed using the fluxes derived from the pointed observations. The luminosity in relation to the peak frequency of the synchrotron branch is shown in Figure 5.32. The correlation is significant on a $> 95\%$ level.

In summary, the results from the pointed observations support the conclusions based on the RASS-BSC data. Nevertheless for single objects the results from pointings and all-sky survey differ greatly. This might be due to variability of the sources but can also originate from larger errors within the BSC. But the statistical use of the BSC data for a sample large enough, like the HRX-BL Lac sample, yields to correct results.

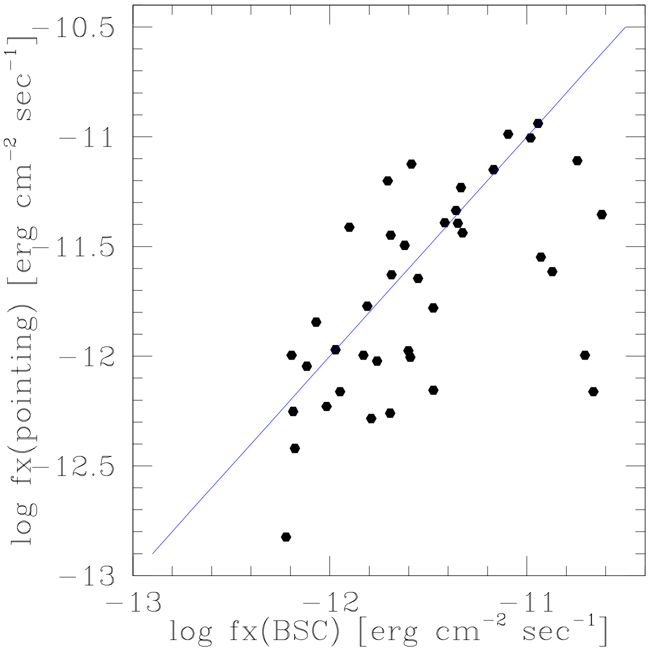

Figure 5.29: X-ray fluxes (logarithmic scaling) in the PSPC ($0.5 - 2.0\,\mathrm{keV}$) energy band from pointed observations vs. Bright Source Catalogue values. The mean higher flux within the BSC is a selection effect.

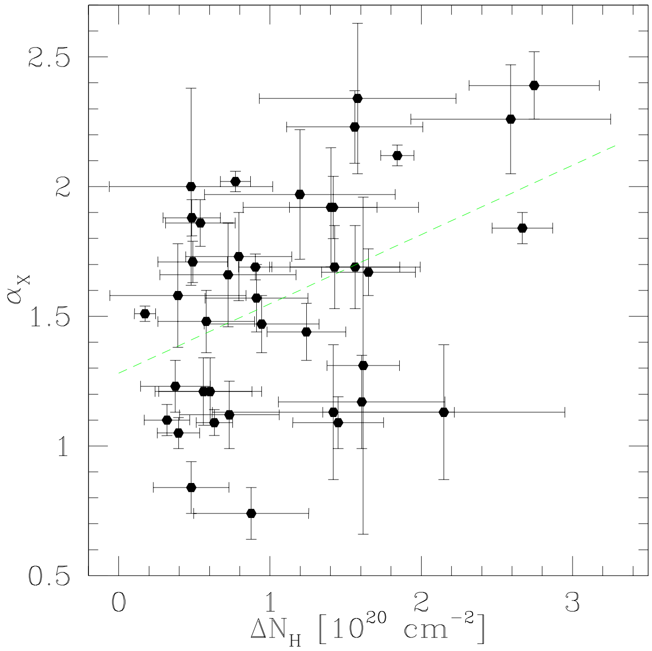

Figure 5.30: X-ray spectral slope α_X versus difference in absorption ΔN_H. A higher value of fitted absorption refers to steeper X-ray spectra.

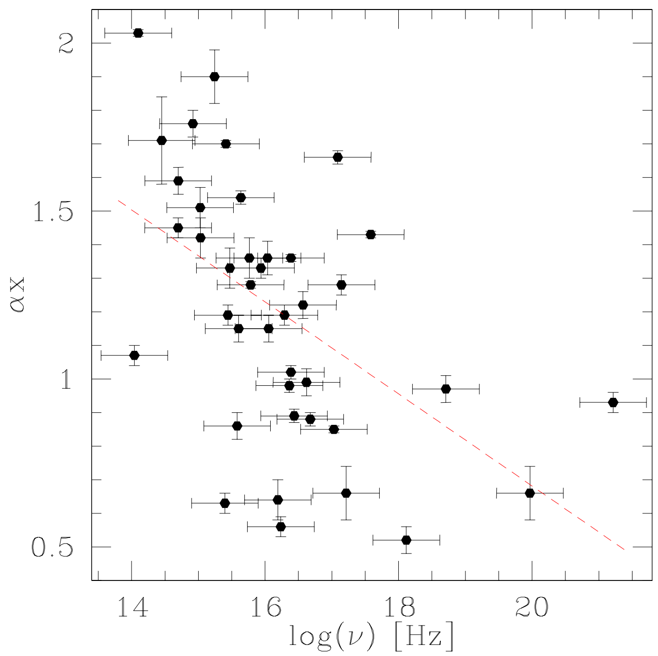

Figure 5.31: α_X versus peak frequency for the ROSAT-PSPC pointed observations. Errors on the peak frequency are assumed to be 0.5.

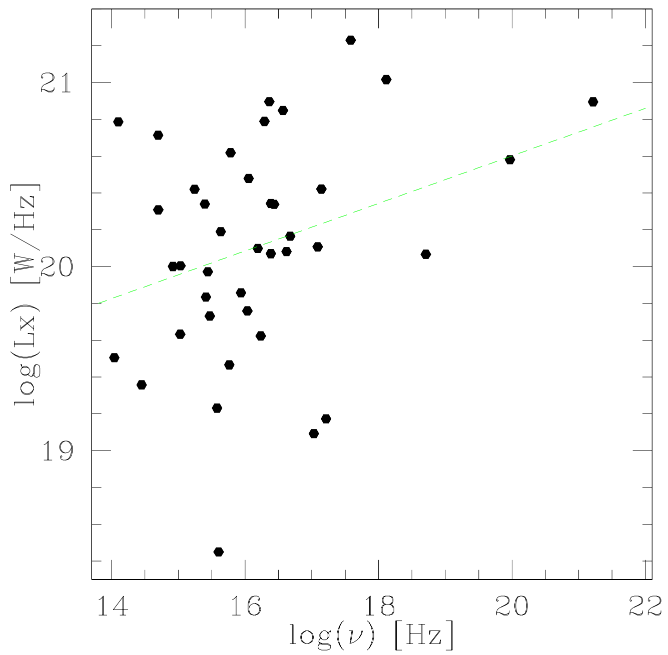

Figure 5.32: Monochromatic X-ray luminosity versus peak frequency for pointed observations. Unknown redshifts are set to $z = 0.3$ (mean sample value).

Table 5.5: The objects of the sample

Name	R.A. (2000.0)	Dec.	Redshift
1ES 0145+138	01 48 29.8	+14 02 16	0.125
1ES 0323+022	03 26 13.9	+02 25 15	0.147
1ES 0507–040	05 09 38.2	–04 00 46	0.304
1ES 0927+500	09 30 37.6	+49 50 26	0.186
1ES 1028+511	10 31 18.5	+50 53 34	0.361
1ES 1118+424	11 20 48.0	+42 12 10	0.124
1ES 1255+244	12 57 31.9	+24 12 39	0.141
1ES 1533+535	15 35 00.7	+53 20 38	0.890[a]
1ES 1544+820	15 40 15.6	+81 55 04	?
1ES 1553+113	15 55 43.2	+11 11 20	0.360
1ES 1959+650	20 00 00.0	+65 08 56	0.047

[a] the redshift for 1ES 1533+535 needs confirmation (Bade et al. 1998)

Table 5.6: Journal of *Beppo*SAX observations

Name	obs. date	LECS [sec]	LECS net counts	MECS [sec]	MECS net counts	PDS [sec]	PDS net counts
1ES 0145+138	30-31/12/97	10576	73.0 ± 9.5	12443	78.7 ± 11.0	-	-
1ES 0323+022	20/01/98	6093	201.6 ± 14.5	14408	607.4 ± 27.2	6845	256 ± 561
1ES 0507–040	11-12/02/99	9116	441.6 ± 21.5	20689	1460.2 ± 40.4	9094	1515 ± 633
1ES 0927+500	25/11/98	8436	568.4 ± 24.3	22712	1967.3 ± 46.5	10129	692 ± 571
1ES 1028+511	1-2/05/97	4552	737.9 ± 28.1	12622	2448.7 ± 50.2	9484	2763 ± 718
1ES 1118+424	1/5/97	6027	236.5 ± 15.6	9982	541.3 ± 24.1	8496	170 ± 147
1ES 1255+244	20/6/98	2484	297.1 ± 17.4	6910	1037.9 ± 33.1	-	-
1ES 1533+535	13-14/02/99	8321	319.4 ± 18.5	26773	931.6 ± 35.5	4056	308 ± 285
1ES 1544+820	13/02/99	8043	170.7 ± 13.6	23249	510.8 ± 26.9	10414	780 ± 363
1ES 1553+113	5/02/98	4421	1179.5 ± 34.5	10618	2157.6 ± 47.3	4671	542 ± 363
1ES 1959+650	4-5/05/97	2252	423.2 ± 20.7	12389	3243.4 ± 57.6	7348	830 ± 516

5.10 *Beppo*SAX pointed observations of BL Lac

This section will also be included in my publication Beckmann et al. 2001.

During the time of my PhD I had the chance to work at the *Osservatorio Astronomico di Brera* for a total of nine months. There I worked with *Beppo*SAX data of BL Lac objects. This enabled me to test the relations found based on ROSAT data with another sample and a different X-ray instrument.

The Slew Survey Sample covers the whole high Galactic latitude sky, while the EMSS has a lower flux limit but only refers to an area of $\sim 800\,\mathrm{deg}^2$. By selecting objects with fluxes $F_X(0.1 - 10\,\mathrm{keV}) \geq 10^{-11} \mathrm{erg\,cm^{-2}\,sec^{-1}}$ in the Slew Survey and $F_X \geq 4 \times 10^{-12} \mathrm{erg\,cm^{-2}\,sec^{-1}}$ in the EMSS, a sample has been obtained that combines the advantage of a flux limited sample with a wide coverage of the parameter space. The objects analyzed here are the second half of a sample, for which the first 10 objects have been presented in Wolter et al. (1998). The 11 objects presented here (for positions and redshifts see Tab. 5.5) have been observed between May 1997 and February 1999. The data have been preprocessed at the *Beppo*SAX SDC (Science Data Center) and retrieved through the SDC archive. Table 5.6 shows the journal of observations, including exposure times and net count-rates for the LECS, MECS, and PDS detector.

5.10.1 Spectral analysis

The three MECS units spectra have been summed together to increase the S/N for data taken in May 1997. On May 6, 1997 a technical failure caused the switch off of unit 1. After this date, only MECS unit 2 and 3 were available, and data from these two detectors have been summed. None of the sources show extension neither in the LECS nor in the MECS image. The same reduction process as in Wolter et al. (1998) has been applied to the data, using FTOOLS v4.0 and XSPEC v.9.0 (Shafer et al. 1991).

I fitted simultaneously LECS and MECS data, leaving free the LECS normalization with respect to the MECS to account for the residual errors in intensity cross-calibration. The assumed spectral shape is a single-power law model plus free low energy absorption, arising from cold material with solar abundances (Morrison and McCammon 1983). For all sources where PDS data were available they were also fitted simultaneously; only for 1ES 1255+244 there are no PDS data and for 1ES 0145+138 the exposure time was too short to result in a detection in the PDS. The best fit parameters with free N_H and single-power law are listed in Table 5.7. Galactic values were taken from the Leiden/Dwingeloo Survey (Hartmann & Burton 1997). The errors are 90% confidence levels. Fluxes are given in the 2–10 keV band and also in the 0.5–2.0 keV band for comparison with ROSAT-PSPC fluxes. Also listed are the normalization factors of the LECS relative to the MECS.

For all objects I checked if a broken-power law fit would give a significantly better result than the single-power law. In five cases I find a significantly better fit with this model. The results for these objects are also listed in Table 5.7. Fluxes and the quality of the fit refer to the best fit model. For the broken-power law I used the MECS/LECS relation as derived from the single-power law fit and Galactic values of N_H for absorption. Previous I checked a broken-power law model with free fitted absorption; this increases the number of fit parameters and therefore the complexity of the fit. Nevertheless I find all free fitted N_H values lying in between the Galactic value and the value derived from the single-power law. Only in one case (1ES 1959+650) is the free fitted N_H from the broken-power law in better agreement to the fitted N_H from the single-power law than the Galactic value. As I assume that there is no low energy absorption in the source (but only due to the intervening material which is well approximated by the Galactic neutral hydrogen). I therefore fixed the N_H in the broken-power law model to the Galactic value. We have five free parameters in both models. All broken-power laws show a flat slope in the low energy range ($\alpha_1 = 0.4 \ldots 0.7$) and a steep high energy tail ($\alpha_2 = 1.2 \ldots 1.9$) with a break energy within the LECS energy band ($E_0 = 1.1 \ldots 1.6$ keV), except 1ES 1118+424 ($E_0 = 5.1$ keV).

All sources except 1ES 1255+244 and 1ES 0145+138 have also been detected (at $\geq 4\sigma$) in the PDS. In all cases the single-power law fit or the broken-power law fit gives a good approximation of the source spectrum in the energy range 0.1keV $\leq E \leq$ 30keV and even up to 100 keV in the case of 1ES 1028+511.

5.10.2 Spectral Energy Distribution

To compute the broadband spectral energy distribution (SED) for the objects presented here I used radio data taken from the VLA surveys NVSS (Condon et al. 1998) or FIRST (White et al. 1997) at 1.4 GHz. Optical data were taken from literature and for some objects determined using the Calar Alto 1.23m telescope. The variability of the objects in the optical band is not expected to be large; all objects presented here are X-ray dominated objects ($\alpha_{OX} < 1.2$, see Table 5.10.2), and these objects show only small optical variability (e.g. Villata et al. 2000, Mujica et al. 1999, Januzzi et al. 1994). For the energy bands I had data for (radio 1.4GHz, optical 4400 Å, X-ray 1 keV) I computed overall spectral energy indices. As in section 5.5.3 a parabolic fit was applied to the data in the $\log(\nu F_\nu) - \log(\nu)$ plane and thus the peak frequency of the SED was determined. The results are listed in Table 5.10.2; I also computed these values at these frequencies for the objects from Wolter et al. (1998) which therefore differ a bit from the values presented there. The values for α_{ox}, α_{ro} and α_{rx} presented here are therefore by ~ 0.17, ~ 0.05, and ~ 0.09 lower than those presented in Wolter et al. (1998). I will use the whole sample of 21 objects for the further discussion. After the publication of Wolter et al. (1998) two other redshifts for sample objects have been determined; 1ES 0502+675 ($z = 0.314$, Scarpa et al. 1999a) and 1ES 1517+656 ($z = 0.702$; Beckmann, Bade & Wucknitz 1999). Thus I lack only redshift information for 1ES 1544+820, for which I assume $z = 0.2$.

As expected, I find a strong correlation between α_{ox} and the value of the peak frequency (Fig. 5.33). Small values of α_{ox} refer to X-ray dominated objects while more optical dominated objects have $\alpha_{ox} > 1$. The correlation is well-represented by a polynomial fit of the third degree as shown in Figure 5.33.

On the other hand I find that a higher peak frequency is related to a flatter spectral slope (Figure 5.34). This can be explained in terms of the SED, because when the peak frequency is rising, the X-ray

Table 5.7: Best fit results for the *Beppo*SAX spectra. Single-power law with free fitted N_H and, if the fit shows better results, broken-power law with Galactic absorption

Name	Energy Index α_X	α_1	α_2	E_0 [keV]	N_H^a (Gal)	N_H^a (Fit)	F_X^b	F_X^c	Nm^d	$\chi^2_\nu(dof)$	Prob.
0145+138	$1.50^{+0.94}_{-0.68}$				4.59	$10.4^{+27.6}_{-8.9}$	0.35	0.45	0.86	0.38 (3)	77%
0323+022	$1.58^{+0.23}_{-0.21}$				7.27	$31.6^{+14.6}_{-11.5}$	2.24	1.93	0.81	0.51 (27)	98%
0507–040	$1.14^{+0.12}_{-0.11}$				7.84	$14.5^{+7.8}_{-5.6}$	3.88	2.72	0.82	0.73 (69)	95%
0927+500	$1.18^{+0.09}_{-0.09}$	$0.40^{+0.18}_{-0.23}$	$1.27^{+0.08}_{-0.08}$	$1.35^{+0.28}_{-0.24}$	1.31	$4.3^{+1.3}_{-0.9}$	4.59	4.59	0.69	0.88 (61)	74%
1028+511	$1.32^{+0.08}_{-0.07}$				1.27	$3.7^{+0.8}_{-0.7}$	10.10	12.50	0.66	0.85 (97)	85%
1118+424	$1.57^{+0.16}_{-0.16}$	$1.43^{+0.08}_{-0.10}$	$3.43^{+0.7}_{-0.7}$	$5.11^{+1.6}_{-2.3}$	2.59	$3.5^{+1.3}_{-1.0}$	2.55	3.65	0.57	0.78 (23)	76%
1255+244	$1.15^{+0.12}_{-0.11}$	$0.61^{+0.19}_{-0.37}$	$1.23^{+0.13}_{-0.04}$	$1.58^{+0.36}_{-0.36}$	1.21	$3.6^{+1.5}_{-1.0}$	8.03	7.81	0.74	0.78 (36)	83%
1533+535	$1.57^{+0.15}_{-0.14}$	$0.68^{+0.19}_{-0.25}$	$1.74^{+0.16}_{-0.15}$	$1.40^{+0.30}_{-0.27}$	1.28	$4.8^{+1.9}_{-1.1}$	1.64	2.89	0.71	0.96 (44)	55%
1544+820	$2.13^{+0.29}_{-0.26}$				3.70	$20.1^{+11.3}_{-8.2}$	0.95	2.06	0.63	0.68 (30)	90%
1553+113	$1.79^{+0.09}_{-0.08}$	$0.57^{+0.18}_{-0.22}$	$1.85^{+0.09}_{-0.08}$	$1.13^{+0.90}_{-0.90}$	3.53	$9.2^{+2.3}_{-1.3}$	9.37	19.16	0.76	1.05 (89)	35%
1959+650	$1.64^{+0.08}_{-0.08}$				0.99	$25.5^{+7.1}_{-6.0}$	12.90	13.52	0.65	0.79 (88)	92%

[a] hydrogen column density in $\times 10^{20}\,\mathrm{cm}^{-2}$

[b] unabsorbed flux in $10^{-12}\,\mathrm{erg\,cm^{-2}\,sec^{-1}}$ in the 2–10 keV MECS energy band

[c] LECS flux in the (0.5–2.0 keV) band in $10^{-12}\,\mathrm{erg\,cm^{-2}\,sec^{-1}}$

[d] Normalization of LECS versus MECS

Table 5.8: Derived quantities: Two-point overall spectral indices[a], X-ray luminosities, and peak frequencies (for the 11 objects from this paper and for the 10 BL Lacs from Wolter et al. (1998)).

Name	$\alpha_{\rm ox}$	$\alpha_{\rm ro}$	$\alpha_{\rm rx}$	$\log L_X$	$\log(\nu_{peak})$
1ES 0145+138	1.19	0.41	0.65	43.42	14.49
1ES 0323+022	1.07	0.34	0.57	44.38	14.89
1ES 0507–040	0.69	0.52	0.58	45.26	18.05
1ES 0927+500	0.81	0.36	0.50	44.89	16.34
1ES 1028+511	0.81	0.33	0.48	45.86	16.08
1ES 1118+424	0.91	0.32	0.51	44.30	15.49
1ES 1255+244	1.14	0.15	0.46	44.88	15.09
1ES 1533+535	0.77	0.37	0.51	46.05	15.77
1ES 1544+820[b]	0.71	0.47	0.55	44.11	16.15
1ES 1553+113	0.81	0.43	0.56	45.89	15.58
1ES 1959+650	1.05	0.31	0.54	44.11	15.00
MS 0158.5+0019	0.72	0.39	0.50	45.12	16.95
MS 0317.0+1834	0.64	0.42	0.49	45.11	18.51
1ES 0347–121	0.67	0.34	0.44	45.05	16.97
1ES 0414+009	0.76	0.42	0.53	45.59	16.25
1ES 0502+675	0.59	0.34	0.42	46.00	18.10
MS 0737.9+7441	0.84	0.39	0.54	44.93	15.72
1ES 1101-232	0.72	0.39	0.49	45.83	17.37
1ES 1133+704	1.04	0.43	0.62	43.69	14.96
MS 1312.1-4221	1.04	0.25	0.50	44.85	15.15
1ES 1517+656	0.75	0.32	0.47	46.55	16.17

[a] source fluxes at 1 keV, 4400 Å, and 1.4 GHz resp.
[b] assuming redshift $z = 0.2$

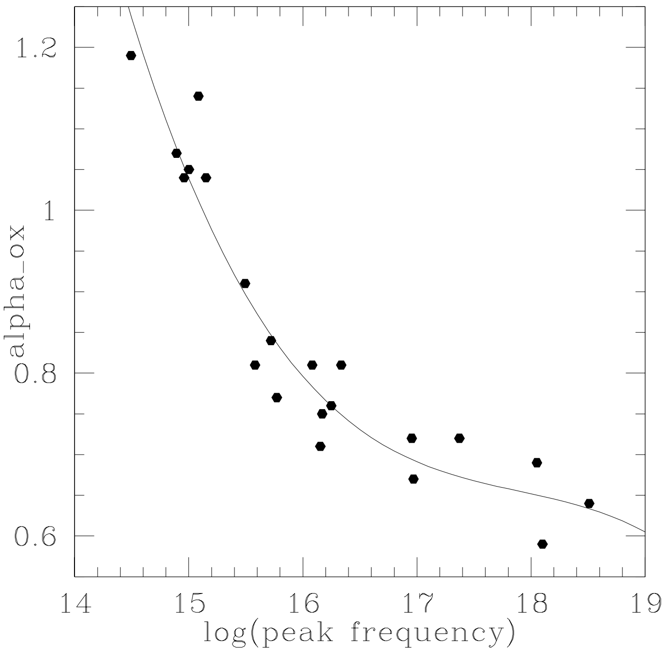

Figure 5.33: X-ray dominance versus peak frequency of the synchrotron branch. The more X-ray dominated objects have a higher peak frequency. The line shows a polynomial fit.

band is located near the maximum of the synchrotron branch. Thus we see a flatter spectrum than in the objects with a lower peak frequency. This is confirmed by the difference between the free fitted absorption and the Galactic N_H. For all fits the value of fitted absorption was above the Galactic value. Comparing the value $\Delta N_H = N_{H,free} - N_{H,gal}$ with the X-ray spectral slope α_X, I find that there is a correlation in the sense that higher ΔN_H is found in steeper X-ray spectra (Figure 5.35) as for the HRX-BL Lac sample. The effect was already explained in section 5.6. Additionally I find in all cases the value for a free fitted N_H in the broken-power law model is in between the Galactic and the free fitted value from the single-power law.

Another strong correlation is that between the X-ray dominance and the X-ray luminosity (Figure 5.36). A linear regression results in $\log L_X = 47.7 - 3.2 \times \alpha_{OX}$ with a correlation coefficient of 0.7. The lack of objects with low L_X and low α_{OX} is not due to a selection effect by missing optical faint counterparts to the weaker X-ray sources, because this correlation is not seen in a comparison of X-ray *fluxes* to X-ray dominance. The effect that X-ray dominated objects seem to have higher X-ray luminosities than the intermediate BL Lacs is also seen if one compares the peak frequency of the synchrotron branch with the X-ray luminosity (left panel of Figure 5.37). This correlation was already reported for the HRX-BL Lac sample in Figure 5.17 for the BSC data, and for the pointed PSPC observations in Figure 5.32.

If a parabolic fit is applied to the radio, optical and X-ray data as described above to determine the total luminosity of the synchrotron branch between radio and X-ray band, there does not seem to be a strong correlation with the peak frequency (right panel of Figure 5.37). The effect of having higher X-ray luminosities for higher peaked objects seems not to be present (or at least less significant) for the total luminosity of the BL Lac objects.

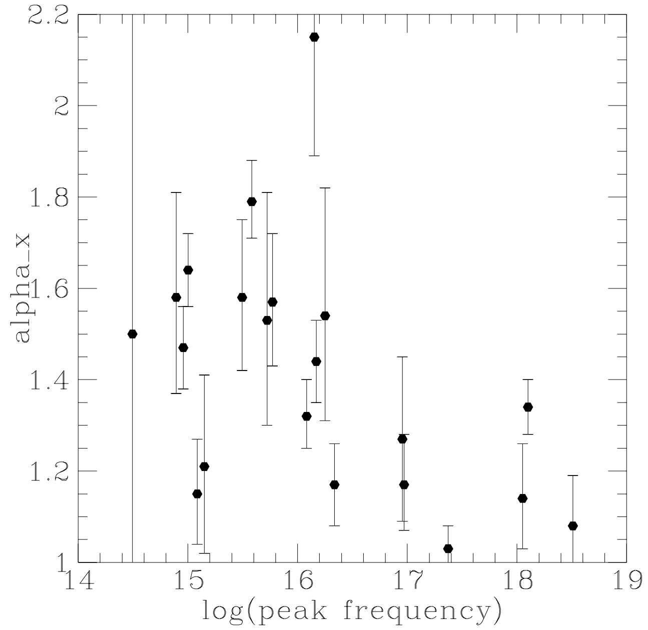

Figure 5.34: X-ray spectral slope versus peak frequency.

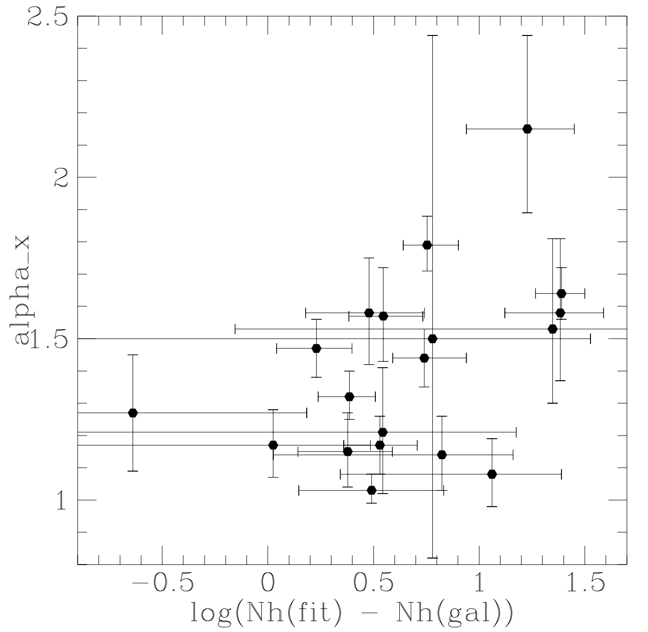

Figure 5.35: Logarithmic difference in absorption ($N_{H,fit} - N_{H,Gal}$ in $10^{20}\mathrm{cm}^{-2}$) versus spectral slope. There is a trend to steeper spectra for higher difference in absorption.

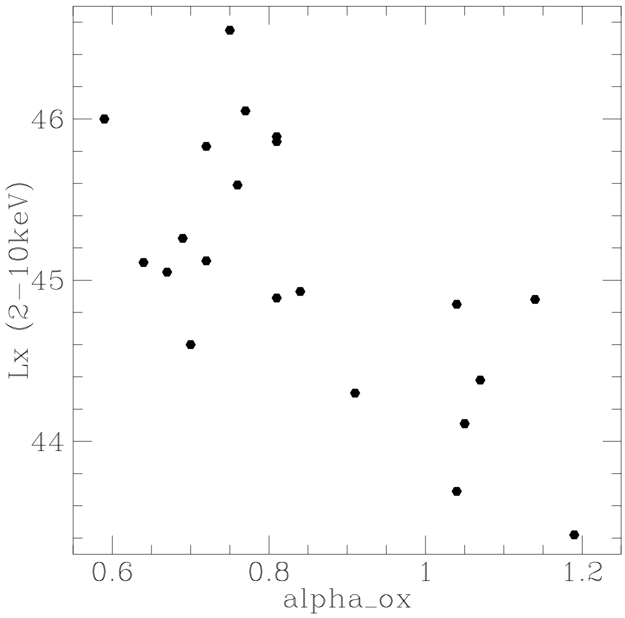

Figure 5.36: X-ray luminosity for the *Beppo*SAX MECS band (2–10 keV) versus X-ray dominance (α_{OX})

5.10.3 Results from the EINSTEIN BL Lac sample

Checking the same correlations for another sample based on a different instrument, the same results as in the HRX-BL Lac sample are obtained:

- the over-all spectral index α_{OX} is a good measurement for the peak frequency of the synchrotron branch.
- the X-ray luminosity is increasing with increasing peak frequency, while this is less clear for the total luminosity.
- IBL show higher difference in absorption (ΔN_H) and are thought to have a more curved spectrum than HBL.

This supports the results based on the HRX-BL Lac sample.

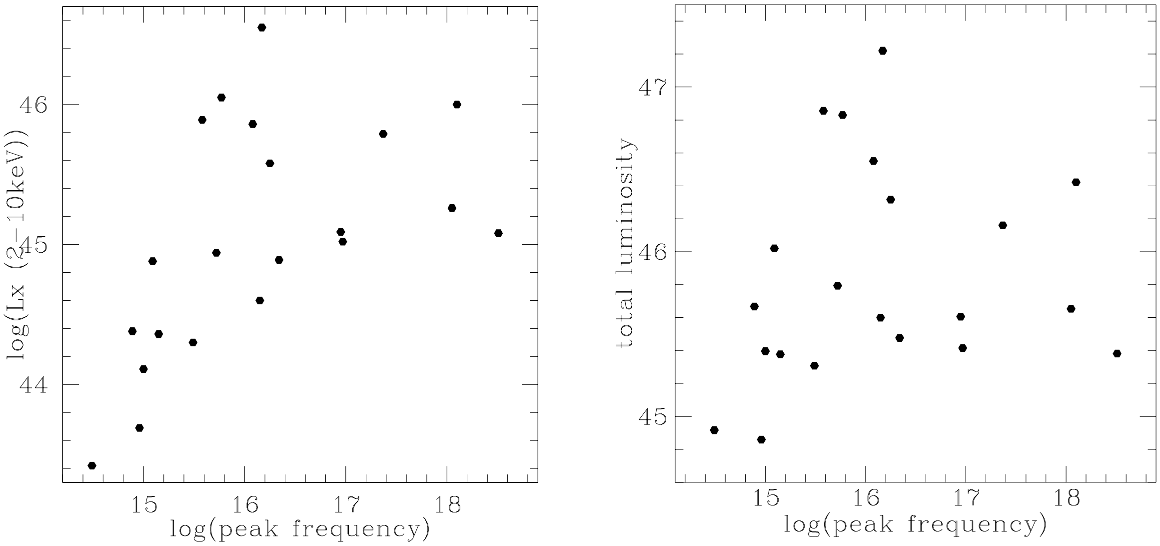

Figure 5.37: Left panel: X-ray luminosity for the *Beppo*SAX MECS band (2–10 keV) versus peak frequency of the synchrotron branch.
Right panel: Total luminosity of the synchrotron branch (derived from the applied parabolic model between radio and X-ray band) versus peak frequency.

Chapter 6

Peculiar objects in the HRX-BL Lac sample

Some objects in the HRX-BL Lac sample show extraordinary properties. This chapter discusses five of them in detail.

6.1 The extreme high frequency peaked BL Lac 1517+656

This section is based on my publication: Beckmann, Bade, Wucknitz, 1999, A&A 352, 395

Even though 1517+656 is an X-ray selected BL Lac, this object was detected in the radio band before being known as an X-ray source. It was first noted in the *NRAO Green Bank* 4.85 GHz catalog with a radio flux density of 39 ± 6 mJy (Becker et al. 1991) and was also included in the *87 Green Bank Catalog of Radio Sources* with a similar flux density of 35 mJy (Gregory & Condon 1991) but in both cases without identification of the source. The NRAO Very Large Array at 1.4 GHz confirmed 1517+656 as having an unresolved core with no evidence of extended emission although a very low surface brightness halo could not be ruled out (Kollgaard et al. 1996). The source was first included as an X-ray source in the HEAO-1 A-3 Catalog and was also detected in the *Einstein* Slew Survey (Elvis et al. 1992) in the soft X-ray band ($\sim 0.2 - 3.5$ keV) of the Imaging Proportional Counter (IPC, Gorenstein et al. 1981). The IPC count rate was 0.91 cts sec^{-1}, but the total Slew Survey exposure time was only 13.7 sec. Even though 1517+656 by then was a confirmed BL Lac object (Elvis et al. 1992) with an apparent magnitude of $B = 15.5$ mag, no redshift data were available. Known as a bright BL Lac, 1517+656 has been studied several times in different wavelengths in the recent years. Brinkmann & Siebert (1994) presented ROSAT PSPC ($0.07 - 2.4$ keV) data and determined the flux to $f_X = 2.89 \cdot 10^{-11}$ erg cm^{-2} sec^{-1} and the spectral index to $\Gamma = 2.01 \pm 0.08$ [1]. Observations of 1517+656 with *BeppoSAX* in the $2 - 10$ keV band in March 1997 gave an X-ray flux of $f_X = 1.03 \cdot 10^{-11}$ erg cm^{-2} sec^{-1} and a steeper spectral slope of $\Gamma = 2.44 \pm 0.09$ (Wolter et al. 1998). The Energetic Gamma Ray Experiment Telescope (EGRET, Kanbach et al. 1988; see also page 39) on the *Compton Gamma Ray Observatory* did not detect 1517+656 but gave an upper flux limit of $8 \cdot 10^{-8}$ photons cm^{-2} sec^{-1} for $E > 100$ MeV (Fichtel et al. 1994). In the hard X-rays 1517+656 was first detected with OSSE with $3.6 \pm 1.2 \cdot 10^{-3}$ photons cm^{-2} sec^{-1} at $0.05 - 10$ MeV (McNaron-Brown et al. 1995). The BL Lac was then detected in the EUVE-All-Sky Survey with a Gaussian significance of 2.6σ during a 1362 sec exposure, giving a lower and upper count rate limit of 0.0062 cps and 0.0189 cps respectively (Marshall et al. 1995). For a plot of the spectral energy distribution see Wolter et al. 1998.

6.1.1 Optical Data

The BL Lac 1517+656 was also included in the HRX-BL Lac sample because of its X-ray and radio properties. In February 1998 a half hour exposure of 1517+656 was taken with the 3.5m telescope on Calar Alto, Spain, equipped with MOSCA. Using a grism sensitive in the $4200 - 6600$ Å range with a resolution of ~ 3 Å it was possible to detect several absorption lines. The spectrum was sky subtracted and flux calibrated by using the standard star HZ44. Identifying the lines with iron and magnesium absorption we determined the redshift of 1517+656 to $z \geq 0.7024 \pm 0.0006$ (see Fig. 6.1). The part of the spectrum with the FeII and MgII doublet is shown in Fig. 6.3. The BL Lac has also been a target for follow-up observation for the HQS (Hagen et al. 1995) in

[1]The energy index α_E is related to the photon index $\Gamma = \alpha_E + 1$

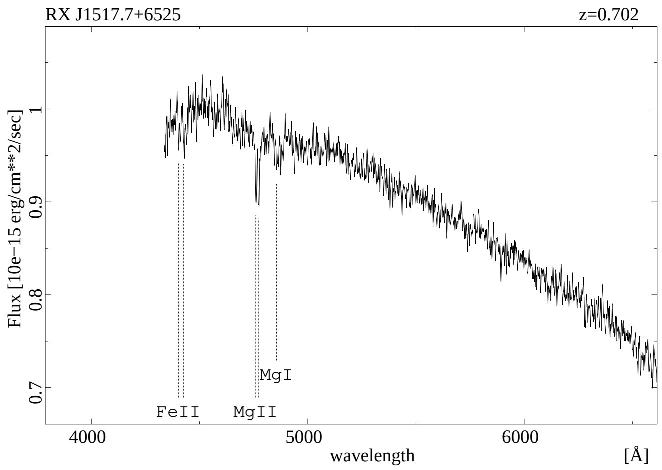

Figure 6.1: The spectrum of 1517+656, taken in February 1998 with the 3.5m telescope on Calar Alto, Spain using the MOSCA spectrograph. The conditions during the exposure where not photometric, so the flux values can only give a hint to the real flux. The curvature at the blue end below $\sim$ 4500Å is due to calibration problems. For the doublets see also Fig. 6.3

Table 6.1: Observed wavelengths and equivalent widths for absorption lines in the February 1998 spectrum

λ_{obs}[Å]	W_λ[Å]	λ_0 [Å]	Ion	Redshift
4194	0.03	2463.4	FeI	0.7025
-	-	2484.0	FeI	not detected
4404	0.15	2586.7	FeII	0.7026
4429	0.17	2600.2	FeII	0.7033
4761	0.48	2796.4	MgII	0.7025
4774	0.52	2803.5	MgII	0.7028
4855	0.15	2853.0	MgI	0.7017
4999	0.09	2937.8	FeI	0.7016

1993, because it had no published identification then and was independently found by the quasar selection of the HQS. The 2700 sec exposure, taken with the 2.2m telescope on Calar Alto and Boller & Chivens spectrograph, showed a power-law like continuum; the significance of the absorption lines in the spectrum was not clear due to the moderate resolution of $\simeq 10$ Å (Fig. 6.2). Nevertheless the MgII doublet at 4761 and 4774Å is also detected in the 1993 spectrum, though only marginally resolved (see Table 2). The equivalent width of the doublet is comparable in both images ($W_{\text{Å}} = 0.8/0.9$ for the 1993/1998 spectrum respectively). Also the Fe II absorption doublet at 4403/4228 Å ($\lambda_{\rm rest} = 2586.6/2600.2$ Å) and Mg I at 4859 Å ($\lambda_{\rm rest} = 2853.0$ Å) is detectable. For a list of the detected lines, see Table 1. Comparison with equivalent widths of absorption lines in known elliptical galaxies is difficult because of the underlying non-thermal continuum of the BL Lac jet. But the relative line strengths in the FeII and MgII doublet are comparable to those measured in other absorption systems detected in BL Lac objects (e.g. 0215+015, Blades et al. 1985). Because no emission lines are present and the redshift is measured using absorption lines, the redshift could belong to an absorbing system in the line of sight, as e.g. detected in the absorption line systems in the spectrum of 0215+015 (Bergeron & D'Odorico 1986). A higher redshift would make 1517+656 even more luminous; we will consider this case in the further discussion, though we assume that the absorption is caused by the host galaxy of the BL Lac. Assuming a single power law spectrum with $f_\nu \propto \nu^{-\alpha_o}$ the spectral slope in the $4700 - 6600$ Å band can be described by $\alpha_o = 0.86 \pm 0.07$. The high redshift of this object is even highly plausible, because it was not possible to resolve its host galaxy on HST snap shot exposures (Scarpa et al. 1999a). The apparent magnitude varies slightly through the different epochs, having reached the faintest value of $R = 15.9$ mag and $B = 16.6$ mag in February 1999 (direct imaging with Calar Alto 3.5m and MOSCA). These values were derived by comparison with photometric standard stars in the field of view (Villata et al. 1998). $H_0 = 50$ km sec^{-1} Mpc^{-1} and $q_0 = 0.5$ leads to an absolute optical magnitude of at least $M_R = -27.2$ mag and $M_B \leq -26.4$ (including K-correction).

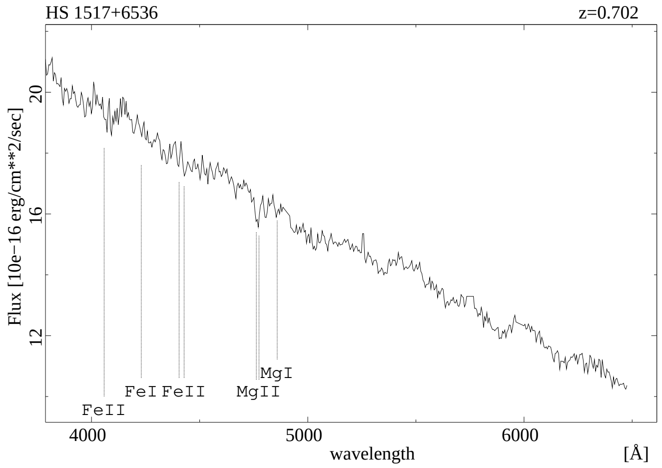

Figure 6.2: The spectrum of 1517+656, taken with the 2.2m telescope on Calar Alto in August 1993. Observation conditions were not photometric.

Table 6.2: Observed wavelengths and equivalent widths for absorption lines in the 1993 spectrum

$\lambda_{obs}[\AA]$	$W_\lambda[\AA]$	λ_0 [Å]	Ion	Redshift
4194	0.2	2463.4	FeI	0.7025
4231	0.1	2484.0	FeI	0.7033
4401	0.3	2586.7	FeII	0.7014
4429	0.4	2600.2	FeII	0.7033
4761	0.4	2796.4	MgII	0.7025
4771	0.4	2803.5	MgII	0.7018
4855	0.15	2853.0	MgI	0.7017
-	-	2937.8	FeI	not detected

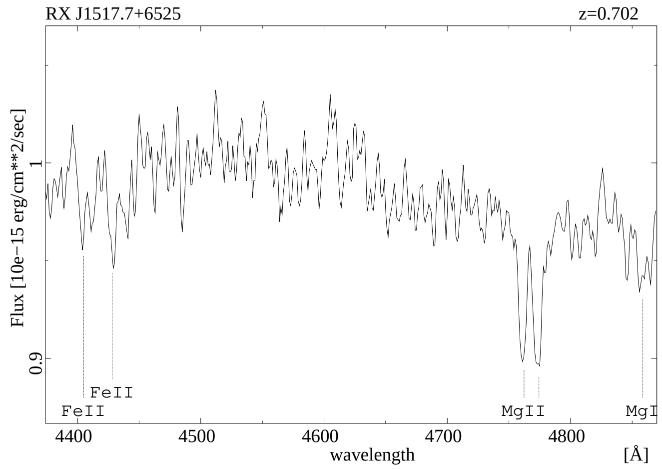

Figure 6.3: Detail of the February 1998 spectrum with the FeII and MgII doublets.

6.1.2 Mass of 1517+656

Scarpa et al. (1999b) report the discovery of three arclike structures around 1517+656 in their HST snapshot survey of BL Lac objects. The radius of this possible fragmented Einstein ring is 2.4 arc-sec. If this feature indeed represents an Einstein ring, the mass of the host galaxy of 1517+656 can easily be estimated. As the redshift of these background objects is not known, we can only derive a lower limit for the mass of the lens.

For a spherically symmetric mass distribution (with θ being the radius of the Einstein ring, $D_{\rm d}$ the angular size distance from the observer to the lens, $D_{\rm s}$ from observer to the source, and $D_{\rm ds}$ the distance from the lens to the source) we get (cf. Schneider et al. 1993):

$$M = \theta^2 \frac{D_{\rm d}\, D_{\rm s}}{D_{\rm ds}} \frac{c^2}{4G} \tag{6.1}$$

Thus the lower limit for the mass inside the Einstein ring is $M = 1.5 \cdot 10^{12}\, M_{\odot}$ for Einstein-de Sitter cosmology and $H_0 = 50\,{\rm km\,sec^{-1}\,Mpc^{-1}}$. For other realistic world models (also including a positive cosmological constant), this limit is even higher.

Assuming an isothermal sphere for the lens, the velocity dispersion in the rest frame can be calculated by

$$\sigma_v^2 = \frac{\theta}{4\pi} \frac{D_{\rm s}}{D_{\rm ds}} c^2 \tag{6.2}$$

Independent of H_0 we get a value of at least $330\,{\rm km\,sec^{-1}}$ for Einstein-de Sitter cosmology, and slightly less ($320\,{\rm km\,sec^{-1}}$) for a flat low-density universe ($\Omega_{\rm M} = 0.3$, $\Omega_\Lambda = 0.7$). Other models again lead to even higher values. The true values of the mass and velocity dispersion might be much higher if the redshift of the source is significantly below $z \approx 2$. Figures 6.4 and 6.5 show the mass and velocity dispersion as a function of the source redshift.

If the observed absorption is caused by a foreground object and the redshift of 1517 is higher than 0.7, the mass and velocity dispersion of the host galaxy have to be even higher.

More detailed modeling of this system will be possible when the redshift of the background object is measured. If the arcs are caused by galaxies at different redshift, the mass distribution in the outer parts of the host galaxy of 1517+656 can be determined which will provide very important data for the understanding of galaxy halos. High resolution and high S/N direct images may allow to use more realistic models than symmetrical mass distributions by providing further constraints.

6.1.3 Classification of 1517+656

The BL Lac 1517+656 with $M_R \leq -27.2$ mag and $M_B \leq -26.4$ is the most luminous BL Lac object in the optical band. Padovani & Giommi (1995b) presented in their catalogue of 233 known BL Lacertae objects an even brighter candidate than 1ES 1517+656: PKS 0215+015 (redshift $z = 1.715$, $V = 15.4$ mag, Véron-Cetty & Veron 1993). This radio source has been identified by Bolton & Wall (1969) as an 18.5 mag QSO. The object has been mainly in a bright phase starting from 1978, and became faint again since mid-1983 (Blades et al. 1985). Its brightness is now $V = 18.8$ mag ($M_V = -26.2$ mag; Kirhakos et al. 1994, Véron-Cetty & Veron 1998).
Also the X-ray properties of 1517+656 are extreme: with an X-ray flux of $f_{\rm X}(0.07 - 2.4\ {\rm keV}) = 2.89 \cdot 10^{-11}\ {\rm erg\ cm^{-2}\ sec^{-1}}$ in the ROSAT PSPC band we have a luminosity of $L_X = 7.9 \cdot 10^{46}\ {\rm erg\ sec^{-1}}$ which is a monochromatic luminosity at 2 keV of $L_X = 4.6 \cdot 10^{21}\ {\rm W\ Hz^{-1}}$. The radio flux of 37.7mJy at 1.4 GHz leads to $L_R = 1.02 \cdot 10^{26}\ {\rm W\ Hz^{-1}}$. Thus 1517+656 is up to now one of the most luminous known BL Lac in X-rays, radio and optical band, also compared to newest results from HST observations (Falomo et al. 1999). They give detailed analysis for more than 50 BL Lac objects with redshift $z < 0.5$, showing none of them having an absolute magnitude $M_R < -26$. Compared to the 22 BL Lac in the complete EMSS sample (Morris et al. 1991), 1517+656 is even more luminous in the radio, optical and X-ray band than all of those high frequency peaked BL Lac objects (HBL). Finding an HBL, like 1517+656 with $\nu_{\rm peak} = 4.0 \cdot 10^{16}$ Hz (Wolter et al. 1998), of such brightness is even more surprising, because the HBL are usually thought to be less luminous than the low frequency peaked ones (e.g. Fossati et al. 1998, Perlman & Stocke 1993, Januzzi et al. 1994). In comparison to the SED for different types of Blazars, as shown in Fossati et al. (1998), 1517+656 shows a remarkable behavior. The radio-properties are similar to an HBL ($\log(\nu L_{4.85\ {\rm GHz}}) = 42.7$), in the V-Band ($\log(\nu L_{5500\ \AA}) = 46.1$) and in the X-rays ($\log(\nu L_{1\ {\rm keV}}) = 46.4$) between bright LBL and faint FSRQ objects.

On the other hand it is not surprising to find one of the most luminous BL Lac objects in a very massive galaxy with $M > 2 \cdot 10^{12} M_{\odot}$. This mass is a lower limit, as long as the redshift of 1517+656 could be larger than $z = 0.702$, and is depending on the cosmological model and on the redshift of the lensed object (see Fig. 6.4).

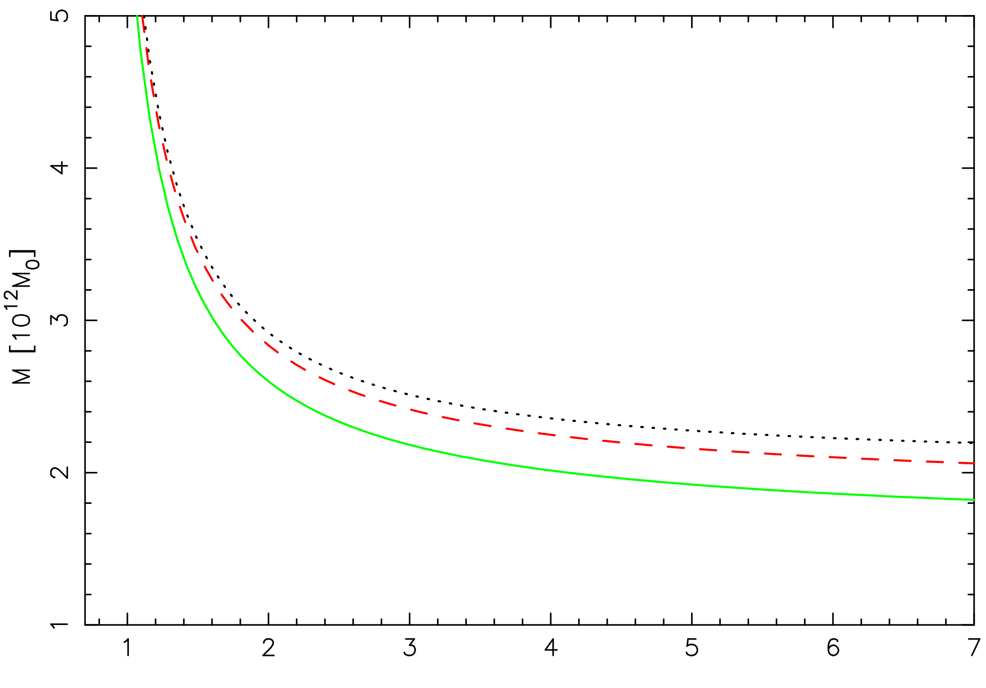

Figure 6.4: Mass of the host galaxy of 1517+656 for different redshift of the background source. The dotted line is for a low-density universe without cosmological constant ($\Omega_{\rm M} = 0.3$, $\Omega_\Lambda = 0$), the dashed one for a flat low-density universe ($\Omega_{\rm M} = 0.3$, $\Omega_\Lambda = 0.7$), and the solid for Einstein-de Sitter cosmology ($\Omega_{\rm M} = 1$, $\Omega_\Lambda = 0$). We assumed $H_0 = 50\,{\rm km\,sec^{-1}\,Mpc^{-1}}$.

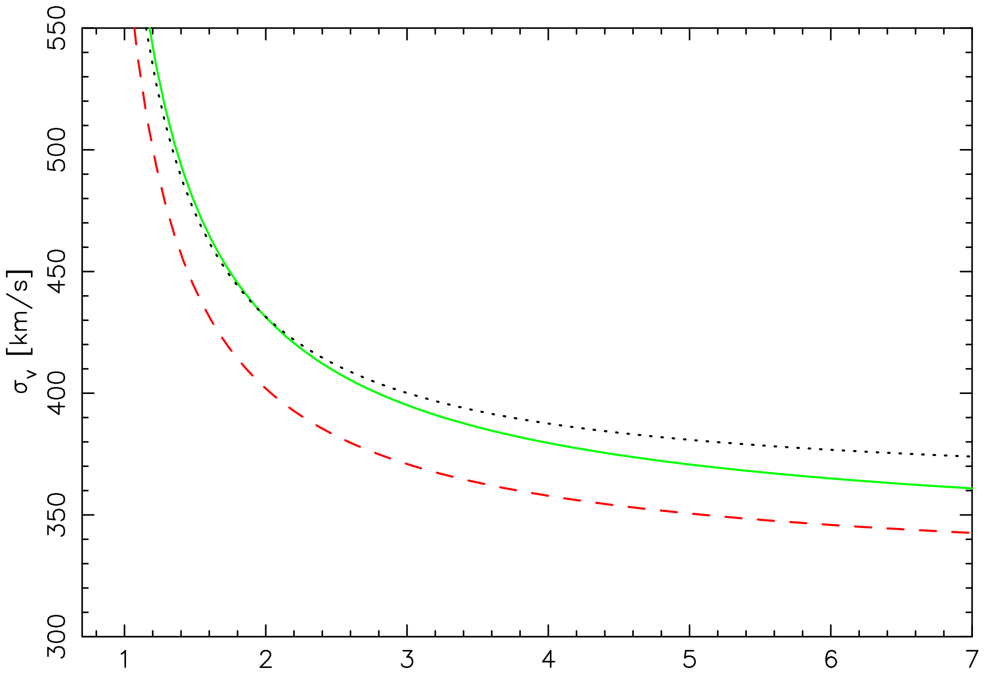

Figure 6.5: Velocity dispersion of the host galaxy of 1517+656 for the same cosmological models as in Fig. 6.4.

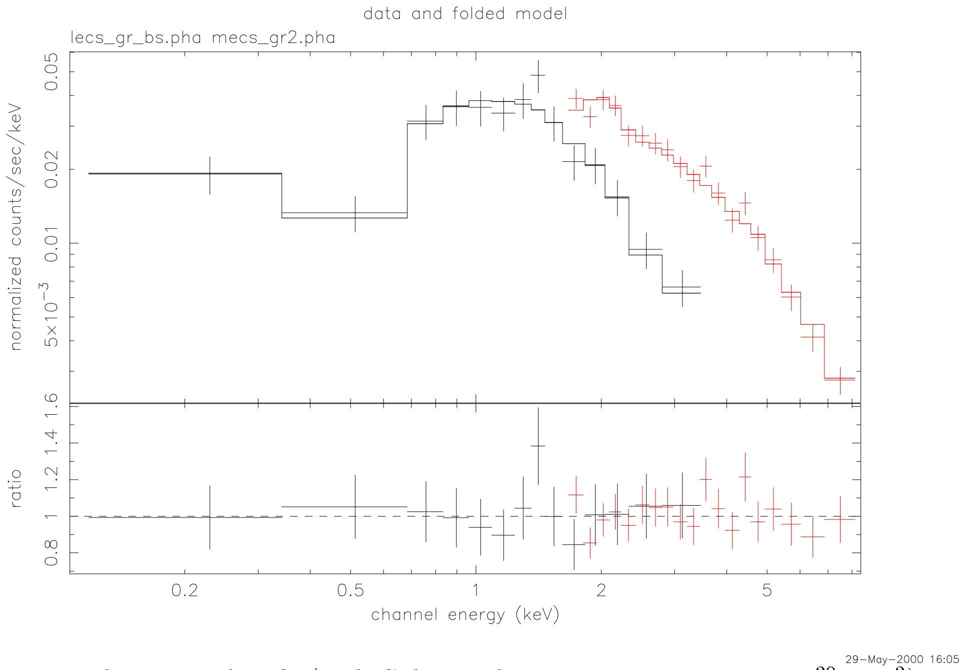

Figure 6.6: Broken power law fit (with Galactic absorption $N_{H,gal} = 1.31 \cdot 10^{20}$ cm^{-2}) to the *Beppo*SAX spectrum of 1ES 0927+500. Spectral indices are $\Gamma_1 = 1.4$ and $\Gamma_2 = 2.2$ with a break energy of 1.4 keV.

6.2 1ES 0927+500 - First detection of a X-ray line in BL Lac?

The object 1ES 0927+500 is an X-ray selected BL Lac object, which was first detected in X-rays during the Einstein Slew Survey (Perlman et al. 1996). Optical spectroscopy determined the nature and redshift (z=0.188) of this object (Nass et al. 1996). 1ES 0927+500 was detected in the ROSAT All Sky Survey with a flux of $1.81 \cdot 10^{-11}$ erg cm^{-2}sec^{-1} in the hard (0.5 – 2.0 keV) PSPC energy band (Voges et al. 1999). It was also included in three pointed ROSAT-PSPC observation and was the target of one HRI observation. From ROSAT archive data we computed fluxes varying between $2.4 \cdot 10^{-12}$ erg cm^{-2}sec^{-1} (October 1995) and $13.3 \cdot 10^{-12}$ erg cm^{-2}sec^{-1} (November 1996), while the spectral index was quite stable ($\Gamma \simeq 2.4$). In the ROSAT HRI image, with a resolution of 5", 1ES 0927+500 had a FWHM of $\sim$ 6", meaning that no significant extension was detected. In November 1998 a spectrum was taken with the *Beppo*SAX satellite during one of our programs. The exposure time was 8573 / 22711 sec in the LECS/MECS energy band, and the flux (0.5 – 2.0 keV) is now $3.2 \cdot 10^{-12}$erg cm^{-2}sec^{-1}.

A good representation of the *Beppo*SAX spectrum is given by a broken power law fit (Fig. 6.6). For all models the spectrum shows a significant enhancement within the LECS (Parmar et al. 1997) in the 1.3 – 1.5 keV energy range. Fitting a Gaussian line to the spectrum gives a central energy for this line of $E = 1.4 \pm 0.1$ keV and a line width of $FWHM \simeq 200$ eV (comparable to the energy resolution of the LECS at this energy); since the redshift of the BL Lac object is $z = 0.188$, the rest frame energy is ~ 1.7 keV (Fig. 6.7, left panel). The ROSAT-PSPC data do not allow to detect the line, but some enhancement in the energy region might be possible (see right panel of Fig. 6.7). An F-test gives a 99.9% probability that the fit with the Gaussian line is better than the fit without a line. On the other hand, it is not possible to fit a reasonable Raymond-Smith model to our data, and we also tested for the superposition of hot gas over the power law slope expected from the BL Lac nucleus, but no combination of a power law or broken power law with a Raymond-Smith model gives a good fit to the *Beppo*SAX spectrum. Also different extraction radii, binning values, and background aperture where used to check if the line could be due to instrumental or extraction effects. In all cases the line around 1.4 keV was clearly detectable. We also know that uncertainties in the LECS calibration is $\simeq 5\%$ in this energy range (Fossati & Haardt 1998).

A possible explanation for the line could be the silicon K_α line at 1.74 keV, though for a hot plasma one would then expect an even stronger line of aluminum at 1.49 keV (in our spectrum at ~ 1.25 keV), but there is no other line detectable. It is not plausible that the line comes from an X-ray bright galaxy cluster in the line of sight. In the HRI image no extension was detectable and the optical HST image showed an elliptical galaxy

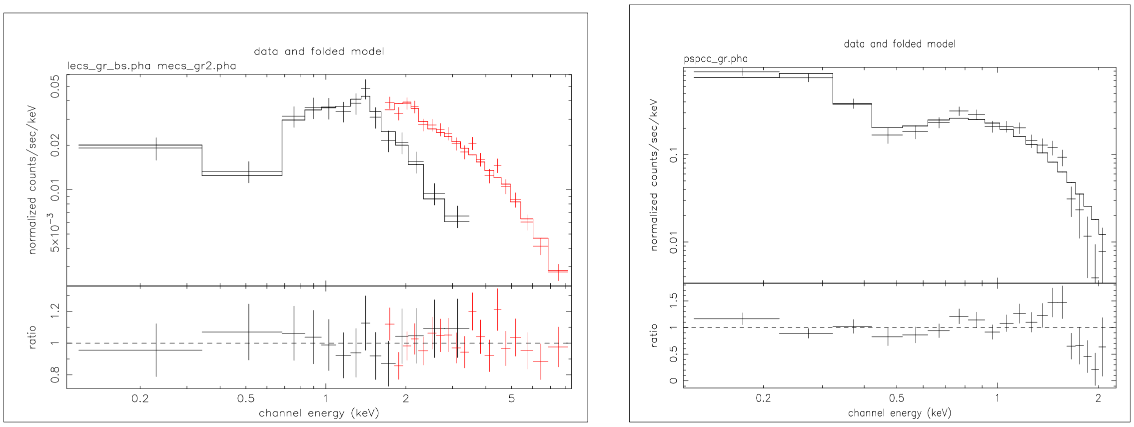

Figure 6.7: Left panel: Broken power law fit to the *Beppo*SAX spectrum with an additional Gaussian line at 1.4 keV. Right panel: Single power law fit to the longest ROSAT-PSCP exposure of 1ES 0927+500.

(effective radius of $r = 2.0 \pm 0.45$ arc-sec) as host galaxy; the ratio between core and galaxy flux is $\simeq 1$ (Scarpa et al. 2000). Also there is no other source within a circle of 10 arcmin radius, which could produce the strong X-ray emission. But if the line is produced somewhere in the line of sight, the most plausible origin would be aluminum. With a rest frame wavelength of $E_0 = 1.487$ keV this would correspond to a redshift of $z = 0.05$. If the line in our spectrum is iron $K\alpha$ the redshift would be $z \simeq 3.5$, but this would make 1ES 0927+500 as bright as $3 \cdot 10^{48}$ ergs in the 2 – 10 keV band.

Lines in the X-ray region have been detected also in other X-ray bright Blazars, such as a possible iron $K\alpha$ line in the spectrum of 0836+710 (Tavecchio et al. 2000) and in PKS 0528+134 (Reeves et al. 1997), but 1ES 0927+500 would be the first bona fide BL Lacertae object which shows emission lines in the X-ray band.

If the line is due to hot plasma, then also the aluminum line at $E = 1.8$ keV, and the iron $K\alpha$ line ($E_0 =$ 6.4 keV) at $E = 5.4$ keV should be detected depending on the actual temperature. The lines could be produced in the shock fronts of the jet coming towards us from the central engine of the BL Lac. But because the host galaxy seems to be as bright as the unresolved core, the detected line might also be produced in the elliptical galaxy, which hosts the BL Lac object.

To confirm the presence of this line a follow-up observation with Chandra or XMM-Newton would be necessary. For the assumed single power law the slope is well determined from 2.0 to ~ 10 keV. To the single power law the 1.4 keV line has been added, as fitted to the *Beppo*SAX spectrum. The simulated spectrum as expected from a Chandra exposure is shown in Fig. 6.8.

Unfortunately a proposal for a short Chandra exposure with ASIS-I has been rejected in August 2000 (see the basic comment from Impey (1988) on page 35).

6.3 RX J1054+3855 and RX J1153+3517

Two objects within the HRX-BL Lac sample exhibit strange properties. Both were found by correlating X-ray (ROSAT Bright Source Catalogue) with radio data (NVSS Catalogue). The basic properties are listed in Table 6.3. Both show similar fluxes in all observed bands. Near infrared data (taken from the *2MASS Second Incremental Release Point Source Catalog*) are only available for RX J1054+3855. Optical variability was measured between February 1998 and April 2000. Also nightly monitoring was done during a 7 night observation run on Calar Alto in April 2000. Both objects do not show significant variability (see Figure 6.9 for a lightcurve of RX J1054+3855). The optical spectra were taken in February 1998 with the Calar Alto 3.5m telescope and MOSCA. Wavelength calibration was done using a Helium-Argon-Neon lamp. The spectra have been bias subtracted and flat fielded, using skyflats taken with the same configuration as for the scientific exposure. Standard star HZ44 was used to do the flux calibration.

Both objects show only one prominent line at ~ 6650Å and 6610Å, respectively. Additionally in both spectra two breaks within in the continuum are visible. For RX J1054+3855 at 4850Åand 5480Å, in RX J1153+3617 at 4840Åand 5460Å(the difference is not significant while the wavelength of the break is difficult to measure).

RX J1153+3617 has been observed again in March 2000 with the Calar Alto 2.2m telescope using CAFOS. The results from two exposures (each 30 min) are shown in Figure 6.12 and 6.13. Though the conditions during

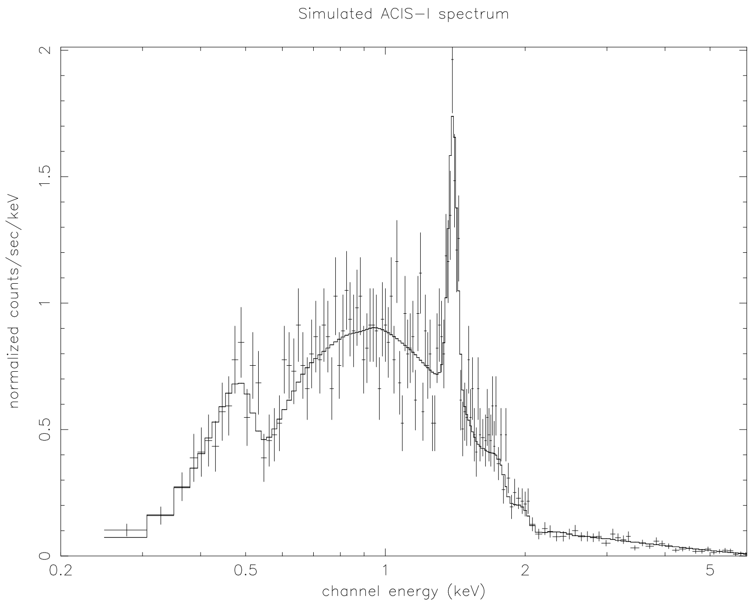

Figure 6.8: Simulated Chandra ACIS-I spectrum, 3 ksec, 6 arcmin off axis. Input parameters from the best model fit of the *Beppo*SAX spectrum.

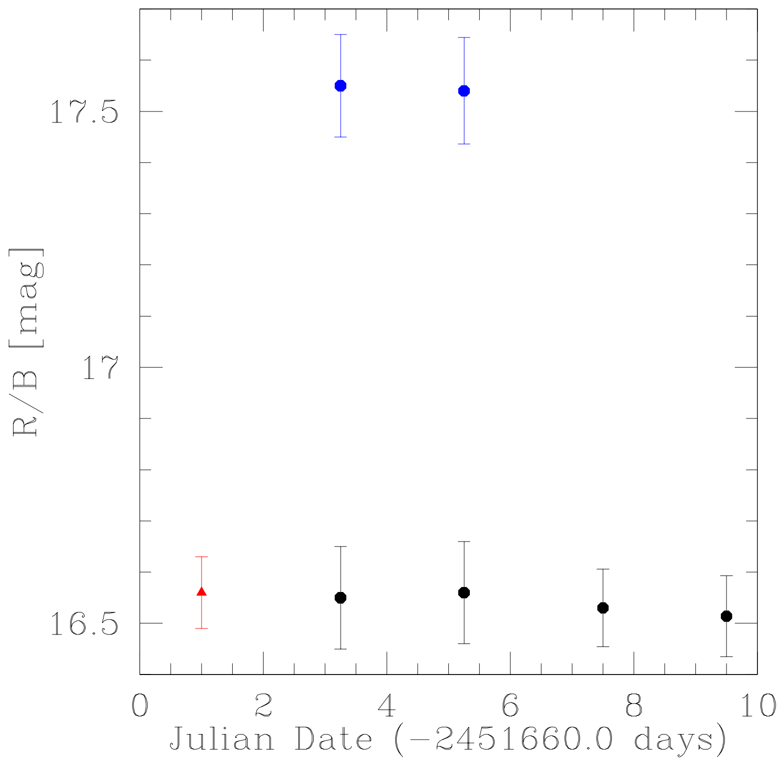

Figure 6.9: Lightcurve of RX J1054+3855. The two points on top refer to B magnitudes, points at the bottom to R band. The data for the triangle on the left was taken in February 1998 (Jul. Date 2450866.5).

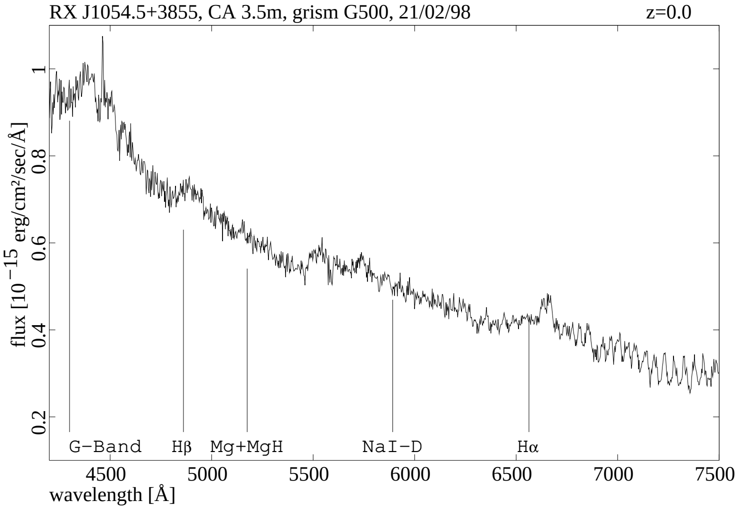

Figure 6.10: The spectrum of RX J1054+3855, observed in February 1998 at the Calar Alto 3.5m telescope (20 min exposure). The line is at $\sim$ 6650Å.

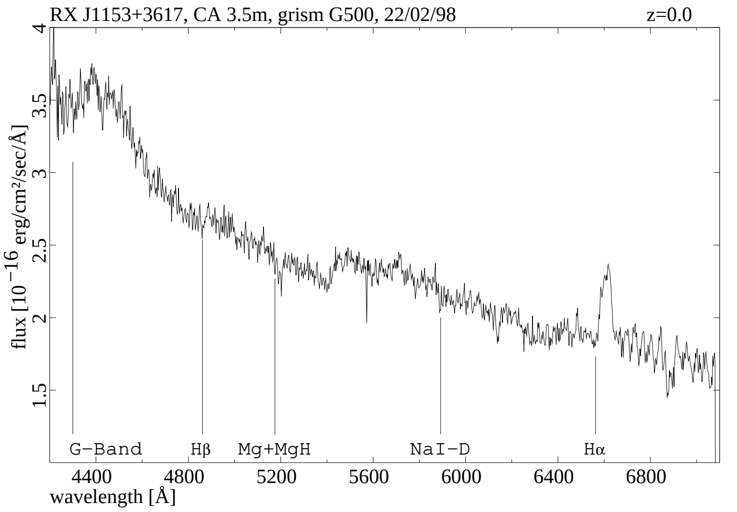

Figure 6.11: The spectrum of RX J1153+3617, observed in February 1998 at the Calar Alto 3.5m telescope (30 min exposure). The strong emission line is located at 6610Å

.

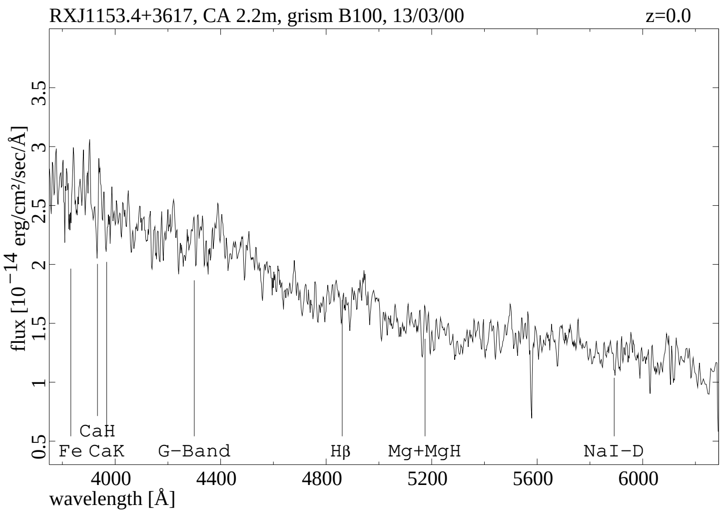

Figure 6.12: The spectrum of RX J1153+3617, observed in March 2000 at the Calar Alto 2.2m telescope. The breaks in the continuum are less significant.

Table 6.3: Properties of RX J1054+3855 and RX J1153+3617

Object	$hcps^a$	fx^b	fr^c	B-mag	J-mag	H-mag	K-mag
RX J1054	0.061	7.20	6.17	17.55	16.2	15.9	15.6
RX J1153	0.060	7.15	6.10	17.51	-	-	-

[a] ROSAT-PSPC "hard" $(0.5-2\ \mathrm{keV})$ countrate $[\mathrm{sec}^{-1}]$
[b] X-ray flux in $10^{-13}\,\mathrm{erg\,cm^{-2}\,sec^{-1}}$
[c] Radio flux at 1.4 GHz in mJy

the exposures are less good than for the February 1998 observation, the line and the break are still visible. The second break at ~ 4840Åis not clearly detectable. The redshift of both objects remains uncertain. If the redshift would be $z \simeq 0.35$, the line would be H_β and the break at 6610Å would refer to the calcium break. But then also MgII should be clearly detectable at ~ 3780 Å.

If the detected line would be MgII, the redshift of both objects would be $z \simeq 1.35$ and the properties in optical, radio, and X-rays would support the identification as a BL Lac objects. But in this case, both objects would lie far out of the common distributions of BL Lac objects, i.e. in a $\log L_X$ vs. α_{OX} diagram. On the other hand the spectrum is similar to this of HE 1258–0823, a quasar at redshift $z = 1.15$ with weak MgII and only marginally detected CIII line (Reimers, Köhler and Wisotzki 1996). Also the breaks in the continuum can be seen at the same rest frame wavelengths (see also HE 0950–0852). Nevertheless this would seems to be implausible. The whole NVSS/BSC correlation does include only one object at redshift $z > 0.9$, the blazar 0836+710 at $z = 2.172$ (see Table 11.1). Therefore, these two objects would exhibit exactly the same properties while being clearly separated ($\Delta Position \sim 5°$).

An intensive optical monitoring campaign is planned for spring 2001 with the Hamburg 1.2m Oskar Lühning telescope. If the objects are interacting binaries, they could show periodicity within their light curve on short timescales.

6.4 RX J1211+2242 and other possible UHBL within the HRX-BL Lac sample

Within the 95% confidence radius (53 arcmin) of the EGRET object 3EG J1212+2304 there is the HRX-BL Lac RX J1211+2242 at a distance of 24 arc-minutes to the gamma-ray source. This BL Lac could be the counterpart to the gamma-ray source. The redshift of this HBL is $z = 0.455$ as derived from absorption lines within the optical

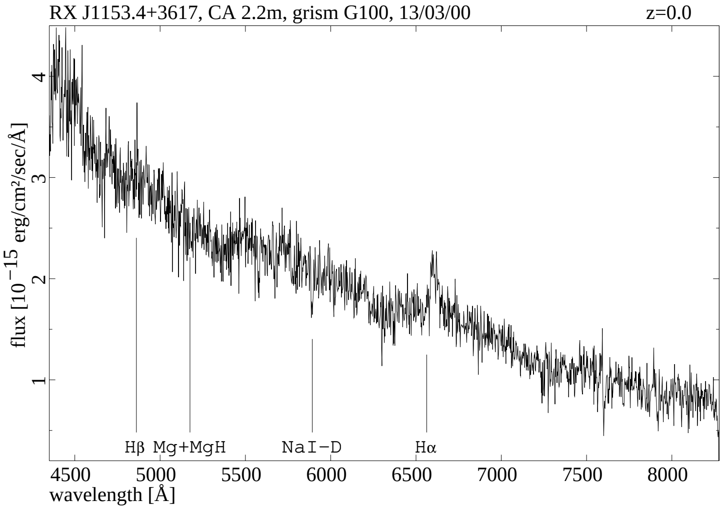

Figure 6.13: RX J1153+3617 observed with grism G100. The break at 5460 Å and the line at 6610 Å are still existing.

Table 6.4: Sources (except normal galaxies) within the 3EG J1212+23 error circle as derived from the NED

Name	α	δ	Distance [arcmin]	Type
3EG J1212+23	12 12 36	+23 04 48	0	Gamma-ray source
RX J1211+2242	12 11 59	+22 42 32	24	BL Lac object
ROSE 11	12 12 56	+22 35 19	30	Comp. Gal. Group
RX J1212+2232	12 12 06	+22 32 07	33	unidentified X-ray Source
Abell 1494	12 13 14	+23 56 19	52	Galaxy Cluster

spectrum (see Figure 6.16). Checking the NED I found 134 objects inside the 53 arcmin circle. Most of them (130) are normal galaxies which should not produce any detectable gamma-ray emission. Other identifications are listed in Table 6.4. From this list only the source RX J1212+2232, which is up to now unidentified, could be a possible gamma bright counterpart. The galaxy cluster and also the compact group could produce thermal X-ray emission up to a few keV but cannot be a relevant gamma-ray source. Figure 6.14 shows the spectral energy distribution for the three HRX-BL Lacs which are also EGRET sources (see Table 4.7 on page 39), and for the possible counterpart of 3EG J1212+2304. Only the data discussed here are included in this graphic. A more detailed SED for MRK 421 can be found in Maraschi et al. (1999), the SED of 0716+714 is described by Kubo et al. (1998). Compared to the spectral energy distribution of the other objects it is possible that RX J1211+2242 is the true counterpart of the gamma-ray source. The gamma-ray point seems to be the continuation of the SED from the radio to the X-ray region. It is worth noticing that the spectral slope in the X-rays is only based on RASS data and therefore might be wrong. The errors shown for the slope result from the fit to the hardness ratios only and might be significantly larger and even a flat X-ray spectral slope might be possible. In this case RX J1211+2242 could be one of the Ultra High Frequency Peaked BL Lacs (UHBL), which were first assumed to exist by Ghisellini (1999). This assumption is based on the work of Guilbert, Fabian & Rees (1983) who derived a limit on the maximum synchrotron frequency that can be reached by shock-accelerated electrons. They draw the conclusion that $\nu_{peak,max} \simeq 70$ MeV, independent on the applied magnetic field strength B. Finally Ghisellini suggests that ~ 1 MeV can be considered a limit for the observed maximum frequency in BL Lac objects. This value is certainly much lower than the frequency at which the EGRET observations have been made ($\sim$ 300 MeV). Nevertheless the restriction to this lower value by Ghisellini is based on the following formula:

$$\nu_{peak} = 0.36 \cdot \frac{R_{16}\Gamma_1}{\gamma_{min}^2 (L'_{s,42})^{3/2}} MeV \qquad (6.3)$$

Here R_{16} is the cross sectional radius of the jet (in units 10^{16} cm), Γ_1 the bulk Lorentz factor of the jet, and $L'_{s,42}$ is the synchrotron intrinsic power (in units $10^{42}\,\mathrm{erg\,sec^{-1}}$). This can result in peak frequencies as high as $\nu_{peak} \sim 10^{22}$ Hz, as has been demonstrated by Ghisellini 1998.

Two objects of this class, which have the peak of the synchrotron branch at frequencies $\nu_{peak} \geq 10^{19} Hz$, are claimed to have been found. The first one is 1ES 1426+428, a BL Lac which is also included in the HRX-BL Lac *complete sample*. This blazar peaks near or above 100 keV (Costamante et al. 2000). A second UHBL has been found by Giommi et al. (2000). This object is 1RXS J123511.1-14033 and is thought to be the X-ray counterpart of the EGRET gamma-ray source 2EG J1233-1407. The spectral energy distribution (Fig. 6.15) is very similar to that of RX J1211+2242. All information gathered together makes it possible that RX J1211+2242 is indeed the counterpart to the EGRET source 3EG J1212+2304. A follow-up observation at $\sim 10^{20}$ Hz could clarify, if the BL Lac has continuous slope between the ROSAT-PSPC and the EGRET data point, or if there is the gap between the synchrotron and the inverse Compton branch. Therefore an observation with the SPI spectrograph on-board the INTEGRAL satellite (Pace, Pawlak, & Winkler 1994; Winkler 1999) is planed.

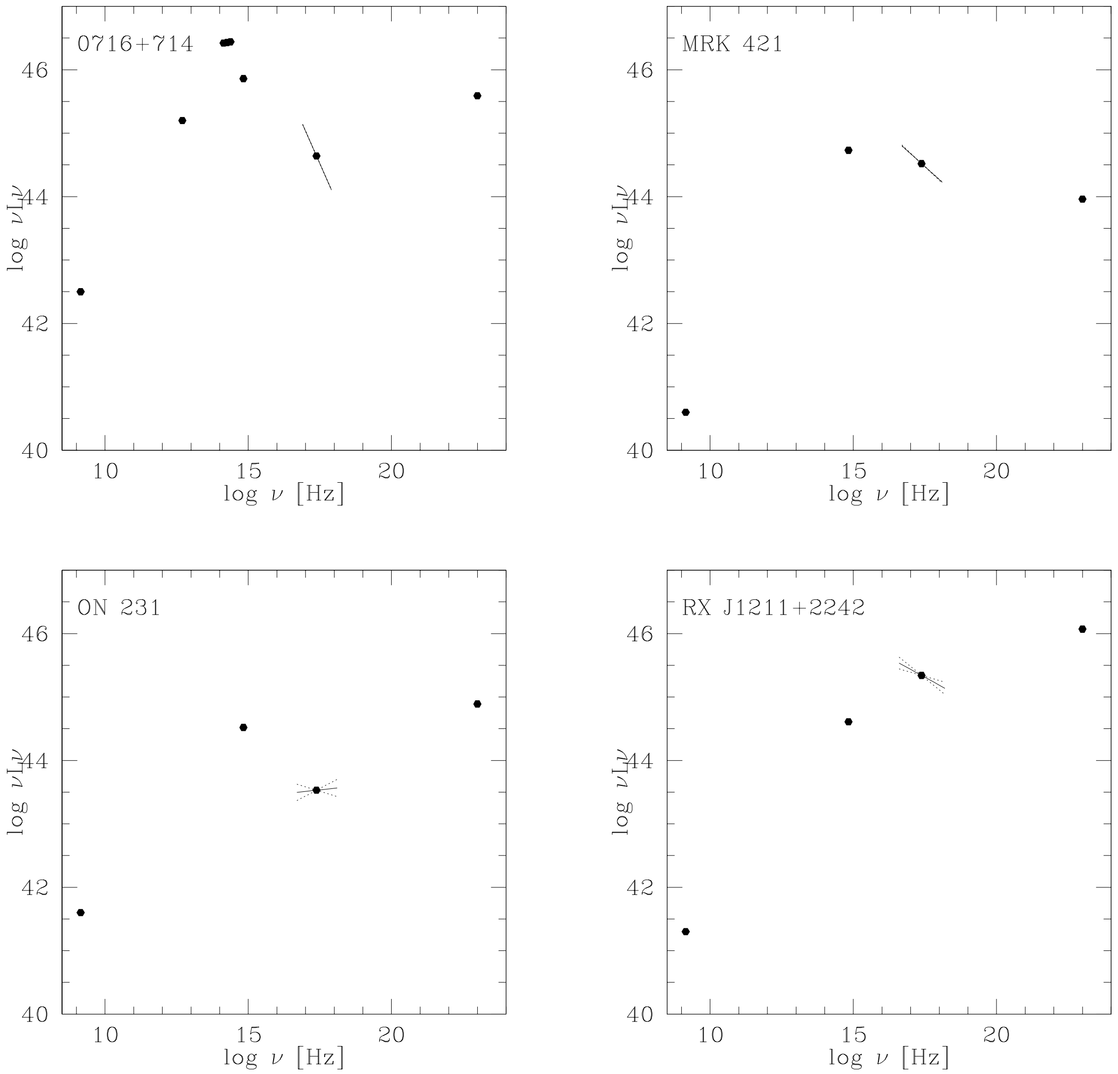

Figure 6.14: The three HRX-BL Lac with a counterpart in the EGRET Catalogue (RX J0721+7120, Mkn 421, ON 231) and RX J1211+2242, possible counterpart to 3EG J1212+2304. Only data points presented in this work have been included.

Besides RX J1211+2242 there are seven more objects within the HRX-BL Lac *complete sample* which show peak frequencies above 10^{19} Hz. These objects are also promising targets for INTEGRAL mission, although the

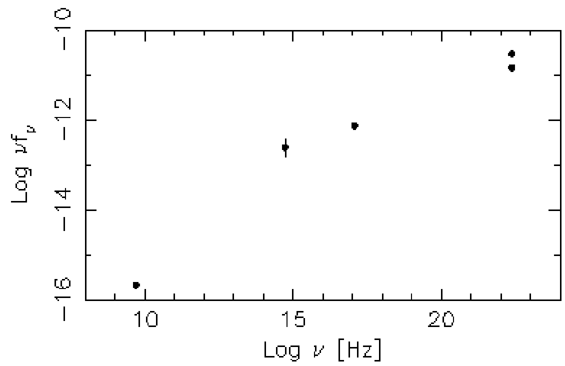

Figure 6.15: The spectral energy distribution of the UHBL 1RXS J123511.1-14033 (as presented by Giommi et al. 2000).

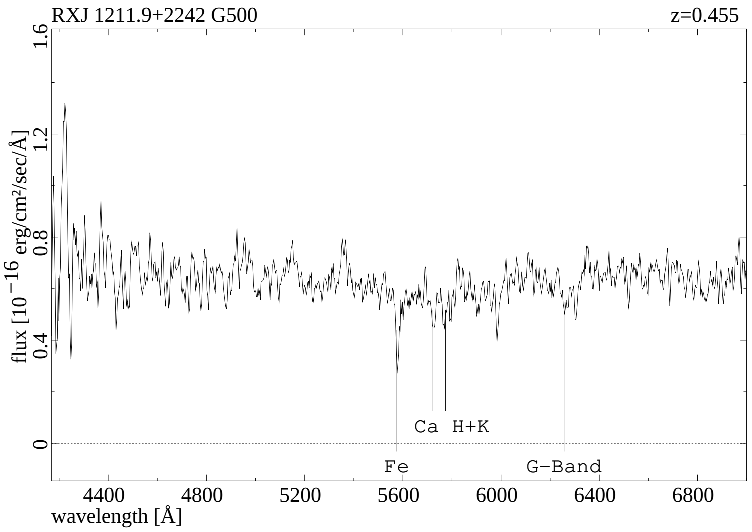

Figure 6.16: Optical spectrum of RX J1211+2242 taken with Calar Alto 3.5m / MOSCA.

expected fluxes in the gamma-ray region might be low. The spectral energy distribution for these objects is shown in Figure 6.17. Details to these objects can be found in Table 6.5. It is worth mentioning that the determined peak frequency is based on non-simultaneous data. Therefore it is possible that the peak frequency determined by the parabolic fit is wrong. Nevertheless the high frequency peaked objects are not expected to vary a lot. The spectral slope in the X-rays was determined from the PSPC pointed observations in the cases of RX J0928+7447 and RX J1008+4705. For the other objects the α_X results from the hardness ratios within the RASS. Although in these cases the errors on the photon index are large, the determined slope can give a hint to the real value.

Table 6.5: UHBL candidates within the HRX-BL Lac *complete sample*

Name	z	f_R[mJy]	B[mag]	f_X^a	α_X
RX J0710+5908	0.125	159	18.4	10.2	0.93
RX J0913+8133	0.639	4.9	20.7	2.3	0.65
RX J0928+7447	0.638	85.8	20.8	1.1	0.66[b]
RX J1008+4705	0.343	4.7	19.9	4.4	0.93[b]
RX J1111+3452	0.212	8.4	19.7	2.7	1.13
RX J1237+3020	0.700	5.6	20.0	3.2	0.94
RX J1458+4832	0.539	3.1	20.4	2.7	0.88

[a] PSPC flux $(0.5 - 2.0\,\mathrm{keV})$ in $[10^{-12}\mathrm{erg\,cm^{-2}\,sec^{-1}}]$
[b] PSPC spectral slope derived from pointed observation

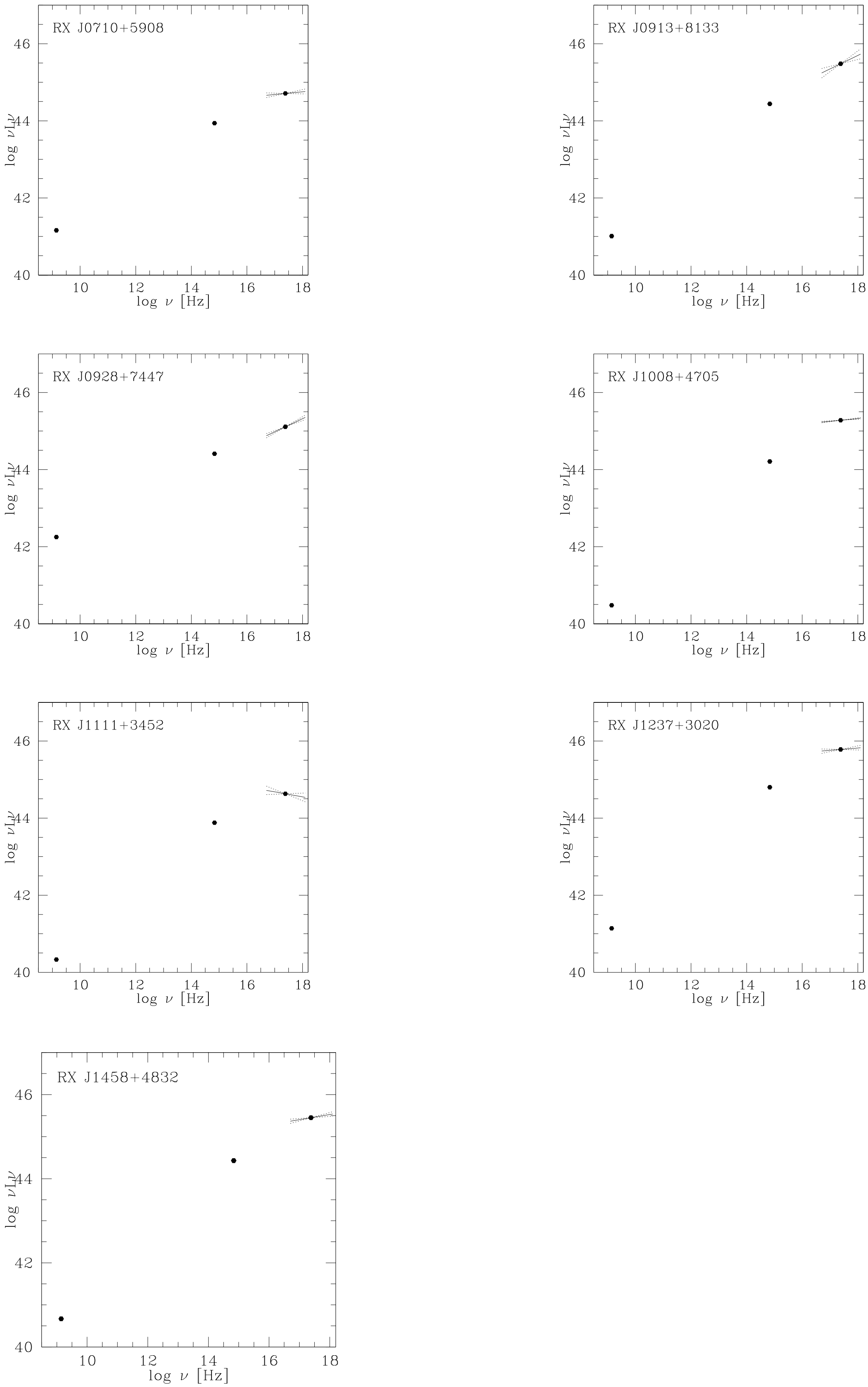

Figure 6.17: UHBL candidates within the HRX-BL Lac *complete sample*. Data points refer to 1.4 GHz, B-band, and 1 keV, respectively.

Chapter 7

A unified scenario for BL Lac objects

This chapter summarizes briefly the results from Chapter 5 and tries to explain the properties in a framework of a unified scheme for all types of BL Lacs .

7.1 Properties of HBL, IBL and LBL

The properties and correlations investigated and found within this work can be summarized as follows:

- The objects within the HRX-BL Lac sample exhibit properties between HBL and IBL type.
- A stronger calcium break is correlated with lower luminosity (see Figure 5.6).
- Objects with a calcium break 25% < $\mathrm{Ca_{break}}$ < 40% can be included into the BL Lac sample (page 42), when they exhibit BL Lac properties.
- No HRX-BL Lacs with moderate emission lines ($EW > 5$ Å) are found (page 45.)
- The spectral energy distribution can be well described by the peak frequency ν_{peak} (see page 50 ff.).
- The peak frequency is strongly correlated with the overall spectral index α_{OX} (see Figure 5.12).
- HBL show flatter X-ray spectra than IBL (see Figure 5.16).
- There is an excess of absorption (ΔN_H) when fitting a single-power law to the X-ray data (page 52).
- HBL show a lower ΔN_H than IBL. This is interpreted as stronger curvature in the IBL spectra (page 53).
- HBL show lower luminosities in the radio, near-infrared, and optical band, but higher luminosities in the X-ray region compared to IBL (Figure 5.17).
- HBL show the same total luminosity within the synchrotron branch as IBL (Figure 5.18).
- HRX-BL Lacs have a mean redshift of $\bar{z} = 0.31 \pm 0.20$ (page 60).
- HBL show a more negative evolution than IBL (Table 5.4).
- For radio dominated[1] HRX-BL Lacs the V_e/V_a is consistent with no evolution.
- The luminosity function of HRX-BL Lacs is consistent with the FR-I population (Section 5.8.4).

This list of properties can be evolved to the LBL objects. LBL show positive or no evolution (Morris et al. 1991), and for most of the properties listed above the term "IBL" can also be read as "LBL" (but for some facts, like difference in absorption and the smooth transition of evolution, this is not tested yet). A schematic representation of the results concerning the differences between HBL and LBL in general is shown in Figure 7.1 on page 101.

7.2 Comparison of the results with previous investigations

Several of the effects reported here have been revealed before by other authors, as already mentioned within the description of the HRX-BL Lac properties.

But the HRX-BL Lac survey offers the first possibility to study a large sample of objects of the HBL/IBL type with low flux limits in both the radio and the X-ray band. The correlation of the calcium break with luminosity in the various bands has been done before only for blazars in general in the radio band and for a smaller sample

[1] large α_{RO} and/or α_{RX}

(Landt & Padovani 1999). The effect that the break strength is related to the luminosity in all observed energy regions is reported here for the first time. The fact that objects which exhibit BL Lac properties but show a calcium break $25\% < \mathrm{Ca}_{\mathrm{break}} < 40\%$ can also be classified as BL Lac objects (Marchã et al. 1996), is supported by the correlation of break strength to luminosity within the HRX-BL Lac sample.

The fact that no HRX-BL Lac exhibits emission lines with equivalent widths $EW > 5$ Å leads to the assumption that this criterion still can be used when searching for BL Lac objects based on X-ray surveys with flux limits as high as the RASS-BSC. Nevertheless the existence of BL Lac objects with emission lines ($EW > 5$ Å), as expected by e.g. Marchã et al. 1996, is not ruled out for the LBL class.

The dependency of several properties on the spectral energy distribution (SED) has been reported by many authors before. The idea to describe the SED by the peak frequency of the synchrotron and the inverse Compton branch was proposed by Padovani & Giommi (1995a). The parabolic form of the synchrotron branch was used by many authors (e.g. Landau et al. 1986; Sambruna, Maraschi & Urry 1996; Comastri, Molendi & Ghisellini 1995a) to derive information about the total flux within this part of the SED. Comastri, Molendi & Ghisellini 1995a reported that the peak frequency is correlated with the spectral slope, while this work shows the HBL having flatter X-ray spectra than the IBL, which is also in better agreement with the SED having its maximum within the X-ray region in the case of HBL and at lower frequencies for LBL.

The relation between $\log \nu_{peak}$ and α_X was shown for *Beppo*SAX data of BL Lac objects by Wolter et al. (1998), but the HRX-BL Lac sample demonstrates the dependency of the peak frequency on the optical/X-ray overall spectral index α_{OX}. Also it has been shown here for the first time that the peak frequency for IBL ($\log \nu_{peak} < 18$) can be well determined only by α_{OX}.

Sambruna, Maraschi & Urry (1996) showed the dependency of the bolometric luminosity of blazars on the peak frequency, but the work presented here offers a larger insight to the transition of the HBL/IBL class on a large sample of objects. The continuous total luminosity in the synchrotron branch for HBL and IBL measured for the HRX-BL Lac sample is not in contradiction to an increasing bolometric luminosity with decreasing peak frequency. As has been shown by Fossati et al. 1998 and Ghisellini 1999 the ratio between the emitted radiation in the IC and synchrotron branch is related to the peak frequency in a sense that HBL show a small Compton dominance, while in LBL the Compton emission hosts the majority of the bolometric luminosity. Therefore one mean total luminosity of the synchrotron branch in the case of HBL and IBL refers to lower bolometric luminosity for HBL in comparison to IBL.

The dependency of the X-ray spectral slope on the peak frequency of the synchrotron branch was already discussed by e.g. Padovani & Giommi (1996) for ROSAT data and by Wolter et al. (1998) for X-ray data taken with the *Beppo*SAX satellite. It was also included in the α_X - α_{RO} relation revealed by Maraschi et al. (1995) for radio selected blazars.

In comparison to the EMSS sample of BL Lac objects this work extends the research on objects with lower α_{RO} and α_{OX} values and therefore to the radio quiet and stronger X-ray dominated objects. The HRX-BL Lac sample is of course the largest complete sample of X-ray selected BL Lac objects, also when compared with the RGB sample (Laurent-Muehleisen et al. 1999).

The investigations on the curvature of the X-ray spectra had been done before by using the $\alpha_{XOX} - \alpha_X$ relation (Sambruna et al. 1996). This relation applied to the HRX-BL Lac sample did not lead to such strong results. But the same effect (HBL having less curved spectra than LBL) can be derived when studying the additional absorption $\Delta N_H = N_{H,fit} - N_{H,gal}$ which was done within this work for the first time.

Also the correlation between X-ray luminosity with peak frequency being accompanied by an anti-correlation of radio, near-infrared, and optical luminosity with peak frequency was shown here for the first time in such a significant way.

Most of the results from Bade et al. (1998) for the HRX-BL Lac *core sample* are also valid for the HRX-BL Lac *complete sample* presented here. The most significant discrepancy seems to be the different results for the V_e/V_a test. While the no-evolution for the IBL objects is confirmed by my investigations, the evolution for the HBL is less negative than detected for the *core sample*. This might have two reasons: the most important one is the lack of redshift information for 12 IBL, while only for 3 HBL the redshifts are unknown within the *complete sample*. While the missing redshifts are expected to be high ($z \gtrsim 0.5$) the V_e/V_a should increase particularly for the IBL. Another reason for the differences between Bade et al. (1998) and this work could arise from the "patchy" area used for the *core sample*. In fact the survey area for the *core sample* was chosen in a way to include several prominent and up to then identified BL Lac objects. This might cause some selection effect in a way that objects with redshifts easier to determine are more likely to be enclosed in Bade et al. (1998). The candidate selection for the *complete sample* is done in a more homogeneous way.

The more negative evolution for the HBL in comparison to IBL/LBL has been noticed before by many authors, but here it was possible to detect the smooth transition of evolution while examining the SED of the different types BL Lac objects. The well determined luminosity function allows the direct comparison of the luminosity function at high and low cosmological distances.

7.3 Models for the BL Lac physics

As described e.g. by Ghisellini (1999) the jets of LBL (characterized by small values of ν_{peak}) have their synchrotron peak in the mm to far IR and their Compton maximum in the MeV band. The Compton component is stronger than the synchrotron one, and the contribution of photons produced externally to the jet to the scattering process is more important than the synchrotron one. On the other hand the HBL have spectra which peak in the keV and in the GeV-TeV band. The Compton emission is as powerful as the synchrotron one and the contribution of externally produced photons is negligible. Fossati (1999) and Ghisellini et al. (1998) interpret this as a consequence of different cooling efficiency within the jets. The jets of the LBL are more powerful and in some cases the external field is responsible for the cooling. The stronger cooling limits electrons energy implying that the synchrotron and inverse Compton emission peak at lower frequencies, in the optical and GeV bands, respectively, with a larger Compton dominance compared to the HBL. The HBL are sources with the lowest intrinsic power and the weakest external radiation field, which results in no or weak emission lines. The cooling in this class of objects is less dramatic and electrons can therefore reach energies high enough to produce X-ray synchrotron emission and TeV radiation. Being the inverse Compton cooling ineffective, the Compton dominance is expected to be small. This picture can even be extended for the whole blazar class: BL Lacs in total show lower power and beaming factors than the Flat Spectrum Radio Quasars (FSRQs), as revealed by e.g. Madau et al. (1987), Padovani (1992), Ghisellini et al. (1993), Hartman (1999).

This model explains the different types of BL Lac objects only by different global intrinsic power (Maraschi & Rovetti 1994), and not by a different viewing angle. Nevertheless different orientation is not excluded within this model, because it could explain the large scatter of observed quantities. Of course this cannot explain the different evolution, which is negative for HBL and slightly positive for LBL.

An extension of this model was given by Georganopoulos & Marscher (1998, 1999). They assume a combination of different intrinsic power and orientation to explain the observed quantities of the BL Lac types. They argued that an increase of the viewing angle is shifting the type of an object from the RBL to the XBL class but that this shift is not enough to explain the range of physical parameters observed in BL Lac objects. They propose that a combination of viewing angle and electron kinetic luminosity of the jet determine the observed characteristics of a BL Lac object. They proposed a smooth transition of LBL to HBL and predicted the existence of IBL with an evolution near to the no-evolution value $V_e/V_a \simeq 0.5$. Such objects have been found within the HRX-BL Lac sample.

The HRX-BL Lac sample contributes to these models with a large and complete sample of X-ray selected BL Lac objects. While previous studies (e.g. Fossati et al. 1998) used a compilation of different BL Lac surveys, like the EMSS, 1Jy sample, and FSRQ derived from the 2Jy radio sample of Wall & Peacock (1985), the HRX-BL Lac survey is homogeneous with the same selection criteria for all objects included in the *complete sample.* While it covers only a small fraction of the different "flavours" of BL Lacs, the same trends are found and draw a continuous picture of the BL Lac subclasses.

7.4 Results from the HRX-BL Lac sample in a unified scenario

How can these properties be explained in a unified model of BL Lac objects, including the different evolutionary behavior of LBL and HBL as well as the smoothly transition of physical parameters when moving from one object type to the other as shown for the IBL within the HRX-BL Lac sample? The existence of transition objects and the majority of similar properties between LBL and HBL make it plausible that both classes belong to the same parent population. Different luminosities throughout the spectral energy distribution can be explained by the higher peak frequency in HBL compared to the LBL. Also observed spectral parameters, i.e. curvature and spectral slope, fit into this model smoothly.

A solution to this problem would be a transformation of LBL to HBL as the BL Lac objects grow older. In this model, BL Lac objects start with high energetic jets with high energy densities and low cutoff frequencies. This results in steep X-ray spectra with strong curvature. The core would outshine the host galaxy which would result in a low calcium break value.

When by the time the source of the jet gets less powerful the energy density within the jet decreases and also the magnetic field energy densities decrease (Tavecchio, Maraschi & Ghisellini 1998). This results in higher cutoff frequencies. Therefore the X-ray spectra are flatter and less curved than in the LBL state. The bolometric luminosity of the BL Lac would decrease. But due to the higher peak frequency of the synchrotron branch the X-ray luminosity would increase. The core is less powerful in comparison to the host galaxy, thus the light of the host galaxy gets more and more dominant and the calcium break values increase to a value near to the value of non-active elliptical galaxies. This would also explain why we miss redshift information preferentially for the IBL within the HRX-BL Lac sample. Only three HBL suffer from missing redshift, whereas 12 IBL do ($\alpha_{OX} > 0.9$).

The observed anti-correlation between break strength and the luminosity in radio, near infrared, optical, and X-rays is in agreement to the results of Landt & Padovani (1999) who found an increase in radio core luminosity as the calcium break gets more and more diluted. Landt & Padovani argue that this is supporting their assumption that the only difference between BL Lac objects and their parent population is due to the orientation. Nevertheless this result can also originate from different luminosities of the non-thermal source, while the host galaxies seem to have approximately constant contribution to the emitted flux. The higher the luminosity of the central source, the more the BL Lac outshines the hosting galaxy. Also, a mixture of both scenarios is possible.

The possible transformation from LBL to HBL would result in a more positive evolution of LBL compared to HBL. At cosmological distances the LBL would dominate and in the local universe, when most of the LBL have jets with decreased energy density, the HBL would be more numerous.

An object which is not fitting into this scenario is doubtlessly the extremely bright HBL 1517+656. The scenario presented here assumes the HBL to be in average less luminous than the LBL. Apart from the exceptionally high X-ray luminosity, this object also shows an optical luminosity typical for a Flat Spectrum Radio Quasar (FSRQ). The high energy density in the jet should lead to a low frequency cut-off of the synchrotron branch. The fact that this is not seen in 1517+656 might be explained in a way that in this case the jet is orientated exactly along the line of sight. Therefore the Doppler enhancement could be larger than for BL Lacs in average.

7.5 The unified scenario in a cosmological context

A unified scenario, as described in the previous section, has to be confirmed by implementation into the cosmological context of the BL Lac objects. The type of evolution, which assumes that the LBL evolve to HBL by fading down the energy of the jet, is a kind of *passive evolution*. This means, the system of the AGN is thought to be undisturbed during this period by e.g. merger events.

The passive evolution of BL Lac objects is supported by other theoretical investigations on this topic. Cavaliere & Malquori (1999) argue that the lack of emission lines and the non-thermal continuum are supporting the assumption that accretion is low in BL Lacs, much lower than in quasars. Therefore the accretion disk of BL Lacs provides little gas and has a weak ionizing continuum. The main power source for the BL Lac emission is provided by the extraction in electromagnetic form of rotational energy that is stock-piled in the central black hole associated with the inner accretion disk (Blandford 1993). The luminosities are quite moderate: based on the assumption that the Doppler enhancement is of the order $\Gamma^{3\ldots4}$ (Sambruna, Maraschi, & Urry 1996) and on the fact that a Kerr black hole provides energies of $E \sim 5 \times 10^{61} M_8$erg, the expected lifetime of BL Lac objects should be long (several billion years). This is different to the expected life time of QSO flashes (0.1 Gyr, Cavaliere & Vittorini 1998). This led Ghisellini et al. (1998) to the conclusion that the kinetic component of the jets is unlikely to increase the power budget of BL Lacs beyond some 10^{45} erg. The long time scales which are needed to remove the energy of the Kerr hole imply slow or little evolution which results in a $V_e/V_a \simeq 0.5$. The expected life times are of the order $\tau \geq 8$ Gyr (Cavaliere & Malquori 1999). A substantial loss of angular momentum ($|\Delta j|/j \simeq 1$) seems to be possible only by interactions and merging events (Cavaliere & Vittorini 1998). These events would trigger gas inflow towards the nucleus for some 0.1 Gyr. QSO evolution since $z \simeq 3$ would then be governed by high accretion episodes driven by interactions (every $1 - 2$ Gyr). A last interaction would then leave the AGN with low accretion at $z \lesssim 1.5$ in a stable state, powered by a Kerr hole by the Blandford-Znajek process (Blandford & Znajek 1977). This object would then exhibit the BL Lac phenomenon (Cavaliere & Malquori 1999).

Can we link the phenomenon of passive evolution of BL Lac objects to the host galaxies of this type of active galactic nuclei? Most BL Lac objects are located in giant elliptical galaxies (see section 2.2.4). These elliptical galaxies could have been formed by major mergers[2] (Toomre & Toomre 1972). A major merger would transform nearly all of the gas in a way that most of the cold gas will be within the galaxy remnant in the core ($r < 0.5$ kpc). The hot gas ($T \simeq 10^4 K$) will form an "atmosphere" (Barnes 1999). The transformation time is thought to be quite short, i.e. for two spiral galaxies of the size of our Galaxy $\sim 4 \times 10^8$ years (Schweizer 2000). The scattering within the age of the elliptical galaxies formed by merging events seems to be large. The age varies between 2 and 12 billion years for elliptical galaxies in the field (Trager et al. 2000), and even older for ellipticals in clusters (de Carvalho & Djorgovski 1992). It seems that $z \simeq 2$ marks the maximum of the merging activity within the universe and therefore the starting time for the majority of elliptical galaxies (Schweizer 2000), and that afterwards the elliptical galaxies seem to stay stable (passive evolution). For cosmological distances up to $z \sim 2$ Abraham (1999) revealed a relation between redshift and merging in a way that the merging rate is proportional to $(z + 1)^{3\pm1}$.

[2]A merging process is called *major merger* when the masses of the interacting systems are similar. A *minor merger* is an event with a ratio of masses of the interacting galaxies of $m_1/m_2 = 0.1 - 0.5$, as is thought to be seen in the case of the dwarf Sagittarius galaxy which interacts with the Galaxy (Lin et al. 1995).

The passive evolution detected for the elliptical galaxies with an active BL Lac core is also found when studying the non-active elliptical galaxies. Passive evolution of elliptical galaxies is also found when studying the Fundamental Plane or the Kormendy relation, which describes the correlation between the mean effective surface brightness $\overline{\mu_e}$ and the effective radius of the elliptical galaxy R_e (e.g. van Dokkum & Franx 1996; Kelson et al. 1997; Bender et al. 1998; Ziegler et al. 1999). The detected change in brightness from high-redshift to nearby ellipticals is small and the star formation rate seems to be only slightly higher at $z > 1$. This effect is also seen while studying the relation between the line strength of $\mathrm{Mg_b}$ and the velocity dispersion σ of the ellipticals (Ziegler & Bender 1997). Here it can be seen that the metalicity of elliptical galaxies at cosmological distances is only slightly lower than in the nearby universe. This reveals a slow and undisturbed evolution of the star formation rate. The conclusion is that elliptical galaxies have been formed at $z > 2$ (or even higher) and that the star-formation within these objects evolves passively.

Additionally, the AGN phenomenon is thought to be linked to the star-formation of the host galaxy. The progenitor of AGN are thought to be star-burst galaxies (e.g. Maiolino et al. 2000, Blain et al. 1999).

The reason why BL Lac objects avoid clusters might be the same as for the lower star formation activity observed in clusters compared to field galaxies. Ziegler & Fricke (2000) revealed that the environment of even poor clusters seems to suppress the star-formation within the cluster galaxies. A similar effect might be visible for the BL Lac objects. The activity within the core might be disturbed by ram-pressure stripping within the host galaxy.

Another similarity between the star-formation processes and the AGN phenomenon is also found when studying the evolution. Franceschini et al. (1999) revealed recently that the evolution of luminous QSOs evolves like the star-formation rate of early type galaxies, while that of the total AGN population may evolve like the star-formation rate of all kinds of galaxies.

Taking all this information together reveals a picture in which giant elliptical galaxies have been formed at $z > 2$ by merging events of spiral galaxies. At the same time the star-burst activity of the ellipticals starts. AGN activity would be triggered by merging events for which the rate is highest at $z \sim 2$. The quasar phase can be followed by a BL Lac phenomenon after a last interaction (Cavaliere & Malquori 1999). This state of the AGN seems to be quite stable and evolves passively and slowly from LBL to HBL. Whenever BL Lac objects fall into a cluster of galaxies, the BL Lac core activity is suppressed by the intra-cluster medium.

7.6 Outlooks and predictions of the unified scenario

What could be the final state of the BL Lac objects? Sambruna, Maraschi, & Urry (1996) argued that objects with cutoff frequencies higher than 10^{18} Hz would be detected only in hard X-ray surveys but should be faint at lower frequencies, which would make their discovery difficult. Nevertheless 16 HBL within the HRX-BL Lac sample show peak frequencies $\nu_{peak} > 10^{18}$ Hz and seven objects even $\nu_{peak} > 10^{19}$ Hz. RX J1211+2242 might even be a UHBL with a peak frequency $\nu_{peak} > 10^{20}$ Hz (see section 6.4). To confirm the high peak frequencies, observations above the X-ray energy region are necessary. Investigations in the gamma region ($\sim 1\,\mathrm{MeV}$) are needed to decide whether these energies are dominated by the synchrotron emission or if already the inverse Compton branch is rising. The SPI spectrograph on-board the INTEGRAL mission (see e.g. Winkler 1999), which is planed to be launched in April 2001, will allow us to see this energy region ($20\,\mathrm{keV} - 8\,\mathrm{MeV}$) in a spectroscopically resolved way.

Another prediction of this scenario is the lack of BL Lac objects at redshifts $z \gg 2$. But before studying the sources at these high redshifts, one has to investigate the BL Lac population at redshifts $z > 1$. Only a very few sources are known, and it is necessary to clarify whether there are indeed HBL at redshifts $z \gtrsim 1.3$ (Padovani & Giommi 1995b). To find these extreme objects it is necessary to detect fainter sources. As seen in the $\alpha_{OX} - \alpha_{RO}$ plane of HRX-BL Lac objects the HBL can be radio quiet ($\alpha_{RO} < 0.2$). Surveys like the REX (Caccianiga et al. 1999) will miss these interesting objects as long as they apply a radio flux limit of $f_R > 5\,\mathrm{mJy}$. An approach could be the investigation of faint X-ray sources within the RASS, which have no optical counterpart on the POSS plates, and are even radio silent within e.g. the NVSS or the FIRST. These objects should have extreme low α_{OX} and α_{RO} values.

An example for these sources is RX J0323+0717, which is optically faint ($B > 21\,\mathrm{mag}$). This RASS source with an X-ray flux of $f_X(0.1 - 2.4\,\mathrm{keV}) \simeq 5.3 \times 10^{-12} \mathrm{erg\,cm^{-2}\,sec^{-1}}$ ($L_X = 1.8 \times 10^{46} \mathrm{erg/sec}$) was re-observed by myself during the February 1999 observation run at the Calar Alto 3.5m telescope. The optical spectrum is shown in Figure 7.2. There is only little doubt about the BL Lac nature of this object, because of its small α_{OX} and of apparently no emission lines within the optical spectrum. But it has to be noted that the redshift given here ($z \simeq 0.78$) is only tentative and needs to be confirmed by a spectrum with a higher signal-to-noise. The radio flux at 1.4 GHz given by the NVSS is only $f_R = 4\,\mathrm{mJy}$. Although the optical magnitude of the objects is not well determined, the X-ray dominance is very high ($\alpha_{OX} < 0.4$), while $\alpha_{RO} \simeq \alpha_{RX} \simeq 0.45$. Therefore the object is far from being radio quiet, but near to the flux limits of the radio catalogues NVSS and FIRST. Objects like this would not have been found neither within the RGB survey, nor by the DXRBS, due to their higher radio flux limits. Objects like this can be found by the REX survey, but the area of the pointed observations, used for the candidate selection of the REX, is significantly lower. RX J0323+0717, for example, would not have been found by the REX survey, just because it is not inside a ROSAT-PSPC pointing.

The investigation of sources like RX J0323+0717 might reveal the first generation of HBL at high redshifts. A similar approach should be done in the radio domain by examining faint radio sources. Of course this would be much more telescope-time consuming than the follow-up observations on faint X-ray sources without optical counterparts. A basis for this could be the *Hamburg/RASS Catalogue of optical identifications* (HRC, Bade et al. 1998b; see also Section 4.1). Within the identification procedure 105 X-ray sources ($\sim$ 2.7% of the investigated RASS-BSC sources) without a counterpart on the POSS plates were found. Therefore these sources have $\alpha_{OX} < 0.88$ (if the X-ray flux is at the limit of the BSC and the apparent magnitude is at the limit of the POSS plate). A higher X-ray flux limit will also reveal objects with lower α_{OX}. Identification of faint X-ray sources without optical counterparts will also reveal a number of galaxy clusters ($\sim$ 12%, Landt 1997). Nevertheless the fraction of BL Lac objects within these candidates should be large ($\gtrsim$ 10%, as found by complete identification of X-ray sources in the course of the HRX, but the fraction of stars will be lower for lower X-ray flux limit). The identification of the ROSAT All-Sky Survey sources without a counterpart in the known catalogues can also give an answer to the question, if there are really no radio silent BL Lac objects, as claimed by Stocke et al. (1990).

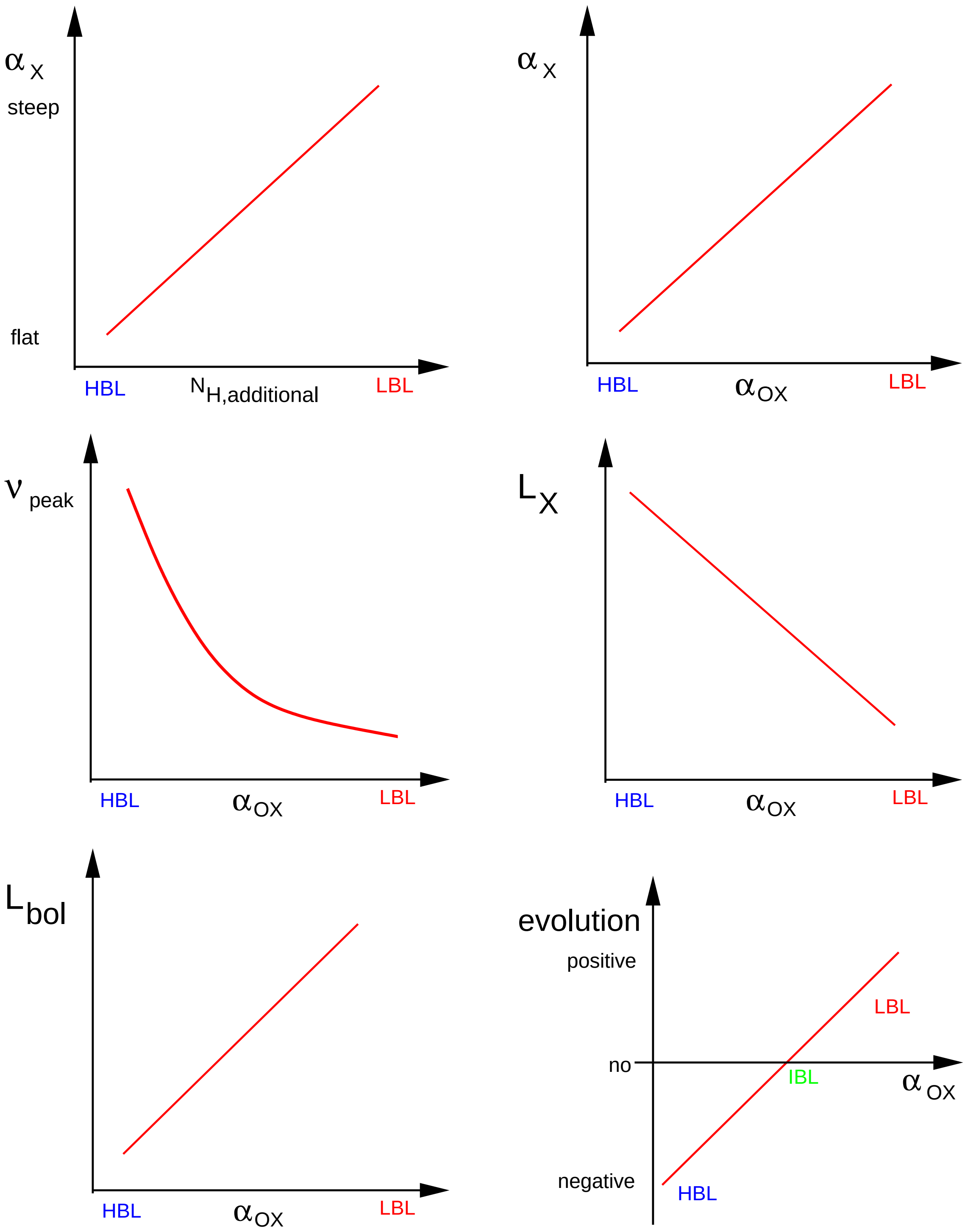

Figure 7.1: Schematic representation of the results concerning the differences between the high and low frequency cut-off objects.

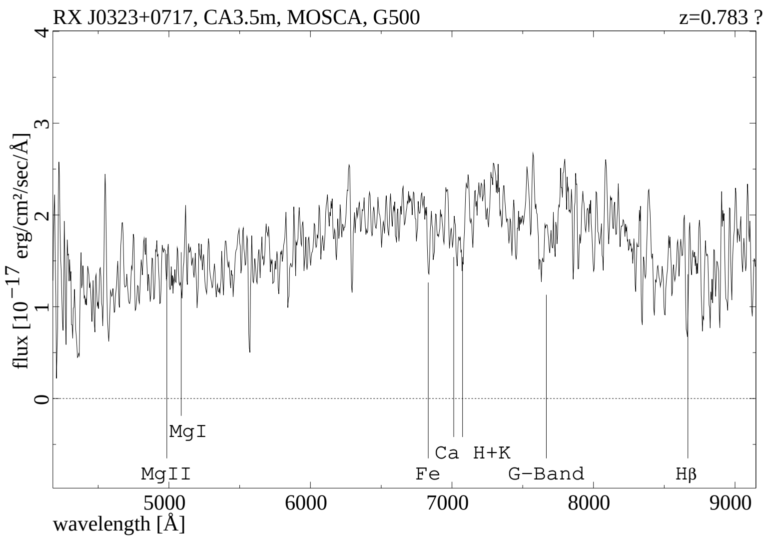

Figure 7.2: The X-ray dominated object RX J0323+0717, observed with MOSCA at the Calar Alto 3.5m telescope in February 1999. The redshift of $z \simeq 0.783$ is tentative.

Chapter 8

Local luminosity function of Seyfert II galaxies

In the second part of this work I will examine another class of AGN, the Seyfert II galaxies.

An important fraction of galaxies show narrow emission lines within their optical spectra. It has been noticed in the early eighties that at $M \sim -21$ mag about 1% of all field galaxies are Seyfert galaxies (Meurs & Wilson 1984). At higher absolute magnitudes, the fraction of Seyfert galaxies increases. For $M \sim -23$ nearly all galaxies have an active galactic nucleus. Seyfert I galaxies, the apparently most frequent type of AGN, have bright, semi-stellar nuclei, and optical spectra with broad emission lines covering a wide range of ionization (Khachikian & Weedman 1974). Seyfert galaxies with narrow emission lines are called Seyfert II galaxies. They are absolute more numerous compared to the Seyfert I objects, but more difficult to detect due to lower brightness and less strong emission lines. In Seyfert II objects the allowed and forbidden lines within the optical spectrum have comparable line widths of the order 500 km sec^{-1}. The basic idea to unify both types of Seyfert galaxies is that the broad line region in Seyfert II galaxies is hidden by a dusty torus. One can assume that Seyfert I and II galaxies only differ in their orientation to the line of sight i.e. that the torus in Seyfert I galaxies is existing but that we watch the accretion disk in these galaxies "face on". In this case the torus geometry of the Seyferts can be estimated by the number relation of Seyfert I compared to Seyfert II. The fraction of Seyfert II galaxies should then show directly the fraction of the AGN which is obscured by the dusty torus. The problem up to now was the lack of sufficiently complete samples of Seyfert II galaxies. Köhler et al. (1997) determined the local luminosity function of Seyfert I galaxies. The work presented here is focusing on the optically weaker but (absolutely) more numerous Seyfert II galaxies.

The basis for this work are the objective prism data from the Hamburg/ESO Survey (HES, Reimers 1990). The survey design and candidate selection method is described in Wisotzki et al. (1996). This survey was originally conceived as a twin of the Hamburg Quasar Survey (HQS, Hagen et al. 1995) which has been mentioned on page 27. The survey was designed to find bright ($12.5 \lesssim B \lesssim 17.5$ mag) QSO at high galactic latitudes ($|b| > 30°$) on the southern hemisphere over a total area of $\sim 5000\,\mathrm{deg}^2$. The objective prism plates were taken by ESO staff members at the ESO 1m Schmidt telescope, equipped with a prism of 4° opening angle, yielding a reciprocal dispersion of 450 Å/mm at H_γ. Therefore the spectral resolution of the HES is larger compared to the HQS, but for the same reason the HES suffers for a larger fraction of overlapping spectra. The seeing limited spectral resolution of objective prism spectra can be as high as 10 Å at H_γ. The HES plates cover a field of $25\,\mathrm{deg}^2$ in the sky. Each spectral plate is scanned in high resolution mode using the PDS 1010G microdensitometer at the Hamburger Sternwarte (Hagen 1987) with an aperture of $30 \times 30\mu$m and a step width of 20μm. This results in a resolution of 15 Å at H_γ. Spectra are extracted from these digitized data at positions determined from the direct plates of the *Digitized Sky Survey I* (DSS-I). For point-like sources the extraction is done by fitting a Gaussian profile to the central 2-3 pixels of the spectrum. This is done along the entire spectrum and the maximum of the fitted profile is taken as extraction value. Objects which appear extended on the direct plate are extracted in a similar way, but the width of the spectral profile is not fixed along the dispersion of the spectrum but fitted individually. Therefore more pixels are used taking into account the extended character of the source. Objects close to saturation on the photographic plate are extracted by integrating the fitted Gaussian curve at each pixel of the spectrum perpendicular to the dispersion. This yields in determined densities higher than the saturation limit of the spectral plate.

The extraction procedure results in one-dimensional spectra, each containing 300 pixels between the sensitivity cutoff of the photographic dispersion at 5300 Å and the atmospheric cutoff at the blue end at 3200 Å.

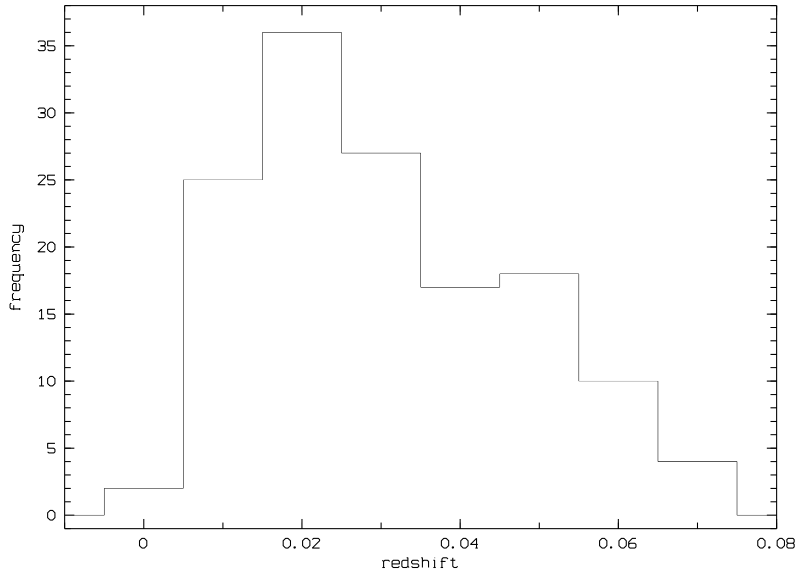

Figure 8.1: The redshift distribution of the Seyfert II sample derived from the Véron Catalogue.

The extracted spectra are automatically searched for emission lines by template matching techniques (Hewett et al. 1985), and pseudo-colors are determined referring to the special properties of the density spectra. This is done by defining several "half power points" which are bisecting points of a part of a spectrum (Wisotzki et al. 2000, Christlieb 2000). Thus the half power point x_hpp1 is the bisecting point in the wavelength range $3240 < \lambda < 4840$ Å (equivalent to $U - B$) and x_hpp2 refers to $3890 < \lambda < 5360$ Å ($B - V$).

Although first constructed to search for QSO which often exhibit a strong emission line within the density spectra of the HES, it was realized from the beginning that this data base can be used as well to search for various kinds of astronomical sources (Reimers 1990).

8.1 Candidate selection for the Seyfert II sample

The candidate selection for the Seyfert II sample was done by using the density spectra provided by the objective prism plates of the HES. Because of the huge number of spectra on each photographic plate, the candidate selection process was done in a semi-automatic way. In the first part of this process, the density spectra are examined automatically by using MIDAS procedures. In the second part the automatically selected candidates are checked and sorted into four categories depending on the probability that the candidate is a true Seyfert II galaxy.

To find rules to establish an automatic selection system, a sample of known Seyfert II galaxies was used. This sample was taken from the Véron catalogue (Véron-Cetty and Véron 1998). It includes 390 Seyfert II galaxies in the redshift range between $z = 0.001$ and $z = 0.07$. 139 of those Seyfert II have $\delta < 0°$ and $|b| > 30°$ and are therefore within the area of the HES. Figure 8.1 shows the redshift distribution of this subsample. These objects were used to define the properties of Seyfert II galaxies in the HES and to program an automatic filter to select Seyfert II candidates from density spectra. In principle the filter was based on line and color criteria.

The automatic search was done by two different methods: one group of candidates was selected by examining objects with detectable lines in the spectrum, and the other group by applying color criteria. The parameters of the automatic process were optimized to include all Seyfert II galaxies of the learning sample within the HES database. A drawback of this procedure is doubtlessly the fact that Seyfert II galaxies with other properties than that of the learning sample, for example extreme color, could be rejected by the optimized selection. For flux limitation the *spcmag* was used. This magnitude is derived from the density spectra by applying a Johnson-B filter to the objective prism data.

The selection criteria for objects with detectable lines are as follows:

- Spectrum does not include an overlap

- 13.0 mag < *spcmag* < 17.0 mag[1]
- Effective radius on the direct plate > 64 pixel
- No narrow lines in the range 4103 ... 4774 Å and 3639 ... 3773 Å. In this interval no narrow lines are expected
- No narrow lines blue-wards of 3346 Å
- No broad emission lines with 3960 Å < λ < 4902 Å
- No broad emission lines blue-wards of 3773 Å
- In addition I used a color criterion, to reject normal galaxies. For Seyfert II galaxy candidates the colors had to be in the range $1550 < xhpp1 < 2314$ and $650 < xhpp2 < 1150$
- Objects which showed calcium H and K lines, but were not "red enough", were rejected by the candidate selection.

The selection of Seyfert II candidates from objects without detectable emission lines was done by applying the following criteria:

- Spectrum does not include an overlap
- Effective radius on the direct plate > 120 pixel[2]
- 13.0 mag < *spcmag* < 17.0 mag
- Additionally a color selection was used which was optimized for the learning sample[3]

Seyfert II candidates found by this selection procedure were then checked for counterparts in the NASA/IPAC Extragalactic Database (NED)[4]. The information from the NED was used in the following way:

An object classified as a galaxy without redshift information was still taken as a Seyfert II candidate. Only objects with a secure classification and redshift were counted as "identified". If there were any doubts due to extreme density spectra, those objects were still included in the candidate procedure. The fraction of objects which could be clearly identified with the information from the literature and from the NED was ~ 30%, strongly depending on the field. Objects which had been classified as Seyfert II galaxies were included into the Seyfert II sample.

The reduced list of candidates was then checked one by one. A major fraction of the selected candidates were obvious stars: often the automatic line detection algorithm mis-identified the absorption doublet of calcium at 3933/3968 Å as an emission line. Furthermore, when possible, the redshift of the candidates was estimated using the detected lines. Candidates which clearly showed a redshift $z \gg 0.07$ were sorted out.

The remaining candidates were sorted interactively into categories of the likelihood of Seyfert II nature of the object. Chosen categories were:
1 – candidate with several clear Seyfert II characteristics, like strong [OII]3727 Å line, [NeV]3426 Å emission or [OIII]5007 Å line.
2 – candidate with one Seyfert II characteristic. At least one of the criteria of (1) should be fulfilled.
3 – candidate for which it is not impossible to be a Seyfert II galaxy.

Using this semi-automatic procedure, in total 67 ESO fields have been worked through. Of ~ 700,000 overlap free density spectra, the semi-automatic procedure selected ~ 1,700 candidates which were all cross checked with the NED. After the final selection, 393 candidates were left over, which are distributed into the different categories as follows:
candidate class 1: 21 objects
candidate class 2: 87 objects
candidate class 3: 285 objects

Figure 8.2 shows an example of a density spectrum of a Seyfert II candidate. This candidate has been selected due to line criteria from the point-like sources in the HES data base. The [OIII]5007 Å line is clearly visible on the red (left) end of the spectrum. The slit spectrum of this object is presented in Figure 8.4. For comparison Figure 8.3 shows a color selected candidate. No lines are detected within the density spectrum and the selection is based on color criteria only. Also this object turned out to be a Seyfert II galaxy with a weak active core within a relatively bright galaxy.

---

[1] Here 17 mag is the lower flux limit. The upper limit of 13 mag was chosen to reject bright stars, which are often mis-identified as galaxies because of there large apparent extension on the direct plates.

[2] The selection based on colors only is very difficult, therefore it was necessary to apply a more strict extension criterion than for the line-based sample

[3] exact criterion for Seyfert II color based selection: $1550 < x\_hpp1 < 2314$, $650 < x\_hpp2 < 1150$, and $1350 < xqd < 2382$

[4] The NED is operated by the Jet Propulsion Laboratory, California Institute of Technology, under contract with the National Aeronautics and Space Administration.

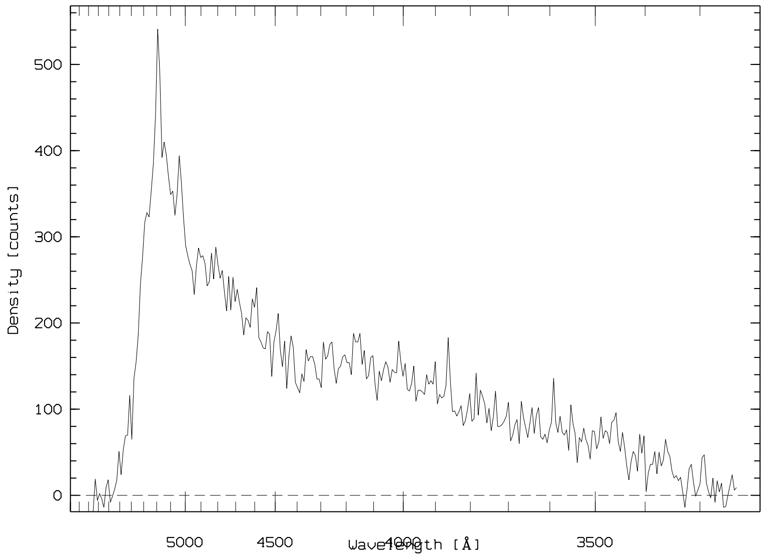

Figure 8.2: The density spectrum of HE 0201-3029. This candidate turned out to be a Seyfert II galaxy. Note that the blue end of the spectrum is on the left.

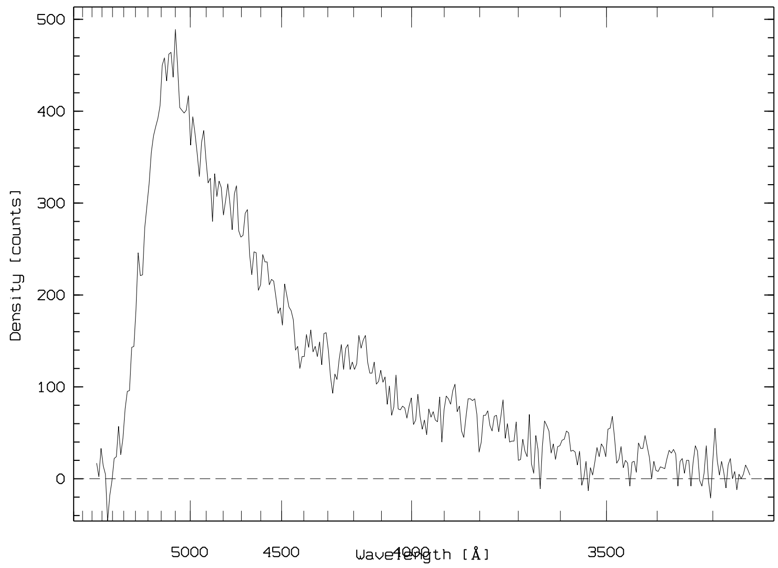

Figure 8.3: The density spectrum of HE 0411-4131, a color selected Seyfert II candidate.

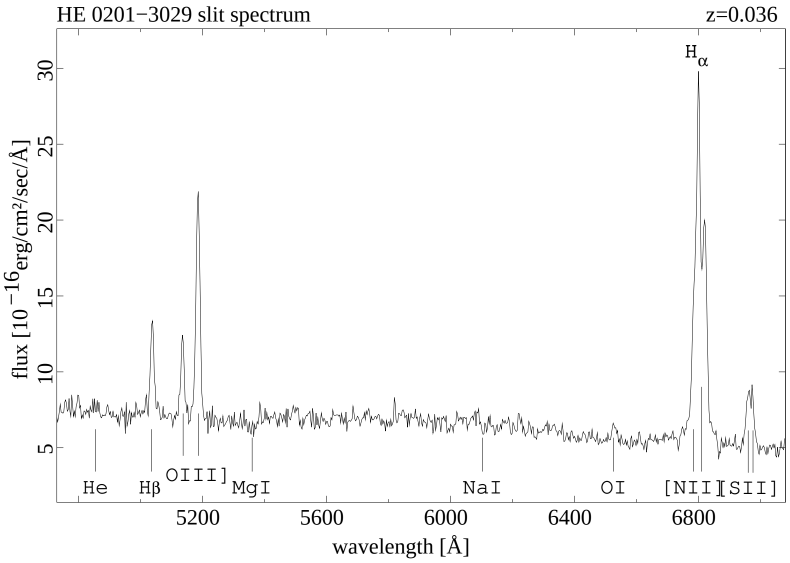

Figure 8.4: Slit spectrum of HE 0201-3029 taken with the Danish 1.54m telescope using DFOSC in December 1999. The slit spectrum reveals the Seyfert II properties of this object.

8.2 Follow-up spectroscopy of Seyfert II candidates

To determine the true object type of the candidates, follow up spectroscopy was necessary. Two observation runs were done at the Danish 1.54m telescope on La Silla, using the Danish Faint Object Spectrograph and Camera (DFOSC). The first one was in January 1999 with a total of 3 nights. Due to bad weather conditions, observations were only possible for 2 nights. Nevertheless, 58 candidates on 41 ESO fields covering $\sim 1000\,\mathrm{deg}^2$ were observed. The second run in December 1999 was again 3 nights long, but again bad weather conditions and technical problems reduced the effective observing time to 1.5 nights. It was possible to do spectroscopy on 33 objects, including re-observations of six objects from the January campaign with insufficient signal-to-noise spectra. In total 85 objects have been observed (80 objects of category one or two, five out of category three). The direct images are subtracted by a bias, determined using the overscan area of the CCD. After that the images have been corrected with combined flat fields which were taken on the bright evening and morning sky. The spectra have been bias subtracted and corrected with flat fields, which were taken with the same slit width and grism as the scientific exposures. The extraction of the spectra was done using the optical data reduction package developed by Hans Hagen at the Hamburger Sternwarte.

Figure 8.4 shows an example of a slit spectrum of a confirmed Seyfert II candidate. The density spectrum is shown in 8.2.

The redshift has been determined using the prominent lines within the spectral range ($\sim 3800 - 8000\,\text{Å}$). Finally a correction to the redshift has been applied due to the movement of the solar system within the Galaxy (Aaronson et al. 1982):

$$v = \sin l \cdot \cos b \cdot 300 \cdot \frac{\mathrm{km}}{\mathrm{sec}} \tag{8.1}$$

This effect changes the redshift of the objects by maximal $\Delta z \simeq \pm 0.001$. The resulting redshifts are therefore Galactocentric. The movement of the earth with respect to the barycentre of solar system was neglected, because this effect is ten times smaller than the movement of the solar system.

For the identification of Seyfert II galaxies and the separation of other AGN with narrow emission lines, the diagrams by Veilleux and Osterbrock (1987) have been used. Here the main criteria to distinguish are the line ratios of [OIII]5007 Å/H_β4861 Å, [NII]6583 Å/H_α6563 Å, [SII](6716 Å + 6731 Å)/H_α6563 Å, and [OI]6300 Å/H_α6563 Å. The detailed criteria can be found in Veilleux and Osterbrock (1987). The principle way is to look for ionization lines, like [OIII], [SII], and [NII] and compare them with the hydrogen Balmer-lines. Seyfert II exhibit higher ionization than Seyfert I, which is seen in a ratio of [OIII]5007 Å/H_β4861 Å ≥ 3 for Seyfert II galaxies (Shuder and Osterbrock 1981). This is of course also seen within the spectra of HII galaxies (French 1980), while LINERs exhibit [OIII]5007 Å/H_β4861 Å ≤ 3 (Keel 1983). HII galaxies can be distinguished from the Seyfert II galaxies by the weakness of low-ionization lines such as [NII], [SII], and [OI]. The [SII] and [OI] emission lines arise

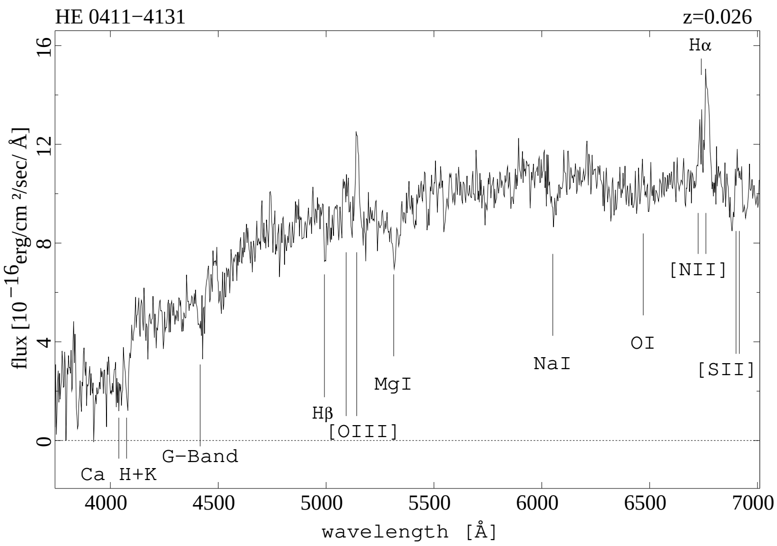

Figure 8.5: Slit spectrum of HE 0411-4131. The Seyfert II core is very weak ($V \simeq 17.2$ mag) compared to the host galaxy ($V \simeq 14.1$ mag).

preferentially in a zone of partly ionized hydrogen.

The measurement of the line fluxes was done by applying a Gaussian fit to the line. Often lines were blended (like H_α6562 Å and [NII]6548 Å). In these cases the single line fluxes have been estimated by using two Gaussian line fits in comparison with the total flux within the blend.

The whole Seyfert II sample finally comprises 22 Seyfert II galaxies with a secure identification. The spectra of 7 objects do not allow the distinction between Seyfert II and LINER/NELG.The list of Seyfert II and probable Seyfert II galaxies is shown in Table 11.5 within the appendix. A fraction of 24 candidates turned out to be LINER or NELG, 28 are normal galaxies, and 2 candidates are stars. For two objects the identification is uncertain up to now, but they are most probable galaxies without emission lines. The objects which are not Seyfert II galaxies are listed in Table 11.6 on page 142.

For the determination of the luminosity function it is necessary to have a complete identified sample of objects. No known Seyfert II galaxy was classified as a candidate class 3 object. None of the five objects of category 3 which have been re-observed turned out to be Seyfert II galaxies. Therefore, fields in which all objects up to candidate class 2 (with indication of Seyfert II property) have been observed are counted as *complete*. In this complete sample there are 16 secure Seyfert II galaxies and 22 Seyfert II if we include the probable candidates. Thus the fraction of Seyfert II galaxies compared to the number of candidates is $\sim 30\%$.

Another observation run is going to take place in December 2000. Within the two nights at the Danish 1.54m on La Silla it should be possible to complete the up to now incomplete identified fields and to determine the object type of the up to now uncertain identification. Additionally I am grateful to Dirk H. Lorenzen, who re-observed the seven candidates with up to now uncertain identification (Seyfert II or LINER/NELG) to clarify the object types. The reduced data will be available in early 2001.

8.3 Photometry of Seyfert II objects

To retrieve a luminosity function one needs beside the redshifts of the sample objects also their apparent brightnesses. This is also important to compute the examined survey volume. The magnitudes for the Seyfert II sample presented here have been derived in two independent ways whenever there were suitable data available. First I did absolute photometry at the Danish 1.54m telescope on La Silla. For absolute calibration of the CCD direct frames I used the spectrophotometric standards and known photometric standards. This method of absolute photometry is only possible under very good weather conditions ("photometric weather"). Most of the time during the observation runs, these conditions were not fulfilled. Especially during the second period of observation in December 1999 absolute photometry was not possible. Often only CCD magnitudes from exposures directly before or after the exposure of a standard star could be used.

The second method to derive magnitudes is based on the internal calibration of the photographic plates of the

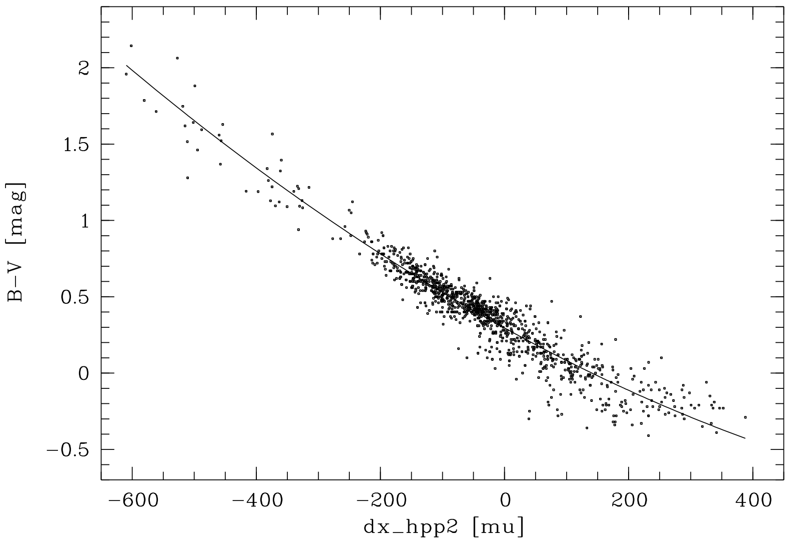

Figure 8.6: The $B-V$ color of objects versus the half power point dx_hpp2 determined for the objective prism plates of the HES. Graphic kindly provided by Norbert Christlieb.

Hamburg/ESO Survey. In this procedure standard stars with well determined magnitudes (like the GSPC stars; Lasker et al. 1988) have been used to get sequences of faint stars around them. This was done using the Dutch 90cm telescope on La Silla during several observation runs, and also partly with the Danish 1.54m telescope.

The derived magnitudes for Johnson-B filters have to be transformed to photographic magnitudes (B_J magnitudes) using the formula derived by Hewett et al. (1995):

$$B = B_J + 0.28 \cdot (B - V) \tag{8.2}$$

This equation is valid for objects with $(B-V)$ values between -0.1 and 1.6. The color $(B-V)$ can be derived from the objective prism spectra. Here dx_hpp2 is a good indicator for the color of an object. This has been studied for the spectral plates of the HES in detail by Christlieb (2000), who finds the following correlation:

$$B - V = 0.79 + 5.06 \cdot 10^{-5} \cdot dx\_hpp2 + 3.37 \cdot 10^{-6} \cdot (dx\_hpp2)^2 \tag{8.3}$$

This equation has been derived for cool, red carbon stars with a dx_hpp2 value below -300, respectively for a $(B-V)$ value larger than 1.1. For stars on the main sequence with $1.1 > B - V > 0.3$ the relation is given by:

$$B - V = 0.31 - 2.25 \cdot 10^{-3} \cdot dx\_hpp2 \tag{8.4}$$

For hot blue stars and AGN with colors of $B - V < 0.3$ again a quadratic approximation is necessary:

$$B - V = 0.28 - 3.19 \cdot 10^{-3} \cdot dx\_hpp2 + 5.13 \cdot 10^{-6} \cdot (dx\_hpp2)^2 \tag{8.5}$$

The given relation between dx_hpp2 and $(B-V)$ is based on the evaluation of spectra from 36 carbon stars, 281 main sequence stars and spiral galaxies, and 271 hot stars and AGN. Figure 8.6 shows the correlation of dx_hpp2 and $(B-V)$ color for the observed data and the fitted curve for the different color bins.

Finally, a correction due to the Galactic extinction had to be applied. The extinction can be approximated as (Seaton 1979):

$$A_V = R \cdot E(B-V) = (3.2 \pm 0.1) \cdot \frac{N_H}{5.2 \cdot 10^{21}\,\mathrm{cm}^{-2}} = N_H \cdot 6.2 \cdot 10^{-22}\,\mathrm{cm}^2 \tag{8.6}$$

It has to be noted that this correction is neglected by other authors studying Seyfert samples, like Boyle et al. (1988) and Hewett et al. (1995). Individual absorption within the sample presented here have been computed using the N_H values from the Leiden/Dingeloo Survey (LDS, Hartmann and Burton 1997) for objects north of $\delta = -30°$ and from Stark et al. (1992) for the other.

Both methods, based on the photographic plates and on the CCD photometry, led to the same calibration ($\Delta m \lesssim 0.1\,\mathrm{mag}$).

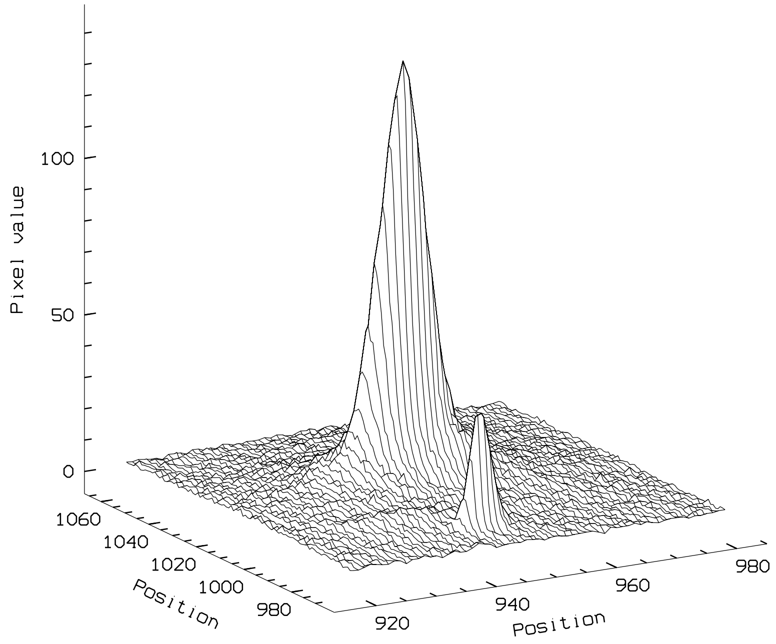

Figure 8.7: HE 1045-2435 as an example of a Seyfert II core on top of the bulge of the host galaxy. The smaller object in front is a star which shows the point spread function for this exposure.

8.4 Separation of core and galaxy

The luminosity function of the Seyfert II should be determined for the active cores only and not for the combined flux of AGN and galaxy. Because of the absorption of the core originating from the dusty torus around the accretion disk, the AGN cores in Seyfert II galaxies are apparently much fainter than in Seyfert I. Thus, the separation of core and galaxy is more important and also more difficult than for the Type I AGN. The procedure to separate core and galaxy has been developed by Knud Jahnke at the Hamburger Sternwarte and is described and discussed in Jahnke (1998).

The idea is to subtract a scaled point spread function (PSF) from the direct image of the object to get a smooth galaxy profile as a residual. An example for the profile of a Seyfert II object and a PSF is shown in Figure 8.7. To determine the brightness profile of the host galaxy, elliptical isophotes are determined around the center of the object to determine the surface brightness within these elliptical areas. For Seyfert galaxies the host galaxies are expected to be more spiral or disk-like than elliptical. The profile of the intensity of a spiral or disk-like galaxy can be described by an exponential function (Freeman 1970):

$$I_S(z) = I_{S0}(z) \cdot \exp\left(-1.68\frac{r}{r_0}\right) \tag{8.7}$$

The isophotes in the outer part of the galaxy can have elliptical form, depending of the form of the host galaxy and the viewing angle with respect to the disk of the galaxy. In the inner part, where the PSF is dominating the brightness profile, the isophotes should be circles. This profile analysis is also done for a bright unsaturated star within the same exposure to represent the PSF in the field. The full width at half maximum (FWHM) of the star and the core of the AGN should be the same, because this value is only affected by the conditions during the observation, not by intrinsic parameters. After computing the mean profile of the isophotes of the object and the star there are several ways to analyze the contribution of the core to the total flux of the object. Typically the PSF is scaled and than subtracted from the object in a way that yields certain properties for the residual profile. Thus the problem is to find the correct scaling parameter. In principle there are two possible criteria. The first is to scale the PSF to a height that the residual host galaxy has zero intensity in the center (Veron-Cetty & Woltjer 1990, Dunlop et al. 1993). The other one is to use a scaling of the PSF resulting in a residual which has a continuous flat shape at the center (Gehren et al. 1984, McLeod & Rieke 1994a/b, Rönnback et al. 1996, Boyce

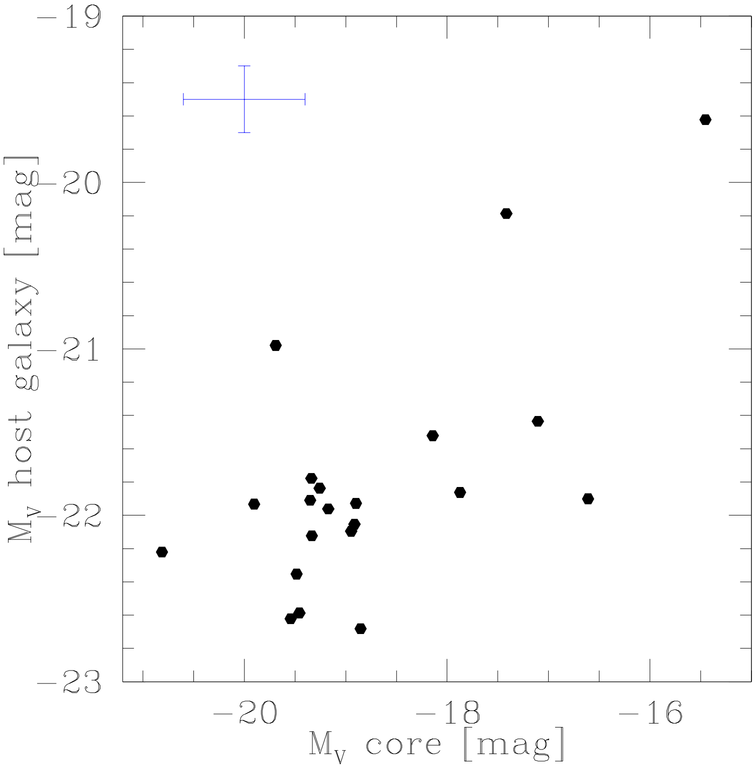

Figure 8.8: Absolute magnitude of the host galaxy versus core brightness. The mean difference between core and galaxy is $\overline{\Delta M_V} = (2.8 \pm 1.0)$ mag. Typical error bars are shown in the upper left corner.

et al. 1996, Jahnke 1998). In this work the criterion with a monotone profile of the galaxy was used because the Seyfert II cores are weak and in most objects the galaxy dominates the core emission.

The separation of core and galaxy showed that the active cores are comparably faint. In Figure 8.8 the absolute magnitudes of the cores and galaxies are shown for the confirmed Seyfert II. There is a mean brightness difference between the AGN and the galaxy of $\overline{\Delta M_V} = (2.8 \pm 1.0)$ mag. The mean error of the magnitude of the host galaxy are $\sigma_{M_V} \sim 0.2$ mag and significant lower than the errors of the core magnitudes ($\sigma_{M_V} \sim 0.6$ mag). The errors the core magnitudes are larger due to the separation procedure, which affects the faint core stronger than the comparatively bright host galaxy.

8.5 Survey characteristics

A survey for whatever kind of objects based on objective prism plates suffers from several problems which originate from the photographic plates. Some characteristics shall be discussed here only briefly, as a detailed discussion can be found in Köhler (1996). Nevertheless, some solutions to problems have been developed during this work to take into account the special properties of a search for Seyfert II galaxies.

The area which is surveyed by this work is not only depending on the number of ESO-fields which have been investigated. Because every object above the plate limit causes an elongated spectrum on the objective prism plates, those spectra can overlap and thus objects are lost for the candidate selection. To reduce the number of false candidates I applied the criterion that candidates do not have to show any overlap within the HES. The overlap rate depends strongly on the individual quality of the HES plate which was used for candidate selection, the galactic latitude (as fields near to the galactic plane are more crowded with objects and therefore show a higher overlap rate), and on the extension of the objects. These objects can overlap if the extension is large enough and so is the brightness of the outer parts of i.e. a galaxy. The overlap rate for extended objects is by a factor of 1.4 ± 0.35 higher than for the point sources (based on the 41 ESO-field examined here). Because most objects (> 90%) have been selected within the extended object sample of the HES, the correction applied to this

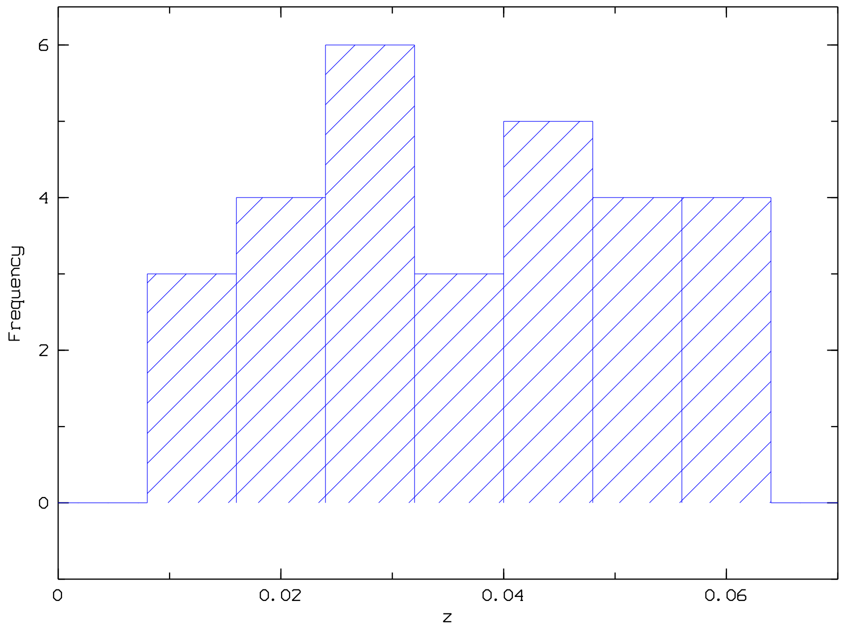

Figure 8.9: Redshift distribution of the Seyfert II sample. The detected redshifts are in the range $0.011 < z < 0.060$.

investigation is based on the overlap statistic of extended objects. Another criterion for the candidate selection is the spectral magnitude *spcmag*. This magnitude is determined from the density spectra on the objective prism plates. The same magnitude regime ($13\,\mathrm{mag} < spcmag < 17\,\mathrm{mag}$) has been examined to determine the loss due to overlaps. Thus for each spectral plate which was used for the Seyfert II survey, the overlap rate was determined by counting the extended objects in overlaps in relation to all extended objects within the brightness limits. The overlap rate ranges from 35.6% to 84.0% with a mean value of $(55 \pm 14)\%$. Thus more than half of the plate area is lost due to overlapping spectra. When computing the area covered by the spectral plates one has to take into account also the overlapping plates. In cases where plates overlap the area from the deeper spectral plate is used. Additionally a fraction of 3% of the area was subtracted due to the loss of objects in the apparent vicinity to bright stars which outshine parts of the plates (Hewett et al. 1995). The characteristics of the individual fields are listed in Table 11.7 on page 143.

This results in a total area of $994\,\mathrm{deg}^2$ which is covered by the 41 spectral plates on which identification was done, but in an effective area of $449\,\mathrm{deg}^2$ which is surveyed within the course of this work. Taking only into account the 27 fields which have been classified as *complete* reduces the effective area to $307\,\mathrm{deg}^2$.

8.6 Luminosity function of the Sy2 sample

To derive a luminosity function (LF) it is necessary to have a complete and well-defined sample. A test for completeness for the sample presented here is the $\overline{V_e/V_a}$ test, already described in section 5.8.2 on page 58. An evolution in the small redshift range ($0.00 < z < 0.07$) is not expected, therefore a complete sample should have $\langle V_e/V_a \rangle = 0.5$. The test for all detected Sy2 galaxies, including those where the Sy2 character is not firm yet also including incomplete identified fields, results in $\langle V_e/V_a \rangle = 0.48 \pm 0.05$. For the Seyfert II objects within the complete identified fields we get $\langle V_e/V_a \rangle = 0.49 \pm 0.06$, and $\langle V_e/V_a \rangle = 0.43 \pm 0.07$ if I omit the insecure detections. Therefore the sample of Seyfert II is consistent with no evolution, although there might be a small amount of incompleteness indicated by the slightly lower values of $\langle V_e/V_a \rangle$ compared to the expected 0.5. This might be caused by missing some Seyfert II galaxies near the survey limit ($spcmag = 17.0\,\mathrm{mag}$). Nevertheless the sample seams to be homogeneous. Figure 8.9 shows the distribution of redshifts for the Seyfert II sample. No gap or non-uniform distribution within the redshift range $0.01 < z < 0.06$ is detectable.

This enables us to compute the local LF of Seyfert II galaxies. The LF is determined only for those objects which are inside the 27 completely identified fields. Therefore this subsample contains 16 secure Seyfert II galaxies,

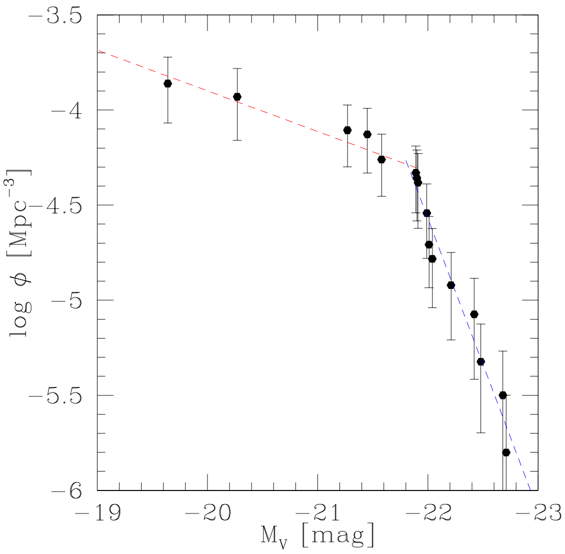

Figure 8.10: Cumulative luminosity function (space density vs. luminosity) for the absolute magnitude of the 16 secure Seyfert II galaxies (core + galaxy, left panel) and for the host galaxies only (right panel) within the completely identified fields. The lines refer to the linear regression. Due to the low luminosity of the AGN cores, the host galaxy LF nearly matches the LF for the total luminosities of the objects.

and 6 possible Seyfert II. As will be shown, the density of Seyfert II galaxies in this work is larger than in previous studies. Therefore I restrict the analysis to the secure Seyfert II galaxies, giving a *lower* limit to the true Seyfert II galaxy density.

To construct the cumulative LF for each object the accessible volume V_a is determined by using the maximal redshift at which this object could have been detected due to its flux and individual survey limit. The density ϕ_{object} is then the reciprocal value $1/V_a$. Then for every object with an absolute magnitude $M_{abs,object}$ the density ϕ of objects with $M_{abs} > M_{abs,object}$ is determined by

$$\phi = \sum_{i=1}^{n} \frac{1}{V_{a,i}} \tag{8.8}$$

Thus the cumulative LF shows directly the expected density of objects of a given absolute magnitude.

Many authors use the total luminosity of the objects of interest to derive LFs. This method was also applied when studying the BL Lac sample within the first part of this thesis. This is in fact useful when studying Quasars where the fraction of light which is contributed by the host galaxy is negligible (see e.g. Wisotzki 2000b). When examining the lower luminosity objects, like faint Seyfert I and Seyfert II, the fraction of flux provided by the galaxy can be several times larger than the contribution by the core (Cheng et al. 1985, Köhler et al. 1997).

For comparison reasons Figure 8.10 shows the cumulative luminosity function for the total flux of the Seyfert II objects, i.e. core plus galaxy. The slope of the LF shows a break around $M_V \sim -21.9$ mag. This might be a hint to incompleteness of the Seyfert II sample presented here for faint luminosities. Below this luminosity the emission lines might be more difficult to detect and/or the host galaxy is outshining the core and thus the core is not detectable within the HES density spectra anymore. Nevertheless the LF in the range $-23\,\text{mag} < M_V < -21.9\,\text{mag}$ seems to be well determined. A linear regression for this regime results in gradient of 1.58 ± 0.11.

Because the host galaxies of the objects are much brighter than the Seyfert II cores itself (as shown in Figure 8.8), the LF of the host galaxies nearly matches the LF of the total luminosity shifted. It is only shifted a bit in absolute magnitude. As shown in Figure 8.10 (right panel) the break is visible at $M_V \simeq -22$ mag with a slope of the steep part 1.14 ± 0.08 and therefore slightly flatter than the LF for the total luminosity.

The LF of the cores is more interesting, because it is connected directly to the AGN phenomenon within these sources.

Also, the core LF shows a break (at $M_V \simeq -19$ mag) with five objects being fainter than the turning point (Fig. 8.11). The slope of the cumulative core LF is flatter than for the total luminosity. For Seyfert II cores with $M_V > -19$ mag the gradient is 0.77 ± 0.05. The analysis presented up to here was done under the assumption

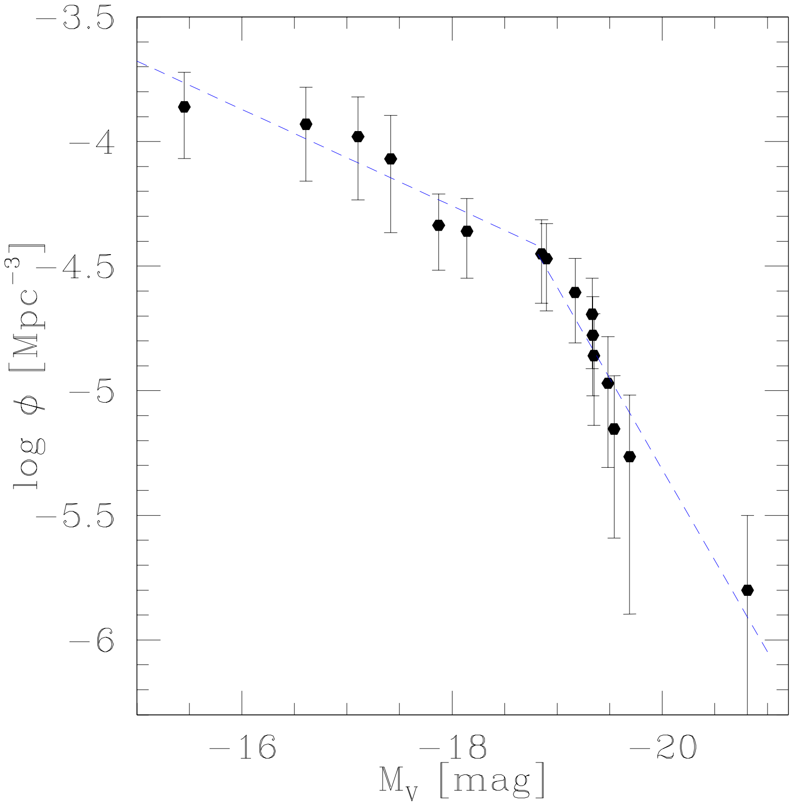

Figure 8.11: Cumulative luminosity function for the Seyfert II cores of secure identifications within the complete identified fields. The lines refer to linear regression.

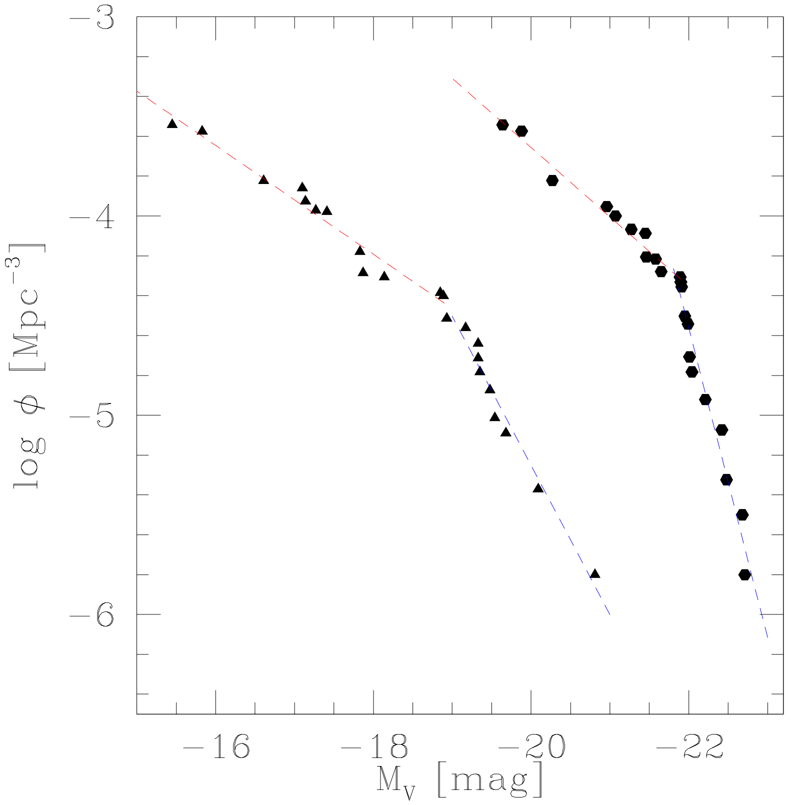

Figure 8.12: Cumulative LF for the Seyfert II galaxies within complete identified fields, including those objects where the identification is not secure up to now. The triangles show the luminosity function of the AGN cores, and the circles represent the LF for the total flux of the objects. One object where the separation between core and galaxy was not possible is not included in the core LF.

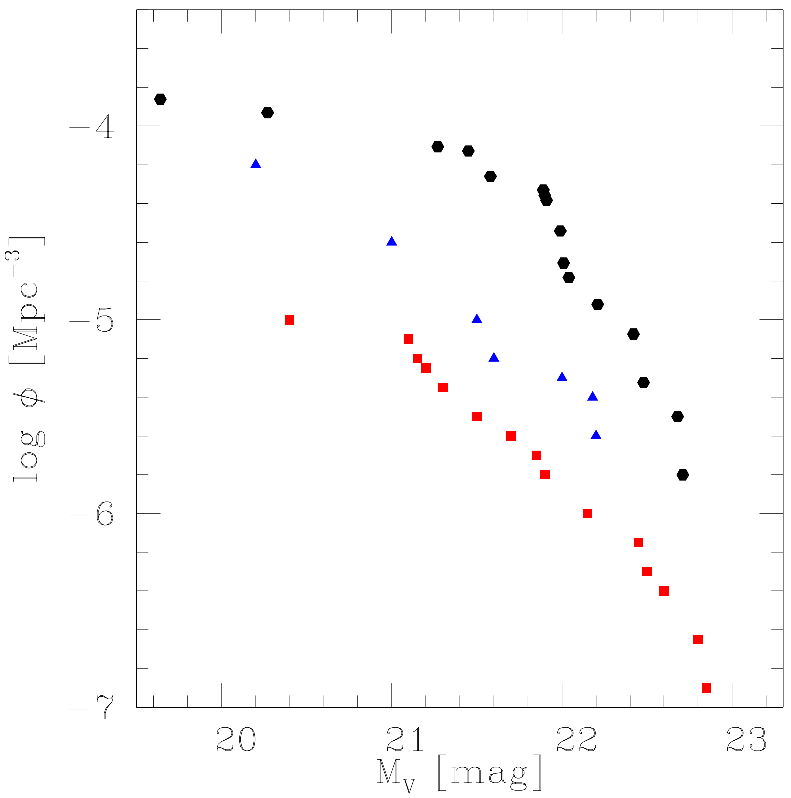

Figure 8.13: Cumulative LF for the total luminosity of the Seyfert II objects. Hexagons refer to the sample presented here, triangles from Köhler 1996, and squares from Cheng et al. 1985.

that none of those galaxies is a Seyfert II. Figure 8.12 shows the other extreme, assuming that *all* 6 objects belong to the Seyfert II class. The slope of the LF is a little bit flatter than in the case when excluding insecure identifications. For the steep part of the core LF the gradient is 0.75 ± 0.04 and for the total flux 1.55 ± 0.10.

In any selection of objects the LF of the total flux shows the same slope as the LF of the cores, and the magnitude difference between core and galaxy increases with decreasing total luminosity.

8.7 Comparison to other Sy2 samples

This work does not represent the first attempt to derive the local LF of Seyfert II galaxies. There have been two major investigations on this topic.

One is also based on the HES and was presented in the dissertation of Köhler (1996). The major goal of that work was to derive the local LF of Seyfert I objects and to compare it with the Quasar LF. Additionally, a search for Seyfert II galaxies based on their emission lines within the low resolution density spectra of the HES was implemented. The full high-resolution scan of the spectral plates was not possible at that time due to lower storage capabilities. The resulting sample consisted of 7 Seyfert II galaxies.

A larger sample was derived from the CfA Redshift Survey. The CfA (Davis, Huchra & Latham 1983, Huchra et al. 1983) is a magnitude limited sample of 2399 galaxies with essentially complete spectroscopic information. This survey was not designed to find Seyfert galaxies, therefore the fraction of AGN compared to the total number of objects is quite low (25 Seyfert I and 23 Seyfert II galaxies). Osterbrock & Martell (1993) presented the local luminosity function of the CfA Seyfert galaxies, using the photometry of Zwicky, Herzog & Wild (1961) based on photographic direct plates. The photometry for the Seyfert galaxies was presented by Huchra & Burg (1992).

The comparison with the CfA and the Köhler-HES sample is shown in Figure 8.13 for the total luminosity of the Seyfert II galaxies. As already revealed by Köhler (1996) the CfA sample seems to suffer from incompleteness. But the comparison between this sample and the sample presented here again gives a factor of ~ 3 higher space density for Seyfert II galaxies.

The incompleteness of the CfA sample was already discussed in Köhler (1996). The higher density of objects found within this work can be based on several reasons:

- incompleteness of the survey area. The sample presented here is based on 27 complete identified fields. Due to bad weather conditions a selection of fields to do follow-up had to be done. Fields in which already promising candidates for Seyfert II galaxies had been found were preferentially re-observed. In the worst case, if I will not find any more Seyfert II galaxies in the incomplete identified fields, the survey area will be $\sim 449\,\mathrm{deg}^2$ and therefore ~ 1.5 higher than the survey area applied here. At the same time the number of (securely identified) Seyfert II galaxies would increase to 22, which is only a factor of ~ 1.4 higher. Therefore it can be concluded that the higher density of objects presented here cannot be due to the "patchy" area of the complete identified fields.

- different overlap statistic. As already discussed, the overlap statistic determines the fraction of effective area in comparison to the area covered by the photographic plates on the sky. The mean overlap rate based on the extended objects is $\simeq 55\%$. For point sources this rate would be $\sim 40\%$. If I would apply the overlap statistic of the point sources, the effective area would increase and therefore the space density of the objects would decrease by a factor of ~ 1.3. Thus also this cannot be the only reason for the higher density

- candidate selection. The candidate selection for Seyfert II objects within this work was not only based on line, but also on color criteria. These objects would not have been found by the selection process applied by Köhler (1996). Additionally, I had the advantage that I could search for objects on the complete digitized high resolution scan of the photographic plates. It is obvious that a selection based on the low resolution scans, as applied by Köhler (1996) will miss objects with weak emission lines. Furthermore, the selection procedure applied here was not optimized to find Seyfert galaxies in general but to search effectively for Seyfert II galaxies only. The improved procedure might be the main reason for the higher space density of Seyfert II galaxies found within this work in comparison to Köhler (1996) and Osterbrock & Martell (1993)

Additionally, I did not apply a lower survey limit but estimated the accessible volume from $z = 0$ up to the detection limit of each object. When restricting the survey volume to the lowest detected redshift of a Seyfert II within the sample ($z = 0.01$) or to the lowest detected redshift of all objects observed ($z_{min} = 0.006$) the survey volume would decrease a bit and therefore the density of objects would be even higher.

Another way to investigate the distribution of objects in comparison to their absolute magnitude is to create the differential LF. In this case the data are binned due to their absolute magnitude (e.g. in bins of 0.5 mag width) and then the space density of the objects within this bin is determined as described in Formula 8.8. This density is then divided by the width of the luminosity bin to derive a density per volume and magnitude. This method suffers from the sensitivity of the applied binning when using small samples. For the Seyfert II sample presented here I used bins of width 0.5 mag. The resulting differential luminosity function for the total luminosity is presented in Figure 8.14. For comparison the values from Oserbrock & Martell (1993) for the CfA are also shown. It seems that the CfA sample misses objects preferentially at the bright end but is more complete for faint objects than the Seyfert II sample presented here. It has to be noted that the number of objects seems to be to small to derive a good determined differential LF. The errors for the densities computed for the sample presented here are that large that still the LF for the CfA and for this sample are consistent. Hence the use of the differential LF can only give a hint to the real situation, as long as the number of objects is small.

Adding all this information together, I assume that the density of Seyfert II galaxies in the nearby universe ($z < 0.07$) is much higher than estimated before.

This work presented also the first attempt to derive a local luminosity function of the Seyfert II cores. As there is, to the authors knowledge, no equivalent work to compare with, this LF is compared to the core LF of Seyfert I galaxies. Two major works are taken into account: The HES based Seyfert I LF by Köhler et al. (1997), and the core LF by Cheng et al. (1985) who examined Markarian galaxies. The comparison is shown in Figure 8.15. Can we draw some conclusion based on a comparison of the LF between different types of objects? If we expect the parent population of Seyfert I and II to be the same, and if we assume that the Seyfert II objects are obscured, we would expect the cores of the Seyfert II objects to have lower absolute magnitudes. Within the luminosity function of the cores this should result in an offset in brightness. The LF of the Seyfert II should have a similar slope as the one for the Seyfert I, but shifted by the extinction of the absorbing material. Based on X-ray observations one expects the column density of the absorbing material to be as high as $10^{23} \ldots 10^{25}\,\mathrm{cm}^{-2}$. The expected extinction in the optical V band should be high, even if we assume only a small amount of dust being associated with the hydrogen which causes the absorption in the X-rays. But a large offset between the core LF of Seyfert I and II is not seen in 8.15. Even though the uncertainties are large because different techniques had to be applied to derive the core magnitudes from the two classes of objects, the offset is clearly $\lesssim 1\,\mathrm{mag}$.

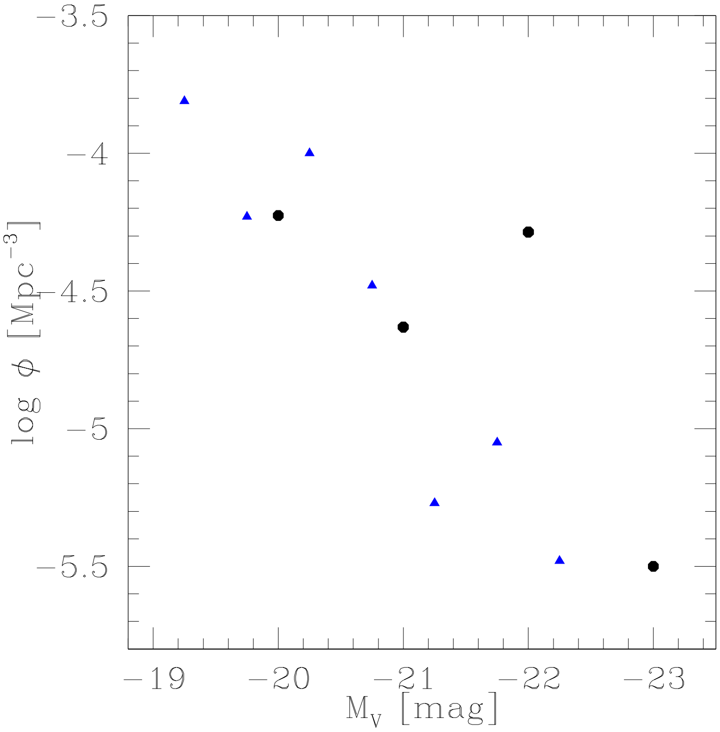

Figure 8.14: Differential LF for the Seyfert II galaxies presented here (filled circles) in comparison to the Seyfert II LF from Osterbrock & Martell (1993) based on the CfA survey (triangles).

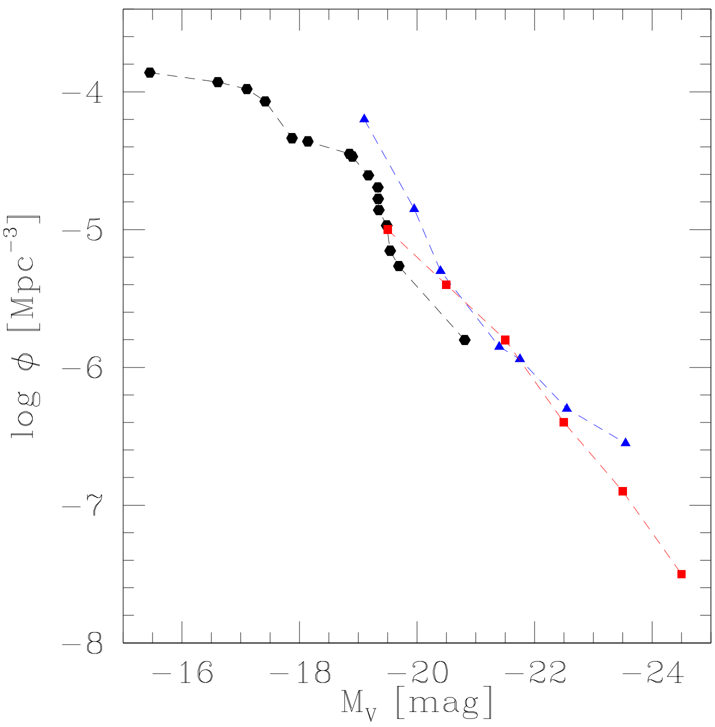

Figure 8.15: Cumulative LF for the Seyfert II cores of the sample presented here (filled hexagons) in comparison to the Seyfert I LF from Köhler et al. 1997 (triangles) and Seyfert I LF based on Markarian galaxies by Cheng et al. 1985 (squares). All samples have the restriction to $z_{max} = 0.07$.

8.8 Consequences based on the Sy2 Luminosity Function

Because the data base was the same for Köhler et al. (1997) as for the work presented here, the results for the luminosity function for Seyfert I and II can be compared directly. Köhler et al. (1997) found 7 Seyfert I objects with $z < 0.07$ over 477 deg^2, while the work presented here derives $16 \dots 22$ (depending on the fraction of Seyfert II objects within the objects where the type could not be determined up to now) over 307 deg^2. This simple comparison results in a ratio of Seyfert1 : Seyfert2 $\sim 3.5 \dots 5.0$. Of course, the simple counting of objects does not take into account the more complicated luminosity functions of these objects and the different core dominance in both classes.

Using the comparison of the LF of Seyfert II and Seyfert I (Figure 8.13) results in a magnitude dependent ratio of number densities of both classes. If we take into account the total luminosity (core + galaxy) of both classes, the expected space density for luminosities $M_V \gtrsim -23$ mag of Seyfert II galaxies appears to be higher than for Seyfert I galaxies (in comparison with Köhler et al. 1997 or Osterbrock & Martell 1993). At the turnover point ($M_V = -22$ mag) of the Seyfert II cumulative LF presented here, the ratio is expected to be $Sy1 : Sy2 \gtrsim 10$. Because of the flattening of the Seyfert 2 LF towards lower luminosities the same ratio is expected for luminosities of $M_V = -21$.

A different result can be derived when examining the core luminosity functions only. This is caused by much fainter Seyfert II cores compared to the Type I objects. Between $M_{V,core} = -19$ mag and $M_{V,core} = -21$ mag the luminosity functions of the cores of Seyfert I and Seyfert II objects are nearly parallel (Figure 8.15). The offset is ~ 0.5 mag or a factor of ~ 2 in space density with the Seyfert II cores being *less* numerous than the Seyfert I. Within the 1σ errors the LFs of type I and type II objects are even consistent.

This could origin from two classes of objects, which have the same luminosity distribution and also the same space density. But it could also be a result from an absorbed type of objects (i.e. the Seyfert II galaxies) in which the cores appear to have a lower luminosity, but which are more frequent. Due to a missing prominent break in the Seyfert I LF a quantitative estimation of this effect is not possible.

The luminosity function can be used to estimate the number of Seyfert II objects of a given absolute magnitude. This can be used to derive an estimation of space density for Type II AGN. If we apply the LF for the total flux, we should find ~ 600 type II Quasars (with $M_V \leq -23$ mag) up to $z = 0.1$ if we explore the entire sky. The number of Quasars decreases dramatically if we look for higher luminosities. For $M_V \leq -24$ mag we should only find ~ 20 up to $z = 0.1$. These objects should be easy to detect due to their apparent magnitude of $m_V \lesssim 15$ mag. Up to $z = 1$ we should find ~ 160 type 2 QSO with $M_V \leq -25$ ($m_V \lesssim 19.3$ mag), and five objects with $M_V \leq -26$ ($m_V \lesssim 18.3$ mag). Even though the extrapolation up to high luminosities is difficult due to the large errors which occur for small errors in the local LF and also because the LF will not extrapolate up to whatever luminosity, the conclusion can be drawn that there might not exist type II QSO with luminosities as high as $M_V \leq -27$ mag within the universe. The local LF of Seyfert II results in one object as bright as -27 mag per $\sim 10^{12}$ Mpc^3.

The same analysis can be done for the LF of the Seyfert II cores, even though this LF suffers from a larger error due to the core/galaxy separation which had been applied. Though the Seyfert cores are much fainter than the total Seyfert II objects, the slope of the LF is flatter and therefore higher luminosities of Seyfert II cores could be possible, when extrapolating the core LF to brighter absolute magnitudes, even though for objects with $M_V \lesssim -25$ mag fewer objects are expected. The local LF of the cores presented here would result in ~ 200 Seyfert II objects with $M_V \leq -25$ mag up to $z = 1$ and ~ 40 Seyfert II with $M_V \leq -26$ mag in the same volume. Seven objects with luminosities as high as $M_V \leq -27$ mag and even one with $M_V \leq -28$ mag should then be possible to be found up to $z = 1$.

Of course extrapolation over eight magnitudes in total luminosity is daring. It is possible that the dusty torus, which is thought to be the reason for the absorption in Seyfert II objects, is blown away if the luminosity of the core exceeds a certain threshold. Nevertheless the extrapolation can give a hint to the expected number of Type II AGN.

Another result based on the ratio between Seyfert I and II galaxies can be an approximation of the absorbed fraction of the Seyfert galaxies in total. Assuming that Seyfert I and II galaxies are intrinsically equal, the fraction of Seyfert II galaxies within the Seyfert population would represent the fraction of the AGN which is absorbed, i.e. covered by dusty torus (Figure 8.16). The simplest method is to assume a symmetric torus. Then the fraction of the Seyfert which is covered by the torus is equal to the ratio of Seyfert II in comparison to all Seyfert galaxies and the relation to the opening angle θ of the unabsorbed part of the Seyfert would be

$$\frac{number\, of\, Seyfert\, I}{number\, of\, all\, Seyfert\, galaxies} = \frac{unabsorbed\, area}{4\pi} = 1 - \cos\frac{\theta}{2} \tag{8.9}$$

Based on the luminosity functions of the Seyfert cores this would result in an opening angle of $\theta \sim 140°$, if we

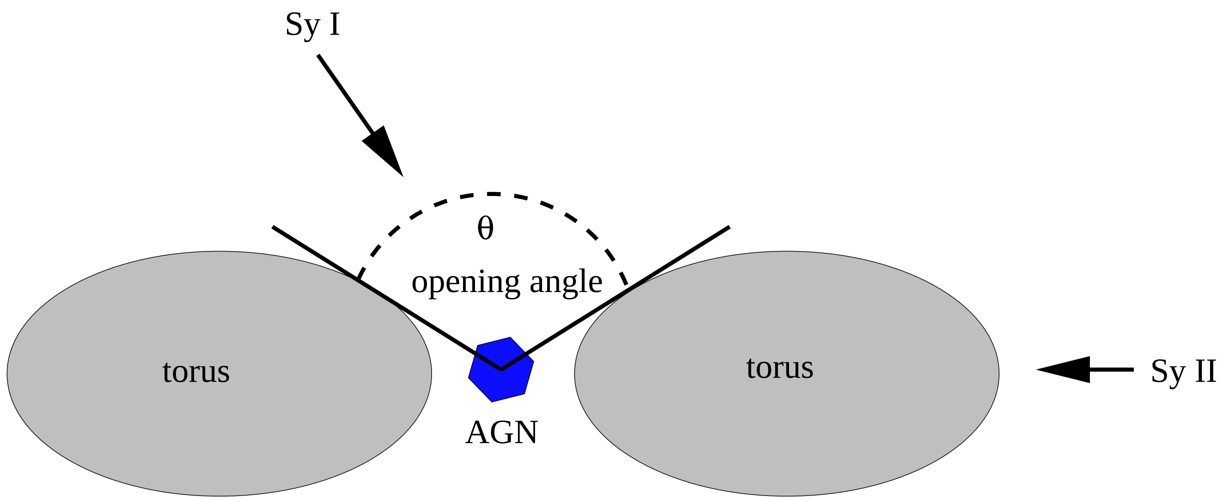

Figure 8.16: Schematic view of the simple Seyfert model with the "dusty torus". In this model the Seyfert would appear as a Sy I object if the line of sight is not affected by the torus and as a Sy II when looking at the torus.

assume the Seyfert II cores are a factor of two less numerous than the Seyfert I cores as might result from Figure 8.15.

8.9 Evidence for interaction and merging

An unsolved problem in the study of the AGN is how the central engine is fueled. If the interstellar gas is fueling the AGN there still remains the question, how this gas is transported from kiloparsec scales within the galaxy onto the supermassive black hole. In principal there are two models to achieve accretion rates of $\sim 0.01 M_o \mathrm{yr}^{-1}$ as is needed to power the AGN in a Seyfert galaxy. One assumes that stellar bars within galaxies transport the gas onto the AGN (Schwarz 1981), the other model assumes tidal forces caused by galaxy-galaxy interactions and merging events (Toomre & Toomre 1972).

The formation of a bar within a galaxy will lead to the formation of a shock front at the leading edge of the bar. Material builds up in this shock and falls into the nuclear region (see e.g. Athanassoula 1992). This model is confirmed by recent observation, carried out by Regan, Vogel, & Teuben (1997), who studied the velocity distribution in barred galaxies, which are in general agreement with inflow models. Since the large scale bar transports the gas only into a kiloparsec-scale disk, a second "nuclear bar" is proposed to transport the material within approximately 10 pc of the galactic nucleus. Here the AGN can accrete the gas directly by its potential. Because this "nuclear bars" are a factor of 5 to 10 times smaller than the large scale bars, they are difficult to detect. Up to now they are only seen in nearby galaxies (Buta 1986a, 1986b). A recent study of 24 CfA Seyfert II galaxies by Martini & Pogge (1999) using the Hubble Space Telescope found only five galaxies with a nuclear bar. They therefore rule out small-scale nuclear bars as the primary means of removing angular momentum from interstellar gas to fuel the Seyfert II AGNs. They consider minor merging events to transport material into the innermost regions of the Seyfert II galaxies.

While nuclear bars cannot be studied using the direct images of the Seyfert II sample presented here, because the resolution is not sufficient, they can be used to search for interaction and merging events. No additional spectra were taken and thus the redshifts of apparently interacting systems are not determined yet. But in most cases where galaxies seemed to interact with each other, the evidence for merging was quite obvious. The morphology of the Seyfert II host was disturbed or even disrupted by an apparently passing through companion galaxy. Only those objects, which showed clear evidence for interaction, were taken as a *merger/interacting* event. In total I found 7 of the Seyfert II galaxies being within interacting/merging systems (six secure identifications, one possible Seyfert II). This results in a rate of $\gtrsim 25\%$ of the Seyfert II objects being in interacting/merging systems. Figure 8.17 is an example for a Seyfert II merging system. The Seyfert II galaxy is the (brighter) object in the upper left corner. The true rate of merging might be higher, due to the fact that minor merging events would not have been seen in the direct images of the sample presented here.

The rate within the NELG/LINER group found within the identification process with evidence for merging

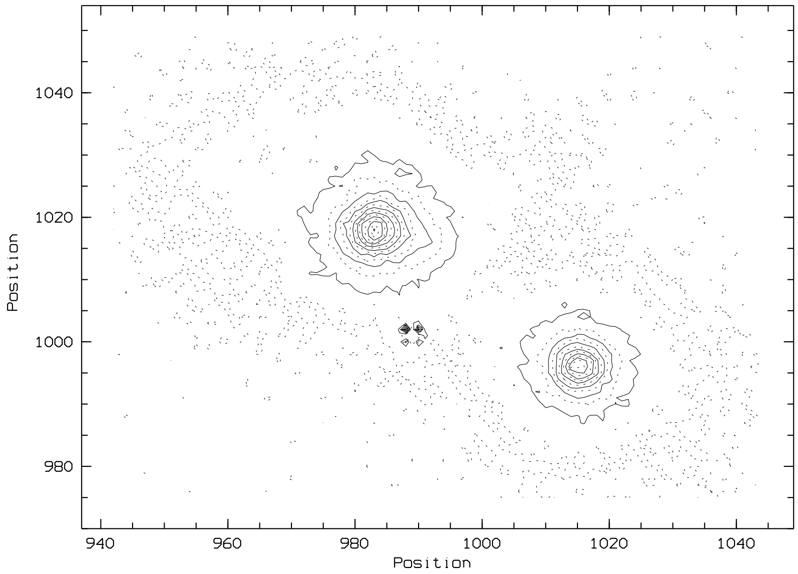

Figure 8.17: Intensity contour plot of the merging system with HE 1335-2344. The Seyfert II is the object on the upper left.

is of the same order ($\simeq$ 33%). This result is close to the values determined by Balzano (1983) who found the percentage of interacting galaxies in a sample of 102 star-burst galaxies to be $\simeq$ 30%, and also close to the $\sim$ 25% found for emission-line galaxies in the HQS by Vogel et al. (1993).

Hence it seems that merging an important way to fuel the AGN and to trigger the star-formation rate within galaxies. Nevertheless the connection between star-burst activity and the AGN phenomenon is an unsolved riddle. Colina & Arribas (1999) studied the nearby galaxy NGC 4303. In this object they detected a low-excitation Seyfert II nucleus, a compact nuclear star-forming spiral structure connected to the AGN core, a massive rotating nuclear disk, and radially flowing high-excitation gas. Colina & Arribas conclude that the massive nuclear disk with a large fraction of mass in the form of cold gas becomes gravitationally unstable, produces gas inflow with a configuration resembling a spiral structure, and forms stars before the gas reaches the core of the galaxy. A similar case might be the galaxy NGC 7679 which also shows evidence for Seyfert and star-forming activity (Della Ceca et al. 2001).

Chapter 9

X-ray based search for Seyfert II galaxies

Another approach to find Seyfert II AGN are their special X-ray properties. Due to the assumption that a torus absorbs the radiation of the AGN, we expect the X-ray spectra of Type II AGN to be much harder (i.e. flatter spectral slope) than for Seyfert I type objects. Therefor Type II AGN can be found within X-ray surveys due to their extraordinary flat X-ray spectra.

9.1 Type II AGN and the cosmic X-ray background

Despite the success of the ROSAT deep surveys in resolving and identifying a large ($\sim 80\%$) fraction of the soft ($E < 2$ keV) Cosmic X-ray Background (CXB: see e.g. Hasinger et al. 1998, Schmidt et al. 1998), the origin of the CXB at harder energies, where the bulk of the energy density resides, remain elusive. The so called "spectral paradox" (i.e. none of the single classes of known X-ray emitters is characterized by an energy spectral distribution similar to that of the CXB) and the lack of faint, large and complete samples of X-ray sources selected in this energy range, led a number of authors to propose different classes of X-ray sources as the major contributors to the hard CXB (e.g. star-burst galaxies, absorbed Type 2 AGN as predicted from the Unification Scheme of AGNs, reflection dominated AGN, see e.g. Griffiths and Padovani 1990, Comastri et al. 1995b). Recent results from ASCA and *Beppo*SAX (Akiyama et al. 1998, Fiore et al. 1999) favor the strongly absorbed AGN hypothesis. Finally Mushotzky et al. detected hard X-ray sources in a deep survey using the Chandra satellite, which account for at least $\sim 75\%$ of the hard X-ray background. Most of those hard X-ray sources are associated unambiguously with either the nuclei of otherwise normal bright galaxies, or with optically faint sources. But deeper investigations are still needed to confirm this scenario and to test competing models. For example it is not clear if high luminosity Type 2 AGN exist or not (see e.g. Halpern et al. 1998). In collaboration with Roberto Della Ceca from the Osservatorio Astronomico di Brera we carried out spectroscopic identification of the "flatter" hard X-ray selected ASCA sources, to clarify this long-standing problem of modern cosmology.

Identifications of X-ray sources in the low energy band (< 2keV) like the EMSS (Stocke et al. 1991), the Hamburg/RASS catalogue (HRC, Bade et al. 1998b), the RIXOS (Mason et al. 2000) and the RDS (Schmidt et al. 1998) gave a clear picture of the nature of the X-ray sources in this energy region down to a flux limit of $f_X \sim 0.5 - 1 \cdot 10^{-14}$ergsec^{-1}cm^{-2}.

9.2 The ASCA Hard Serendipitous Survey

With the X-ray satellites like ASCA and *Beppo*SAX it is now possible to examine the situation at harder energies. At the *Osservatorio Astronomico di Brera*, a serendipitous search for hard (2-10 keV band) and faint ($f_X \sim 10^{-13}$erg cm^{-2} sec^{-1}) X-ray sources using data from the GIS2 instrument on board the ASCA satellite has been carried out (Cagnoni, Della Ceca & Maccacaro 1998; Della Ceca et al. 2000) and a sample of 189 serendipitous sources (over a total of $\sim 71\,\mathrm{deg}^2$) has been defined. These sources form the ASCA Hard Serendipitous Survey (HSS). From these sources, 46 have been already spectroscopically identified (33 Type 1 AGN, 2 Type 2 AGN, 5 BL Lacs, 5 clusters of galaxies and 1 star). In Della Ceca et al. (1999) the spectral properties of the serendipitous ASCA sources have been investigated using the "hardness-ratio" (HR) method. They defined $HR1 = \frac{M-S}{M+S}; HR2 = \frac{H-M}{H+M}$ (where S,M and H are the observed counts in the 0.7-2.0, 2.0-4.0 and 4.0-10.0 keV

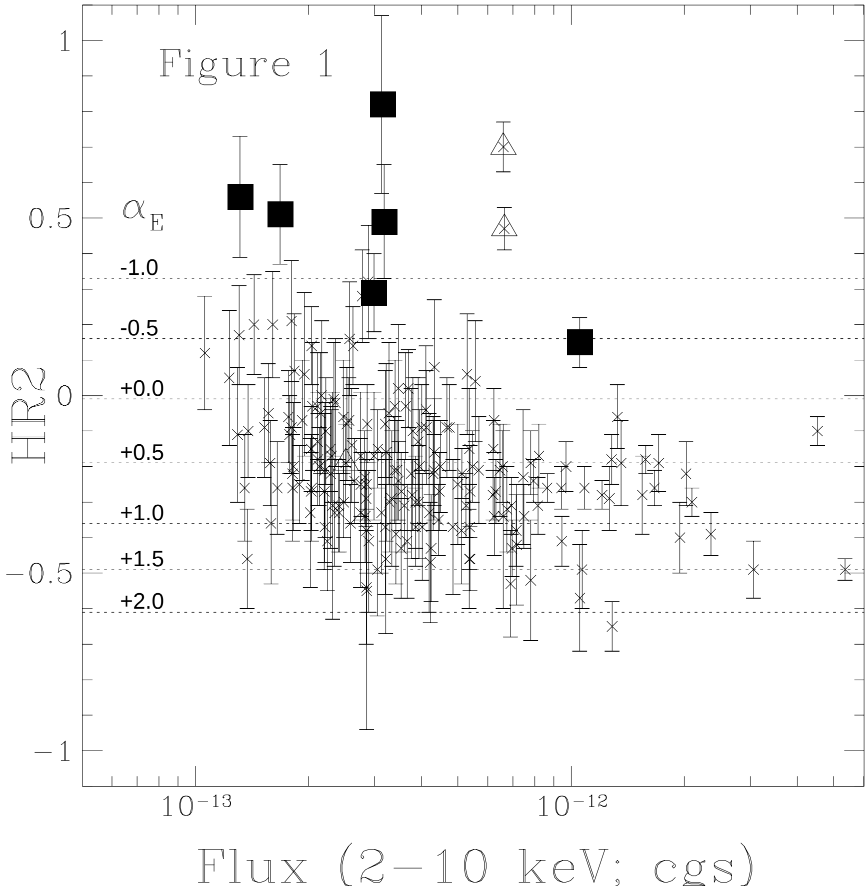

Figure 9.1: ASCA hardness ratios vs. the flux within the HSS sample. The triangles refer to already known type II AGN. The squares are candidates for Type II AGN.

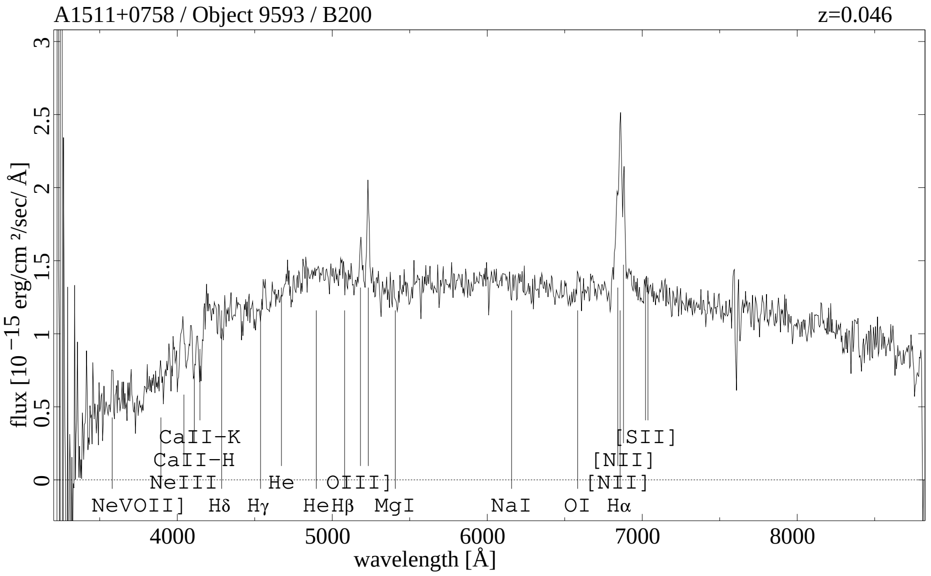

Figure 9.2: The CAFOS spectrum of the optical counter part of the ASCA source A1511+0758. Despite a strong host galaxy, the Seyfert II core is clearly detectable.

energy band) and compared the position of the sources in the HR diagram with a grid of theoretical spectral models. In Figure 9.1, for all sources, I plot the HR2 value versus the 2-10 keV flux and compare it with that expected from a non-absorbed power-law model ($f_X \propto E^{-\alpha_E}$). This figure clearly shows a broadening and flattening of the HR2 distribution going to fainter flux. The 2-10 keV "stacked" spectra of the sources with $f_X \leq 5 \times 10^{-13} \mathrm{erg\,cm^{-2}\,sec^{-1}}$ can be described by a power-law model with $\alpha_E \sim 0.4$, thus it is clear that we are beginning to detect those sources having a combined X-ray spectrum consistent with that of the 2-10 keV CXB. It is worth noting the presence of many sources which seem to be characterized by a very flat 2-10 keV spectrum with $\alpha_E \leq 0.5$ and of a number of sources with "inverted" spectra (i.e. $\alpha_E \leq 0.0$); this is particularly evident below $5 \times 10^{-13} \mathrm{erg\,cm^{-2}\,sec^{-1}}$ where $\sim 50\%$ of the sources seem to be described by $\alpha_E \leq 0.5$ and $\sim 20\%$ by "inverted" spectra. These latter objects could represent a new population of very hard serendipitous sources or, alternatively, a population of very absorbed sources as expected from the CXB synthesis models based on the AGN Unification Scheme.

It is worth noting that the two objects marked as open triangles in Figure 9.1 have been spectroscopically identified as Low Luminosity Type 2 AGN: one is the well known Seyfert 2 galaxy NGC 6552 (Fukazawa et al. 1994), while the other one is a nearby Seyfert 2 galaxy (UGC 12237) which was discovered in the HSS survey.

9.3 Follow up spectroscopy of hardest ASCA sources

Follow-up spectroscopy of hardest ASCA sources was done within two nights (10/11 March 2000) with the Calar Alto[1] 2.2m telescope using the Calar Alto Faint Object Spectrograph (CAFOS). In total we tried to identify six ASCA sources; pre-identification of bright objects using the objective prism plates of the Hamburg quasar Survey (Hagen et al. 1995) reduced the number of candidates within the ASCA error circle ($\sim$ 2 arcmin). Turning the slit of the instrument allowed us to take spectra of at least two objects with one exposure. Exposure times to identify the possible optical counterparts varied between 10 and 90 minutes. In total we observed 27 optical sources, identifying 13 stars, three galaxies, one possible Seyfert 2 (A1313+3033) and one definite Seyfert 2 galaxy (A1511+0758, see Fig. 9.2). For nine observed spectra it was not possible to give a clear identification. For the clearly identified Seyfert 2 galaxy A1511+0758, we took a spectrum with higher resolution ($\Delta\lambda \simeq 6$ arcsec) on the 14th of March using CAFOS again. We measured line properties within this spectrum, fitting Gaussian profiles to the detected lines (Table 9.1). Using the direct images of A1511+0758, we performed a separation of

[1]German-Spanish Astronomical Center, Calar Alto, operated by the Max-Planck-Institut für Astronomie, Heidelberg, jointly with the Spanish National Commission for Astronomy

Table 9.1: Line properties in the spectrum of A1511+075

	H_β 4861 Å	OIII 4959 Å	OIII 5007 Å	OI 6300 Å	NII 6548 Å	H_α 6562 Å	NII 6583 Å
flux[a]	0.4	3.2	6.3	0.3	1.3	11.0	4.5
EW [Å]	~ 0.7	6	12	~ 0.5	~ 2	~ 20	8
FWHM [Å]	~ 7	~ 9	8.3	~ 4	~ 9	~ 11	8.9
FWHM [km $\sec^{-1}$]	430	540	500	200	410	500	410

[a] Line flux in units $10^{-15}\mathrm{erg\,cm^{-2}\,sec^{-1}}$

the core from the galaxy. Fitting a point spread function to the core we find the difference in magnitudes to be $m_{\rm core} - m_{\rm galaxy} = 1.43$ in the Johnson-I band, and $m_{\rm core} - m_{\rm galaxy} = 1.18$ in the Johnson-R band. Since the flux of the galaxy seems not to differ between the R and the I band, the core is significant brighter in the bluer R-band, as expected for an AGN.

This investigations shows that it is possible to find Type II AGN. Never the less this does not solve the question about the possible existence of Type II quasars. But the method described here to find possible Type II AGN seems to be very promising as it detected one Type II AGN out of six candidates.

Chapter 10

Outlook

This work investigated the classes of two AGN types, the BL Lac objects and the Seyfert II galaxies, using two new samples of objects. Deriving luminosity functions and getting an insight to the physical nature of the objects studied here, it is necessary to focus on what has to be done in the future for a better understanding of the AGN phenomenon.

In the case of the BL Lac research, no former surveys based on both X-ray and radio catalogues are needed. Doubtlessly, the larger ongoing projects are useful. But it can be called into question whether a project like the Deep X-ray Radio Blazar Survey (DXRBS, Perlman et al. 1998, Padovani et al. 1999) will reveal basically new insights to the BL Lac topic, as long as it works with a fairly high (50 mJy) flux limit and again with ROSAT pointed observations ($f_{limit}(0.1 - 2.4\,\mathrm{keV}) \sim 2 \times 10^{-14}\mathrm{erg\,cm^{-2}\,sec^{-1}}$), as already done by the REX survey (Caccianiga et al. 1999). The DXRBS also applies a criterion on the radio spectra ($\alpha_R < 0.7$), optimized to find blazars. This work focuses more strongly on the transition between the FSRQ and the BL Lac class, but seems not to derive a better insight to the BL Lac phenomenon itself.

A drawback when selecting objects according to several properties is the possibility of creating classes of objects without any physical importance. One example for this are the categories of Seyfert I galaxies and Quasars. The only difference nowadays is the limiting magnitude. Another example might be the classification of BL Lac objects into XBL and RBL. Also, to distinguish between normal giant elliptical galaxies and faint HBL is getting more and more difficult, as there exist also HBL with an optical spectrum similar to that of a non-active galaxy.

The consequence has to be to study more intensely the conversion from one class to another, as was done in this work with the intermediate BL Lac objects. To really find the extreme end of the BL Lac population it is necessary to extend the search to faint sources, i.e. X-ray sources without an optical and radio counterpart. This might reveal the high-redshift end of the BL Lac population.

The investigation of objects with synchrotron branches rising up to frequencies $\nu_{peak} > 10^{20}\,\mathrm{Hz}$ should reveal the extreme UHBL class and will tell us something about this end of the BL Lac distribution. The upcoming INTEGRAL mission will investigate this interesting part of the BL Lac spectral energy distribution. Still the question is, whether the UHBL really mark the low energy end. The bright HBL 1517+656 shows that the anti-correlation of luminosity and peak frequency is not true in every case. The deep fields observed by XMM-Newton and Chandra will detect numerous X-ray bright BL Lac objects with perhaps even more extreme properties than for up to now known sources.

An important topic in the BL Lac research which was not studied for the HRX-BL Lac sample is the connection to the parent population. While there are many observations and theoretical considerations seem to favourate the FR-I population as the parent population, this question is still in debate.

One basic question still to be solved is the connection between AGN activity and star formation within the host galaxy. The connection between star-formation, merging, interaction, and AGN activity is not sufficiently understood yet. In the case of the Seyfert II sample presented here, the influence of major merger events was obvious. Doubtlessly, minor mergers or merging events which had taken place a longer time ($\tau \gtrsim 0.5\,\mathrm{Gyr}$) are not seen in the direct images I used for the merging-test. In the case of the BL Lac sample, merging is not seen directly within the optical images. But the redshifts of the objects within the HRX-BL Lac sample are too high to study those effects on the poorly resolved direct images. Nevertheless it seems that also in the case of BL Lac objects the environment and the interaction with nearby companions plays a major role. The host galaxies are thought to be formed by merging events, and the lack of emission lines can be explained by very low accretion rates in the core of the accretion disk of the AGN. Therefore, it would not be surprising to miss high frequency cut-off BL Lacs when looking for merging events. The BL Lac phenomenon could be the quiescent state of a

QSO.

To solve the question about the connection between Seyfert II and Seyfert I galaxies it is necessary to study the Type II AGN at higher redshifts. One approach for this can be the optical identification of hard X-ray sources. The XMM-Newton and Chandra X-ray mission will provide a lot of faint X-ray sources, where the hardest one could be used to find Type II AGN and, if they exist, Type II QSO. Another way to achieve Seyfert II galaxies at higher redshifts is the use of the objective prism plates of both, the HQS and HES. Here the search for objects with [OII]3727 Å line can push the detection limit in redshift up to $z \sim 0.45$. Using the MgII line at 2798 Å could increase this limit to $z \sim 0.9$.

Chapter 11

Appendix

All positions throughout this thesis are given in J2000.0

11.1 Tables to the HRX-BL Lac sample

Table 11.1: Objects from the NVSS/BSC correlation

α	δ	Name	Redshift	Classification
07 01 32.1	25 09 51.0	1RXS J070132.1+250950		
07 04 27.0	63 18 56.0	KUG 0659+633	0.095	G
07 07 02.9	27 06 51.0	1RXS J070702.9+270650		
07 07 13.5	64 35 58.0	VII Zw 118	0.080	Sy1
07 09 07.6	48 36 57.0	NGC 2329	0.019	G S0-:
07 10 24.2	22 40 13.0	MG2 J071027+2239		
07 10 30.0	59 08 08.0	87GB 070609.2+591323	0.125	BL Lac
07 11 48.0	32 19 02.0	PGC 020369	0.067	G
07 13 39.7	38 20 43.0	IRAS F07102+3825	0.123	NLSy1
07 18 00.7	44 05 27.0	IRAS F07144+4410	0.061	Sy1
07 20 19.1	23 49 04.0	1RXS J072019.1+234904		
07 21 32.9	26 09 39.0	1RXS J072132.9+260939		
07 21 53.2	71 20 31.0	0716+714		BL Lac
07 22 17.4	30 30 52.0	HS 0719+3036	0.100	Sy1
07 29 27.4	24 36 25.0	2MASX1 J0729277+24362		G
07 31 52.4	28 04 23.0	2MASX1 J0731526+28043		
07 32 21.5	31 37 51.0	1RXS J073221.5+313750	0.350	GClstr
07 36 24.8	39 26 08.0	FBS 0732+396	0.118	Sy1
07 40 58.5	55 25 33.0	CGCG 262-019	0.034	GGroup
07 41 44.8	74 14 45.0	ZwCl 0735.7+7421	0.216	GClstr
07 42 32.9	49 48 30.0	UGC 03973	0.022	Sy1.2
07 42 50.3	61 09 31.0	87GB 073825.7+611711		star (K0)
07 43 18.7	28 53 07.0	Sigma Gem		star (K1IIIRSCVn)
07 44 05.6	74 33 56.0	MS 0737.9+7441	0.315	BL Lac
07 45 41.2	31 42 50.0	[HB89] 0742+318	0.461	Sy1
07 47 29.4	60 56 01.0	UGC 04013	0.029	Sy1.2
07 49 06.2	45 10 40.0	B3 0745+453	0.190	Sy1
07 49 29.4	74 51 43.0	87GB[BWE91] 0743+7458	0.605	BL Lac
07 51 22.1	55 11 57.0	1RXS J075122.1+551156	0.340	Sy1
07 52 43.6	45 56 53.0	NPM1G +46.0092	0.060	G
08 01 32.3	47 36 19.0	87GB 075755.8+474440	0.158	Sy1

(continued on the next page)

X-ray count rate limit $hcps \geq 0.09$ (RASS-BSC), radio flux limit $f_R(1.4\,\mathrm{GHz}) \geq 2.5\,\mathrm{mJy}$ (NVSS)

The objects of the NVSS/BSC correlation

α	δ	Name	Redshift	Classification
08 01 47.8	56 33 16.0	NGC 2488	0.029	G, S0-:
08 05 25.8	75 34 24.0	WN B0759.1+7542	0.121	BL Lac
08 06 25.5	59 31 06.0	87GB 080212.8+593933		BL Lac
08 09 38.5	34 55 45.0	MG2 J080937+3455	0.082	BL Lac
08 09 49.2	52 18 56.0	87GB 080601.8+522753	0.138	BL Lac
08 10 59.0	76 02 45.0	PG 0804+761	0.100	Sy1
08 15 17.8	46 04 29.0	KUG 0811+462	0.041	Sy1.5
08 19 26.6	63 37 41.0	KOS NP6 038	0.118	G, E
08 19 29.5	70 42 21.0	1RXS J081929.5+704221	0.001	HolmbergII
08 22 09.5	47 06 01.0	RGB J0822+470	0.127	GClstr (Abell 0646)
08 32 25.1	37 07 37.0	FIRST J083225.3+37073	0.091	Sy1.2
08 32 51.9	33 00 11.0	RX J0832.8+3300	0.671	BL Lac
08 36 58.3	44 26 13.0	[HB89] 0833+446	0.255	QSO
08 38 11.0	24 53 36.0	NGC 2622	0.029	Sy1.8
08 41 25.1	70 53 43.0	[HB89] 0836+710	2.172	Blazar
08 42 03.4	40 18 30.0	KUV 08388+4029		star (sdB)
08 42 55.9	29 27 52.0	ZwCl 0839.9+2937	0.194	GClstr
08 59 16.5	83 44 50.0	1RXS J085916.5+834450	0.327	BL Lac
08 59 30.1	74 55 10.0	RX J0859.5+7455	0.276	QSO
09 09 53.9	31 05 58.0	MG2 J090953+3104	0.274	BL Lac
09 13 24.6	81 33 18.0	1RXS J091324.6+813318	0.639	BL Lac
09 15 52.2	29 33 35.0	B2 0912+29 / TON 0396		BL Lac
09 16 51.8	52 38 29.0	87GB 091315.6+525108	0.190	BL Lac
09 20 15.3	86 02 54.0	1RXS J092015.3+860254		
09 23 43.0	22 54 37.0	CGCG 121-075	0.032	Sy1
09 25 12.3	52 17 17.0	MRK 0110	0.035	Sy1
09 27 02.8	39 02 21.0	[HB89] 0923+392	0.695	Sy1
09 28 04.2	74 47 15.0	87GB 092308.0+745942	0.638	BL Lac
09 30 37.1	49 50 28.0	1ES 0927+500	0.188	BL Lac
09 33 46.5	62 49 44.0	1RXS J093346.5+624943		star
09 35 27.4	26 17 14.0	RX J0935.4+2617		AGN
09 47 13.2	76 23 17.0	RBS 0797	0.354	LINER
09 52 25.8	75 02 17.0	RX J0952.4+7502		BL Lac
09 55 34.7	69 03 38.0	MESSIER 081	-0.00011	LINER/Sy1.8
09 55 50.4	69 40 52.0	MESSIER 082	0.00068	Starburst G
09 59 29.8	21 23 40.0	87GB 095643.1+213755	0.367	BL Lac
10 00 28.9	44 09 10.0	RX J1000.4+4409	0.153	GClstr
10 02 35.9	32 42 19.0	NGC 3099	0.051	G
10 05 42.2	43 32 44.0	IRAS 10026+4347	0.178	Sy1
10 06 39.1	25 54 51.0	PGC 029375	0.116	GClstr
10 08 11.5	47 05 26.0	RX J1008.1+4705	0.343	BL Lac
10 09 16.7	71 10 40.0	87GB 100504.8+712548		AGN
10 10 27.9	41 32 42.0	[HB89] 1007+417	0.612	QSO
10 12 44.4	42 29 59.0	B3 1009+427	0.376	BL Lac
10 15 04.3	49 26 04.0	[HB89] 1011+496	0.200	BL Lac
10 16 16.4	41 08 18.0	FIRST J101616.8+41081	0.270	BL Lac
10 16 55.5	73 23 59.0	NGC 3147	0.009	Sy2
10 17 18.0	29 14 39.0	IRAS F10144+2929	0.048	Sy1
10 19 00.8	37 52 50.0	FIRST J101900.4+37524	0.133	Sy1
10 19 12.1	63 58 03.0	MRK 141	0.042	Sy1.5

(continued on the next page)

X-ray count rate limit $hcps \geq 0.09$ (RASS-BSC), radio flux limit $f_R(1.4\,\mathrm{GHz}) \geq 2.5\,\mathrm{mJy}$ (NVSS)

The objects of the NVSS/BSC correlation

α	δ	Name	Redshift	Classification
10 22 12.5	51 24 06.0	MS 1019.0+5139	0.141	BL Lac
10 22 28.9	50 06 30.0	ABELL 0980:[CAE99]	0.158	G
10 30 58.8	31 03 06.0	[HB89] 1028+313	0.178	Sy1
10 31 05.7	82 33 27.0	1RXS J103105.7+823327		star
10 31 18.6	50 53 41.0	1ES 1028+511	0.361	BL Lac
10 32 14.3	40 16 07.0	[BBN91] 102920+403136	0.078	GPair
10 34 23.1	73 45 25.0	NGC 3252	0.004	G, SBd?sp
10 34 38.7	39 38 34.0	KUG 1031+398	0.042	Sy1
10 34 59.5	30 41 39.0	Abel 1045	0.141	GClstr
10 38 46.7	53 30 02.0	SN 1991N	0.003	SNR in NGC3310
10 40 43.7	39 57 06.0	IRAS F10378+4012	0.139	Sy2
10 44 27.6	27 18 13.0	1RXS J104427.6+271813		G
10 44 39.4	38 45 42.0	CGCG 212-045	0.036	G
10 45 20.5	45 34 04.0	1RXS J104520.5+453404		star
10 51 25.1	39 43 30.0	FIRST J105125.3+39432	0.498	BL Lac
10 55 44.0	60 28 10.0	1RXS J105544.0+602810		star
10 57 23.5	23 03 17.0	1RXS J105723.5+230317	0.378	BL Lac
10 58 25.9	56 47 16.0	RX J1058+5647		prob. GClstr
10 58 37.5	56 28 16.0	87GB 105536.5+564424	0.144	BL Lac
11 00 21.3	40 19 33.0	FIRST J110021.0+40192	0.225	BL Lac
11 04 12.4	76 58 59.0	PG 1100+772	0.312	QSO (Opt.var.)
11 04 27.1	38 12 32.0	MRK 421	0.030	BL Lac
11 06 43.5	72 34 07.0	NGC 3516	0.009	Sy1.5
11 11 31.2	34 52 12.0	FIRST J111130.8+34520	0.212	BL Lac
11 11 37.2	40 50 31.0	ABELL 1190:[SBM98]	0.079	GClstr
11 14 22.6	58 23 18.0	8C 1111+586	0.206	G (cD)
11 17 06.3	20 14 10.0	87GB 111429.0+203022	0.137	BL Lac
11 18 03.6	45 06 57.0	LEDA 139560	0.106	Sy1
11 19 08.1	21 19 15.0	PG 1116+215	0.176	Sy1
11 20 47.5	42 12 17.0	1ES 1118+424	0.124	BL Lac
11 21 09.9	53 51 25.0	RX J1121.1+5351		AGN
11 23 49.2	72 30 02.0	RX J1123+7230		BL Lac
11 23 57.4	21 29 14.0	[CWH99] 112356.7+2129	0.199	GClstr
11 31 08.9	31 14 09.0	TON 0580	0.289	QSO
11 31 21.4	33 34 47.0	RX J1131.3+3334	0.222	G
11 32 22.4	55 58 28.0	RX J1132.3+5558	0.051	GClstr
11 36 26.6	70 09 32.0	MRK 180	0.045	BL Lac
11 36 29.4	21 35 53.0	MRK 739b	0.030	Sy1
11 36 30.9	67 37 08.0	HS 1133+6753	0.135	BL Lac
11 41 16.2	21 56 25.0	PG 1138+222	0.063	Sy1
11 44 29.9	36 53 14.0	KUG 1141+371	0.040	Sy1
11 45 09.3	30 47 25.0	[HB89] 1142+310	0.060	Sy1.5
11 47 54.9	22 05 48.0	RX J1147.9+2205	0.276	BL Lac
11 49 30.4	24 39 28.0	RGB J1149+246	0.402	BL Lac
11 53 24.4	49 31 09.0	[HB89] 1150+497	0.334	QSO
11 55 18.9	23 24 32.0	MCG +04-28-097	0.143	G
11 57 56.1	55 27 17.0	NGC 3998	0.003	Sy1;LINER
12 03 08.9	44 31 55.0	NGC 4051	0.002	Sy1.5
12 03 43.3	28 36 02.0	RX J1203.7+2836	0.373	Sy1
12 05 11.7	39 20 43.0	RX J1205.1+3920	0.037	GClstr

(continued on the next page)

X-ray count rate limit $hcps \geq 0.09$ (RASS-BSC), radio flux limit $f_R(1.4\,\mathrm{GHz}) \geq 2.5\,\mathrm{mJy}$ (NVSS)

The objects of the NVSS/BSC correlation

α	δ	Name	Redshift	Classification
12 09 46.0	32 17 03.0	FIRST J120945.2+32170	0.145	Sy1
12 11 58.1	22 42 36.0	RX J1211.9+2242	0.455	BL Lac
12 13 45.2	36 37 55.0	NGC 4190	0.001	G
12 15 06.7	33 11 30.0	NGC 4203	0.004	LINER
12 17 52.1	30 07 05.0	ON 325 / B2 1215+30	0.130	BL Lac
12 18 27.0	29 48 53.0	NGC 4253	0.013	Sy1.5
12 20 44.5	69 05 33.0	RX J1220+6905		
12 21 21.7	30 10 41.0	FBQS J1221+3010	0.182	BL Lac
12 21 44.4	75 18 48.0	MRK 205	0.071	Sy1
12 24 54.9	21 22 52.0	PG 1222+216	0.435	Blazar
12 25 12.5	32 13 54.0	MAPS-NGP O-267-076115	0.061	G
12 26 23.9	32 44 31.0	NGC 4395:[R97] 12	0.242	Sy1
12 30 14.2	25 18 05.0	MG2 J123013+2517	0.135	BL Lac
12 31 32.5	64 14 20.0	[HB89] 1229+645	0.164	BL Lac
12 32 03.6	20 09 30.0	MRK 771	0.064	Sy1
12 36 51.1	45 39 07.0	CGCG 244-033	0.029	Sy1.5
12 36 58.8	63 11 11.0	ABELL 1576:[HHP90]	0.302	G
12 37 05.6	30 20 03.0	FIRST J123705.5+30200	0.700	BL Lac
12 37 39.2	62 58 43.0	[HB89] 1235+632	0.297	BL Lac
12 38 08.3	53 26 04.0	87GB 123550.3+534219	0.347	Sy1
12 39 23.1	41 32 45.0	FIRST J123922.7+41325		BL Lac
12 41 41.2	34 40 32.0	FIRST J124141.3+34403		BL Lac
12 41 44.4	35 03 53.0	NGC 4619	0.023	Sy1
12 42 11.3	33 17 03.0	WAS 61	0.044	Sy1
12 43 12.5	36 27 43.0	TON 0116		BL Lac
12 47 01.3	44 23 25.0	RGB J1247+443		AGN
12 48 18.9	58 20 31.0	PG 1246+586		BL Lac
12 50 52.5	41 07 13.0	MESSIER 94	0.001	LINER
12 53 01.0	38 26 29.0	FIRST J125300.9+38262	0.360	BL Lac
12 57 31.7	24 12 46.0	1ES 1255+244	0.141	BL Lac
13 02 55.6	50 56 21.0	RX J1302.9+5056	0.688	BL Lac
13 05 52.6	30 54 06.0	ABELL 1677	0.183	GClstr
13 13 27.2	36 35 42.0	NGC 5033	0.003	Sy1.9
13 19 57.2	52 35 33.0	RX J1319.9+5235	0.092	Sy
13 20 16.3	33 08 29.0	RX J1320.1+3308	0.036	GClstr
13 22 48.5	54 55 27.0	RX J1322.8+5455	0.064	Sy1
13 24 00.2	57 39 19.0	87GB 132204.6+575429	0.115	BL Lac
13 25 49.2	59 19 37.0	ABELL 1744:[HHP90]	0.151	GClstr
13 26 15.0	29 33 33.0	87GB 132354.7+294853	0.431	BL Lac
13 34 47.5	37 11 00.0	BH CVn		star (F2IVRSCVn)
13 35 08.2	20 46 41.0	RX J1335.1+2046		star
13 37 18.8	24 23 07.0	[HB89] 1334+246	0.108	Sy1
13 40 29.9	44 10 08.0	87GB 133822.3+442514	0.548	BL Lac
13 41 04.8	39 59 42.0	B3 1338+402	0.163	BL Lac
13 41 52.6	26 22 30.0	1RXS J134152.6+262230		GClstr
13 45 45.1	53 33 01.0	87GB 134352.4+534755	0.135	Sy1
13 48 52.6	26 35 41.0	ABELL 1795:[MK91]	0.062	GClstr
13 53 04.8	69 18 33.0	UGC 08823	0.029	Sy1.5
13 53 28.2	56 01 02.0	RX J1353.4+5601	0.370	BL Lac
13 54 20.2	32 55 47.0	UGC 08829	0.026	Sy1

(continued on the next page)

X-ray count rate limit $hcps \geq 0.09$ (RASS-BSC), radio flux limit $f_R(1.4\,\mathrm{GHz}) \geq 2.5\,\mathrm{mJy}$ (NVSS)

The objects of the NVSS/BSC correlation

α	δ	Name	Redshift	Classification
13 55 15.9	56 12 44.0	RX J1355.2+5612	0.122	Sy1
13 55 53.3	38 34 28.0	MRK 464	0.051	Sy1.5
14 04 50.2	65 54 34.0	RX J1404.8+6554	0.364	BL Lac
14 06 22.2	22 23 50.0	PG 1404+226	0.098	Sy
14 10 31.6	61 00 21.0	RX J1410.5+6100	0.384	BL Lac
14 13 42.6	43 39 38.0	MAPS-NGP O-221-004710	0.089	G
14 13 58.3	76 44 56.0	1RXS J141358.3+764456	0.068	Sy1
14 17 56.8	25 43 29.0	1E 1415+259	0.237	BL Lac
14 17 59.6	25 08 18.0	SN 1984Z	0.017	SNR in NGC5548
14 21 36.4	49 33 05.0	MCG +08-26-021	0.071	G
14 21 39.7	37 17 43.0	RX J1421.6+3717	0.160	GClstr
14 22 39.1	58 02 00.0	RGB J1422+580	0.638	BL Lac
14 23 13.4	50 55 37.0	87GB 142127.2+510856	0.274	Sy1
14 23 53.6	40 15 33.0	RX J1423.8+4015		GClstr
14 23 56.0	26 26 30.0	1RXS J142356.0+262630		Prob. GClstr
14 26 01.3	37 49 36.0	ABELL 1914	0.171	GClstr
14 27 00.5	23 48 03.0	PG 1424+240		BL Lac
14 28 32.6	42 40 28.0	1ES 1426+428	0.129	BL Lac
14 31 04.8	28 17 16.0	MRK 684	0.046	Sy1
14 31 06.2	25 38 15.0	RX J1431.1+2538	0.096	GClstr
14 32 36.0	31 38 55.0	RX J1432.5+3138	0.132	GClstr
14 39 17.7	39 32 49.0	PG 1437+398		BL Lac
14 42 07.7	35 26 32.0	MRK 478	0.079	Sy1
14 42 18.9	22 18 20.0	UGC 09480	0.097	GClstr
14 43 02.8	52 01 41.0	3C 303	0.141	G
14 44 33.9	63 36 04.0	MS 1443.5+6349	0.299	BL Lac
14 48 01.0	36 08 33.0	[WB92] 1446+3620		BL Lac
14 49 32.3	27 46 30.0	RBS 1434	0.228	BL Lac
14 51 08.5	27 09 33.0	PG 1448+273	0.065	Sy1
14 56 03.4	50 48 24.0	RX J1456+5048	0.480	BL Lac
14 57 15.4	22 20 26.0	MS 1455.0+2232	0.258	GClstr
14 58 27.3	48 32 50.0	RX J1458.4+4832	0.539	BL Lac
15 00 20.7	21 22 14.0	LEDA 140447	0.153	G
15 01 01.7	22 38 12.0	MS 1458.8+2249	0.235	BL Lac
15 04 13.1	68 56 10.0	[HB89] 1503+691	0.318	Sy1
15 07 44.6	51 27 10.0	MRK 845	0.046	Sy1
15 08 42.2	27 09 11.0	RBS 1467	0.270	BL Lac
15 10 40.8	33 35 15.0	RX J1510.6+3335	0.116	BL Lac
15 14 43.1	36 50 59.0	[HB89] 1512+370	0.371	QSO/Sy1?
15 17 47.3	65 25 23.0	1517+656	0.702	BL Lac
15 21 53.0	20 58 30.0	1RXS J152153.0+205830		star
15 23 46.0	63 39 30.0	4C +63.22	0.204	G
15 29 07.5	56 16 05.0	IRAS F15279+5626	0.099	Sy1
15 32 02.3	30 16 32.0	87GB 152959.0+302636	0.064	BL Lac
15 32 53.7	30 21 03.0	RBS 1509	0.361	LINER/GClstr
15 33 24.9	34 16 41.0	87GB 153121.5+342710		BL Lac
15 35 01.1	53 20 42.0	1ES 1533+535	0.890	BL Lac
15 35 52.0	57 54 04.0	MRK 290	0.030	Sy1
15 39 50.3	30 43 05.0	RX J1539.8+3043	0.097	GClstr
15 40 16.4	81 55 05.0	1ES 1544+820		BL Lac

(continued on the next page)

X-ray count rate limit $hcps \geq 0.09$ (RASS-BSC), radio flux limit $f_R(1.4\,\mathrm{GHz}) \geq 2.5\,\mathrm{mJy}$ (NVSS)

The objects of the NVSS/BSC correlation

α	δ	Name	Redshift	Classification
15 47 44.2	20 51 56.0	3C 323.1	0.264	QSO
15 54 24.3	20 11 16.0	MS 1552.1+2020	0.222	BL Lac
15 58 18.7	25 51 18.0	MRK 864	0.072	Sy2
15 59 09.5	35 01 45.0	UGC 10120	0.032	Sy1

Table 11.2: The HRX-BL Lac sample

Name	α	δ	z^a	$hcps^b$	f_R^c	B mag	Comment^d
RX J0710+5908	07 10 30.1	+59 08 20	0.125	0.803	159.2	18.4	*
RX J0712+5719	07 12 18.9	+57 19 48	0.095	0.078	7.9	20.1	Ca-break $\simeq$ 34%
0716+714	07 21 53.5	+71 20 36		0.103	727.2	15.5	*
MS 0737.9+7441	07 44 05.1	+74 33 58	0.0311	0.360	23.3	16.9	*
RX J0749+7451	07 49 29.7	+74 51 45	0.605	0.230	44.8	18.9	*
RX J0803+4816	08 03 22.9	+48 16 19	0.503	0.074	12.6	18.8	
RX J0805+7534	08 05 26.9	+75 34 25	0.121	0.209	52.6	18.1	*
RX J0806+5931	08 06 25.9	+59 31 06		0.162	60.9	17.9	*
RX J0809+3455	08 09 38.5	+34 55 37	0.082	0.204	223.4	17.0	*
RX J0809+5218	08 09 49.0	+52 18 56	0.138	0.371	182.8	15.6	*
RX J0816+5739	08 16 22.7	+57 39 09		0.075	100.0	18.8	
RX J0832+3300	08 32 52.0	+33 00 11	0.671	0.099	6.6	20.7	*
RX J0833+4726	08 33 57.1	+47 26 51	0.496	0.067	11.6	19.7	
RX J0854+4408	08 54 09.8	+44 08 31		0.063	79.8	18.5	
RX J0854+6218	08 54 50.5	+62 18 50	0.267	0.061	387.6	19.0	
RX J0859+8344	08 59 10.1	+83 45 04	0.327	0.100	10.2	19.7	*
RX J0903+4056	09 03 14.7	+40 56 01	0.190	0.080	38.2	19.3	
B2 0906+31	09 09 53.3	+31 06 02	0.274	0.185	195.5	18.3	*
RX J0913+8133	09 13 20.4	+81 33 06	0.639	0.190	4.9	20.7	*
B2 0912+29	09 15 52.2	+29 33 20		0.286	342.0	16.3	*
RX J0916+5238	09 16 52.0	+52 38 27	0.190	0.175	138.9	18.3	*
RX J0924+0533	09 24 01.1	+05 33 50		0.108	7.5	19.6	
RX J0928+7447	09 28 03.0	+74 47 19	0.638	0.093	85.8	20.8	*
1ES 0927+500	09 30 37.6	+49 50 24	0.186	1.154	21.4	18.0	*, Ca-break $\simeq$ 25%
RX J0930+3933	09 30 56.9	+39 33 37	0.641	0.068	13.0	19.5	Ca-break $\simeq$ 30%
RX J0940+6148	09 40 22.5	+61 48 25	0.212	0.070	12.8	18.4	Ca-break $\simeq$ 30%
RX J0952+3936	09 52 14.0	+39 36 08	0.810	0.056	3.0	19.8	*
RX J0952+7502	09 52 23.8	+75 02 13		0.165	12.2	19.3	
RX J0954+4914	09 54 09.8	+49 14 59	0.207	0.067	2.7	19.3	
RX J0959+2123	09 59 30.0	+21 23 19	0.367	0.193	40.8	19.1	*
RX J1006+3454	10 06 56.3	+34 54 44	0.612?	0.058	6.6	18.7	
RX J1008+4705	10 08 11.4	+47 05 20	0.343	0.383	4.7	19.9	*
RX J1012+4229	10 12 44.2	+42 29 57	0.376	0.332	79.5	18.4	*
GB 1011+496	10 15 04.0	+49 25 59	0.200	0.594	378.1	16.5	*
RX J1016+4108	10 16 16.8	+41 08 12	0.281	0.216	14.8	19.5	*
MS 1019.0+5139	10 22 11.3	+51 24 15	0.141	0.286	5.1	18.0	*
1ES 1028+511	10 31 18.6	+50 53 34	0.361	1.561	37.9	16.8	*
RX J1037+5711	10 37 44.3	+57 11 56		0.054	71.7	16.7	
RX J1041+3901	10 41 49.0	+39 01 22	0.210	0.061	33.9	18.5	Ca-break $\simeq$ 30%
RX J1051+3943	10 51 25.4	+39 43 26	0.498	0.145	10.8	19.0	*
RX J1056+0252	10 56 06.3	+02 52 28	0.235	0.488	4.3	19.4	
RX J1057+2303	10 57 23.0	+23 03 15	0.378	0.185	7.9	19.7	*

[a] possible redshift marked with a "?"
[b] ROSAT PSPC (0.5 - 2.0 keV) count rate
[c] radio flux at 1.4 GHz in mJy
[d] objects forming the complete HRX-BL Lac sample marked with an asterix

The HRX-BL Lac sample

Name	α	δ	z^a	$hcps^b$	f_R^c	B mag	Comment^d
RX J1058+5628	10 58 37.8	+56 28 09	0.144	0.120	228.5	15.8	*
RX J1100+4019	11 00 21.0	+40 19 29	0.225?	0.192	18.3	18.6	*
MRK 421	11 04 27.3	+38 12 32	0.030	9.970	768.5	13.3	*
RX J1107+1502	11 07 48.2	+15 02 17		0.188	43.5	18.4	
RX J1111+3452	11 11 30.9	+34 52 01	0.212	0.233	8.4	19.7	*
RX J1117+2014	11 17 06.3	+20 14 08	0.137	2.060	103.1	16.0	*
1ES 1118+424	11 20 48.1	+42 12 12	0.124	0.383	24.1	18.0	*
RX J1123+7230	11 23 49.2	+72 30 18		0.155	12.5	18.6	*
MRK 180	11 36 26.6	+70 09 25	0.046	1.711	328.4	14.7	*
HS 1133+6753	11 36 30.3	+67 37 05	0.135	0.977	45.8	17.6	*
RX J1147+2205	11 47 54.9	+22 05 34	0.176	0.117	4.1	21.0	*, Ca-break $\simeq$ 33%
RX J1149+2439	11 49 30.3	+24 39 27	0.402	0.215	28.5	19.0	*
RX J1211+2242	12 11 58.7	+22 42 32	0.455	0.217	20.2	19.6	*
ON 325 / B2 1215+30	12 17 52.0	+30 07 02	0.130	1.007	572.7	15.6	*
PG 1218+304	12 21 21.8	+30 10 37	0.182	0.776	71.5	17.7	*
ON 231 / W Comae	12 21 31.7	+28 13 58	0.102	0.084	732.1	16.5	
RX J1224+2436	12 24 24.2	+24 36 24	0.218	0.082	25.9	17.7	
RX J1230+2518	12 30 14.0	+25 18 07	0.135	0.115	244.0	16.0	*
MS 1229.2+6430	12 31 31.5	+64 14 16	0.164	0.166	58.8	18.0	*
RX J1231+2847	12 31 43.9	+28 47 51	0.236	0.071	141.5	17.5	
RX J1237+3020	12 37 06.0	+30 20 05	0.700	0.276	5.6	20.0	*
MS 1235.4+6315	12 37 39.1	+62 58 41	0.297	0.139	12.5	18.9	*
RX J1239+4132	12 39 22.7	+41 32 52		0.099	9.1	20.3	*
RX J1241+3440	12 41 41.4	+34 40 31		0.091	10.2	20.2	*
RX J1243+3627	12 43 12.7	+36 27 45		0.402	147.9	16.6	*
RX J1248+5820	12 48 18.8	+58 20 29		0.152	245.3	14.9	*
RX J1253+3826	12 53 00.9	+38 26 26	0.360	0.373	4.8	18.9	*
1ES 1255+244	12 57 31.9	+24 12 40	0.141	0.412	14.7	15.4	*
RX J1302+5056	13 02 58.0	+50 56 18	0.688	0.241	2.8	19.3	*
RX J1324+5739	13 24 00.0	+57 39 16	0.115	0.096	44.2	17.8	*
RX J1326+2933	13 26 15.0	+29 33 30	0.431	0.128	5.6	18.7	*
RX J1340+4410	13 40 29.5	+44 10 07	0.548	0.163	57.2	19.3	*
RX J1341+3959	13 41 04.9	+39 59 35	0.163	0.333	88.8	18.6	*
RX J1345+4257	13 45 55.3	+36 50 14	0.255	0.035	144.8	20.3	Ca-break $\simeq$ 34%
RX J1353+5601	13 53 28.0	+56 00 55	0.370	0.114	14.9	19.1	*
RX J1404+6554	14 04 49.6	+65 54 30	0.364	0.091	15.4	19.4	*
RX J1410+6100	14 10 31.7	+61 00 10	0.384	0.116	11.4	19.9	*
1E 1415+259	14 17 56.6	+25 43 25	0.237	0.889	89.6	16.0	*
RX J1419+5423	14 19 46.6	+54 23 15	0.151	0.055	788.7	15.7	
RX J1422+5801	14 22 39.0	+58 01 55	0.638	0.867	13.2	17.9	*
RX J1424+3434	14 24 22.7	+34 33 57	0.571?	0.069	10.0	18.3	
RX J1427+2348	14 27 00.5	+23 48 03		0.167	430.1	16.4	*
1ES 1426+428	14 28 32.6	+42 40 21	0.129	1.880	58.8	16.5	*
RX J1436+5639	14 36 57.8	+56 39 25		0.087	21.3	18.8	
RX J1439+3932	14 39 17.5	+39 32 43		0.445	42.8	16.0	*
MS 1443.5+6349	14 44 34.9	+63 36 06	0.299	0.091	18.9	19.7	*
RX J1448+3608	14 48 01.0	+36 08 33		0.135	36.2	17.2	*
RX J1449+2746	14 49 32.7	+27 46 22	0.228	0.293	90.7	20.0	*

[a] possible redshift marked with a "?"
[b] ROSAT PSPC (0.5 - 2.0 keV) count rate
[c] radio flux at 1.4 GHz in mJy
[d] objects forming the complete HRX-BL Lac sample marked with an asterix

The HRX-BL Lac sample

Name	α	δ	z^a	$hcps^b$	f_R^c	B mag	Comment^d
RX J1451+6354	14 51 26.0	+63 54 24	0.650	0.077	10.0	19.6	
RX J1456+5048	14 56 03.7	+50 48 25	0.480	0.734	4.0	18.6	*
RX J1458+4832	14 58 28.0	+48 32 40	0.539	0.224	3.1	20.4	*
RX J1501+2238	15 01 01.9	+22 38 06	0.235	0.165	32.4	15.5	*
RX J1508+2709	15 08 42.7	+27 09 09	0.270	0.242	39.9	18.8	*
RX J1510+3335	15 10 42.0	+33 35 09	0.116	0.148	8.8	18.5	*, Ca-break $\sim$ 35%
1517+656	15 17 47.5	+65 25 24	0.702	0.673	37.7	16.9	*
RX J1532+3016	15 32 02.2	+30 16 29	0.064	0.227	54.4	15.5	*
RX J1533+3416	15 33 24.3	+34 16 40		0.112	30.0	17.9	*
1ES 1533+5320	15 35 00.8	+53 20 35	0.890?	0.691	18.2	18.9	*
RX J1535+3922	15 35 29.1	+39 22 47	0.257	0.006	19.7	19.8	
1ES 1544+820	15 40 15.7	+81 55 06		0.322	69.9	17.1	*
RX J1554+2414	15 54 11.9	+24 14 28	0.301	0.075	12.7	20.4	
MS 1552.1+2020	15 54 24.1	+20 11 25	0.222	0.194	79.4	18.5	*

Table 11.3: Photometry of HRX-BL Lac

Name	Jul. Date	Exp. Time[a]	B [mag]	1σ[mag]	Standard[b]
RX J0859+8345	2451669.3484	600	19.73	0.19	P066-B
RX J0909+3105	2451667.3408	240	18.28	0.07	P313-D
RX J0913+8133	2451667.3582	600	20.7	0.10	P125-E P006-D
RX J0916+5238	2451667.3471	600	18.33	0.05	P313-D P125-E
RX J0924+0533	2451669.3724	500	19.60	0.09	P547-B
RX J0928+7447	2451667.3694	800	20.7	0.10	P006-D P018-E
RX J0952+7502	2451669.3713	500	19.20	0.19	P066-B P018-B
RX J0959+2133	2451669.3817	400	19.06	0.06	P547-B P371-A
RX J1008+4705	2451669.3959	400	19.92	0.10	P212-D P167-C
RX J1012+4229	2451669.3890	300	18.42	0.05	P371-A P212-D
RX J1016+4108	2451669.4036	200	19.46	0.05	P167-C P212-D
RX J1051+3943	2451665.3856	800	19.0	0.18	P213-A P551-C
RX J1054+3855	2451663.3643	120	17.8		P213-A
RX J1054+3855	2451665.3759	300	17.3		P213-A
RX J1056+0252	2451667.3871	900	19.39	0.05	P018-E P551-C
RX J1057+2303	2451663.3798	600	19.74	0.05	P213-A P373-D
RX J1100+4019	2451667.4236	300	18.56	0.05	P214-E P214-D
RX J1107+1502	2451667.4153	400	18.4	0.20	P491-A
RX J1111+3452	2451667.4031	800	19.7	0.05	P551-C P491-A
RX J1120+4212	2451667.4313	200	18.0	0.20	P214-D
RX J1149+2439	2451667.4403	400	19.0	0.20	P265-C
RX J1153+3617	2451663.3941	120	17.51		P273-D P265-C
RX J1211+2242	2451663.4011	500	19.55	0.05	P265-C P376-F
RX J1230+2518	2451663.4146	60	16.04	0.10	P376-F P377-A
RX J1230+2518	2451667.4591	150	15.94	0.05	P377-A
RX J1231+6414	2451667.4515	300	18.0	0.20	P064-A
RX J1237+6258	2451663.4359	600	18.85	0.05	P095-D
RX J1239+4132	2451663.4240	600	20.34	0.10	P377-A
RX J1241+3440	2451663.4466	600	20.18	0.16	P267-C
RX J1243+3627	2451667.4660	300	16.60	0.10	P377-A P267-E
RX J1248+5820	2451667.4749	200	14.89	0.05	P267-E
RX J1253+3826	2451663.4631	500	18.9	0.20	P267-C
RX J1302+5056	2451663.4761	600	19.3	0.20	P131-A
RX J1324+5739	2451667.4944	200	17.75	0.05	P219-D P096-A
RX J1326+2913	2451663.4868	500	18.69	0.05	P131-A P173-F
RX J1340+4410	2451663.4965	400	19.25	0.11	P173-F
RX J1341+3959	2451667.4868	400	18.6	0.22	P219-D
RX J1353+5600	2451667.5000	600	19.10	0.05	P096-A P097-A
RX J1404+6554	2451663.5053	600	19.36	0.08	P066-A
RX J1410+6100	2451667.5774	1200	19.89	0.07	P066-E
RX J1422+5801	2451663.5169	400	17.82	0.07	P098-A
RX J1444+6336	2451663.5600	600	19.7	0.20	P067-E
RX J1449+2746	2451667.5362	600	20.03	0.10	P382-B PKS1510-089
RX J1456+5048	2451663.5506	400	18.57	0.07	P067-E
RX J1458+4832	2451667.5146	1200	20.37	0.09	P382-B
RX J1501+2238	2451667.6018	180	15.53	0.05	P066-E P382-B
RX J1508+2709	2451663.5842	600	18.77	0.05	1517+656 P327-G
RX J1510+3335	2451663.6097	500	18.50	0.07	P385-B P327-G
RX J1517+6525	2451663.5756	150	16.87	0.04	Standard field
RX J1535+5320	2451663.6192	400	18.9	0.20	P327-G P008-B

[a] exposure time in seconds
[b] photometric standard from the GSCPC used for calibration

Photometry of HRX-BL Lac

Name	Jul. Date	Exp. Time	B [mag]	1σ[mag]	Standard
RX J1544+8155	2451663.6287	300	17.1	0.18	P008-B
RX J1554+2011	2451663.6021	300	18.45	0.05	P327-G P385-B
RX J1554+2414	2451663.6413	300	20.4	0.20	P385-D

Table 11.4: BL Lac candidates which turned out to be no BL Lacs

Name	α	δ	z	Type
RX J0751+5512	07 51 22.3	+55 12 09	0.340	Sy1
RX J0754+4316	07 54 07.9	+43 16 10	0.388	Sy1
RX J0806+7248	08 06 38.9	+72 48 20	0.097	NLSy1
RX J0807+3400	08 07 30.8	+34 00 42	0.208	Gal. (Ca break 51%)
RX J0819+6337	08 19 25.8	+63 37 26	0.118	Gal. (Ca break 59%)
RX J0826+3108	08 26 53.5	+31 08 05	0.205	Gal. (Ca break 59%)
RX J0900+2054	09 00 35.5	+20 54 51	0.31	Gal. (Ca break 42%)
RX J0918+3156	09 18 33.9	+31 56 20	0.451	Sy1
RX J1005+4332	10 05 41.0	+43 32 27	0.178	Sy1
RX J1054+1506	10 54 43.0	+15 06 57	0.582	Sy1
RX J1119+4130	11 19 07.1	+41 30 15	0.094	Sy1[a]
RX J1131+3334	11 31 20.9	+33 34 46	0.222	Gal.[b]
RX J1226+3244	12 26 24.0	+32 44 33	0.242	Sy1
RX J1238+5325	12 38 08.2	+53 25 56	0.347	Sy1
RX J1324+2802	13 24 22.8	+28 02 32	0.124	Sy1
RX J1345+5332	13 45 45.6	+53 32 55	0.135	Sy1
RX J1353+2809	13 53 08.4	+28 09 09	0.516	Sy1
RX J1408+2409	14 08 27.3	+24 09 29	0.129	NLSy1
RX J1413+7644	14 13 58.0	+76 44 57	0.068	Sy2
RX J1424+2514	14 24 24.5	+25 14 28	0.237	Gal.[c]
RX J1434+2317	14 34 44.9	+23 17 43	0.100	Sy1
RX J1535+7948	15 35 31.7	+79 48 49	0.072	Sy1.5
RX J1551+1911	15 51 55.1	+19 11 08	2.821	QSO
RX J1701+3404	17 01 02.6	+34 04 09	0.094	Sy1

[a)] two more galaxies ($z = 0.096$, $z = 0.094$) within the BSC error circle
[b)] calcium break $\sim 46\%$. The core shows strong [NII], H_α and [SII] lines - Seyfert II core?
[c)] equivalent width of $H_\alpha = 67$ Å

11.2 Formulae to the HRX-BL Lac description

11.2.1 Parabola

Given three points $[x_i, y_i]; i = [1..3]$ the parameters for a parabola $y = a \cdot x^2 + b \cdot x + c$ are given by

$$a = \frac{y_3 - y_1 - \frac{y_2 - y_1}{x_2 - x_1} \cdot x_3 + x_1 \cdot \frac{y_2 - y_1}{x_2 - x_1}}{((x_3^2 + x_1^2 \cdot \frac{x_3}{x_2 - x_1} - x_2^2 \cdot \frac{x_3}{x_2 - x_1} - x_1^2) - x_1^3) \cdot (x_2 - x_1)} + \frac{x_1 \cdot x_2^2}{x_2 - x_1} \tag{11.1}$$

$$b = \frac{y_2 - y_1 + a \cdot x_1^2 - a \cdot x_2^2}{x_2 - x_1} \tag{11.2}$$

$$c = y_1 - a \cdot x_1^2 - b \cdot x_1 \tag{11.3}$$

The peak of the parabola occurs at the point x_{peak} which is simply

$$x_{peak} = \frac{-b}{2a} \tag{11.4}$$

with a peak value

$$y_{peak} = \frac{a \cdot b^2}{4} - \frac{b^2}{2a} + c \tag{11.5}$$

11.2.2 Student's distribution

To test the probability of a correlation between n observed pairs of parameter $[X_i, Y_i]_{i=1..n}$ the hypothesis H_0 is tested, if the two parameters are *not* correlated. The Pearsons correlation-coefficient r_{XY} can be used for this

Table 11.5: Seyfert II sample

Name	α	δ	ESO-field	z	Cand.[a]	Type[b]
HE 0058-4740	01 01 14.2	-47 24 31	195	0.025	2	2
HE 0113-5027	01 15 55.3	-50 11 22	195	0.024	1	1
HE 0047-5107	00 49 45.2	-50 50 41	195	0.060	1	2
HE 0209-4956	02 10 52.5	-49 41 56	197	0.047	1	1
HE 0348-5027	03 50 23.0	-50 18 10	201	0.037	1	1
HE 0506-5047	05 08 06.3	-50 43 52	203	0.049	1	1
HE 0508-5016	05 10 14.4	-50 12 48	203	0.049	2	1
HE 0411-4131	04 13 24.0	-41 23 44	303	0.027	2	1
HE 0201-3029	02 03 25.1	-30 14 55	414	0.036	1	1
HE 0235-2913	02 37 15.2	-29 00 22	416	0.050	2	3
HE 0246-3122	02 49 03.9	-31 10 21	416	0.020	1	1
HE 0254-3223	02 56 21.5	-32 11 09	417	0.016	1	1
HE 0436-3017	04 29 52.4	-30 15 22	421	0.055	2	1
HE 0436-2908	04 38 48.3	-29 02 18	421	0.044	2	1
HE 1132-3015	11 35 25.7	-30 32 26	439	0.031	1	3
HE 1202-2937	12 04 51.0	-29 54 04	440	0.059	2	3
HE 1146-3206	11 49 31.0	-32 23 04	440	0.021	1	1
HE 0051-2420	00 53 54.4	-24 04 36	474	0.056	1	1
HE 0128-2609	01 30 26.0	-25 53 47	476	0.031	1	3
HE 1045-2453	10 48 23.5	-25 09 43	501	0.012	1	1
HE 1103-2519	11 05 54.7	-25 35 20	502	0.012	2	3
HE 1223-2319	12 26 02.4	-23 36 22	506	0.048	1	1
HE 1252-2640	12 54 56.3	-26 57 02	507	0.058	1	1
HE 1331-2311	13 34 39.6	-23 26 48	509	0.034	1	1
HE 1335-2344	13 37 49.9	-23 59 41	509	0.030	1	1
HE 0136-2042	01 39 20.4	-20 27 12	543	0.045	1	1
HE 0154-2047	01 57 00.7	-20 33 02	543	0.045	2	3
HE 0448-2125	04 50 20.3	-21 20 20	552	0.032	2	3
HE 1020-1925	10 22 57.1	-19 40 47	568	0.022	2	2

[a)] candidate type within selection process: 1 = secure, 2 = probably
[b)] spectroscopic type: 1 = Seyfert II, 2 = probable SyII, 3 = Sy2, LINER, or NELG

test. This coefficient has a value within the interval $[-1;+1]$. If $r_{XY} = 0$, no correlation is detected. Assuming that X and Y are normal distributed then r_{XY} can be used to test if X and Y are independent. If the (unknown) correlation coefficient $\rho = 0$ then

$$t = \frac{r_{XY} \cdot \sqrt{n-2}}{\sqrt{1 - {r_{XY}}^2}} \tag{11.6}$$

is the realization of a t-distributed random variable with $n-2$ degrees of freedom. The t-distribution, also called Students distribution, is tabulated for different n and t values (e.g. Bronstein & Semendjajew 1987). This results in a significance level on which the assumption that X and Y are uncorrelated can be rejected.

11.3 Tables to the Seyfert II sample

Table 11.6: False Seyfert II candidates

Name	α	δ	ESO field	z	type
HE 0146-5217	01 48 00.0	-52 02 59	197	0.047	galaxy
HE 0346-4856	03 47 46.6	-48 47 17	201	0.050	galaxy
HE 0345-5023	03 46 43.7	-50 13 53	201	0.054	galaxy

(continued on the next page)

False Seyfert II candidates

Name	α	δ	ESO field	z	type
HE 0403-4743	04 05 20.0	-47 35 13	201	0.055	galaxy
HE 0350-5035	03 52 22.9	-50 26 11	201	0.038	not clear
HE 0510-4812	05 12 16.4	-48 08 58	203	0.074	galaxy
HE 0513-4740	05 15 12.5	-47 37 26	203	0.039	NELG/LINER
HE 0504-5109	05 05 21.4	-51 05 51	203	0.055	NELG/LINER
HE 0459-494	05 00 41.0	-49 44 48	203	0.035	galaxy
HE 0204-4330	02 06 55.1	-43 15 56	245	0.078	galaxy
HE 0420-3856	04 22 38.6	-38 49 07	303	0.053	galaxy
HE 0303-2854	03 05 44.6	-28 43 03	417	0.073	galaxy
HE 0253-3002	02 55 16.1	-29 50 01	417	0.022	galaxy
HE 0313-2924	03 15 36.6	-29 13 39	417	0.068	NELG/LINER
HE 0312-3037	03 14 10.2	-30 26 47	417	0.068	galaxy
HE 0311-3020	03 13 49.0	-30 09 07	417	0.054	NELG/LINER
HE 0358-2755	04 00 39.3	-27 47 19	419	0.066	NELG/LINER
HE 0431-2924	04 33 13.7	-29 18 44	421	0.022	NELG/LINER
HE 0436-2908	04 38 01.0	-30 11 45	421	0.051	NELG/LINER
HE 0427-3021	04 27 14.4	-30 33 40	421	0.036	galaxy
HE 0455-2829	04 57 19.3	-28 29 30	422	0.018	galaxy
HE 1118-3127	11 20 42.1	-31 43 57	438	0.062	NELG/LINER
HE 1123-2837	11 25 50.2	-28 53 33	439	0.030	NELG/LINER
HE 1151-3029	11 53 48.5	-30 46 22	440	0.056	galaxy
HE 1159-3216	12 01 36.3	-32 33 38	440	0.000	star
HE 1213-3005	12 16 22.3	-30 22 10	441	0.049	NELG/LINER
HE 1218-3113	12 20 39.3	-31 30 00	441	0.009	NELG/LINER
HE 1224-3215	12 26 44.4	-32 32 01	441	0.015	galaxy
HE 1349-3135	13 52 07.2	-31 49 54	445	0.016	NELG/LINER
HE 1350-2819	13 52 55.5	-28 34 01	445	0.050	galaxy
HE 1353-2833	13 56 50.3	-28 48 34	445	0.038	galaxy
HE 0222-2458	02 24 30.0	-24 44 44	478	0.009	NELG/LINER
HE 0508-2546	05 10 30.8	-25 42 34	486	0.035	galaxy
HE 1041-2540	10 44 05.4	-25 56 13	501	0.000	star
HE 1037-2536	10 40 01.6	-25 52 13	501	0.047	galaxy
HE 1102-2334	11 05 14.8	-23 50 47	502	0.012	NELG/LINER
HE 1141-2454	11 44 01.1	-25 11 10	504	0.042	NELG/LINER
HE 1203-2315	12 06 06.7	-23 31 46	505	0.060	galaxy
HE 1209-2603	12 12 06.5	-26 19 43	505	0.000	galaxy
HE 1227-2558	12 30 10.1	-26 15 26	506	0.024	galaxy
HE 1250-2622	12 53 40.0	-26 39 15	507	0.009	galaxy
HE 1300-2644	13 02 59.9	-27 01 05	507	0.009	galaxy
HE 1250-2711	12 53 11.2	-27 27 53	507	0.011	NELG/LINER
HE 1303-2242	13 06 19.4	-22 58 49	508	0.009	NELG/LINER
HE 0314-1945	03 16 41.3	-19 34 11	547	0.029	galaxy
HE 0304-1821	03 06 24.7	-18 09 44	547	0.006	NELG/LINER
HE 0411-1931	04 13 25.1	-19 24 03	550	0.019	NELG/LINER
HE 0425-1744	04 28 11.8	-17 37 53	551	0.032	not clear
HE 0459-2007	05 01 41.3	-20 02 47	552	0.015	NELG/LINER
HE 0501-1911	05 03 54.3	-19 07 42	552	0.045	galaxy
HE 0456-2137	04 58 26.0	-21 32 47	552	0.023	galaxy
HE 0453-1901	04 55 47.9	-18 56 54	552	0.025	galaxy
HE 0515-1935	05 17 51.7	-19 32 20	553	0.018	NELG/LINER
HE 0504-2003	05 06 51.6	-19 59 40	553	0.025	NELG/LINER

(continued on the next page)

False Seyfert II candidates

Name	α	δ	ESO field	z	type
HE 1036-1947	10 38 57.2	-20 02 42	568	0.008	NELG/LINER
HE 1126-1733	11 29 10.9	-17 49 52	571	0.026	NELG/LINER

Table 11.7: Field characteristics of the Seyfert II sample

ESO field	B_J limit[a]	V limit[b]	N_H^c	C[d]	area[e]
195	17.8	17.0	3.35	2	15.2
197	17.6	16.8	2.55	1	14.2
201	17.4	16.7	1.59	2	14.6
203	17.8	17.0	1.53	2	13.9
245	17.5	16.7	1.53	1	15.3
303	17.0	16.3	2.22	2	13.8
411	17.5	16.7	2.10	0	11.6
413	17.3	16.5	1.81	0	10.5
414	17.4	16.6	1.64	2	12.1
416	17.5	16.8	2.13	2	10.3
417	17.6	16.9	1.47	2	15.2
419	17.7	17.1	0.92	2	14.1
421	17.5	16.7	2.86	2	13.0
422	17.3	16.7	1.06	2	11.4
438	17.2	16.3	5.02	2	5.3
439	17.3	16.5	5.32	2	6.0
440	17.2	16.5	4.52	2	5.9
441	17.1	16.2	5.15	1	6.5
445	16.7	15.9	5.26	1	3.8
474	17.6	16.8	1.25	1	11.6
476	17.3	16.6	1.37	2	12.1
478	17.3	16.6	1.37	1	9.9
485	17.1	16.5	1.74	1	9.0
486	17.1	16.5	1.79	2	11.6
501	17.0	16.1	4.54	2	8.1
502	17.0	16.2	5.28	2	13.8
503	16.9	16.1	3.91	2	6.8
504	16.8	16.0	3.99	2	9.6
505	17.5	16.5	6.74	2	9.0
506	17.7	16.6	7.32	1	7.1
507	16.7	15.7	6.46	2	7.5
508	17.0	16.1	7.11	2	6.3
509	17.6	16.7	5.07	1	5.5
543	17.4	16.7	1.08	2	13.7
547	16.9	16.2	2.32	2	13.0
550	16.7	16.0	2.23	2	12.0
551	16.7	16.0	2.27	2	10.5
552	16.9	16.1	3.10	1	8.7
553	16.6	15.9	3.12	2	12.5
568	16.5	15.7	5.09	1	9.5
571	17.0	16.2	4.05	0	14.7

[a)] B_J limit of the plate corresponding to *spcmag* = 17.0
[b)] V limit of the plate, corrected for galactic extinction
[c)] galactic hydrogen column density at the center of the field
[d)] Completeness; 0 = not complete, 1 = complete for type 1 candidates, 2 = complete for type 2 candidates
[e)] effective surveyed area, corrected for overlapping fields and spectra

Chapter 12

References

In cases where the reference is not published in a "standard" Journal, the Internet address is added, or, if available, the preprint number for the astro-ph preprint server[1]

Aaronson M., Huchra J., Mould J., et al., 1982, ApJ **258**, 65

Abraham R. G., Tanvir N. R., Santiago B. X., et al., 1996, MNRAS **279**, L49

Akiyama M., Ohta K., Yamada T., et al., 1998, ApJ **500**, 173

Anders E., Ebihara M., 1982, Geochim. Cosmochim. Acta, **46**, 2363

Andrew B. H., MacLeod J. M., Locke J. L., et al., 1969, Nature **223**, 598

Antonucci R., 1993, ARA&A **31**, 473

Athanassoula E., 1992, MNRAS **259**, 345

Avni Y., Bahcall J. N., 1980, ApJ **235**, 694

Bade N., Fink H. H., Engels D., 1994, A&A **286**, 381

Bade N., Beckmann V., Douglas N. G., et al., 1998, A&A **334**, 459

Bade N., Engels D., Voges W., Beckmann V., et al., 1998b, A&AS **127**, 145

Ball L., Kirk J. G., 1992, ApJ **396**, L42

Barnes J. E., 1999, in *Galaxy Interactions at Low and High Redshifts* (eds. J. E. Barnes & D. B. Sanders), pp. 137, Dordrecht: Kluwer

Becker R. H., White R. L., Edwards A. L., 1991, ApJS **75**, 1

Becker R. H., White R. L., Helfand D. J., 1995, ApJ **450**, 559

Beckmann V., 1996, diploma thesis, Hamburg University, http://www.hs.uni-hamburg.de/english/persons/beckmann3.html

Beckmann V., Bade N., Wucknitz O., 1999, A&A **352**, 395

Beckmann V., 1999, in: PASPC Vol. **159**, eds. L. O. Takalo, A. Sillanpää, p. 493, astro-ph/9810154

Beckmann V., Wolter A., 2000, accepted for publication in *Astrophysical Letters and Communications*, astro-ph/0007089

Beckmann V., 2000, *BLAZAR Data* **2**, 3, http://bldata.pg.infn.it/articles.html

Beckmann V., Wolter A., Giommi P., et al., 2001, A&A in prep.

[1]see e.g. http://xxx.uni-augsburg.de/find/astro-ph

Bender R., Saglia R. P., Ziegler B. L., et al., 1998, ApJ **493**, 529

Bergeron J., D'Odorico S., 1986, MNRAS **220**, 833

Biraud F., Véron P., 1968, Nature **219**, 254

Birkle K., 1984, In: Astronomy with Schmidt-type Telescopes ed. Capaccioli (Reidel, Dordrecht) 203

Blades J. C., Hunstead R. W., Murdoch H. S., Pettini M., 1985, ApJ **288**, 580

Blain A. W., Jameson A., Smail I., 1999, MNRAS **309**, 715

Blake G. M., 1970, Ap. Letters **6**, 201

Blandford R. D., Znajek R. L., 1977, MNRAS **179**, 433

Blandford R. D., Rees M. J., 1978, in Pittsburgh Conference on BL Lac objects, ed. A. M. Wolfe

Blandford R. D., 1993, in *Astrophysical Jets*, ed. D. Bulgarella, M. Livio, & C. P. O'Dea (Cambridge: Cambridge Univ. Press), p. 15

Blandford R. D., Levinson A., 1995, ApJ **441**, 79

Bloom S. D., Marscher A. P., 1996, ApJ **461**, 657

Boella G., Chiappetti L., Conti G., et al., 1997, A&AS **122**, 327

Bolton J. G., Wall J. V., 1969, Astrophysical Letters **3**, 177

Bolzano V. A., 1983, ApJ **268**, 602

Boyce P. J., Disney M. J., Blades J. C., et al., 1996, ApJ **473**, 760

Boyle B. J., Shanks T., Peterson B. A., 1988, MNRAS **235**, 935

Brinkmann, W., 1991, In: Physics of Active Galactic Nuclei, Proceedings of the International Conference, Heidelberg, 3.-7.June 1991, Eds. Duschl, W. J., Wagner, S.J.

Brinkmann W., Siebert J., 1994, A&A **285**, 812

Brinkmann W., Siebert J., Feigelson E. D., et al., 1997, A&A **323**, 739

Bronstein I. N., Semendjajew K. A., 1987, "Taschenbuch der Mathematik", eds. Grosche et al., Teubner, Leipzig, and Nauka, Moscow

Buckley J. H., Akerlof C. W., Biller S., et al., 1996, ApJ **472**, L9

Bulgarella D., Livio M., O'Dea C. P. (editors), 1993, *Astrophysical Jets*, Cambridge, Cambridge University Press

Buta R., 1986a, ApJS **61**, 609

Buta R., 1986b, ApJS **61**, 631

Caccianiga A., Maccacaro T., Wolter A., et al., 1999, ApJ **513**, 51

Cagnoni I., Della Ceca R., Maccacaro T., 1998, ApJ **493**, 54

Caon N., Capaccioli M., D'Onofrio M., 1993, MNRAS **265**, 1013

Capetti A., Trussoni E., Celotti A., et al., 2000, MNRAS **318**, 493, astro-ph/0007434

Catanese M., Akerlof C. W., Badran H. M., et al., 1998, ApJ **501**, 616

Cavaliere A., Vittorini V., 1998, in PASPC **146**, ed. S. D'Odorico, A. Fontana, E. Giallongo, p. 26, astro-ph/9802320

Cavaliere A., Malquori D., 1999, ApJ **516**, L9

Celotti A., Maraschi L., Ghisellini G., et al.., 1993, ApJ **416**, 118

Chadwick P. M., Lyons K., McComb T. J. L., et al., 1999, ApJ **513**, 161

Cheng F. Z., Danese L., De Zotti G., Franchesini A., 1985, MNRAS **212**, 857

Christlieb N., 2000, Doctoral thesis, Hamburg University, http://www.hs.uni-hamburg.de/german/persons/nchristlieb/homepage/publications/onlinediss/ncdiss.html

Ciliegi P., Maccacaro T., 1996, MPE Report **263**, 437

Colina L., Arribas S., 1999, ApJ **514**, 637

Comastri A., Molendi S., Ghisellini G., 1995a, MNRAS **277**, 297

Comastri A., Setti G., Zamorani G., Hasinger G., 1995b, A&A **296**, 1

Condon J.J., Cotton W. D., Greisen E. W., et al., 1998, AJ **115**, 1693

Cooke B. A., Ricketts M. J., Maccacaro T., et al., 1978, MNRAS **182**, 489

Cordis L., Bade N., Engels D., Voges W., 1996, MPE Report **263**, 441

Costamante L., Ghisellini G., Celotti A., 2000, accepted for publication in *Astrophysical Letters and Communications*, astro-ph/0007020

Davis M., Huchra J., Latham D., 1983, in IAU Symp. 104, Early Evolution of the Universe and Its Present Structure, ed. G. Abell & G. Chincarini (Dordrecht: Reidel)

de Carvalho R. R., Djorgovski S., 1992, ApJ **389**, L49

Della Ceca R., Zamorani G., Maccacaro T., et al., 1996, ApJ **465**, 650

Della Ceca R., Castelli G., Braito V., et al., 1999, ApJ **524**, 674, astro-ph/9904101

Della Ceca R., Braito V., Beckmann V., et al., 2000, in: Proceedings of the Fourth Italian Conference on AGNs, Trieste (Italy) May 15-18 2000. To be published in Mem. Soc. Astr. It., astro-ph/0007431

Della Ceca R., Pellegrini S., Beckmann V., et al., 2001, in prep.

Dermer C. D., Schlickeiser R., 1993, ApJ **416**, 458

Dressler A., Shectman S., 1987, AJ **94**, 899

Dunlop J. S., Taylor G. L., Hughes D. H., Robson E. I., 1993, MNRAS **264**, 455

Du Puy D., Schmitt J., McClure R., 1969, ApJ **156**, L135

Elvis M., Plummer D., Schachter J., Fabbiano G., 1992, A&AS **80**, 257

Engels D., Hagen H.-J., Cordis L., et al., 1997, A&AS **128**, 507

Falomo R., Kotilainen J. K., 1999, A&A **352**, 85

Falomo R., Urry C. M., Scarpa R., et al., 1999, in: PASPC Vol. **159**, eds. L. O. Takalo, A. Sillanpää, p. 389, astro-ph/9812353

Fanaroff B. L., Riley J. M., 1974, MNRAS **167**, 31

Ferrari A., 1998, ARA&A **36**, 539

Fichtel C. E., Bertsch D. L., Chiang J., et al., 1994, ApJS **94**, 551

Fink H. H., 1992, Contributions to the Sympos. "Space science with part. emphasis on High Energy Astrophysics"

Fiore F., La Franca F., Giommi P., et al., 1999, MNRAS **306**, L55

Forman W., Jones C., Cominsky L., et al., 1978, ApJS **38**, 357

Fossati G., Maraschi L., Celotti A., et al., 1998, MNRAS **299**, 433

Fossati G., Haardt, 1998, astro-ph/9804282

Fossati G., 1999, in: PASPC Vol. **159**, eds. L. O. Takalo, A. Sillanpää, p. 351, astro-ph/9810230

Franceschini A., Hasinger G., Miyaji T., Malquori D., 1999, MNRAS **310**, L5

Freeman K. C., 1970, ApJ **160**, 812

French H. B., 1980, ApJ **240**, 41

Frontera F., Costa E., Dal Fiume D., et al., 1997, A&AS **122**, 357

Fukazawa Y., Makishima K., Ebisawa K., et al., 1994, PASJ **46**, L141

Gehren T., Fried J., Wehinger P. A., Wyckoff S., 1984, ApJ **278**, 11

Georganopoulos M., Marscher A. P., 1998, ApJ **506**, 621

Georganopoulos M., Marscher A. P., 1999, in: PASPC Vol. **159**, eds. L. O. Takalo, A. Sillanpää, p. 359

Ghisellini G., Padovani P., Celotti A., Maraschi L., 1993, ApJ **407**, 65

Ghisellini G., Madau P., 1996, MNRAS **280**, 67

Ghisellini G., Celotti A., Fossati G., et al., 1998, MNRAS **301**, 451

Ghisellini G., 1998, "MeV synchrotron BL Lacs", invited paper for the Third INTEGRAL Workshop: "The Extreme Universe", Taormina 1998, astro-ph/9812419

Ghisellini G., 1999, in: PASPC Vol. **159**, eds. L. O. Takalo, A. Sillanpää, p. 311, astro-ph/9810230

Giacconi R., Branduardi G., Briel U., et al., 1979, ApJ **230**, 540

Gioia I. M., Maccacaro T., Schild R. E., et al., 1984, ApJ **283**, 495

Gioia I. M., Maccacaro T., Schild R. E., et al., 1990, ApJS **72**, 567

Giommi P., Menna M. T., Padovani P., 1999, MNRAS **310**, 465

Giommi P., Ghisellini G., Padovani P., Tagliaferri G., 2000, accepted for publication in *Astrophysical Letters and Communications*, astro-ph/0003021

Gorenstein P., Harnden R. F., Fabricant D. E., 1981, IEEE Trans. Nucl. Sci. NS-28, 869

Gower J. F. R., 1969, Nature **224**, 569

Gregory P. C., Condon J. J., 1991, ApJS **75**, 1011

Griffiths R. E., Padovani P., 1990, ApJ **360**, 483

Grundahl F., Hjorth J., 1995, MNRAS **275**, L67

Guainazzi M., Matteuzzi A., 1997, SDC-TR 011

Hagen H.-J., 1987, Doctoral thesis, Hamburg University

Hagen H.-J., Groote D., Engels D., Reimers D., 1995, A&AS **111**, 195

Hagen H.-J., Engels D., Reimers D., 1999, A&AS **134**, 483

Halpern J. P., Eracleous M., Forster K., et al., 1998, ApJ **501**, 103

Hartman R. C., 1999, in: Takalo L. et al. eds., "The BL Lac phenomenon", Turku, Finland, PASPC Vol. **159**, p. 199

Hartman R. C., Bertsch D. L., Bloom S. D., et al., 1999, ApJS **123**, 79

Hartmann D., Burton W. B., 1997, Cambridge University Press

Hasinger G., Burg R., Giacconi R., et al., 1998, A&A **329**, 482

Heidt J., Wagner S. J., 1998, A&A **329**, 853

Heidt J., 1999, in: Takalo L. et al. eds., "The BL Lac phenomenon", Turku, Finland, PASPC Vol. **159**, p. 367, astro-ph/9812259

Henke B. L., Lee P., Tanaka T. J., Shimabukuro R. L., Fujikawa B. K., 1982, Atomic Data and Nucl. Data Tables, **27**, 1

Hewett P. C., Foltz C. B., 1994, PASP **106**, 113

Hewett P. C., Foltz C. B., Chaffee F. H., 1995, AJ **109**, 1498

Hoffmeister C., 1929, Astron. Nachr. **236**, 233

Huchra J. & Burg R., 1992, ApJ **393**, 90

Huchra J., Davis M., Latham D., Tonry J., 1983, ApJS **52**, 89

Impey C., 1988, in "BL Lac Objects", proceedings of a workshop held in Como, Italy, eds. L. Maraschi, T. Maccacaro, M.-H. Ulrich, page 473

Impey C., Neugebauer G., 1988, AJ **95**, 307

Jahnke K., 1998, Diploma thesis, Hamburg University, http://www.hs.uni-hamburg.de/german/persons/kj/dipl/dipl.ps.gz

Januzzi B. T., Smith P. S., Elston R., 1994, ApJ **428**, 130

Kanbach G., et al., 1988, Space Sci. Rev. **46**, 69

Kedziora-Chudczer L., Jauncey D. L., Wieringa M. H., et al., 1997, ApJ **490**, L9

Keel W. C., 1983, ApJ **269**, 466

Kelson D. D., van Dokkum P. G., Franx M., et al., 1997, ApJ **478**, L13

Khachikian E. Y., Weedman D. W., 1974, ApJ **192**, 581

Kinman T. D., 1975, ApJ **197**, L49

Kirhakos S., Sargent W. L. W., Schneider D. P., et al., 1994, PASP **106**, 646

Kirk J. G., Rieger F. M., Mastichiadis A., 1999, in: Takalo L. et al. eds., "The BL Lac phenomenon", Turku, Finland, PASPC Vol. **159**, p. 325

KODAK, 1973, Plates and Films, Eastman Kodak Company

Köhler T., Groote D., Reimers D., Wisotzki L., 1997, A&A **325**, 502

Köhler T., 1996, Doctoral thesis, Hamburg University

Kollgaard R. I., Palma C., Laurent-Muehleisen S. A., Feigelson E. D., 1996, ApJ **465**, 115

Krull F., 1997, Doctoral thesis, Eberhard-Karls Universität Tübingen

Kubo H., Takahashi T., Madejski G., et al., 1998, ApJ **504**, 693

Kühr H., Schmidt G. D., 1990, AJ **99**, 1

Landau R., Golisch B., Jones T. J., et al., 1986, ApJ **308**, 78

Landt H., 1997, Diploma thesis, Hamburg University

Landt H., Padovani P., 1999, American Astronomical Society Meeting **195**, 65.07

Lasker B. M., Sturch C. R., Lopez C., Mallama A. D., McLaughlin S. F., et al., 1988, ApJS **68**, 1

Lähteenmäki A., Valtaoja E., 1999, ApJ **521**, 492

Laurent-Muehleisen S. A., Kollgaard R. I., Ciardullo R., et al., 1998, ApJS **118**, 127

Laurent-Muehleisen S. A., Kollgaard R. I., Feigelson I. D., et al., 1999, ApJ **525**, 127

Ledden J. E., O'Dell S. L., 1985, ApJ **298**, 630

Lin Y. C., Bertsch D. L., Chiang J., et al., 1992, ApJ **401**, L61

Lin D. N. C., Jones B. F., Klemola A. R., 1995, ApJ **439**, 652

Maccacaro T., Gioia I. M., Wolter A., et al., 1988a, ApJ **326**, 680-690

Maccacaro T., Gioia I. M., Schild R. E., et al., 1988b, in "BL Lac Objects", proceedings of a workshop held in Como, Italy, eds. L. Maraschi, T. Maccacaro, M.-H. Ulrich, page 222

Maccacaro T., Wolter A., McLean B., et al., 1994, Astron. Letters & Communication **29**, 267

Maccacaro T., Caccianiga A., Della Ceca R., Wolter A., 1998, AN **319**, 15

Maccagni D., Maraschi L., Tanzi E. G., et al., 1983, ApJ **273**, 75

MacLeod J. M., Andrew B. H., 1968, Ap. Letters **1**, 243

Madau P., Ghisellini G., Persic M., 1987, MNRAS **224**, 257

Maiolino R., Alonso-Herrero A., Anders S., 2000, ApJ **531**, 219

Mannheim K., 1993, A&A **269**, 67

Maraschi L., Ghisellini G., Tanzi E. G., Treves A., 1986, ApJ **310**, 325

Maraschi L., Ghisellini G., Celotti A., 1992, ApJ **397**, L5

Maraschi L., Rovetti F., 1994, ApJ **436**, 79

Maraschi L., Fossati G., Tagliaferri G., Treves A., 1995, ApJ **443**, 578

Maraschi L., Fossati G., Tavecchio F., et al., 1999, ApJ **526**, L81

Marchã M. J. M., Browne I. W. A., Impey C. D., Smith P. S., 1996, MNRAS **281**, 425

Margon B., Jones T. W., Wardle J. F. C., 1978, AJ **83**, 1021

Marscher A. P., 1993, in "Physics of AGN", W. Duschl & S. Wagner (Eds.), p. 510

Marshall H. L., 1985, AJ **299**, 109

Marshall H. L., Fruscione A., Carone T. E., 1995, ApJ **439**, 90

Martini P., Pogge R. W., 1999, AJ **118**, 2646

Mason K. O., Carrera F. J., Hasinger G., et al., 2000, MNRAS **311**, 456

Mattig W., 1958, AN **284**, 109

Mattox J. R., Wagner S. J., Malkan M., et al., 1997 , ApJ **476**, 629

McHardy I. M., 1996, ASP Conf. Series **110**, 293

McLeod K. K., Rieke G. H., 1994a, ApJ **420**, 58

McLeod K. K., Rieke G. H., 1994b, ApJ **431**, 137

McNaron-Brown K., Johnson W. N., Jung G. V., et al., 1995, ApJ **451**, 575

Meurs E. J. A., Wilson A. S., 1984, A&A **136**, 206

Morris S. L., Stocke J. T., Gioia I. M., et al., 1991, ApJ **380**, 49

Morrison, R., Mc Cammon, D., 1983, ApJ., **270**, 119

Mujica R., Zickgraf F.-J., Appenzeller I., et al., 1999, in: PASPC Vol. **159**, eds. L. O. Takalo, A. Sillanpää, p. 513

Mushotzky R. F., Cowie L. L., Barger A. J., Arnaud K. A., 2000, Nature **404**, 459

Nass P., Bade N., Kollgaard R. I., et al., 1996, A&A **309**, 419

Oke J. B., Neugebauer G., and Becklin E. E., 1969, ApJ **156**, L41

Oke J. B., Gunn J. E., 1974, ApJ **189**, L5

Orr A., Parmar A. N., Yaqoob T., Guainazzi M., 1998, in: Proceedings of the Active X-ray Sky symposium, October 21-24, 1997, Rome, eds. Scarsi et al., astro-ph/9712274

Owen F. N., Ledlow M. J., Keel W. C., 1996, AJ **111**, 53

Pace O., Pawlak D., Winkler C., 1994, ApJS **92**, 339

Padovani P., Urry C. M., 1990, ApJ **356**, 75

Padovani P., 1992, MNRAS **257**, 404

Padovani P., Giommi P., 1995a, ApJ **444**, 567

Padovani P., Giommi P., 1995b, MNRAS **277**, 1477

Padovani P., Giommi P., 1996, MNRAS **279**, 526

Padovani P., Landt H., Perlman E., Giommi P., 1999, AAS **195**, 1603

Parmar A. N., Martin D., Bavdaz M., et al., 1997, A&AS **122**, 309

Perlman E. S., Stocke J. T., 1993, ApJ **406**, 430

Perlman E. S., Stocke J. T., Schachter J. F., et al., 1996, APJS **104**, 251

Perlman E. S., Padovani P., Giommi P., et al., 1998, AJ **115**, 1253

Pigg J. C., Cohen M. H., 1971, PASPC **83**, 680

Press W., Teukolsky S., Vetterling W., Flannery B., 1994, "Numerical Recipes in C", Sec. Edt., Cambridge Univerity Press

Punch M., Akerlof C. W., Cawley M. F., et al., 1992, Nature **358**, 477

Pursimo T., Takalo L. O., Sillanpää A., et al., 2000a, A&AS **146**, 141

Pursimo T., 2000b, Doctoral thesis, Annales Universitatis-Turkuensis **260**, Turku, Finland

Pursimo T., Smith P. S., Nilsson K., et al., 2000c, A&A submitted

Pursimo T., Nilsson K., Takalo L. O., et al., 2000d, A&A submitted

Qian S. J., Quirrenbach A., Witzel A., et al., 1993, A&A **241**, 15

Quinn J., Akerlof C. W., Biller S., et al., 1996, ApJ **456**, L83

Quinn J., 1999, in: PASPC Vol. **159**, eds. L. O. Takalo, A. Sillanpää, p. 239

Rector T. A. & Stocke J. T., 2000, in prep.

Rector T. A., Stocke J. T., Perlman E. S., et al., 2000, AJ **120**, 1626

Reeves J. N., Turner M. J. L., Ohashi T., Kii T., 1997, MNRAS **292**, 468

Reimers D., 1990, The Messenger **60**, 13

Reimers D., Köhler T., Wisotzki L., 1996, A&AS **115**, 235

Ricketts M. J., Cooke B. A., Pounds K. A., 1976, Nature **259**, 546

Rönnback J., Van Groningen E., Wanders I., Örndahl E., 1996, MNRAS **283**, 282

Salvati M., Maiolino R., 2000, in: "Large Scale Structure in the X-ray Universe", Proceedings of the 20-22 September 1999 Workshop, Santorini, Greece, eds. Plionis, M. & Georgantopoulos, I., Atlantisciences, Paris, France, p.277, astro-ph/0001332

Sambruna R. M., Maraschi L., Urry C. M., 1996, ApJ **463**, 444

Sarajedini V. L., Green R. F., Griffiths R. E., Ratnatunga K., 1999, ApJ **514**, 746

Scarpa R., Urry C. M., Falomo R., et al., 1999a, ApJ **521**, 134

Scarpa R., Urry C. M., Falomo R., et al., 1999b, in: PASPC Vol. **159**, eds. L. O. Takalo, A. Sillanpää, p. 413

Scarpa R., Urry C. M., Falomo R., et al., 2000, ApJ **532**, 740

Schartel N., Fink H., Brinkmann W., Trümper J., 1992, MPE Report **235**, 195

Schartel N., 1994, Doctoral thesis, MPE Garching

Schmidt M., Green R. F., 1983, ApJ **269**, 352

Schmidt M., Green R. F., 1986, ApJ **305**, 68

Schmidt M., Hasinger G., Gunn J., et al., 1998, A&A **329**, 495

Schmitt J. L., 1968, Nature **218**, 663

Schneider P., Ehlers J., Falco E. E., 1993, "Gravitational Lenses", Springer Verlag

Schwarz M. P., 1981, ApJ **247**, 77

Schweizer F., 2000, to appear in the Philosophical Transactions of the Royal Society, Series A, astro-ph/0002263

Schwope A. D., Hasinger G., Lehmann I., et al., 2000, Astron. Nachr. **321**, 1

Seaton M. J., 1979, MNRAS **187**, 73

Shuder J. M., Oserbrock D. E., 1981, ApJ **250**, 55

Siebert J., Brinkmann W., Laurent-Muehleisen S. A., Matsuoka M., 1998, in: Makishima K., Piro L. (Eds.), Proceedings of the 32nd COSPAR Scientific Assembly, Nagoya, Japan, Advances in Space Research, astro-ph/9808231

Sikora M., Begelman M. C., Rees M. J., 1994, ApJ **421**, 153

Sillanpää A., Haarala S., Valtonen M. J., et al., 1988, ApJ **325**, 628

Sillanpää A., Takalo L. O., Pursimo T., et al., 1996, A&A **305**, L17

Skrutskie M. F., Beichman C., Capps R., 1995, "The 2MASS", American Astronomical Society Meeting **187**, 75.07

Smith E. P., O'Dea C. P., Baum S. A., 1995, ApJ **441**, 113

Stark A. A., Gammie C. F., Wilson R. W., et al., 1992, ApJS **79**, 77

Stein W. A., O'Dell S. L., Strittmatter P. A., 1976, ARA&A **14**, 173

Stein W. A., 1978, in Pittsburgh Conference on BL Lac objects, ed. A. M. Wolfe

Stickel M., Fried J. W., Kühr H., 1991, ApJ **374**, 431

Stickel M., Padovani P., Urry C. M., et al., 1993, A&AS **98**, 393

Stiening R., Skrutskie M. F., Capps R., 1995, "The 2MASS: Survey Telescopes and Cameras", American Astronomical Society Meeting **187**, 75.08

Stocke J. T., Morris S. L., Gioia I. M., Maccacaro T., et al., 1991, ApJS **76**, 813

Stocke J. T., Morris S. L., Gioia I. M., et al., 1990, ApJ **348**, 141

Stocke J. T., Liebert J., Schmidt G. D., 1985, ApJ **298**, 619

Strittmatter P. A., Serkowski K., Carswell R. F., et al., 1972, ApJ **175**, L7

Takalo L. O., 1996, in "Blazar Continuum Variability" eds. H. R. Miller, J. Noble, and J. Webb, PASPC **110**, 70

Tananbaum A., Avni Y., Branduardi G., et al., 1979, ApJ **234**, L9

Tavecchio F., Maraschi L., Ghisellini G., 1998, ApJ **509**, 608

Tavecchio F., Maraschi L., Ghisellini G., et al., 2000, accepted for publication in *Astrophysical Letters and Communications*, astro-ph/0003019

Tesch F., 2000, Doctoral thesis, Hamburg University

Thompson D. J., Bertsch D. L., Dingus B. L., 1996, ApJS **107**, 227

Tody D., 1993, in: Astronomical Data Analysis Software and Systems II, A.S.P. Conference Series **52**, R. J. Hanisch, R. J. V. Brissenden, and Jeannette Barnes, eds., p. 173

Toomre A., Toomre J., 1972, ApJ **178**, 623

Trager S. C., Faber S. M., Worthey G., Gonzalez J. J., 2000, AJ **119**, 1645

Trümper J., 1983, Adv. Space Res. **2**, 241

Trümper J., Hasinger G., Aschenbach B., et al., 1991a, Nature **349**, 579

Trümper, J., 1991b, ROSAT call for proposals for the second observing perios: technical appendix

Urry C. M., Shaefer R. A., 1984, ApJ **280**, 569

Urry C. M., Padovani P., Stickel M., 1991, ApJ **382**, 501

Urry C. M., Padovani P., 1995, PASP **107**, 803

Urry C. M., 1999, in: Takalo L. et al. eds., "The BL Lac phenomenon", Turku, Finland, PASPC Vol. **159**, p. 3, astro-ph/9812420

Urry C. M., Scarpa R., O'Dowd M., et al., 2000, ApJ **532**, 816 van Dokkum P. G., Franx M., 1996, MNRAS **281**, 985

van Schewick H., 1941, Kleine Veröffentlichungen der Universitätssternwarte Berlin-Babelsberg, No. **24**

Veilleux S., Osterbrock D. E., 1987, ApJS **63**, 295

Verner D. A., Barthel P. D., Tytler D., 1994, A&AS **108**, 287

Véron-Cetty M.-P., Woltjer L. J., 1990, A&A **206**, 69

Véron-Cetty M.-P., Véron P., 1993, A&AS **100**, 521

Véron-Cetty M.-P., Véron P., 1998, ESO Sci. Rep. 18, 1

Villata M., Raiteri C. M., Lanteri L., et al., 1998, A&AS **130**, 305

Villata M., Raiteri C. M., Popescu M. D., et al., 2000, A&AS **144**, 481

Visvanathan N., 1969, ApJ **155**, L133

Vogel S., Engels D., Hagen H.-J., et al., 1993, A&AS **98**, 193

Voges, W., 1992, in Proceedings on European International Space Year Meeting ESA ISY-3, 9

Voges W., Gruber R., Paul J., et al., 1992a, in Proceedings on European International Space Year Meeting ESA ISY-3, 223

Voges W., Aschenbach B., Boller Th., et al., 1999, A&AS **349**, 389

Wagner S. J., 1999, in: Takalo L. et al. eds., "The BL Lac phenomenon", Turku, Finland, PASPC Vol. **159**, p. 279

Wagner S. J., Witzel A., 1995, ARA&A **33**, 163

Wall J. V., Peacock J. A., 1985, MNRAS **216**, 173

Walter R., Fink H. H., 1993, A&A **274**, 105

White R. I., Becker, R. H., Helfand D. J., Gregg M. D., 1997, ApJ **475**, 479

Winkler C., 1999, 3rd INTEGRAL workshop, Sep 1998, Taormina/Italy, to be published in *Astrophys. Letters & Communications*, astro-ph/9901088

Wisotzki L., Köhler T., Groote D., Reimers D., 1996, A&AS **115**, 227

Wisotzki L., Christlieb N., Bade N., Beckmann V., et al., 2000, A&A **358**, 77

Wisotzki L., 2000a, A&A **353**, 853

Wisotzki L., 2000b, A&A **353**, 861

Wolter A., Caccianiga A., Della Ceca R., Maccacaro T., 1994, ApJ **433**, 29

Wolter A., Comastri A., Ghisellini G., et al., 1998, A&A **335**, 899

Wurtz R., Stocke J. T., Yee H. K. C., 1993, AJ **106**, 869

Wurtz R., Stocke J. T., Yee H. K. C., 1996, ApJS **103**, 109

Wurtz R., Stocke J. T., Ellingson E., Yee H. K. C., 1997, ApJ **480**, 547

Zhang Y. H., Celotti A., Treves A., et al., 1999, ApJ **527**, 719

Ziegler B. L., Bender R., 1997, MNRAS **291**, 527

Ziegler B. L., Saglia R. P., Bender R., et al., 1999, A&A **346**, 13

List of Publications

Refereed articles

Bade N., Beckmann V., Douglas N. G., Barthel P. D., Engels D., Cordis L., Nass P., Voges W., 1998, "On the evolutionary behaviour of BL Lac objects", A&A **334**, 459-472

Bade N., Engels D., Voges W., Beckmann V., et al., 1998, "The Hamburg/RASS Catalogue of optical identifications", A&AS **127**, 145

Reimers D., Jordan S., Beckmann V., Christlieb N., Wisotzki L., 1998, "Four magnetic DB white dwarfs discovered by the Hamburg/ESO survey", A&A **337**, L13

Beckmann V., Bade N., Wucknitz O., 1999, "The extreme high frequency peaked BL Lac 1517+656", A&A **352**, 395

Wu X.-B., Bade N., Beckmann V., 1999, "X-ray luminous radio-quiet high redshift QSOs in the ROSAT All-Sky Survey", A&A **347**, 63

Sanchez-Fernandez C., Castro-Tirado A. J., Duerbeck H. W., Mantegazza L., Beckmann V., Burwitz V., Bianchini A., Della Valle M., Dirsch B., Hook I., Yan L., Gimenez A., 1999, "Optical observations of the black hole candidate XTE J1550-564 during the September/October 1998 outburst", A&A **348**, L9

Watson D., McBreen B., Smith N., Hanlon L., Tashiro M., Foley T., Metcalfe L., Beckmann V., Sanchez S., Terasranta H., 1999, "Simultaneous Multifrequency Observations of the BL Lac MS0205.7+3509", A&A **345**, 414

Wisotzki L., Christlieb N., Bade N., Beckmann V., et al., 2000, "The Hamburg/ESO survey for bright QSOs. III. A large flux-limited sample of QSOs", A&A 358, 77

Pursimo T., Takalo L. O., Sillanpää A., Beckmann V., et al., 2000, "Intensive Monitoring of OJ 287", A&AS **146**, 141

Beckmann V., Wolter A., 2000, "New results from the Hamburg BL Lac sample", accepted for publication in *Astrophysical Letters and Communications*, astro-ph/0007089

Beckmann V., 2000, "Absolute photometry of 49 X-ray selected BL Lacs", *BLAZAR Data* **2**, 3, http://bldata.pg.infn.it/articles.html

Beckmann V., Wolter A., Giommi P., et al., 2001, " *Beppo*SAX Spectral Survey of BL Lacs - new spectra and results", in prep.

Della Ceca R., Pellegrini S., Beckmann V., et al., 2001, "Unveiling the AGN powering the "Composite" Seyfert/Star-forming galaxy NGC 7679: BeppoSAX results", in prep.

Wilhelm R., Beckmann V., Vierling W., 2001, "Influence of calcium and magnesium on membrane surface potential in mammalian heart ventricular cells", Biophysical Journal in prep.

Conference proceedings

Beckmann V., 1999a, "Evolutionary behaviour of BL Lac objects", in: Takalo L. et al. eds., "The BL Lac phenomenon", Turku, Finland, PASPC Vol. **159**, p. 493, astro-ph/9810154

Della Ceca D., Braito V., Beckmann V., Cagnoni I., Maccacaro T., 2000, "The ASCA HSS: Looking for Type 2 AGN", Proceedings of the Fourth Italian Conference on AGNs, Trieste (Italy) May 15-18 2000. To be published in Mem. Soc. Astr. It., astro-ph/0007431

Abbreviations

AGN	Active Galactic Nucleus
APM	Automatic Plate Measuring (Institute of Astronomy in Cambridge)
ASCA	Advanced Satellite for Cosmology and Astrophysics
BLR	Broad line region
BSC	ROSAT All-Sky Survey Bright Source Catalogue
CA	Calar Alto Observatory
CAFOS	Calar Alto Faint Object Spectrograph
CCD	Charge-Coupled Device
CfA	Harvard-Smithsonian Center for Astrophysics
CGRO	(Arthur Holley) Compton Gamma-Ray Observatory
CXB	Cosmic X-ray background
DFOSC	Danish Faint Object Spectrograph and Camera
DXRBS	Deep X-ray Radio Blazar Survey
EC	External Compton Scattering model
EGRET	Energetic Gamma-Ray Experiment Telescope
EMSS	EINSTEIN Observatory Extended Medium Sensitivity Survey
EW	equivalent width
FIRST	Faint Images of the Radio Sky at twenty-centimeters
FR	Fanaroff & Riley
FSRQ	Flat Spectrum Radio Quasar
FWHM	Full Width at Half Maximum
GIS	Gas Imaging Spectrometer (ASCA)
GSPC	Guide Star Photometric Catalog
HBL	High frequency cut-off BL Lac object / High frequency peaked BL Lac object
hcps	hard $(0.5 - 2.0\,\mathrm{keV})$ ROSAT-PSPC count rate
HEAO2	EINSTEIN satellite
HES	Hamburg/ESO Survey
HPQ	Highly Polarized Quasars
HQS	Hamburg Quasar Survey
HR	Hardness Ratio
HRC	Hamburg RASS Catalogue of optical identifications
HRI	High-Resolution Imager
HRX	Hamburg/ROSAT X-ray bright sample
HST	Hubble Space Telescope
HSS	ASCA Hard Serendipitous Survey
IC	Inverse Compton Scattering
IBL	Intermediate BL Lac object
IDV	Intraday Variability
INTEGRAL	International Gamma-Ray Astrophysics Laboratory
IPC	*EINSTEIN* Imaging Proportional Counter
IRAF	Image Reduction and Analysis Facility
IRAS	Infrared Astronomical Satellite
ISIS	Intermediate-dispersion Spectrograph and Imaging System

LBL	Low frequency cut-off BL Lac object / Low frequency peaked BL Lac object
LDS	Leiden/Dwingeloo Survey (for Galactic neutral hydrogen)
LECS	Low Energy Concentrator Spectrometer (*Beppo*SAX)
LF	Luminosity Function
MECS	Medium Energy Concentrator Spectrometer
MIDAS	Munich Image Data Analysis System (ESO)
MOS	Multiobject Spectroscopy
MOSCA	Multi-Objekt Spectrograph at the Calar Alto 3.5m telescope
NED	NASA/IPAC Extragalactic Database
NELG	Narrow-Emission-Line Galaxy
NFI	Narrow Field Instruments (*Beppo*SAX)
NLR	Narrow Line Region
NRAO	National Radio Astronomy Observatory (USA-VA)
NVSS	NRAO VLA Sky Survey
OAB	Osservatorio Astronomico di Brera
OSSE	Oriented Scintillation Spectrometer Experiment
OVV	Optical Violent Variable
PDS	Phoswich Detector System (*Beppo*SAX) *or* PDS 1010G microdensitometer
PSC	2MASS Second Incremental Release Point Source Catalog
PSF	Point Spread Function
PSPC	Position Sensitive Proportional Counter (ROSAT)
RASS	ROSAT All-Sky Survey
RBL	Radio selected BL Lac object
RDS	ROSAT Deep Survey
REX	Radio Emitting X-ray survey
RGB	ROSAT All-Sky Survey Green Bank sample
RIXOS	ROSAT International X-ray Optical Survey
ROSAC	A ROSAT based Search for AGN Clusters
SED	Spectral Energy Distribution
SIMBAD	Set of Identifications, Measurements, and Bibliography for Astronomical Data
SIS	Solid-state Imaging Spectrometer (ASCA)
SNR	Supernova Remnant
SRSQ	Steep Radio Spectrum Quasar
SSC	Synchrotron Self Compton Scattering
SSRQ	Steep Spectrum Radio Quasar
UHBL	Ultra High Frequency Peaked BL Lacs
USNO	United States Naval Observatory (USA-DC)
VLA	Very Large Array
WFI	Wide Field Imager
WHT	William Herschel Telescope
XBL	X-ray selected BL Lac object
XSC	2MASS Second Incremental Release Extended Source Catalog
XMM	X-ray Multimirror Mission
2MASS	Two-Micron All-Sky Survey

Acknowledgments

I would like to thank Prof. Dr. Dieter Reimers for giving me the opportunity to work with the Quasar Groups at the *Hamburger Sternwarte*. The friendly and supportive atmosphere inherent to the whole Quasar Group contributed essentially to the final outcome of my studies. In this context I would like to thank particularly Hans Hagen, Dieter Engels, and Olaf Wucknitz. Without their support the completion of this dissertation would not have been possible.

I would like to thank Norbert Bade who initiated the BL Lac project and was always helpful with advice.

For their hospitality I would like to thank the group at the *Osservatorio Astronomico di Brera* at Milan, especially Anna Wolter, Roberto Della Ceca, and Tommaso Maccacaro since this PhD project profitted a lot from our interesting discussions and the many new impulses I received from them.

In addition to the colleagues above mentioned Professora Laura Maraschi supported the process of writing this thesis by giving me important advice how to optimize my work.

I am particularly grateful to Gerry Williger, who was so kind as to read the whole manuscript thoroughly and correct the English spelling and grammar and contributed also to the scientific discussion.

Apart from my colleagues, I would like to thank my family and friends who have never lost faith in this long-term project.

This work received financial support from the *Deutsche Forschungs Gemeinschaft* (DFG), the *Deutsche Akademische Austauschdienst* (DAAD), the *Osservatorio Astronomico di Brera*, the *Consiglio Nazionale delle Ricerche* (CNR), and from my parents.

Erklärung

Ich versichere, dass ich diese Arbeit selbstständig verfasst und nur die angegebenen Quellen und Hilfsmittel verwendet habe.

Hamburg, den 5. Dezember 2000